Search for New Physics with ATLAS at LHC - Z' dilepton resonance at high mass

Vanja Morisbak

THESIS SUBMITTED FOR THE DEGREE
MASTER OF SCIENCE

Department of Physics
University of Oslo

January 2011

Abstract

New, neutral gauge bosons appear in various theories extending beyond the current theory of particle physics, the Standard Model. In this thesis we review the discovery potential of one specific gauge boson, the Sequential Standard Model Z', with the ATLAS detector at LHC. A feasibility study is performed at 10 TeV center of mass collisions, ultimately ending in the discovery reach as a function of the Z' mass. The full 2010 data taken at 7 TeV center of mass energy, corresponding to $\sim$40 pb^{-1}, are analysed first with focus on the Z^0 boson resonance and the performance of the ATLAS detector with leptons. This is then followed by a search for high mass resonances decaying to e^+e^- and $\mu^+\mu^-$. Based on statistical errors only, the SSM Z' with mass up to 995 GeV is excluded at 95% confidence level.

Acknowledgements

First and most of all I would like to thank my supervisor Farid Ould-Saada for ideas, suggestions and inspiration these last couple of years. But there are more people deserving acknowledgement. I found that the EPF group is extraordinary in more ways than one. Not only because of the inspiring working environment, but also because of the people. So thank you, people of EPF, for lunches and cakes and celebrations.

A special thanks to Zofia Czyczula for answering my many questions, and to Silje Hattrem Raddum for relevant and non-relevant conversations.

Last but not least, thanks to Magnar Kopangen Bugge for being my soft place to fall.

Introduction

The last three years, 2008 to 2010, were exciting times to be an experimental particle physicist. During these years, the Large Hadron Collider, located in Geneva, Switzerland, has explored hitherto unknown territory, i.e. collisions at higher center of mass energy than ever reached before, reproducing the conditions that prevailed in the very early Universe.

Before the first collisions in November 2009 the world held its breath. Without warning a great wave of fear had traversed the globe; would the LHC create ever-growing micro black holes that would devour the Earth? The media jumped on the idea. We, however, knew that whatever micro black hole was created would evaporate in a tiny fraction of a second. After the first collisions and the survival of our planet, the collective fear slowly died away. Even though our intention never was to scare people, these events made sure that many now know about the LHC and the exciting times ahead.

November 23rd 2009, 14:22 in the afternoon, the first collision candidate at 900 GeV center of mass energy was seen in the ATLAS detector (figure 1), one of the four main experiments at the LHC. This was a great day for particle physicists all over the world, filled with hope and dreams of grand discoveries. Since that day many hundreds of thousands of millions collisions have been recorded and are as we speak under strict scrutiny, employing thousands of students and researchers worldwide. The result is more than 20 publications only within the ATLAS collaboration.

The focus up till now has been mostly on rediscovering the Standard Model of particle physics and on understanding the detector response to the new energy regime. It is of the greatest importance that we make absolutely sure that we understand and explain everything we observe. The collective knowledge of the field of particle physics is gathered, and past and present are merged, hopefully providing an even better understanding of the surrounding world.

During 2011 we will gather at least 50 times the amount of data we have today. In this vast amount of information we hope to find the infamous needle in the haystack - the Higgs boson. Its existence was predicted in 1964 independently and almost simultaneously by three different groups of physicists (François Englert and Robert Brout[1], Gerald Guralnik, C. R. Hagen, and Tom Kibble[2], and Peter Higgs[2]). After the discovery of the top quark in 1995 and the third neutrino ν_τ in 2000, the Higgs boson remains the only unobserved Standard Model particle. Many within the particle physics community expect LHC to find it, and great confusion will arise if it is not found. The Higgs boson is a vital ingredient in the Standard Model, and without it new theories must take the place of one of the most well

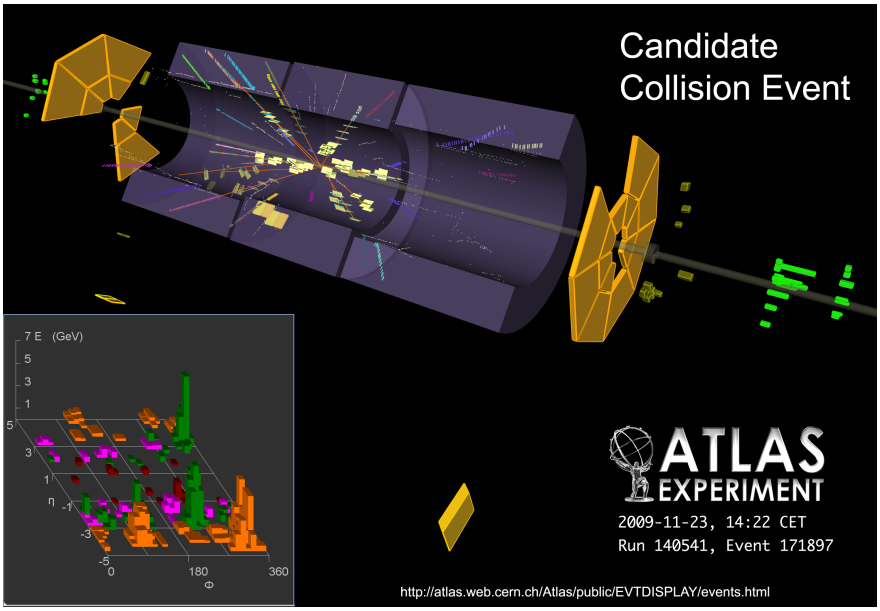

Figure 1: The first collision candidate seen in the ATLAS detector (http://atlas.ch/photos/events-collision.html).

tested theories in history.

Even without the Higgs boson we know that a paradigm shift must occur in the future. The Standard Model is not the final theory of Nature. We believe it to be correct in the electroweak energy regime, but still only an approximation. Many Beyond the Standard Model theories have been developed over the last century. Many have absorbed the Standard Model, making it a part of a bigger picture, and some stand alone. They are all consistent with experiments up to this date, and the only way to find The theory is by exploring higher energy regimes. This is one of the main reasons for the existence of the LHC. It was built to explore new frontiers, to dig deeper still into the true nature of our Universe.

In some of the Beyond the Standard Model theories, a new massive and electrically neutral gauge boson appears. Searching for this boson is thus one way of exploring the phsics beyond the Standard Model. The Z' properties vary greatly depending on what theory it belongs to. Because of this, a toy model was developed to be used as a "standard candle" in experimental searches, giving a way to compare results easily. This Z' is known as the Sequential Standard Model (SSM) Z', and is the main theme of this thesis.

The thesis consists of seven chapters and three appendices.

In chapter 1 the mathematical formalism of the Standard Model is introduced.

Then in chapter 2, we explore the shortcomings of the Standard Model, thus explaining how we know it is not the final theory. A few popular Beyond the Standard Model theories are introduced, and we also provide a quick overview of a few popular theories that incorporate new neutral gauge bosons (Z'). The most resent results from Tevatron and the LEP collider are reviewed in the context of Z' searches.

Chapter 3 gives an overview of particle interactions with matter that are relevant at the high energy scales at the LHC.

In chapter 4 the LHC is introduced together with a few important concepts regarding particle colliders. Important aspects of the ATLAS detector are explained, specifically the definition of the coordinate system used, the different subdetectors, the concept of triggers and some information on event generation.

Chapter 5 marks the start of the analysis with a feasibility study of a hypothetical new neutral gauge boson Z' at 10 TeV center of mass energy collisions. Using only simulated data we explore how to best enhance the signal and reject the background, resulting in the discovery potential of the Sequential Standard Model (SSM) Z' at masses ranging from 1.0 to 1.5 TeV.

Analysis of 2010 data is done in chapters 6 and 7. In chapter 6 we use cuts to enhance the Z boson resonance, and in chapter 7 we use a set of somewhat different cuts to enhance hypothetical SSM Z' resonances at masses ranging from 1.0 to 2.0 TeV. The discovery potential for a SSM Z' is presentend as well as the exclusion limits based on the full 2010 statistics.

The first appendix describes the training required to be a shifter on one of the ATLAS subdetectors (the Semi Conductor Tracker), while appendix B is about Hands on Particle Physics Master Class, which is an arrangement where high school students are introduced to particle physics and data analysis. Finally, there are three parts of appendix C. The first part describes a recent change in electron identification variables. The second part describes a simple truth matching algorithms, and the third part shows a few examples of the most recent ATLAS public results.

Contents

Chapter 1

The Standard Model of particle physics

We all know it, the model that describes so beautifully three of the four known fundamental interactions - the strong, the weak and the electromagnetic (the two latter united to the electroweak) forces - and the elementary particles. It has been tested time and time again, and nothing is found to be inconsistent with the Standard Model (SM), even though there are some unexplained phenomena not yet understood (see section 2.1 for more on this.)

The strong and electroweak forces are described via exchange of 12 gauge bosons - eight massless gluons (g) for the strong force, one massless photon (γ) for the electromagnetic force, and 3 massive bosons for the weak force ($W^{\pm}$ and Z^0) (see Table 1.2). The matter particles are the six quarks and the six leptons with their corresponding antiparticles (table 1.1).

	Particle	**Mass [GeV/c^2]**	**El. charge [+e]**	**Mean life**
Leptons	electron (e^-)	0.5110×10^{-3}	-1	$> 4.6 \times 10^{26}$yr
	electron neutrino (ν_e)	$< 2 \times 10^{-6}$	0	$>$ 15.4s/eV
	muon (μ^-)	0.1057	-1	2.197×10^{-6}s
	muon neutrino (ν_μ)	$< 0.19 \times 10^{-3}$	0	$>$ 15.4s/eV
	tau (τ^-)	1.777	-1	291×10^{-15}s
	tau netrino (ν_τ)	$< 18.2 \times 10^{-3}$	0	$>$ 15.4s/eV
Quarks	up (u)	1.5 to 3.3×10^{-3}	+2/3	-
	down (d)	3.5 to 6.0×10^{-3}	-1/3	-
	strange (s)	104×10^{-3}	-1/3	-
	charm (c)	1.27	2/3	-
	beauty (b)	4.20	-1/3	-
	top (t)	171	+2/3	0.5×10^{-24}[3]

Table 1.1: The fundamental fermions (spin 1/2) in the Standard Model[4]. In addition there are antiparticles for all these fermions. The antiparticles have the same properties as their respective particles, except with the quantum numbers (like charge and color) reversed.

Physics is about symmetries - we require that the Lagrangian, a scalar quantity describing the theory, is invariant under various symmetry operations, reflecting e.g. the fact that a

Particle	Mass [GeV/c^2]	charge [+e]	Full width [GeV]
gluon (g)	0	0	-
photon (γ)	$< 1 \times 10^{-24}$	$< 5 \times 10^{-30}$	-
W boson ($W^{\pm}$)	80.4	± 1	2.141
Z boson (Z^0)	91.2	0	2.495

Table 1.2: The bosons (spin 1) of the Standard Model that mediate the strong (gluon), electromagnetic (photon) and the weak ($W^{\pm}$ and Z^0 boson) interactions[4].

physical system should be the same if it is rotated in space or if we do an experiment now or in a year from now. It is also about the *breaking* of symmetries, under which our obviously massive gauge bosons gain their mass[1].

In 1961 Sheldon Glashow[5] found a way to combine the electromagnetic and weak interactions in a more fundamental interaction; the electroweak. Then, in 1967, Steven Weinberg[6] and Abdus Salam[7] incorporated the Higgs mechanism into the electroweak theory, making the standard electroweak theory as we know it today (also known as the Glashow-Weinberg-Salam model). Then, in 1973, the first observations of neutral current interactions was made with the Gargamelle bubble chamber at CERN[8]. The actual discovery of the W and Z boson did not come until the upgraded Super Proton Synchrotron (SPS) was operational, colliding protons with anti-protons at unprecedented energies, making the resonances directly observable for the very first time. This was a huge victory for the electroweak theory.

1.1 The mathematical framework

It is all about quantum field theory (QFT) - the universe is permeated by various fields, and we experience the ripples in these fields as different particles. The first successful QFT was that of electrodynamics - Quantum ElectroDynamics (QED) developed from the 1920s to 1940s. Feynman, Schwinger and Tomonaga recieved the 1965 Nobel Prize in Physics for this great achievement.

1.1.1 Classical mechanics and field theory

What one learns in school is the Newtonian mechanics. When taking University classes at graduate level one is suddenly introduced to a new, more elegant way of looking at the world. This is the Lagrangian mechanics[2]. From Newtonian mechanics we are used to thinking in terms of forces (just think of Newton's laws of motion). In Lagrangian mechanics we stop thinking about forces and start dealing with potential and kinetic energy instead. The Lagrangian descibes the dynamics of a system. It is given by the difference in the kinetic and potential energy, $L = T - V$.

[1] This mechanism is still not confirmed by experiment.

[2] Actually there are two quite similar formulations of mechanics, the Lagrangian and Hamiltonian. The latter is based on the former..

It is a function of the generalized coordinates q_i and their time derivatives (velocities) $\dot{p}_i$ (referred to as the *conjugate momentum*[3] of that specific coordinate)

$$p_i \equiv \frac{\partial L}{\partial \dot{q}_i} \tag{1.1}$$

When the constraints on the system are time dependent, the Lagrangian also depends on the time t

$$L(q, \dot{q}, t) = T(q, \dot{q}, t) - V(q, t) \tag{1.2}$$

The number of generalized coordinates equals the number of degrees of freedom of the system.

Knowing the Lagrangian of a system means that we know the time evolution of that system through the Euler-Lagrange equations[4]

$$\frac{d}{dt}\left(\frac{\partial L}{\partial \dot{q}_j}\right) - \frac{\partial L}{\partial q_j} = 0, \quad j = 1, 2, \ldots, d \tag{1.3}$$

In field theory the fields themselves, $\phi_r(x^\mu), r = 1, 2, \ldots, N$, are the independent variables, and we exchange the Lagrangian L for the Lagrangian density $\mathcal{L}$ (but usually *refer to it* as the Lagrangian), such that the Lagrangian density is the difference in the kinetic energy density and the potential energy density, $\mathcal{L} = \mathcal{T} - \mathcal{V}$.

The conjugate momenta (equation (1.1)) (now called the conjugate *fields*)

$$\pi_r(x^\mu) \equiv \frac{\partial \mathcal{L}}{\partial \dot{\phi}_r}$$

and the Euler-Lagrange equations (equation (1.3))

$$\frac{\partial \mathcal{L}}{\partial \phi_r} - \partial_\alpha \left(\frac{\partial \mathcal{L}}{\partial(\partial_\alpha \phi_r)}\right) = 0, \quad \partial_\alpha = \frac{\partial}{\partial x^\alpha}$$

are the same as before, with the proper exchanges made as discussed above.

1.1.2 Quantum field theory

To go from classical fields to quantized field, one interprets the generalized coordinates (the fields and the conjugate fields) as operators and subjects them to commutation relations

$$\left[\phi_r(x_\mu), \pi_s(x'_\mu)\right] = i\hbar\delta_{rs}\delta(x_\mu - x'_\mu) \tag{1.4}$$

$$\left[\phi_r(x_\mu), \phi_s(x'_\mu)\right] = \left[\pi_r(x_\mu), \pi_s(x'_\mu)\right] = 0 \tag{1.5}$$

After that it is a matter of finding the right Lagrangian.

The fields have quanta with the well-defined properties of the classical particle. The interaction between these particles can now be described by other fields whose quanta are different

[3] Also called the *canonical momentum* or *generalized momentum*

[4] Which can be obtained through Hamilton's principle, but we will not go into that here.

particles (force carrying bosons). We are quite used to this in fact. Just think of electrons and positrons pushing each other around by the means of the electromagnetic field.

One of the main reasons for quantizing is that the number of particles no longer needs to be constant. With this new formalism one can explore a new range of phenomena, like decaying particles, and vacuum fluctuations.

1.1.3 Quantum electrodynamics - a gauge theory

To help introduce the basic principles of QFT we introduce the theory descibing fermions, i.e particles with spin 1/2, and we start with the Lagrangian describing *free* fermions.

The free-fermion Lagrangian density $\mathcal{L}_0$ is given by

$$\mathcal{L}_0 = \bar{\psi}(x)(i\gamma^\mu \partial_\mu - m)\psi(x)$$

where m is the rest mass of the spin 1/2 particles. The electromagnetic interaction is introduced by means of minimal substitution

$$\partial_\mu \rightarrow D_\mu = [\partial_\mu + iqA_\mu(x)] \tag{1.6}$$

where q is the charge of the fermion.

Because it is only the electromagnetic fields themselves that have physical significance, not the potential A_μ, the theory needs to be invariant under a gauge transformation of the potientials

$$A_\mu(x) \rightarrow A'_\mu(x) = A_\mu(x) + \partial_\mu f(x) \tag{1.7}$$

where $f(x)$ is an arbitrary real, differentiable function.

The Lagrangian is invariant under this transformation only if the Dirac fields themselves $\psi(x)$ and $\bar{\psi}(x)$ undergo the transformations

$$\begin{aligned} \psi(x) &\rightarrow \psi'(x) = \psi(x)e^{-iqf(x)} \\ \bar{\psi}(x) &\rightarrow \bar{\psi}'(x) = \bar{\psi}(x)e^{iqf(x)} \end{aligned} \tag{1.8}$$

Any theory invariant under gauge transformations such as (1.8), is said to be a gauge theory, of which QED is the simplest example.

Let us look at it the other way: Having the free-fermion Lagrangian density $\mathcal{L}_0$ we *demand* that it is invariant under local phase transformations (1.8) since the phase itself (i.e. $iqf(x)$) has no physical meaning. This makes our Lagrangian change

$$\mathcal{L}_0 \rightarrow \mathcal{L}'_0 = \mathcal{L}_0 + q\bar{\psi}(x)\gamma^\mu\psi(x)\partial_\mu f(x)$$

which is not at all what we want; we want it to be invariant. Thus we augment $\mathcal{L}_0$ by a term $\mathcal{L}_I$ in such a way that the new Lagrangian density $\mathcal{L} = \mathcal{L}_0 + \mathcal{L}_I$ is invariant under the

gauge transformations (1.8) above. This is done by replacing the ordinary derivative $\partial_\mu\psi(x)$ by the *covariant derivative* $D_\mu\psi(x) = [\partial_\mu + iqA_\mu(x)]\psi(x)$, and thus $\mathcal{L}$ becomes

$$\begin{aligned}\mathcal{L} &= \bar{\psi}(x)(i\gamma^\mu D_\mu - m)\psi(x) \\ &= \mathcal{L}_0 - q\bar{\psi}(x)\gamma^\mu\psi(x)A_\mu(x) = \mathcal{L}_0 + \mathcal{L}_I\end{aligned} \tag{1.9}$$

The quantity

$$s_\mu(x) = -q\bar{\psi}(x)\gamma^\mu\psi(x) \tag{1.10}$$

is known as the electromagnetic current.

The covariant derivative $D_\mu\psi(x)$ will, under the gauge transformations (1.8), undergo the transformation

$$D_\mu(x)\psi(x) \to e^{-iqf(x)}D_\mu\psi(x)$$

leaving the Lagrangian density invariant.

$\mathcal{L}_0$ is the Lagrangian density of the free Dirac field while $\mathcal{L}_I$ can be interpreted as the *interaction* Lagrangian density. It is $\mathcal{L}_I$ that couples the conserved electromagnetic current $q\bar{\psi}(x)\gamma^\mu\psi(x)$ to the electromagnetic field $A_\mu(x)$. Figure 1.1 illustrates this with a Feynman diagram of this basic QED vertex. Be aware that this is a non-physical process to the first order as it does not conserve energy and momentum at the same time.

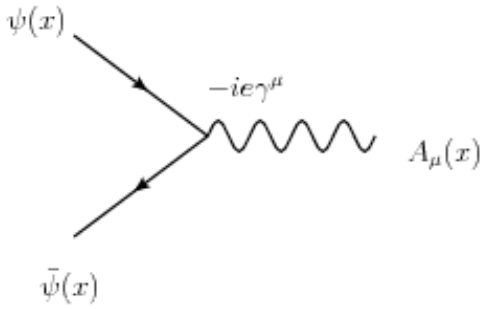

Figure 1.1: A Feynman diagram of the QED basic vertex.

All particle interactions in QED are constructed by combining several of these basic vertices. From this one can calculate the S-matrix.

The S-matrix contains all the information one could possibly want from a collision process to an arbitrary order of perturbation theory. If a system is in the ititial state $|i\rangle$ at an initial time t_i, which in principle is $-\infty$ (in the microscopic world, a few seconds feel like an infinity) and ends up in the final state $|f\rangle$ some time $t_f = \infty$ after the scattering, then the S-matrix is what connects the two states

$$S|i(t_i = -\infty)\rangle = |f(t_f = \infty)\rangle$$

This is what we want in an experiment like ATLAS; we *choose* the inital state (proton-proton collisions[5]), we *measure* the final state, and we ask ourselves "What happened in between?" We wil not get the answer to that just looking at the S-matrix, but we *will* get the probability for that specific final state given our chosen initial state.

$$|\langle f|(S|i\rangle)|^2 = |\langle f|S|i\rangle|^2 \equiv S_{fi}$$

[5]This is flat out wrong of course. What collides is in fact two quarks or gluons.

The S-matrix itself is the solution to the equations of motions for the fields given the initial and final states. It can be calculated to arbitrary orders of perturbation theory

$$S = \sum_{n=0}^{\infty} S^{(n)}$$

where

$$S^{(n)} = \frac{(-1)^n}{n!}\left(\frac{1}{i\hbar}\right)^n \int\int \ldots \int d^4x_1 d^4x_2 \ldots d^4x_n \mathcal{T}\left[\mathcal{H}_I(x_1)\mathcal{H}_I(x_2)\ldots\mathcal{H}_I(x_n)\right]$$

$\mathcal{H}$ is the Hamiltonian density ($\mathcal{H}(x^\mu) = \pi_r(x^\mu)\dot{\phi}_r(x) - \mathcal{L}(\phi_r, \partial_\alpha\phi_r, t)$) and the time-ordered ($\mathcal{T}$) product just means that the operators are written in chronological order (the time runs from right to left).

From the S-matrix one can calculate the things that are experimentally observable, namely cross-sections, decay widths and lifetimes, all of which are of importance to the experimental particle physicist.

Till now we have dealt with free fermions and fermions that interact via the electromagnetic field. But there is still another part of the QED Lagrangian, the part describing the free electromagnetic field, the free Maxwell part, $\mathcal{L}_M$.

This part of the Lagrangian comes from Maxwell's equations, describing electric and magnetic fields. The covariant formulation uses an antisymmetric field tensor, $F^{\mu\nu}(x)$, a 4×4 matrix containing the components of the electric and magnetic fields. The field equations from classical electrodynamics can be derived from the Lagrangian density

$$\mathcal{L} = -\frac{1}{4}F_{\mu\nu}(x)F^{\mu\nu}(x) - \frac{1}{c}s_\mu(x)A^\mu(x)$$

where $s_\mu(x)$ is the electromagnetic current (equation (1.10)), $A_\mu(x)$ is the electromagnetic field (equation (1.6)) and c is the speed of light in vacuum. We recongnize the last term as the fermion-photon interaction.

The field $F^{\mu\nu}$ can be expressed in terms of A^μ as

$$F^{\mu\nu}(x) = \partial^\nu A^\mu(x) - \partial^\mu A^\nu(x) \tag{1.11}$$

This term is invariant under a gauge transformation of the potential $A_\mu(x)$ (see equation (1.7)) and can be added to the QED Lagrangian[6] making the total QED Lagrangian

$$\mathcal{L} = \bar{\psi}(x)(i\gamma^\mu D_\mu - m)\psi(x) - \frac{1}{4}F_{\mu\nu}(x)F^{\mu\nu}(x)$$

QED has been tested experimentally on many occasions[9]. For example the theoretical differential cross-section distribution for several processes (amongst others $e^+e^- \to \gamma\gamma$ and $e^+e^- \to e^+e^-$) has been compared to experimental results. No discrepancies are found.

[6]In reality this is not the formulation used, as problems arise when one tries to do the canonical quantization. A formulation that works is $\mathcal{L} = -\frac{1}{2}(\partial_\nu A_\mu(x))(\partial^\nu A^\mu(x)) - \frac{1}{c}s_\mu(x)A^\mu(x)$. This Lagrangian also returns the Maxwell equations, but only if the potential $A^\mu(x)$ satisfies $\partial_\mu A^\mu(x) = 0$.

1.1.4 Electroweak interactions

Seeing as QED is immensely successful, the same strategy (i.e requiring gauge invariance) is used when developing a framework for the weak interactions as well.

It is important to realize that all of the following requires zero fermion and boson mass. Seeing as both fermions and bosons actually have mass, we want a more realistic model later, incorporating spontaneous symmetry breaking and bringing the Higgs field and its boson to life (see section 1.1.6).

Experiments[10] have shown that the weak force acts on left-handed particles only, leaving the right-handed particles untouched. The chirality (handedness) of a particle is dependent mathematically on whether the particle transforms in a right- or left-handed representation of the Poincaré group. For massless particles the chirality is the same as the helicity[7], giving a more intuitive understanding of the concept.

Because of the fundamental difference between right- and left-handed fields, we write the free-lepton Lagrangian in an asymmetric way, with the left-handed fields grouped in a doublet and the right-handed fields in singlets:

$$\mathcal{L}_0 = i[\bar{\Psi}_l^L(x)\not{\partial}\Psi_l^L(x) + \bar{\psi}_l^R(x)\not{\partial}\psi_l^R(x) + \bar{\psi}_{\nu_l}^R(x)\not{\partial}\psi_{\nu_l}^R(x)], \quad \not{\partial} \equiv \gamma^\mu\partial_\mu \tag{1.12}$$

with

$$\Psi_l^L(x) = \begin{pmatrix} \psi_{\nu_l}^L(x) \\ \psi_l^L(x) \end{pmatrix}$$

We require $\mathcal{L}_0$ to be invariant under local $\mathrm{SU(2)_L}$ and U(1) transformations in analogy with what we did for the free-fermion Lagrangian density in QED.

Introducing the Pauli matrices[8]

$$\tau_1 = \begin{pmatrix} 0 & 1 \\ 1 & 0 \end{pmatrix}, \quad \tau_2 = \begin{pmatrix} 0 & -i \\ i & 0 \end{pmatrix}, \quad \tau_3 = \begin{pmatrix} 1 & 0 \\ 0 & -1 \end{pmatrix}$$

the local $\mathrm{SU(2)_L}$ phase transformations are

$$\begin{aligned} \Psi_l^L(x) \to \Psi_l^{L'}(x) &= e^{\frac{1}{2}ig\tau_j\omega_j(x)}\Psi_l^L(x) \\ \bar{\Psi}_l^L(x) \to \bar{\Psi}_l^{L'}(x) &= \bar{\Psi}_l^L(x)e^{-\frac{1}{2}ig\tau_j\omega_j(x)} \end{aligned} \tag{1.13}$$

where $\omega_j(x)$, $j = 1, 2, 3$ are three real differentiable functions of x, g is a real constant and the Pauli matrices τ_i are the generators of $\mathrm{SU(2)_L}$. We define every right-handed lepton field to be invariant under any $\mathrm{SU(2)_L}$ transformation.

The free-lepton Lagrangian density (1.12) is not invariant under these transformations, and we have to do for this what we did for the free-fermion Lagrangian density of QED. First we replace the ordinary derivatives $\partial^\mu\Psi_l^L(x)$ by the covariant derivatives

$$\partial^\mu\Psi_l^L(x) \to D^\mu\Psi_l^L(x) = [\partial^\mu + \frac{1}{2}ig\tau_j W_j^\mu(x)]\Psi_l^L(x) \tag{1.14}$$

[7]The helicity of a particle is positive if the spin points in the same direction as the direction of motion, and negative if the spin points in the opposite direction.

[8]Satisfying the commutation relations $[\tau_i, \tau_j] = 2i\epsilon_{ijk}\tau_k$ with ϵ_{ijk} being the usual antisymmetric tensor.

giving us a new expression for the Lagrangian density

$$\tilde{\mathcal{L}}_0 = i[\bar{\Psi}_l^L(x)\not{D}\Psi_l^L(x) + \bar{\psi}_l^R(x)\not{\partial}\psi_l^R(x) + \bar{\psi}_{\nu_l}^R(x)\not{\partial}\psi_{\nu_l}^R(x)] \tag{1.15}$$

Notice that we have introduced *three* real gauge fields $W_j^\mu(x)$, one for each $\mathrm{SU(2)_L}$ generator. In QED we only needed one, $A_\mu(x)$.

Secondly we need the covariant derivatives $D^\mu\Psi_l^L(x)$ to transform the same way as the fields themselves. This is achieved by requiring that the gauge fields transform according to

$$\begin{aligned} W_i^\mu(x) \to W_i^{\mu'}(x) &= W_i^\mu(x) + \delta W_i^\mu(x) \\ &\equiv W_i^\mu(x) - \partial^\mu\omega_i(x) - g\epsilon_{ijk}\omega_j(x)W_k^\mu(x) \end{aligned}$$

for small $\omega_j(x)$ [11]. Thus

$$D^\mu\Psi_l^L(x) \to e^{\frac{1}{2}ig\tau_j\omega_j}D^\mu\Psi_l^L(x)$$

Now that we achieved $\mathrm{SU(2)_L}$ invariance, the next step is U(1) invariance: The local phase transformations are

$$\begin{aligned} \psi(x) &\to \psi'(x) = e^{ig'Yf(x)}\psi(x) \\ \bar{\psi}(x) &\to \bar{\psi}'(x) = \bar{\psi}(x)e^{-ig'Yf(x)} \end{aligned} \tag{1.16}$$

where Y is a conserved quantity called the weak hypercharge (to be explained, see equation (1.24)). The Lagrangian density is invariant under the U(1) transformations (1.16) if the ordinary derivatives are replaced by covariant derivatives

$$\partial^\mu\psi(x) \to D^\mu\psi(x) = [\partial^\mu + ig'YB^\mu(x)]\psi(x) \tag{1.17}$$

where $B^\mu(x)$ is a real gauge field that transforms like

$$B^\mu(x) \to B^{\mu'}(x) = B^\mu(x) - \partial^\mu f(x)$$

which is exactly what we saw in QED (equation (1.7)).

Making both replacements (1.17) and (1.14) simultaneously in (1.12) we get the Lagrangian density

$$\mathcal{L} = i[\bar{\Psi}_l^L(x)\not{D}\Psi_l^L(x) + \bar{\psi}_l^R(x)\not{D}\psi_l^R(x) + \bar{\psi}_{\nu_l}^R(x)\not{D}\psi_{\nu_l}^R(x)] \tag{1.18}$$

where now

$$\begin{aligned} D^\mu\Psi_l^L(x) &= \left[\partial^\mu + \frac{1}{2}ig\tau_jW_j^\mu(x) - \frac{1}{2}ig'B^\mu(x)\right]\Psi_l^L(x) \\ D^\mu\psi_l^R(x) &= \left[\partial^\mu - ig'B^\mu(x)\right]\psi_l^R(x) \\ D^\mu\psi_\nu^R(x) &= \partial^\mu\psi_\nu^R(x) \end{aligned} \tag{1.19}$$

Defining the fields $W_i^\mu(x)$ to be invariant under U(1) gauge transformations and $B^\mu(x)$ to be invariant under $\mathrm{SU(2)_L}$ gauge transformations the Lagrangian density $\mathcal{L}$ is invariant under both, and is said to be $\mathrm{SU(2)_L} \times \mathrm{U(1)}$ gauge-invariant.

Before we advance any further, we should take a step back and look at the *global* U(1) and $\mathrm{SU(2)_L}$ transformations.

The global $SU(2)_L$ transformations are the same as the local ones (equation (1.13)), except for the positional dependence of the ω_j ($g\omega_j$ ar now three real numbers, $\mathbf{g}\omega = (g\omega_1, g\omega_2, g\omega_3)$)

$$\begin{aligned} \Psi_l^L(x) &\to \Psi_l^{L'}(x) = e^{\frac{1}{2}ig\omega_j\tau_j}\Psi_l^L(x) \\ \bar{\Psi}_l^L(x) &\to \bar{\Psi}_l^{L'}(x) = \bar{\Psi}_l^L(x)e^{-\frac{1}{2}ig\omega_j\tau_j} \end{aligned} \tag{1.20}$$

When the right handed fields are defined as invariant under these global transformations, the whole free-lepton Lagrangian of Equation (1.12) is obviously invariant as well. We can now use Noether's theorem, stating that the invariance of the Lagrangian implies a conserved quantity, to find the conserved currents. These are the weak isospin currents

$$J_i^\mu(x) = \frac{1}{2}\bar{\Psi}_l^L(x)\gamma^\mu\tau_i\Psi_l^L(x), \quad i = 1, 2, 3 \tag{1.21}$$

With the three conserved currents comes three conserved quantities, the weak isospin charges I_i^W:

$$I_i^W = \int d^3\mathbf{x}J_i^0(x) = \frac{1}{2}\int d^3\mathbf{x}\Psi_l^{L\dagger}(x)\tau_i\Psi_l^L, \quad i = 1, 2, 3$$

We need the expression for J_3^μ:

$$\begin{aligned} J_3^\mu(x) &= \frac{1}{2}\bar{\Psi}_l^L(x)\gamma^\mu\tau_3\Psi_l^L(x) \\ &= \frac{1}{2}\begin{pmatrix}\bar{\psi}_\nu^L(x) & \bar{\psi}_l^L(x)\end{pmatrix}\gamma^\mu\begin{pmatrix}1 & 0\\ 0 & -1\end{pmatrix}\begin{pmatrix}\psi_\nu^L(x)\\ \psi_l^L(x)\end{pmatrix} \\ &= \frac{1}{2}\bar{\psi}_\nu^L(x)\gamma^\mu\psi_\nu^L(x) - \frac{1}{2}\bar{\psi}_l^L(x)\gamma^\mu\psi_l^L(x) \end{aligned} \tag{1.22}$$

This is a neutral current - it couples either electrically charged leptons or neutral neutrinos, just like the electromagnetic current (equation (1.10)). This last part of J_3^μ is a part of the electromagnetic current, except for a constant factor. On this somewhat vague basis we define a new current, the weak hypercharge current J_Y^μ:

$$J_Y^\mu = \frac{1}{e}s^\mu(x) - J_3^\mu(x) = -\frac{1}{2}\bar{\Psi}_l^L(x)\gamma^\mu\Psi_l^L(x) - \bar{\psi}_l^R(x)\gamma^\mu\psi_l^R \tag{1.23}$$

The conserved charge corresponding to the conserved current is called the weak hypercharge Y

$$Y = \int d^3\mathbf{x}J_Y^0(x)$$

The hypercharge Y is intimately linked to the electric charge Q and the weak isocharge I_3^W (which are the conserved quantities of the electromagnetic current and the third weak hypercharge current respectively), as can be seen from equation (1.23)

$$Y = \frac{1}{e}Q - I_3^W \tag{1.24}$$

We are now equipped to return to the Lagrangian density of equation (1.18). If we write it out, we find our original free-lepton Lagrangian, in addition to more terms:

$$\begin{aligned} \mathcal{L} = \mathcal{L}_0 + i\Bigg[&\bar{\Psi}_l^L(x)\gamma_\mu\left(\partial^\mu + ig\tau_jW_j^\mu(x) - \frac{1}{2}ig'B^\mu(x)\right)\Psi_l^L \\ &+ \bar{\psi}_l^R\gamma_\mu\left(\partial^\mu - ig'B^\mu(x)\right)\psi_l^R + \bar{\psi}_\nu^R\gamma_\mu\partial^\mu\psi_\nu^R\Bigg] \end{aligned} \tag{1.25}$$

We rewrite in terms of the weak isospin currents (equation (1.21) and the weak hypercharge current (equation (1.23))

$$\mathcal{L} = \mathcal{L}_0 - gJ_i^\mu(x)W_{j\mu}(x) - g'J_Y^\mu(x)B_\mu(x) \equiv \mathcal{L}_0 + \mathcal{L}_I \tag{1.26}$$

In order to get anywhere, we need to rewrite $\mathcal{L}_I$ in terms of the charged leptonic currents $J^\mu(x)$[9] and $J^{\mu\dagger}(x)$

$$J_\mu(x) = \sum_l \bar{\psi}_l(x)\gamma_\mu(1-\gamma_5)\psi_{\nu_l}(x)$$
$$J_\mu^\dagger(x) = \sum_l \bar{\psi}_{\nu_l}(x)\gamma_\mu(1-\gamma_5)\psi_l(x)$$

and a new (non-hermitian) gauge-field

$$W_\mu(x) = \frac{1}{\sqrt{2}}[W_{1\mu}(x) - iW_{2\mu}(x)] \tag{1.27}$$

This gives us, after some straight forward mathematical manipulations (not shown), the first two terms of the interaction lagrangian of equation (1.26)

$$-g\sum_{i=1}^{2} J_i^\mu(x)W_{i\mu}(x) = \frac{-g}{2\sqrt{2}}[J^{\mu\dagger}(x)W_\mu(x) + J^\mu(x)W_\mu^\dagger(x)] \tag{1.28}$$

From here we can read off the basic vertices for the electroweak interactions, see figure 1.2.

W^μ and $W^{\dagger\mu}$ are interpreted as the charged *physical* (but still massless) $W^\pm$ bosons.

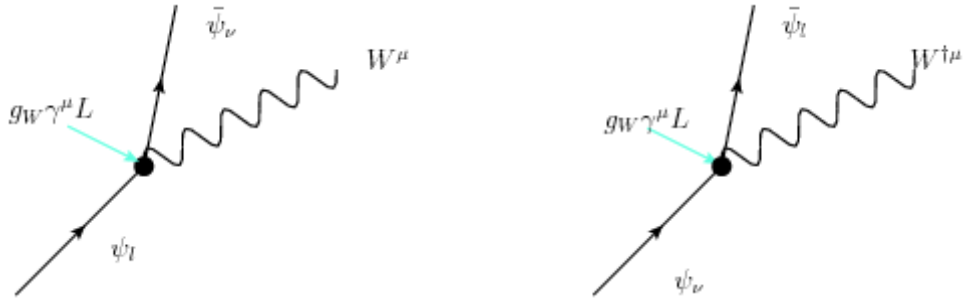

Figure 1.2: The Feynaman diagrams corresponding to Equation (1.28). g_W is equal to $\frac{g}{2\sqrt{2}}$.

Now we return to equation (1.26) and rewrite $W_{3\mu}(x)$ and $B_\mu(x)$ as linear combinations of the two gauge fields $A_\mu(x)$ and $Z_\mu(x)$ in combination with the so called weak mixing angle θ_W[10].

$$W_{3\mu}(x) = \cos\theta_W Z_\mu(x) + \sin\theta_W A_\mu(x)$$
$$B_\mu(x) = -\sin\theta_W Z_\mu(x) + \cos\theta_W A_\mu(x)$$

[9] Experimental data assures us that the weak charged current has this V-A structure[12]

[10] This gives the mixture of weak and electromagnetic interactions. Notice that $\theta_w = 0$ decouples them. This has been proven to be an incorrect description by experiment. The most current and exact value of $\sin^2\theta_W$ is 0.23119(14)[4], corresponding to $\theta_W \approx 30°$.

From this in combination with $J_Y^\mu(x) = \frac{1}{e}s^\mu(x) - J_3^\mu(x)$ we get for the rest of equation (1.26)

$$\begin{aligned}
&-J_3^\mu(x)W_{3\mu}(x) - g'J_Y^\mu(x)B_\mu(x) \\
&\quad = -\frac{g'}{e}s^\mu(x)[-\sin\theta_W Z_\mu(x) + \cos\theta_W A_\mu(x) - \\
&\quad J_3^\mu(x)\Big(g[\cos\theta_W Z_\mu(x) + \sin\theta_W A_\mu(x)] - \\
&\quad g'[-\sin\theta_W Z_\mu(x) + \cos\theta_W A_\mu(x)]\Big)
\end{aligned}$$

Demanding that $A_\mu(x)$ in fact *is* the electromagnetic field and that it is coupled to the electric charges in the way we are used to (equation 1.9), i.e. $-s^\mu(x)A_\mu(x)$, we see that $J_3^\mu(x)A_\mu(x)$ must vanish and that we need to identify

$$g'\cos\theta_W = g\sin\theta_W = e$$

This final step leads us to the the expression for the interaction Lagrangian density

$$\begin{aligned}
\mathcal{L}_I = -s^\mu(x)A_\mu(x) - \frac{g}{2\sqrt{2}}[J^{\mu\dagger}(x)W_\mu(x) + J^\mu(x)W_\mu^\dagger(x)] \\
- \frac{g}{\cos\theta_W}[J_3^\mu(x) - \frac{1}{e}\sin^2\theta_W s^\mu(x)]Z_\mu(x)
\end{aligned} \tag{1.29}$$

We now arrived at the $\mathrm{SU(2)_L} \times \mathrm{U(1)_Y}$ gauge-invariant interaction Lagrangian that Glashow proposed in 1961. The first term we know from QED - this is just the electromagnetic current coupling to the photon field. We interpret the $W(x)$ and $W^\dagger(x)$ gauge field's quanta as the physical (but still massless) $W^\pm$ vector bosons. The last term represents neutral currents. The quanta of the $Z_\mu(x)$ field is the (also still massless) physical Z^0 boson.

This is just a part of what is needed in the theory of electroweak interactions. Up until now we have seen how *leptons* interact with gauge fields. The situation is almost the same for quarks, just with up-type and down-type quarks playing the part of the neutrino and the lepton, i.e $\begin{pmatrix} u \\ d \end{pmatrix}_L$, $\begin{pmatrix} c \\ s \end{pmatrix}_L$, $\begin{pmatrix} t \\ b \end{pmatrix}_L$ and u_R,d_R etc.

One thing that is different for the quarks, in comparison to the leptons, is the flavor changing mechanism. The three quark generations transform into each other. The vertex factors involving quarks are equal to the ones involving leptons, except that it carries an extra factor representing the probability of the process in question. This probability is given by the Cabibbo-Kobayashi-Maskawa (CKM) mixing matrix[4]

$$V_{\mathrm{CKM}} = \begin{pmatrix} |V_{ud}| & |V_{us}| & |V_{ub}| \\ |V_{cd}| & |V_{cs}| & |V_{cb}| \\ |V_{td}| & |V_{ts}| & |V_{tb}| \end{pmatrix} = \begin{pmatrix} 0.97 & 0.23 & 0.0043 \\ 0.21 & 0.96 & 0.042 \\ 0.0074 & 0.041 & 0.78 \end{pmatrix}$$

The probability to transition from flavor i to j is $|V_{ij}|^2$. We see that the largest probabilities are on the diagonal, meaning that the transition probability between quarks of the same generation is largest.

The complete Lagrangian also describes how the gauge bosons interact when no leptons present. We will not go into details about this, just visit the subject briefly.

For the $B^\mu(x)$ field it is an easy task to construct a $\mathrm{SU(2)_L} \times \mathrm{U(1)_Y}$ invariant term. It is just as for QED (equation (1.11))

$$-\frac{1}{4}B_{\mu\nu}(x)B^{\mu\nu}(x), \quad B^{\mu\nu}(x) \equiv \partial^\nu B^\mu(x) - \partial^\mu B^\nu(x)$$

It becomes more difficult for the $W_i^\mu(x)$ fields. We'll just quote the results here, namely

$$-\frac{1}{4}G_{i,\mu\nu}(x)G_i^{\mu\nu}(x), \quad G_i^{\mu\nu}(x) \equiv F_i^{\mu\nu}(x) + g\epsilon_{ijk}W_j^\mu(x)W_k^\nu(x)$$

where ϵ_{ijk} is, as usual, the totally antisymmetric tensor and $F_i^{\mu\nu}$ is given in analogy with equation (1.11) by

$$F_i^{\mu\nu} \equiv \partial^\nu W_i^\mu(x) - \partial^\mu W_i^\nu(x)$$

(see reference [11] for more info). Putting everything together we get

$$\begin{aligned}\mathcal{L}^B = &-\frac{1}{4}B_{\mu\nu}(x)B^{\mu\nu}(x) - \frac{1}{4}F_{i,\mu\nu}(x)F_i^{\mu\nu}(x) \\ &+ g\epsilon_{ijk}W_{i,\mu}(x)W_{j,\nu}(x)\partial^\mu W_k^\nu(x) \\ &- \frac{1}{4}g^2\epsilon_{ijk}\epsilon_{ilm}W_j^\mu(x)W_k^\nu(x)W_{l,\mu}(x)W_{m,\nu}(x)\end{aligned} \tag{1.30}$$

Here we notice something interesting that makes the electroweak interactions different from QED and which is caused by the non-Abelian nature of the theory - the weak gauge bosons self-interact! The three non-Abelian basic vertices are drawn in Figure 1.3.

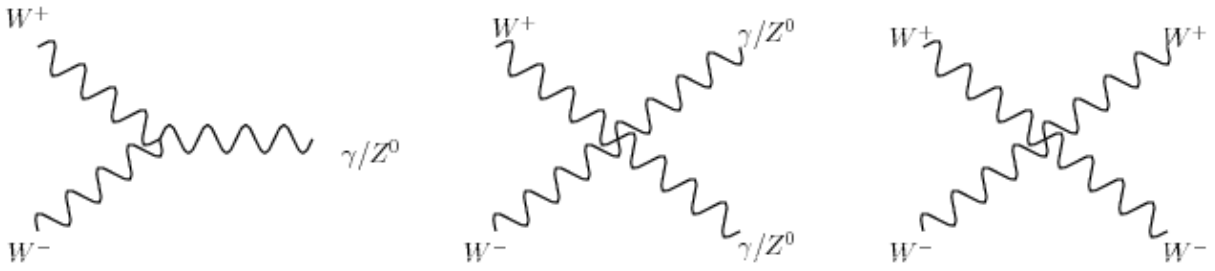

Figure 1.3: Additional basic vertices of the electroweak theory. These show how the weak gauge fields themselves interact.

1.1.5 Quantum Chromodynamics

The quarks have, in addition to electroweak interactions, also strong interaction, which this section addresses.

In the 1950s new particles were springing to life as never before. There were so many that one wondered if they could all be fundamental. In 1963 Gell-Mann and George Zweig proposed

that they were made up of quarks, of which there were three flavours - up, down and strange. After the discovery of Ω^-, made of three strange quarks with parallell spins, a new quantum number was proposed - color. At least three colors had to exist because of the three quarks in the Ω^- and the Pauli principle stating that fermions cannot be in the same quantum state.

Later on one could confirm that there were in fact three colors. One looked at the differential cross-sections of the processes $e^+e^- \rightarrow$ hadrons and $e^+e^- \rightarrow \mu^+\mu^-$. When the collision energy E is well above the particle creating threshold, $E >> mc^2$ (m being the mass of the particles created) the cross-section reduces to[13]

$$\sigma = \frac{\pi}{3}\left(\frac{\hbar Qc\alpha}{E}\right)^2$$

where c is the speed of light in vacuum, α is electromagnetic coupling constant and Q is the electric charge of the created particles. The ratio of the rate of hadron production to the rate of muon pairs $R \equiv \frac{\sigma(e^+e^-\rightarrow\text{hadrons})}{\sigma(e^+e^-\rightarrow\mu^+\mu^-)}$ is thus given by $R = C\sum Q_i^2$, where C is the number of colors. Plotting this ratio as a function of collision energy gives a staircase shaped graph showing that the number C is equal to 3.

For a long time, the quarks were considered a mere mathematical construct by some because every search for them came up negative. Today we believe that they are indeed real particles, but forever imprisoned, or confined[11], in hadrons. The combination of quarks and gluons must be colorless ("white") which greatly reduces the number of possible configurations. Luckily, in addition to being confined they are also asymptotically free, meaning that the more energy is put into the system, the less bound the quarks appear and the smaller the effective coupling is. If this had not been, we could not have used perturbation theory, as we have done for QED and EW theories.

Because of this new quantum number, color, the three versions of each quark are grouped in a triplet

$$\psi_q \equiv \begin{pmatrix}\psi_{q_r}\\ \psi_{q_g}\\ \psi_{q_b}\end{pmatrix} \equiv \begin{pmatrix}\psi_{q_1}\\ \psi_{q_2}\\ \psi_{q_3}\end{pmatrix}$$

Now we just follow the receipe of QED and claim that the free-quark Lagrangian is

$$\mathcal{L}^0_{QCD} = \bar{\psi}_q\left(\gamma^\mu i\partial_\mu - m_q\right)\psi_q$$

Because there are three versions of each quark, in contrast to QED, one postulated that the Lagrangian should be invariant under SU(3)_C transformations[12]:

$$U = e^{i\alpha^a(x)t^a}, \quad t^a \equiv \frac{1}{2}\lambda^a$$

[11]Except for the heaviest quark, top, which decays before being able to hadronize.

[12]The connection between symmetry group and number of force-carrying boson is intimate: the number of bosons equals the number of so-called generators for the group (the three Pauli matrices for SU(2) and the eight Gell-Mann matrices for SU(3)).

U is a 3×3 matrix and λ^a are the eight Gell-Mann matrices, the generators of SU(3). When trying to make $\mathcal{L}^0_{QCD}$ $\mathrm{SU(3)_C}$ invariant, one finds that one needs to exchange the ordinary derivative ∂_μ with the covariant derivative D_μ

$$\partial^\mu \psi_q(x) \rightarrow D^\mu \psi_q(x) = (\partial^\mu + i g_s t^a G^{\mu,a}) \psi_q(x)$$

and that 8 new gauge fields $G^{\mu,a}$ are needed. These are the 8 gluons. When putting it all together the Lagrangian looks like

$$\mathcal{L} = \bar{\psi}_q(x) \left(\gamma^\mu i \partial_\mu - m_q\right) \psi_q(x) - g_s j^a_\mu G^{\mu,a}$$

where the color-octet current j^a_μ is introduced:

$$j^a_\mu \equiv \bar{\psi}_q \gamma^\mu t^a \psi_q, \quad \psi_q \equiv \begin{pmatrix} \psi_{q_1} \\ \psi_{q_2} \\ \psi_{q_3} \end{pmatrix}$$

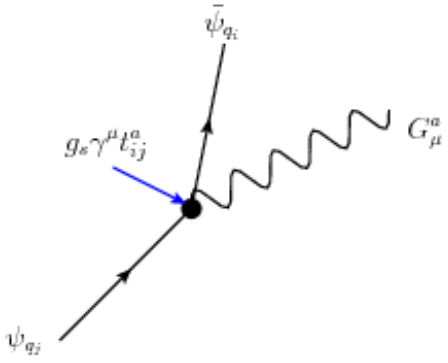

(a)

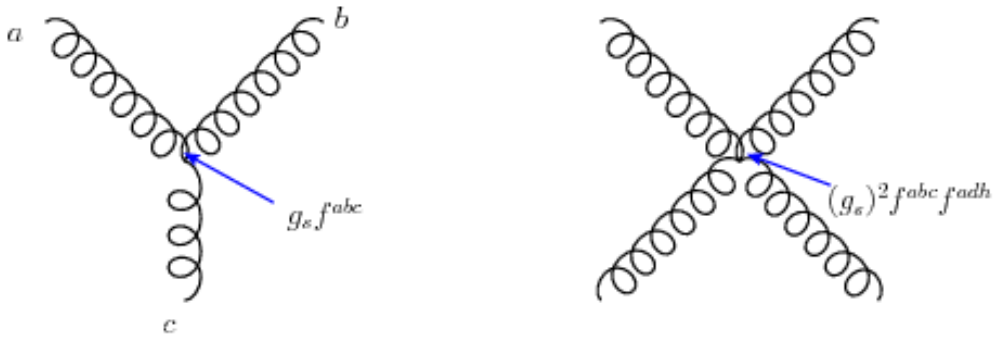

(b)

Figure 1.4: Feynman diagrams of the basic vertices of QCD.

This gives us a basic vertex for QCD, which is drawn in Figure 1.4(a). As for QED, the color-octet current j^a_μ is a conserved current and the conserved quantity is the color charge.

The QCD interaction Lagrangian is

$$\mathcal{L}_G = -\frac{1}{4} G^a_{\mu\nu} G^{\mu\nu,a}, \quad G^a_{\mu\nu} \equiv F^a_{\mu\nu} - g_s f^{abc} G^b_\mu G^c_\nu$$

where $\left[t^a, t^b\right] = i f^{abc} t^c$, $-i g_s t^a G^a_{\mu\nu} \equiv [D_\mu, D_\nu]$ and $F^a_{\mu\nu} \equiv \partial_\mu G^a_\nu - \partial_\nu G^a_\mu$.

We now have the Lagrangian for the strong interaction[13]

$$\begin{aligned} \mathcal{L}_{QCD} &= \bar{\psi}_q(x) \left(\gamma^\mu i \partial_\mu - m_q\right) \psi_q(x) - g_s j^a_\mu G^{\mu,a} \\ &\quad + F^a_{\mu\nu} F^{a,\mu\nu} - 2 g_s F^a_{\mu\nu} f^{abc} G^{b,\mu} G^{c,\nu} + (g_s)^2 f^{abc} f^{adh} G^b_\mu G^c_\nu G^{d,\mu} G^{h,\nu} \end{aligned} \tag{1.31}$$

and the additional basic vertices as shown before in figure 1.4(a) and in the new figure 1.4(b). The non-abelian nature of the $\mathrm{SU(3)_C}$ group means the gluons have self-interactions, leading to the 3- and 4-gluon vertices in figure 1.4(b). The presence of these self-intraction vertices explain asymptotic freedom, i.e. why the strong force between quarks become small at high energies/short distances.

1.1.6 The Higgs mechanism

There exists a model, the Glashow model, that simply introduces mass terms in the Lagrangian density. For leptons these are $-m_l \bar{\psi}_l(x) \psi_l(x)$. The result is a non-gauge invariant and non-renormalizable theory. For some well chosen values of $\sin^2 \theta_W$ and m_z and in first order perturbation theory the model is able to fit the experiments reasonably well[11, p.274]. But we want a better explanation to the non-zero masses of our fermions and bosons. The answer comes in the form of spontaneous symmetry breaking.

From the last sections we have the interaction Lagrangian density $\mathcal{L}$ consisting of a free lepton part and a interaction part, but without any mass terms. To generate the obviously non-zero masses for the leptons, quarks and the $W^\pm$ and Z^0 bosons we have to introduce the Higgs mechanism i.e. modify the electroweak Lagrangian density to contain a term $\mathcal{L}^H$.

We need to break the $\mathrm{SU(2)_L} \times \mathrm{U(1)_Y}$ invariance spontaneously, leaving the $\mathrm{U(1)_Y}$ invariance intact[14]. To do this, we introduce a *Higgs field* which basically is a scalar field[15] with a non-vanishing and constant vacuum expectation value (VEV)

$$\langle 0 | \phi(x) | 0 \rangle = c \neq 0$$

and which is not invariant under the gauge transformations. The clue here is the non-vanishing VEV. It comes from the assumption that the vacuum state is non-unique, degenerate, and this means that one of the degenerate vacuum states can be *chosen* as *the*

[13] Keep in mind that quarks have electromagnetic and weak interactions as well

[14] Because the photons should still be massless and the other three bosons should not.

[15] It needs to be a *scalar* field if one wants it to be invariant under Lorentz transformations.

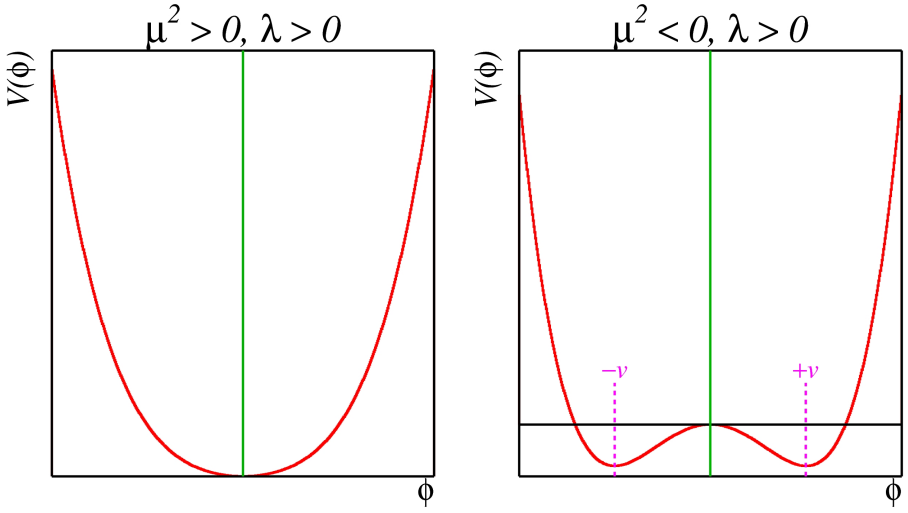

Figure 1.5: One minimum(left). One local maximum, indefinately many minima(right)

vacuum state. This is the spontaneous symmetry breaking that in a not so mysterious, but very mathematical way generates the masses for the three weak gauge bosons, spontaneously breaking down the electroweak group to the electromagnetic subgroup

$$\mathrm{SU(2)_L} \otimes \mathrm{U(1)_Y} \rightarrow \mathrm{U(1)_{QED}}$$

Spontaneous Symmetry Breaking for a U(1) theory

The following is an example of Spontaneous Symmetry Breaking (SSB) for a U(1) theory.

Consider the Lagrangian density

$$\mathcal{L}(x) = [D^\mu \phi(x)]^\star [D_\mu \phi(x)] - \mu^2 |\phi(x)|^2 - \lambda |\phi(x)|^4 \tag{1.32}$$

with $F_{\mu\nu} = \partial_\nu A_\mu - \partial_\mu A_\nu$ as always and $\phi(x)$ a scalar field, and

$$D_\mu \phi(x) = [\partial_\mu + igA_\mu(x)]\phi(x)$$

and

$$\phi(x) = \frac{1}{\sqrt{2}}[\phi_1(x) + i\phi_2(x)]$$

This Lagrangian is invariant under the U(1) gauge transformations

$$\begin{aligned}
\phi(x) &\rightarrow \phi'(x) = \phi(x) e^{-iqf(x)} \\
\phi^*(x) &\rightarrow \phi^{*'}(x) = \phi^*(x) e^{iqf(x)} \\
A_\mu(x) &\rightarrow A'_\mu(x) = A_\mu(x) + \partial_\mu f(x)
\end{aligned}$$

At this point in time the situation is treated in a purely classical manner. Thus $\phi(x)$ should be thought of a classical field, and μ should not be interpreted as the mass of a particle (equation (1.32)).

According to classical mechanics the Hamiltonian density is given by

$$\mathcal{H}(x) = [\partial^0 \phi^*(x)][\partial_0 \phi(x)] + [\nabla \phi^*(x)] \cdot [\nabla \phi(x)] + \mathcal{V}(\phi) \tag{1.33}$$

To ensure that the field has a minimum value we require $\lambda > 0$. For constant $\phi(x)$ the two first terms of equation (1.33) disappear. Thus the minimum value of $\mathcal{H}(x)$ (and the total energy of the field) corresponds to the value of $\phi(x)$ which minimizes $\mathcal{V}(x)$. With $\lambda > 0$ and $\mu^2 > 0$ the potential energy density of the field, $\mathcal{V}(\phi) = \mu^2|\phi(x)|^2 + \lambda|\phi(x)|^4$ has exactly one minimum, see figure 1.5(left). For $\mu^2 < 0$ the situation is very different - the potiential now has the non-unique lowest energy state that we were looking for. The minima are given by[16]

$$\phi(x) = \phi_0 = \left(\frac{-\mu^2}{2\lambda}\right)^{1/2} e^{i\theta}, \quad 0 \leq \theta < 2\pi$$

where θ is a direction in the $\phi_1 - \phi_2$ plane. Seeing as the Lagrangian is invariant under the U(1) phase transformations, the chosen value of θ is not significant, thus we are free to choose it at our convenience. 0 is the obvious choice such that

$$\phi_0 = \left(\frac{-\mu^2}{2\lambda}\right)^{1/2} \equiv \frac{1}{\sqrt{2}} v, \quad v^2 \equiv \frac{-\mu^2}{\lambda}$$

We now rewrite $\phi(x)$ as a function of two new, real fields $\sigma(x)$ and $\eta(x)$, such that these are deviations from the ground state ϕ_0:

$$\phi(x) = \frac{1}{\sqrt{2}} \left(v + \sigma(x) + i\eta(x)\right) \tag{1.34}$$

The Lagrangian density of equation (1.32) then becomes

$$\mathcal{L}(x) = \frac{1}{2}[\partial^\mu \sigma(x)][\partial_\mu \sigma(x)] - \frac{1}{2}(2\lambda v^2)\sigma^2(x) - \frac{1}{4} F_{\mu\nu}(x) F^{\mu\nu}(x) \tag{1.35}$$

$$+ \frac{1}{2}(qv)^2 A_\mu(x) A^\mu(x) + \frac{1}{2}[\partial^\mu \eta(x)][\partial_\mu \eta(x)] + qv A^\mu(x) \partial_\mu \eta(x) \tag{1.36}$$

$$+ \text{cubic and quartic terms} + \text{const}$$

Now we need to eliminate the scalar field $\eta(x)$. This can be done because for a *complex* field $\phi(x)$ there always exists a gauge transformation (called the unitary gauge) that transforms it into a *real* field of the form

$$\phi(x) = \frac{1}{\sqrt{2}}[v + \sigma(x)]$$

When this is introduced into equation (1.32) it can easily be shown that the result is

$$\mathcal{L}(x) = \mathcal{L}_0(x) + \mathcal{L}_I(x)$$

where $\mathcal{L}_0(x)$ is made up of all the quadratic terms

$$\mathcal{L}_0(x) = \frac{1}{2}[\partial^\mu \sigma(x)][\partial_\mu(\sigma(x)] - \frac{1}{2}(2\lambda v^2)\sigma^2(x) - \frac{1}{4} F_{\mu\nu}(x) F^{\mu\nu}(x) + \frac{1}{2}(qv)^2 A_\mu(x) A^\mu(x) \tag{1.37}$$

[16] Just set the derivative of $\mathcal{V}(\phi)$ equal to zero.

and $\mathcal{L}_I(x)$ contains the rest, i.e. the higher-order interaction terms (the constant term has been dropped as it is of no significance)

$$\mathcal{L}_I(x) = -\lambda v\sigma^3(x) - \frac{1}{4}\lambda\sigma^4(x) + \frac{1}{2}q^2 A_\mu(x)A^\mu(x)[2v\sigma(x) + \sigma^2(x)]$$

Now comes the big point: $\mathcal{L}_o(x)$ (equation (1.37)) can be interpreted as the free Lagrangian density of a real Klein-Gordon field ($\sigma(x)$) and a real massive vector field $A_\mu(x)$. These will, after quantization, give rise to bosons of mass $\sqrt{2\lambda v^2}$ and $|qv|$ respectively. This is the famous *Higgs mechanism*, and the ripples in the $\sigma(x)$ field is the *Higgs boson*.

The standard electroweak theory

The last section gave an example of the Higgs mechanism in which the photon actually gains a mass. We know that this is not the case in our world of course. The Standard Model incorporates this mechanism, but it is used on the full Lagrangian density, and the broken symmetry is $\mathrm{SU(2)_L \times U(1)_Y}$ to give masses to the Z^0 and W bosons as well as to the fermions, while keeping the $\mathrm{U(1)_Y}$ symmetry exact and therefor the photon massless.

The electroweak Lagrangian (excluding the quarks for simplicity) is composed of two parts, $\mathcal{L} = \mathcal{L}^{\mathrm{L}} + \mathcal{L}^{\mathrm{B}}$, where the leptonic Lagrangian $\mathcal{L}^{\mathrm{L}}$ is given by equation (1.18) and the bosonic lagrangian $\mathcal{L}^{\mathrm{B}}$ by equation (1.30). We now introduce a scalar field with a non-zero vacuum expectation value, a Higgs field that is not invariant under the $SU(2)_{\mathrm{L}} \times U(1)_{\mathrm{Y}}$ transformations. The $\phi(x)$ field is a doublet, as we want to break the $\mathrm{SU(2)_L}$ symmetry.

$$\Phi(x) = \begin{pmatrix} \phi_a(x) \\ \phi_b(x) \end{pmatrix}$$

where $\phi_a(x)$ and $\phi_b(x)$ are scalar fields.

We want to modify the Lagrangian to contain an additional part, a Higgs part, $\mathcal{L}^{\mathrm{H}}$, in analogy with equation (1.32).

$$\mathcal{L}^{\mathrm{H}} = [D^\mu\Phi(x)]^\dagger[D_\mu\Phi(x)] - \mu^2\Phi^\dagger(x)\Phi(x) - \lambda[\Phi^\dagger(x)\Phi(x)]^2$$

$$D^\mu\Phi(x) = [\partial^\mu + \frac{1}{2}ig\tau_j W_j^\mu(x) + ig'YB^\mu(x)]\Phi(x)$$

This new addition to the family must be $SU(2)_{\mathrm{L}} \times U(1)_{\mathrm{Y}}$ invariant (see for example [11, p.289] for more information).

As before one finds the Higgs field of the vacuum state (see the discussion regarding equation (1.33))

$$\Phi_0 = \begin{pmatrix} 0 \\ v/\sqrt{2} \end{pmatrix} \quad v = \sqrt{\frac{-\mu^2}{\lambda}} \tag{1.38}$$

which is not invariant under $SU(2)_{\mathrm{L}} \times U(1)_{\mathrm{Y}}$ transformations, but must be invariant under $\mathrm{U(1)_Y}$ transformations alone as the photon is masseless

Then, in analogy with (1.34), we rewrite the Higgs field in terms of deviations from the vacuum field

$$\Phi(x) = \frac{1}{\sqrt{2}} \begin{pmatrix} \eta_1(x) + i\eta_2(x) \\ v + \sigma(x) + i\eta_3(x) \end{pmatrix}$$

Rewriting the Lagrangian one finds that the Higgs part is rewritten to be a function of the four real fields $\sigma(x)$, $\eta_i(x)$, $i = 1, 2, 3$.

One can rewrite $\phi(x)$ in the so-called unitary gauge (just meaning a specific transformation, in this case first a SU(2) then a U(1) transformation) so that it becomes

$$\Phi(x) = \frac{1}{\sqrt{2}} \begin{pmatrix} 0 \\ v + \sigma(x) \end{pmatrix}$$

implying that the three η_i fields are unphysical. The fourth, $\sigma(x)$ will on quantization give rize to a massive and electrically neutral scalar particle, the Higgs boson.

The whole Lagrangian must now be transformed into the unitary gauge, but before this is don we add the fermion masses by simply adding another gauge-invariant term, $\mathcal{L}^{\mathrm{FH}}$, to the Lagrangian

$$\mathcal{L} = \mathcal{L}^{\mathrm{L}} + \mathcal{L}^{\mathrm{B}} + \mathcal{L}^{\mathrm{H}} + \mathcal{L}^{\mathrm{FH}}$$

where the Lagrangian for the fermions consist of the lepton part and the quark part. The leptonic part is given by

$$\begin{aligned} \mathcal{L}^{\mathrm{LH}} = &-g_l[\bar{\Psi}_l^L(x)\psi_l^R(x)\Phi(x) + \Phi^\dagger(x)\bar{\psi}_l^R(x)\Psi_l^L(x)] - \\ &g_\nu[\Psi_l^L\psi_\nu^R\tilde{\Phi}(x) + \tilde{\Phi}^\dagger(x)\bar{\psi}_\nu^R(x)\Psi_l^L(x)] \end{aligned} \tag{1.39}$$

with g_l and g_ν as dimensionless coupling constants and

$$\tilde{\Phi}(x) = -i[\Phi^\dagger(x)\tau_2]^{\mathrm{T}}$$

The situation is equivalent for the quarks (up-type and down-type playing the role of the lepton and the neutrino) with the slight complication from the quark mixing.

The full Lagrangian now consists of four parts, the leptonic (L) and bosonic (B) parts, the Higgs part (H) and the interaction between the fermions and the Higgs field part (FH).

After the transformation is complete (not shown, the interested reader is referred to chapter 14 of reference [11]) the Lagrangian contains mass terms for fermions and bosons, actually giving predictions for the masses of the Z^0 and W bosons

$$m_{\mathrm{W}} = \sqrt{\frac{\alpha\pi}{G\sqrt{2}}}\frac{1}{\sin\theta_{\mathrm{W}}}, \quad m_{\mathrm{Z}} = \sqrt{\frac{\alpha\pi}{G\sqrt{2}}}\frac{2}{\sin 2\theta_{\mathrm{W}}}$$

where $\alpha \approx 1/137.036$ is the well-known fine structure constant[4], $G \approx 1.166 \times 10^{-5}$ is the fermi constant[4] and θ_{W} is the weak mixing angle ($\sin^2\theta(M_Z^0) \approx 0.231$)[4]. Thus the prediction for the masses to the first order is $m_{\mathrm{W}} = 76.9$ GeV, $m_{\mathrm{Z}} = 87.9$ GeV. When using higher order perturbation theory one get $m_{\mathrm{W}} = 79.8 \pm 0.8$ GeV and $m_{\mathrm{Z}} = 90.8 \pm 0.6$ GeV[11]. The experimental masses are 80.398(25) GeV and 91.1876(21) GeV respectively, making the predictions very good indeed.

The fermion masses are a function of the free parameters g from equation (1.39), $m_l = \frac{vg}{\sqrt{2}}$ and the exact values are not predicted by the SM. Sadly this is also true for the Higgs scalar, whose mass is a function of μ (equation (1.38)), $m_{\mathrm{H}} = \sqrt{-2\mu^2}$, and can not be calculated from theory.

In this framework the neutrinos actually have mass, but the neutrino field ψ_ν is a combination of left and righthanded neutrino fields. Only lefthanded neutrinos participate in the fundamental forces (not counting gravity). Righthanded neutrinos have no way of coming into existance within the SM.

1.2 Summary

In this chapter we introduced the mathematical framework of the Standard Model, which is the current theory of particle physics. We now proceed to the shortcomings of the Standard Model and review a few popular Beyond the Standard Model thories, including some that introduces a new neutral gauge boson, Z'.

Chapter 2

Going beyond the Standard Model

The Standard Model has been tested time and time again without any discrepancy being detected[1]. In the 1990s it was possible to test it to unpreceeded accuracy thanks to more modern particle accelerators and detectors (for example the Large Electron-Positron Collider (LEP) at CERN, the Stanford Linear Collider (SLC) in California and the Tevatron at Fermilab in Illinois). Here one also measured many of the free parameters of the SM at higher accuracies than before, including the fermion and gauge boson masses, the weak mixing angle and the gauge couplings. Still we know that the Standard Model is not a complete description of nature.

2.1 Shortcomings of the Standard Model

Experiments have revealed a few phenomena that cannot be described within the SM. The following are examples of such.

Neutrino masses The neutrinos are massless within the SM. Experiments with solar and atmospheric neturinos have shown, however, that the three generations of neutrinos mix with each other[14]. This would not be possible had their mass been exactly zero. The most current limit on the neutrino masses are[15] $m_{\nu_e} + m_{\nu_\mu} + m_{\nu_\tau} < 0.28\,\mathrm{eV}$ (95% CL).

Dark energy and matter Cosmology tells us that approximately 5% of the Universe is made of baryonic matter. The rest is Dark Matter (23%) and Dark Energy (72%). The SM offers an explanation for the 5% of ordinary matter only.

Gravity The SM includes the strong and electroweak forces. The last fundamental force, gravity, is left out.

[1] This is not strictly true. The neutrinos are massless within the SM, while experiments show that they have mass.

Baryogenesis At the beginning of the Universe, matter and anti-matter were created in equal amounts. The SM offers no satisfactory explanation for the matter-dominated Universe we observe. (CP-violation incorporated in the CKM matrix is indeed not enough.)

In addition to these unexplained phenomena there are certain aspects of the SM that are not based on theoretical expectations. The following is a non-exhaustive list.

The Higgs potential The Higgs field and the shape of the Higgs potential are introduced in the SM without any fundamental justification.

Fermion generations The SM does not explain why there are exactly three generations of leptons and quarks, nor why the fermion masses span over many orders of magnitude.

Hierarchy problem According to theory the Higgs boson should have a very high mass indeed due to quantum corrections from loop diagrams. It should be of the order of the GUT scale, 10^{16} GeV. This is not what we have observed - its mass is around 100 GeV if it exists. This can only be explained within the SM by an extreme fine-tuning of the parameters.

Unification problem The three gauge groups within the SM, $\mathrm{SU(3)_C}$, $\mathrm{SU(2)_L}$ and $\mathrm{U(1)_Y}$, are associated with individual running coupling constants. It was believed that they converged at some scale, but precision measurements have shown that this is not the case within the SM[16].

2.2 Beyond the Standard Model theories

In attempts to resolve the problems outlined in section 2.1 several Beyond the Standard Model (BSM) theories have been developed. Below are a few examples of popular theories.

Supersymmetry In supersymmetry (SUSY), every SM particle has a supersymmetric counterpiece with the same mass, but with a spin difference of 1/2, i.e. fermions have supersymmetric boson partners and vice versa. These partners have not been observed, thus the symmetry must be broken at some scale.

SUSY offers a solution to the hierarchy problem - the correction loops that should have made Higgs very heavy are now cancelled by the SUSY partners.

Models that conserve R-parity[2] have a stable Lightest Susy Particle (LSP), providing a candidate for Dark Matter.

GUTs In Grand Unified Theories (GUTs) one imagines that the $\mathrm{SU(3)_C} \otimes \mathrm{SU(2)_L} \otimes \mathrm{U(1)_Y}$ symmetry we have today in the Standard Model originates from a larger symmetry

[2]All Standard Model particles are given a R-parity of 1, while the superpartners have R-parity -1. When the R-parity is conserved the lightest supersymmetric particle cannot decay.

group relating quarks and leptons. This addresses the unification problem: the symmetry is unbroken at some higher energy where all interactions are described by a local gauge theory with one running coupling. The scale at which this happens is thought to be 10^{16} GeV[16]. A general problem with most GUT theories is the prediction of proton decay, which has not yet been observed.

Extra dimensions As an example, consider the ADD model where the SM fields are confined to a four-dimensional membrane in a higher-dimensional space. Gravity however travels in additional spatial dimensions, making it seem much weaker than the other fundamental forces in four dimensions. The theory thus offers a solution to the hierarchy problem. It also contributes with a Dark Matter candidate: The graviton travels in all the spatial dimensions, giving rise to several Kaluza-Klein resonances on the four-dimensional brane.

2.3 New weak gauge bosons

In many of the BSM theories new gauge bosons are postulated. The general name put on them are W' for electrically charged gauge bosons and Z' for neutral ones.

The theories predicting one or more Z' can be divided into two rather broad families[17] - the ones that arise from a unification scenario and the ones that do not. A few representative theories are considered below.

GUT models Common for Grand Unified Theories are, as mentioned before, that the strong and electroweak interactions are merged into a single interaction, described by a higher symmetry group. The choice of symmetry group, however, varies. The two most popular scenarios are the Left Right Symmetric Model (LRM) and E_6 smodels[17][18]. In the E_6 scenario, the symmetry is broken down in the following pattern:

$$\mathrm{E}_6 \rightarrow SO(10) \times U(1)_\psi \rightarrow SU(5) \times U(1)_\chi \times U(1)_\psi \rightarrow SM \times U(1)_{\theta_{E_6}}$$

$\mathrm{U}(1)_{\theta_{\mathrm{E}_6}}$ is believed to be broken on the TeV scale. Only one linear combination remains light

$$\cos_{\theta_{E_6}} U(1)_\psi - \sin_{\theta_{E_6}} U(1)_\chi$$

θ_{E_6} is a free parameter in the range $-90^\circ \leq \theta_{E_6} \leq 90^\circ$. Four popular models are ψ ($\theta = 0$), χ ($\theta = -90^\circ$), η ($\theta = \sin^{-1}(\sqrt{3/8}) \approx 37.76^\circ$) and I ($\theta = -\sin^{-1}(\sqrt{5/8})$).

The LRM is based on the group SO(10). It breaks down via the following chain:

$$\mathrm{SO(10)} \rightarrow \mathrm{SU(3)_C} \times \mathrm{SU(2)_L} \times \mathrm{SU(2)_R} \times \mathrm{U(1)_{B-L}}$$

In this model the electric charge of a particle is given by

$$Q = I_{3L} + I_{3R} + \frac{1}{2}(B - L)$$

where I_{3L} and I_{3R} are the weak isospin components of the fields and $B - L$ is the baryon number minus the lepton number. Comparing to equation (1.24) which connects electric charge to weak hypercharge and isospin in the Standard Model, we see that in this theory $Y = I_{3R} + \frac{1}{2}(B - L)$.
This model gives rise to two new gauge bosons, one charged and one neutral, that both couple to right handed quarks and leptons. In addition, a Dark Matter candidate is created - the right-handed neutrino[19].

Stueckelberg extension In the Stueckelberg extension of the Standard Model particle masses are generated without the Higgs mechanism. This is done by adding a new kinetic term for a massive U(1) gauge field to the Lagrangian, i.e. it is based on the gauge group $\mathrm{SU(3)_C} \otimes \mathrm{SU(2)_L} \otimes \mathrm{U(1)_Y} \times U(1)_\mathrm{X}$. After symmetry breaking a second Z boson emerges, namely the Z'. The Stueckelberg gauge field has no couplings to the Standard Model fields and connects with the visible sector only through mixing with the SM gauge bosons. LEP results[4] shows that 10^{-3} is an upper limit on the mixing between SM bosons and Z'. Because the Stueckelberg Z' only couples indirectly to SM fields (i.e. through mixing), it would show up as a very narrow resonance.

SSM The model used as a kind of standard candle for experimentalists is the Sequential Standard Model (SSM) Z'. The SSM $Z'$is a carbon copy of the well known Z^0, only heavier. This model is not gauge invariant and thus not a very realistic model, but it is a useful reference model. If it is created in the proton-proton collision at the LHC it can decay into any known SM fermion-antifermion pair. Decay into gauge bosons is manually suppressed.
In this analysis we chose to look at the e^+e^- and $\mu^+\mu^-$ channels because the experimental signature is very clear - namely two oppositely charged, high transverse momentum leptons going back-to-back in the transverse plane in the detector. The branching ratios to electrons and muons are assumed to be nearly the same as for the Z^0, that is 3.3% in each channel, only modified by the fact that the top channel opens up for Z' masses above 180 GeV.

2.4 Past searches and updated limits

There are two ways of searching for something new - directly or indirectly. With hadron colliders one usually performs direct searches, meaning that the goal is to produce an on-shell new particle. This is the idea behind the Z' search at LHC. The new particle is produced many times, and shows up in an invariant mass plot of its decay products (e^+e^- or $\mu^+\mu^-$).

The other type of search is the indirect one. This is especially useful at lepton colliders, like LEP, because the collision is much cleaner. At hadron colliders the QCD background is huge[3].

[3]Still, it is possible to do. If a particle's lower mass bound is found to be out of reach for direct production

The idea behind indirect searches is to look for deviations in a search variable, like for example cross-section, for a Standard Model process. The process $e^+e^- \to l^+l^-$ consists of $e^+e^- \to \gamma \to l^+l^-$ and $e^+e^- \to Z^0 \to l^+l^-$ in the Standard Model and the cross-section will involve those two Feynman diagrams and the interference between them. If there is a Z' then it will modify the Feynman amplitude and the thus also the cross-section. If the cross-section measurements are at an energy much lower than the Z' mass then the contribution will be small, but possibly non-negligible. This is what is being measured in precision electroweak measurements, these small deviations from the SM.

As an illustration of this a SSM Z' model was created in CompHEP[4]. The mass of the Z' was set to 2 TeV and the width to the Z^0 width scaled up by the ratio of the Z' mass to the Z^0 mass, $\Gamma(Z') = \frac{\Gamma(Z^0)}{M_Z^0} M'_Z = 53.29$ GeV. Figure 2.1 shows the cross-section (leading order) for the process $e^+e^- \to Z' \to \mu^+\mu^-$ at the LEP center of mass maximum energy of 209 GeV and at 1 TeV, with and without the Z' included in the calculations. We see a very small deviation from the SM at 1 TeV, and hardly any difference at all at 209 GeV. If we however take a look at the forward backward asymmetry (the difference in the number of particles going in a "forward" direction in contrast to a "backward" direction as compared to the outgoing electrons) we see that there is a slight difference already at 200 GeV, and it gets increasingly larger at higher energies.

These are examples of how a heavy Z' will influence the lower energy measurements. If one measures the, say, asymmetry and *don't* see any discrepancy, then one can put a lower limit on the Z' mass (because a Z' at a lower mass than the limit will have more influence than what is observed).

It is important to note that the limits from the indirect searches are very model dependent. A little tweak in the Z^0-Z' mixing for example, or the couplings to the SM particles, can yield very different results.

2.4.1 LEP-II limits

The Large Electron-Positron Collider never found any significant evidence for the existence of a Z' boson in any of the Z' models included in the search[20]. Figure 2.3 shows the 95% confidence limits on M'_Z as a function of the model parameter θ_{E_6} for the E_6 GUT models and α_{LR} for the LRM. Table 2.1 shows the lower limits on the Z' mass for the χ, ϕ, η, L-R and SSM models, corresponding to specific values of the parameters. For information on the different models, consult section 2.3.

---

one can try the indirect approach.

[4]From http://http://comphep.sinp.msu.ru/ - "The CompHEP package was created for calculations of multiparticle final states in collison and decay processes. The main idea in CompHEP was to enable one to go directly from the Lagrangian to the cross sections and distributions effectively, with the high level of automation."

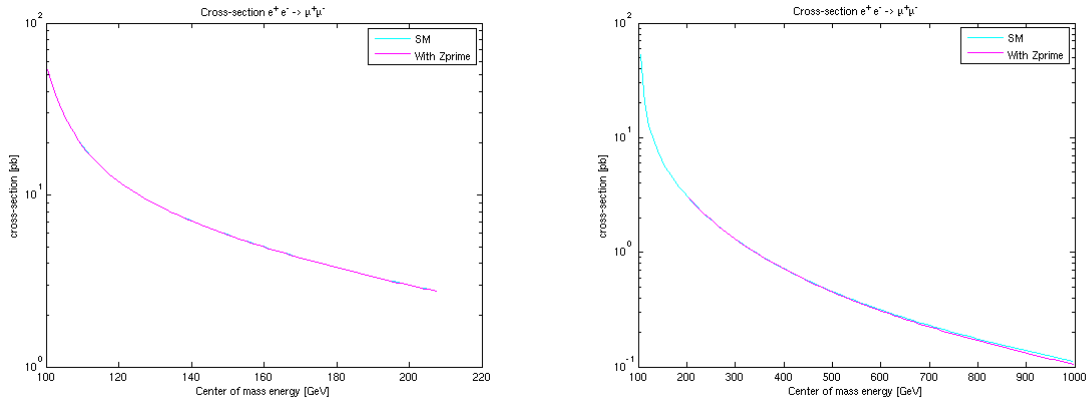

Figure 2.1: Cross-section for the process $e^+e^- \rightarrow \mu^+\mu^-$ with and without a 2 TeV Z' up to center of mass energies of 208 GeV (left) and 1 TeV (right). A small deviation from the SM can be seen at higher energies towards 1 TeV.

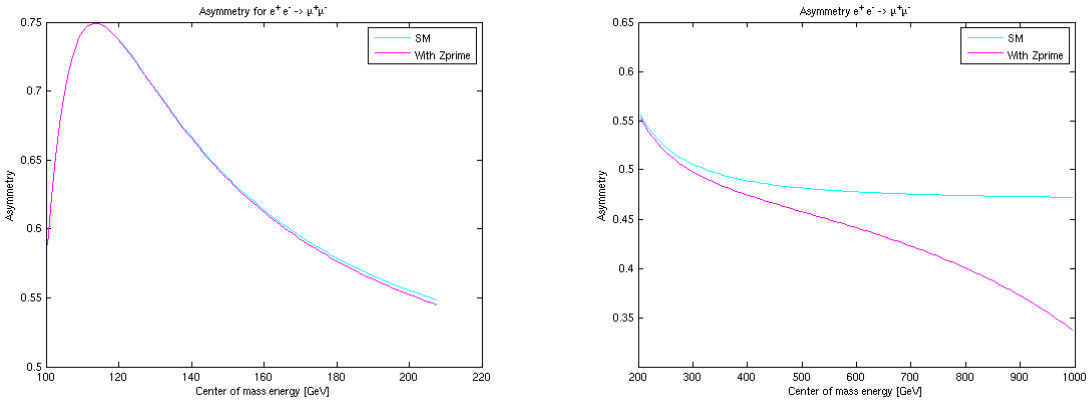

Figure 2.2: Asymmetry (difference in number of particles going "forward" and the ones going "backward" normalized to the total number of particles) for the process $e^+e^- \rightarrow \mu^+\mu^-$ with and without a 2.0 TeV Z' as a function of center of mass energy. A small discrepancy can be seen already at 200 GeV

Z' model	χ	ϕ	η	L-R	SSM	Collider
M'_Z [GeV] (lower limit)	673	481	434	804	1787	LEP

Table 2.1: The 95% CL lower limits on the Z' mass for χ, ϕ, η, L-R and SSM models[20]. The limits are based on measurements by ALEPH, DELPHI, L3 and OPAL detectors at LEP.

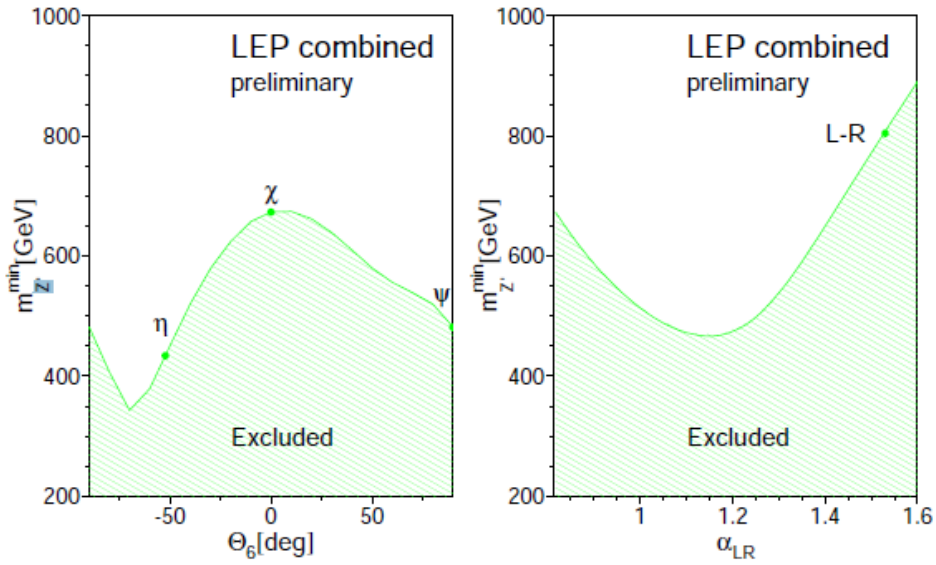

Figure 2.3: The 95% confidence limits on M'_Z as a function of the model parameter θ_{E_6} for the E_6 models and $\alpha_{\rm LR}$ for the LRM[20].

2.4.2 Tevatron limits

Tevatron is a $p\bar{p}$ collider and has searched for high mass particles by looking for resonances, in the same way as we will do here (section 5 and 6). The newest and highest limits from the CDF collaboration based on 4.6fb^{-1} of data in the muon channel [21] are given in table 2.2. The D0 experiment has done an equivalent analysis in the electron channel based on the same amount of data and got about the same results[22]. Figure 2.4 shows the CDF (2.4(a) and the D0 (2.4(b)) exlusion plots. In neither of the analysis any excess above the SM predictions were observed.

Z' model	χ	ϕ	η	SSM	Detector
M'_Z [GeV] (lower limit)	930	917	938	1071	CDF
M'_Z [GeV] (lower limit)	910	898	927	1024	D0

Table 2.2: The 95% CL lower limits on the Z' mass for χ, ϕ, η and SSM models from CDF[21] and D0[22].

2.5 Summary

In this chapter we've reviewed some of the shortcomings of the Standard Model, and a few popular theories offering solutions to some of the challenges. We have also seen the most recent exclusion limits from the LEP collider and Tevatron. Before following up with Z' studies at the LHC from chapter 5, the next two chapters deal with particle interaction with matter (chapter 3) and the LCH and ATLAS (chapter 4).

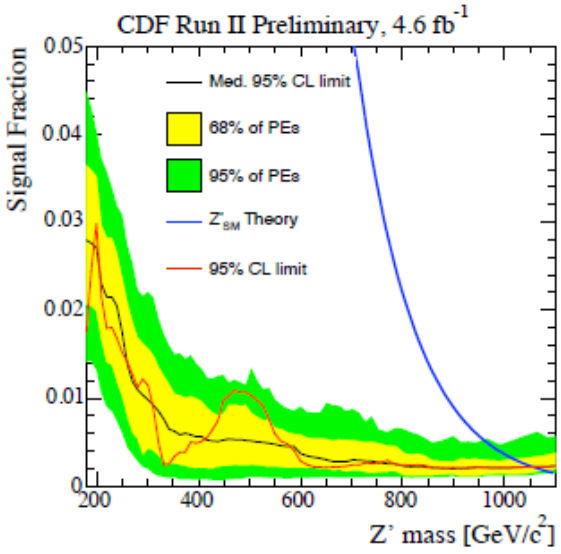

(a) From the CDF Collaboration[21]: The observed and expected 95% confidence level limits on the SSM Z' mass

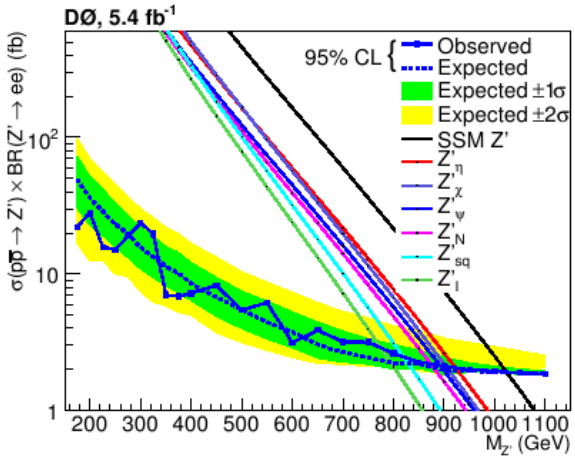

(b) From the D0 Collaboration[22]: The observed and expected upper limits on $\sigma(p\bar{p} \rightarrow Z') \times BR(Z' \rightarrow ee)$ as a function of the Z' mass, compared to theoretical predictions of the cross-sections for Z' arising from the E_6 GUT model and the SSM Z'.

Figure 2.4: 95% confidence level limits on the SSM Z' from the CDF Collaboration (2.4(a), muon channel) and on various Z' bosons arising in E_6 models and the SSM Z' from the D0 Collaboration (2.4(b), electron channel).

Chapter 3

Particle interaction with matter

This chapter is based on reference [4] unless stated otherwise.

Most particles interact with the matter they traverse. Because of this simple fact, we can build detectors to measure their properties. This section will only be about particles and effects that are relevant for the ATLAS detector and our search for new physics at high energy. Thus the effects listed here are not a complete collection.

When a generic particle goes through material two things can happen; the particle can lose some or all of its energy, and/or the particle can be deflected from its original direction. Both of these can be a result of one ore more effects. For example, the particle can emit bremsstrahlung and lose a fraction of its energy. Or it can detect the presence (i.e. collide, elastically or inelastically) of one or more other particles and be deflected (and possibly lose some of its energy, depending on the nature of the collision).

For more detailed information about this, see section 27 in reference [4].

3.1 Heavy charged particles through matter

This section deals with heavy charged particles, where "heavy" means heavier than the electron (the electron will be dealt with in section 3.3).

All charged particles moving through matter interact electromagnetically with it. The so-called electronic energy loss per distance is given by the Bethe-Bloch formula

$$-\frac{dE}{dx} = 2\pi N_a r_e^2 m_e c^2 \rho \frac{Z}{A}\frac{z^a}{\beta^2}\left[\ln\left(\frac{2m_e\gamma^2 v^2 W_{\max}}{I^2}\right) - 2\beta^2\right]$$

where r_e is the classical radius of the electron ($2.817\times10^{-13}\,\mathrm{m}$), m_e is the electron mass, N_a is Avogadro's number, I is the mean exitation potential[1], z is the charge of the incident particle

[1]This is approximately given by $I = 10\mathrm{eV}\cdot Z$ with Z being the atomic number of the atoms in the material being traversed.

and $W_{\max}$ is the maximum energy transfer in a single collision. Z is the atomic number of the matter being traversed and A and ρ its atomic weight and density respectively. Usually two corrections are added: the density effect correction δ and the shell correction C which are important at high and low energies respectively:

$$-\frac{dE}{dx} = 2\pi N_a r_e^2 m_e c^2 \rho \frac{Z}{A}\frac{z}{\beta^2}\left[\ln\left(\frac{2m_e\gamma^2 v^2 W_{\max}}{I^2} - \delta - 2\frac{C}{Z}\right) - 2\beta^2\right] \tag{3.1}$$

The density effect reduces the energy loss at high energies because the electric field from the traversing particle tends to polarize the particles along its path, thus giving a shielding effect. The shell correction is used at low energies when the velocity of the traversing particle is comparable to or smaller than the "orbital velocity" of the bound electrons in the matter.

The $-dE/dx$ for positive muons in copper is shown in Figure 3.1 as a function of $\beta\gamma$. The part of the curve explained by the Bethe-Bloch formula is between the second and third grey band, explaining the energy loss of muons with $p_T$between 0.5 MeV and 500 GeV going through copper. The other parts of the curve are based on different models.

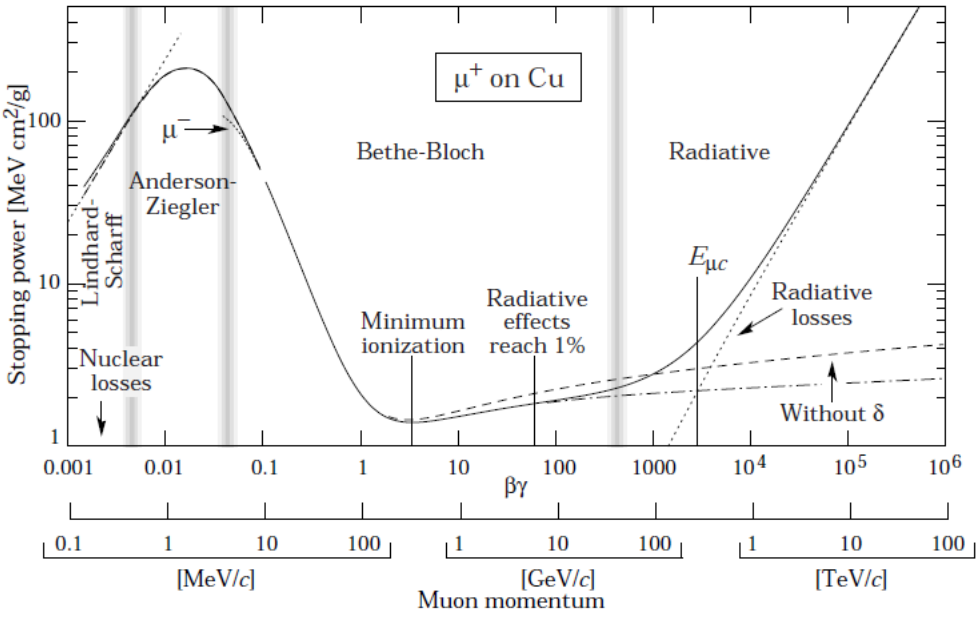

Figure 3.1: The Bethe-Bloch forumula for positive muons in copper as a function of $\beta\gamma$[4] (shown between the second and third grey band. The rest is described by other models.)

The Bethe-Block formula is based on the assumptions that the electrons in the traversed material are free and initially at rest, and that they do not move much during the interaction. Furthermore it is assumed that the incident particle is not deflected. The latter part is obviously not true for electrons, and we will address this in section 3.3.

3.2 Multiple Coulomb Scattering

In addition to what we saw in the last section (3.1), charged particles collide elastically with the matter through which they traverse, making the particles deflect[2].

How to treat this scattering depends on how many scattering one expects[23].

One If the material being traversed is very thin and one deflection is expected, a classical formula (the Rutherford formula) can be used.

Less than 20 If the average number of scatterings is less than 20, the angular distribution is very hard to model. See referances [23] or [23] for more information on this.

20 and more If the average number reaches 20 and above, and the energy loss is small, then one can use statistical methods to find the net angle of deflection as a function of the thickness of the material. A multitude of models are available for this situation. Some explain larger deflection angles, some only look at small angles. See reference [4] for more info.

3.3 Energy loss by electrons and photons

3.3.1 Electrons

Electrons and positrons are a group by themselves because they have a very small mass. Like all particles they can collide directly with other particles, but in addition to this, and more importantly, they lose energy if they scatter off the electric field of a nucleus. When this happens, the electrons can radiate brehmsstrahlung. The emission probability for bremsstrahlung goes as the inverse square of the particle mass[23]. Thus the difference in emission probability for muons goes down 40 000 times in comparison to electrons. At energies above 10 MeV the electronic loss of energy by radiation dominates over energy loss by collisions, see Figure 3.2.

This is what happens in the ATLAS electromagnetic calorimeter (ECAL), see section 4.2.5. Given that the emitted photon has enough energy, i.e. more than two electron masses, it pair produces an electron-positron pair (section 3.3.2), which emits bremsstrahlung, and so on. This is known as an electromagnetic shower. The shower lasts until the electrons and positrons lose so much energy that loss by collision starts to come into play again. Eventually the whole shower stops.

The Bethe-Bloch formula, used to describe energy loss by ionization and atomic excitation, can be used for electrons and positrons only with some modifications. There are two main reasons for these modifications. Firstly it is because of their small mass, as mention before. Secondly, when an electron travels through matter, it is because the interaction is now

[2]For hadrons the strong force also causes scattering.

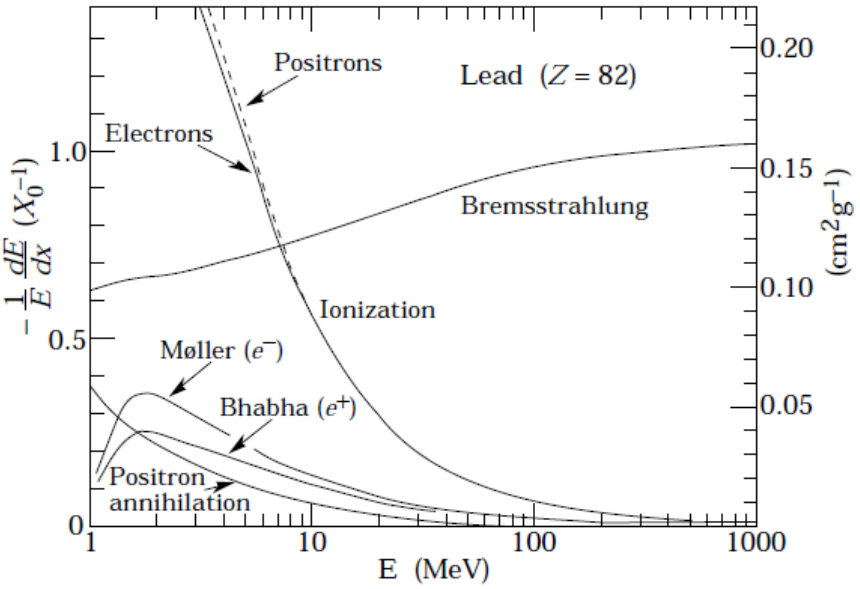

Figure 3.2: The fraction of the energy loss per radiation length in lead as a function of the electron (positron) energy[4]. A radiation length is the mean distance over which an electron (positron) travels before it is left with only $1/e$ of its starting energy.

between two identical particles ($e^{\pm}e^{\pm}$), thus calculations have to take into consideration their indistinguishability. The Bethe-Bloch formula for electrons and positrons goes like this:

$$-\frac{dE}{dx} = 2\pi N_a r_e^2 m_e c^2 \rho \frac{Z}{A}\frac{1}{\beta^2}\left[\ln\left(\frac{\tau^2(\tau+2)}{2(I/m_e c^2)^2}\right) + F(\tau) - \delta - 2\frac{C}{Z}\right]$$

where τ is the kinetic energy of the incident particle in units of $m_e c^2$ and $F(\tau)$ is a specific function for electrons and another one for positrons. We will not go further into this. As already mentioned, collisions don't really contribute to the energy loss of high energy electrons.

3.3.2 Photons

A multitude of things can happen to photons in matter. Some examples are:

Comptom scattering Scattering of photons on charged particles. The photon loses a fraction of it energy.

Rayleigh scattering Elastic sattering of photons on particles with diameter up to about 10% of the photon wavelength.

Photoelectric effect The photon gets absorbed by the material and electrons are emitted.

Pair production The photon pair-produces an electron-positron pair.

Figure 3.3 shows the total photon cross-sectin in carbon and lead. We see that the photoelectric effect dominates at low energies up to about 1 MeV when the pair production threshold is reached (two times the mass of the electron). After 1 Mev, pair production becomes the dominant reaction and an electromagnetic shower (see previous subsection) is initiated.

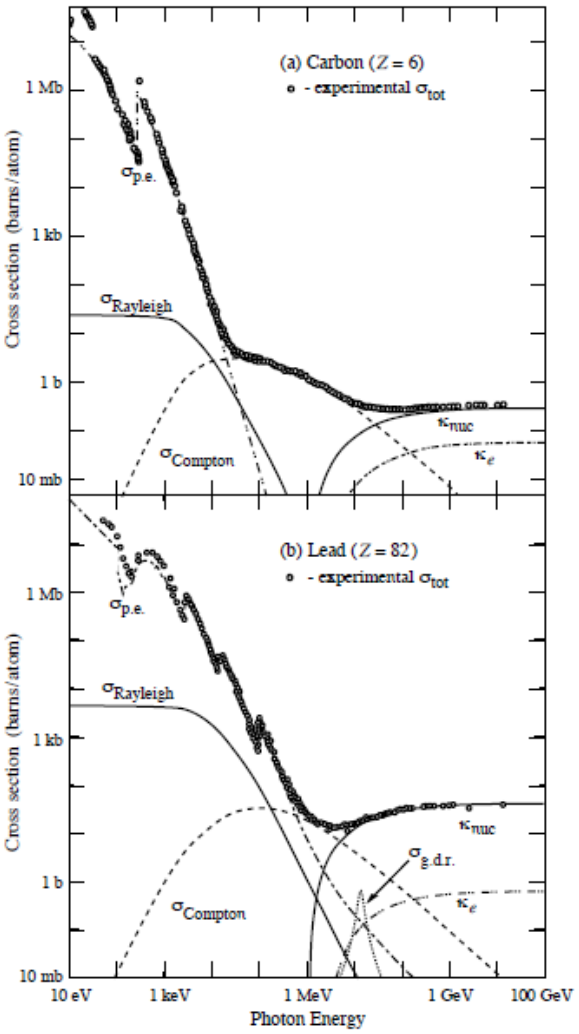

Figure 3.3: Photon total cross-sections as a function of the photon energy. [4] "p.e" stands for "photoelectric effect", "nuc" means pair production in nuclear field and "e" pair production in electron field.

3.4 Energy loss by muons

As for electrons, the dominant energy loss mechanism for muons is radiation at high energies. One can express the average rate of muon energy loss as[24]

$$-\frac{dE}{dx} = a(E) + b(E) \cdot E$$

where E is the total muon energy, $a(E)$ is the ionization energy loss given by the Bethe-Bloch formula (equation (3.1)) and $b(E)$ is the sum of three processes: e^+e^- pair production in a Coulomb field, photonuclear contributions[3] and bremsstrahlung. See Figure 3.4 for a comparison of the three contributions to $b(E)$. Both $a(E)$ and $b(E)$ are slow varying

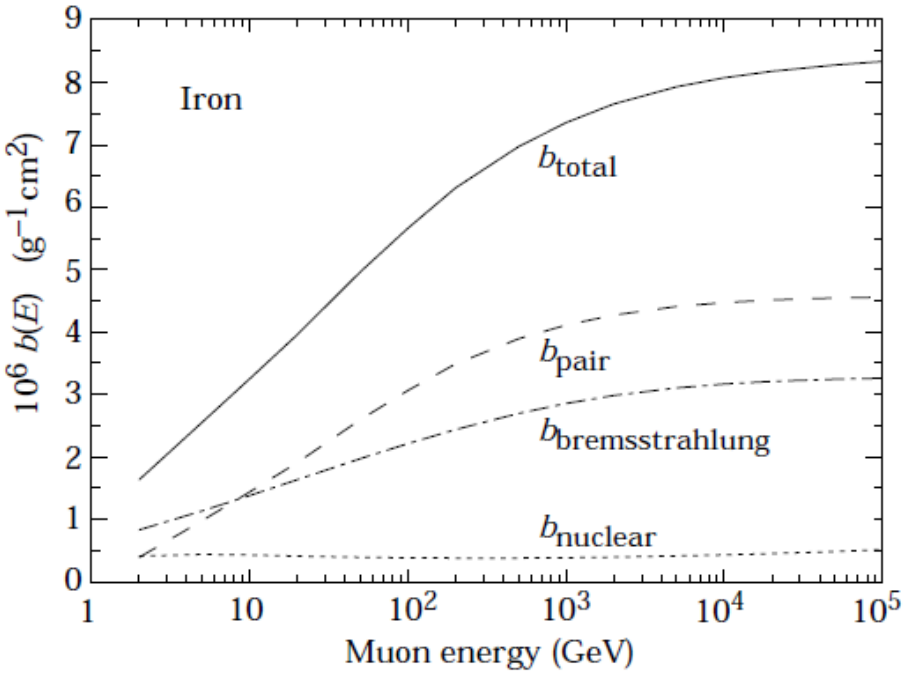

Figure 3.4: The energy loss of muons in iron[4]. b_{pair} is direct e^+e^- pair production, $b_{\text{bremsstarhlung}}$ is emission of photons and b_{nuclear} is inelastic interaction with nuclei.

function of E at high energies. $b(E)E$ contributes less than 1% in comparison to $a(E)$ for $E < 100\,\text{GeV}$.

Most relativistic particles are minimum ionizing particles (MIPs), meaning that they deposit the minimum amount of energy when going through matter. This also applies to the muon. It deposits some energy when going through the ATLAS detector, but because of its high mass it will not be stopped in the ECAL and because it is a lepton (without strong interactions) it will also pass through the ATLAS hadronic calorimeter (HCAL). If it has an initial energy of more than 3 GeV, it reaches the muon system. For an example of the muons ability to punch through materials nearly unaffected see Figure 3.5.

3.5 Energy loss by hadrons

Hadrons lose energy mainly via strong interactions, although electrically charged hadrons also interact electromagnetically. When hadrons traverses dense material, they interact inelastically with the nuclei in the material, initiating a hadronic shower. The hadronic shower

[3]Inelastic interaction of muons with nuclei.

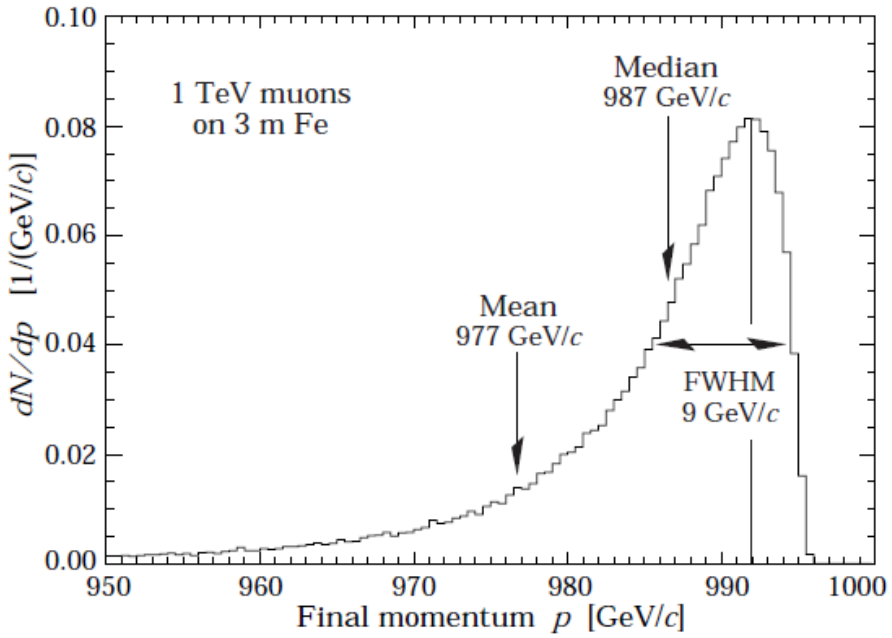

Figure 3.5: The momentum distribution of 1 TeV muons after passing through 3 meters of iron [4].

is the strong version of an electromagnetic shower. New hadrons (most often pions and nucleons) are created in the inelastic collisions, and can interact further with the material.

Hadronic showers are more complicated than their electromagnetic counterpart because of they have an electromagnetic component. For example, π^0 decays almost exclusively to diphotons.

The ATLAS HCAL uses hadronic showers to measure the energies of hadrons (see section 4.2.5).

3.6 Cherenkov radiation

A charged particle emits Cherenkov radiation when traversing a material at a velocity faster than the speed of light in that material. The speed of light in any material is given by

$$\beta c = v = c/n$$

where β is $\beta = v/c$, and n is the index of refraction. Thus for a particle to emit Cherenkov radiation it must travel at a speed faster than

$$v_{\text{particle}} > c/n$$

An electromagnetic shock wave is initiated, just as for sound when a plane breaks the sound barrier, see Figure 3.6. The angle θ is given by $\cos\theta = \frac{1}{n\beta}$.

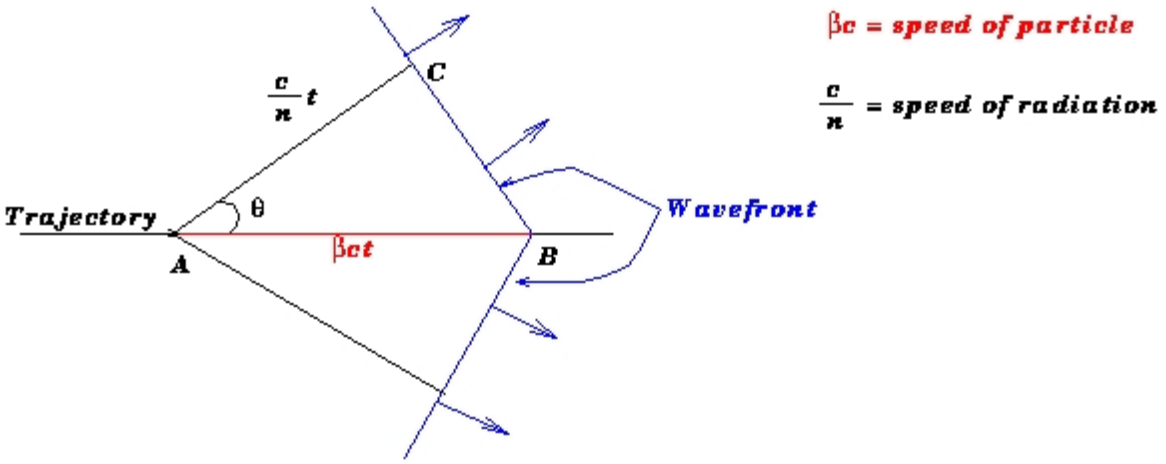

Figure 3.6: Schematics of the shockwave created when a particle breaks the "light barrier" in a material with refractive index n (http://www.physics.upenn.edu/balloon/cerenkov_radiation.html).

The ATLAS luminosity monitor, LUCID (LUminosity measurement using a Cherenkov Integrating Detector), uses Cherenkov detectors to measure the instantaneous luminosity in ATLAS. This is done by counting the number of charged particles per bunch crossing.

3.7 Transition radiation

When a charged particle crosses the boundary between two substances with different plasma frequencies it emits transition radiation. The plasma frequency ω_p is

$$\omega_p = \sqrt{4\pi N_e r_e^3}\frac{m_e c^2}{\alpha\hbar}$$

where N_e is the electron density of the medium, r_e is the classical electron radius, m_e is the electron mass and α the fine structure constant.

For example, if the charged particle (with charge ze) transitions between vacuum and a medium with plasma frequency ω_p, the energy radiated is

$$I = \alpha z^2 \gamma \hbar \omega_p / 3$$

where γ is the usual relativistic factor. The angular distribution of the transition radiation has a sharp maximum at $\theta = 1/\gamma$.

Transition radiation is utilized in the Transition Radiation Tracker (see section 4.2.4) where it assists with the electron identification.

3.8 Summary

In particle detectors, like the ATLAS detector at the LHC, particles are detected through their interactions with matter. In this chapter we described the most important effects at high energy. We now proceed to describe the layout of the ATLAS detector.

Chapter 4

The Large Hadron Collider and the ATLAS detector

In the first part of this chapter we will look at some generic information about circular particle accelerators and specifically the Large Hadron Collider (LHC). We then move on to the ATLAS detector, how it is built and how it manages to make sense out of what goes partly or fully through it. In addition to the physical detector parts, ATLAS also has a very advanced system that reads out the signal and decides what to save and what to throw away.

4.1 The LHC

The LHC is the worlds largest particle accelerator, colliding protons on protons at higher energies than ever before (7 TeV). It is situated at CERN (European Organization for Nuclear Research) partly in France and partly in Switzerland, close to Geneva. The collider resides in a 27 kilometer circumference tunnel located between 50 and 175 meters underground. The actual tunnel was constructed between 1983 and 1988 and housed the Large Electron-Positron (LEP) collider until 2000. LEP reached a center of mass energy of 209 GeV. The reason for tearing down LEP to build LHC was synchrotron radiation. Synchrotron radiation is energy loss by charged particles when accelerated. The energy loss scales as the inverse of the fourth power of the particle mass. An electron has approximately 1/1836 the mass of a proton. Thus the energy loss is scaled down by a huge factor for protons in comparison to electrons.

The LHC was designed to collide 2808 bunches of 10^{11} protons 40 million times per second at a center of mass energy of 14 TeV with a luminosity of $10^{34}\text{cm}^{-2}\text{s}^{-1}$. In November 2010, after taking data at a center of mass energy of 7 TeV for 8 months, the pp-collision period for 2010 was over (and taken over by lead-lead collisions until Christmas shutdown in December). By that time LHC had delivered an integrated luminosity of 48.9 pb^{-1}, and ATLAS had recorded about 45 pb^{-1}. The maximum peak (instantaneous) luminosity was $2.1 \times 10^{32}\,\text{cm}^{-2}\text{s}^{-2}$.

The first beam circulated in LHC September 10 2008. Nine days after, a fatal error occured

and the LHC was shut down for repairs. The repaires were finished in November 2009 and on November 20 proton beams were circulated again. Three days after this the first collision was recorded at 900 GeV center of mass energy. On 30 November 2009 the LHC set the world record of collisons at 1.18 TeV per beam. After the winter shutdown the LHC restarted and the beam energy was ramped up to 3.5 TeV. The first 7 TeV collisions were recorded on March 30 2010.

There are four main LHC experiments, one of which is ATLAS, see figure 4.1. The other three are CMS, LHCb and ALICE. ATLAS and CMS are the two largest and they are both multipurpose detectors. LHCb is made for B-physics, and ALICE mainly for heavy ion collisions. In a particle collider, the (instantaneous) luminosity $\mathcal{L}$ is a very important

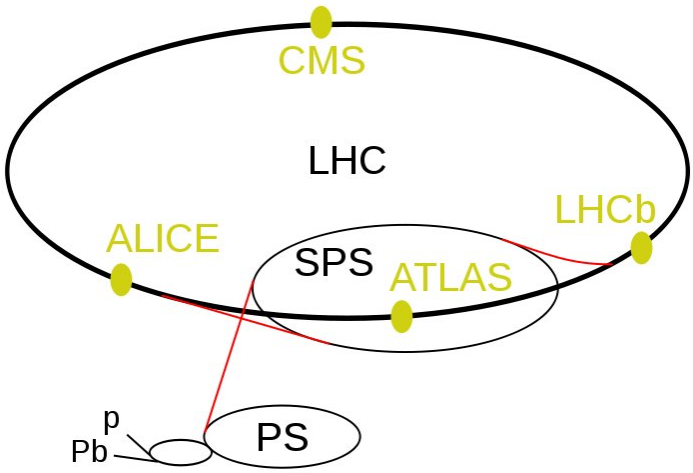

Figure 4.1: The layout of the LHC experiment, showing the four big experiments (ATLAS, CMS, ALICE and LHCb). The points marked "p" and "Pb" are where the paths of protons and ions begin. They go into the booster, and continue to the Proton Synchroton (PS) and to the Super Proton Synchrotron (SPS) before being let into the LHC tunnel.

parameter given by

$$\mathcal{L} = f_B \frac{n_1 n_2}{4\pi\sigma_x\sigma_y} \tag{4.1}$$

where n_1 and n_2 are the number of particles in bunches 1 and 2 going opposite to each other, f_B is the bunch crossing frequency (the number of times per second the two bunches cross each other, equal to revolution frequency f times the total number of bunches N) and σ_x and σ_y are the physical size of the transverse (normal to the direction of motion) beam. The nominal values for the LHC beam parameters are given in table 4.1. To have the luminosity

Parameter	Value	Comments
N	2808	Number of bunches
σ	$16 \times 10^{-4}\text{cm}^2$	Transverse beam size ($\sigma_x = \sigma_y$)
f_B	40×10^6	Bunch crossing frequency
N	1.15×10^{11}	Protons per bunch

Table 4.1: A few nominal beam parameters.

as high as possible many particles are needed in each bunch, meeting each other as often as possible with as small beam area as possible. The luminosity has the unit $\mathrm{cm}^{-2}\mathrm{s}^{-1}$.

The event rate R for a certain process (for us this will be $q\bar{q} \to Z' + X \to l^+l^- + X$ where the lepton is either an electron or a muon) is proportional to the luminosity

$$\frac{dN}{dt} = R = \sigma\mathcal{L}$$

where σ is the theoretical interaction cross-section given by the Standard Model (or a new theory Beyond the SM). Integrating this expression leads to the expected number of events

$$N = \sigma \int \mathcal{L}\, dt \tag{4.2}$$

We now introduce a new concept, namely the *integrated luminosity* $\int \mathcal{L}\, dt$, which is just the instantaneous luminosity integrated over time. This is what is often used when quantifying how much data has been collected. The SI unit is cm^{-2}. This too tends to be a very small number. Therefore a unit called *barn* is used. One barn is $10^{-28}\mathrm{cm}^{-2}$. The cross-section is given in barn, from millibarn ($\mathrm{mb} = 10^{-3}\mathrm{b}$) to femtobarn ($\mathrm{fb} = 10^{-15}\mathrm{b}$) at the LHC as can be seen in figure 4.12. The integrated luminosity is in *inverse* barn, typically between inverse nanobarn (nb^{-1}) to inverse femtobarn ($\mathrm{fb}^{-1} = 10^6\mathrm{nb}^{-1}$).

Tevatron, the second highest energy particle collider in the world, has, since it began running in 1983 collected about 8 fb^{-1}. LHC has only run for about a year and had in November 2010 delivered 48.9 pb^{-1}.

4.2 The ATLAS detector

We now take a closer look at one of the four main detectors, namely the ATLAS detector.

Unless stated otherwise, all information is taken from [25].

4.2.1 Nomenclature

Figure 4.2 shows the ATLAS coordinate system. The interaction point is defined as point $(0, 0, 0)$. The z-axis follows the beam pipe. Side A of ATLAS has a positive z-coordinate, and the C side (said to be pointing towards the local pub Charly's in Saint-Genis-Pouilly) has a negative z-coordinate. The x-y plane is transverse to the direction of the beam - (almost) straight up[1] is the positive y-axis, and the positive x-axis points towards the center of the LHC ring.

The azimuthal angle ϕ is zero in the positive x-direction and increases clockwise when looking in the positive z-direction. ϕ is in the range $[-\pi, +\pi]$.

[1] A tilt in the LHC tunnel has the effect that the y-axis is tilted some 0.7° away from "straight up".

The polar angle θ is measured from the positive z-axis. Pseudorapidity η is defined as

$$\eta = -\ln\left(\tan\left(\frac{\theta}{2}\right)\right)$$

and is thus zero in the transverse plane (xy) and increases towards infinity toward the z-axis.

The transverse momentum p_T, transverse energy E_T and missing transverse energy $\not{E}_T$ are the momentum and energies that are perpendicular to the beam axis.

A distance in the $\eta - \phi$ plane is defined as

$$\Delta R = \sqrt{(\Delta\eta)^2 + (\Delta\phi)^2}$$

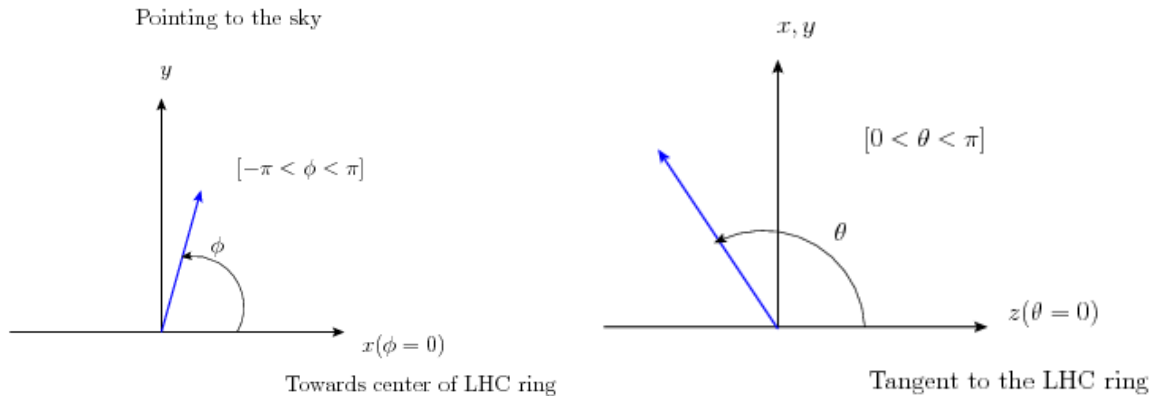

(a) The transverse plane

(b) The longitudinal plane

Figure 4.2: Two projections of the ATLAS coordinate system. One in the transverse plane (4.2(a)) and one in the longitudinal plane (4.2(b)).

4.2.2 A quick overview of the detector

The ATLAS (**A** **T**oroidal **L**HC **A**pparatu**S**) detector has four main parts (see figure 4.3)

- the inner detector (ID) (Section 4.2.4),
- the calorimeters (electromagnetic and hadronic) (Section 4.2.5),
- the muon spectrometer (Section 4.2.6) and
- the magnet systems (Section 4.2.3).

They all function together to try to accurately reconstruct interesting events, see figure 4.4.

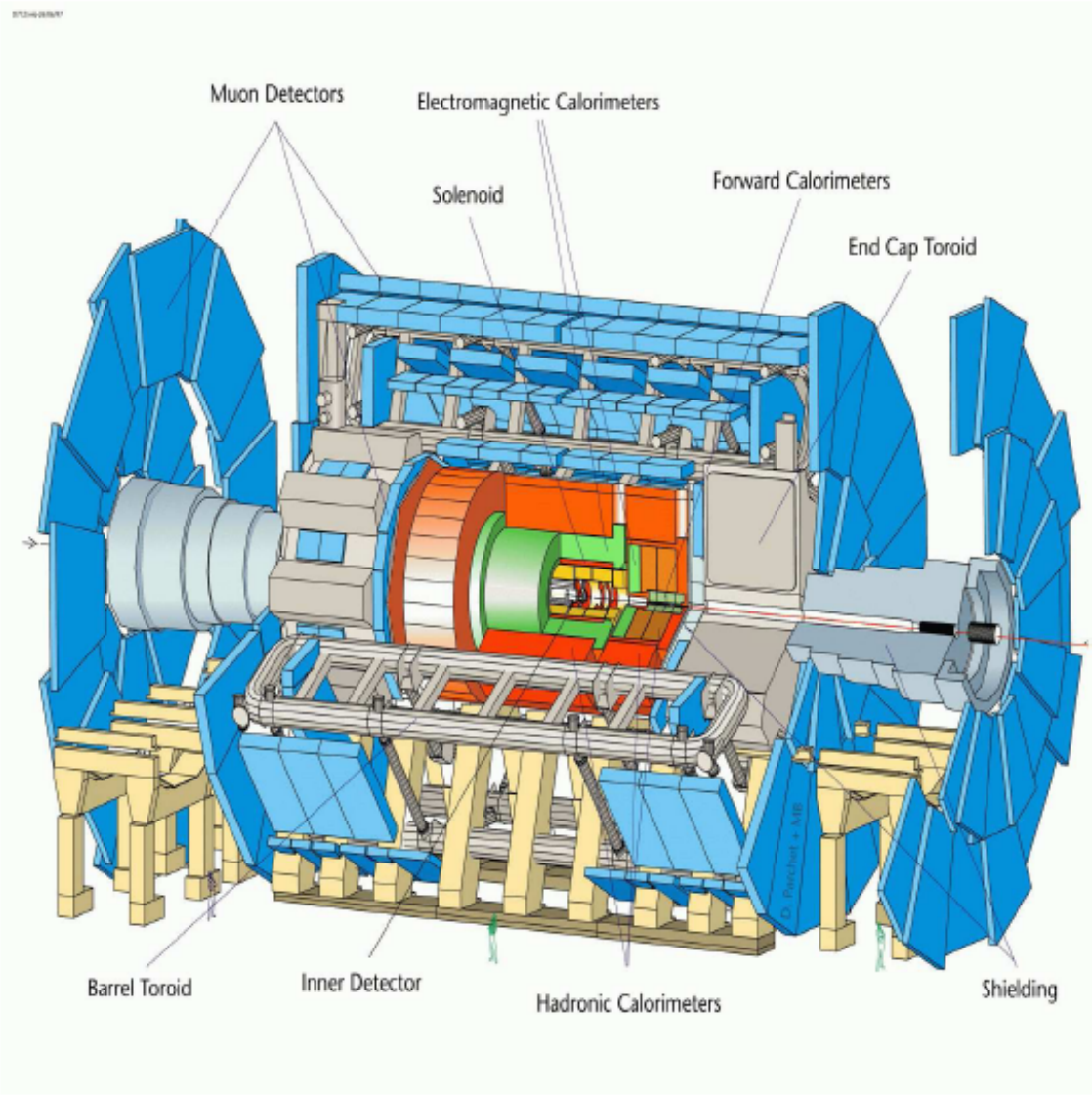

Figure 4.3: An overview of the ATLAS (**A** **T**oroidal **L**HC **A**pparatu**S**) detector showing the main parts[26].

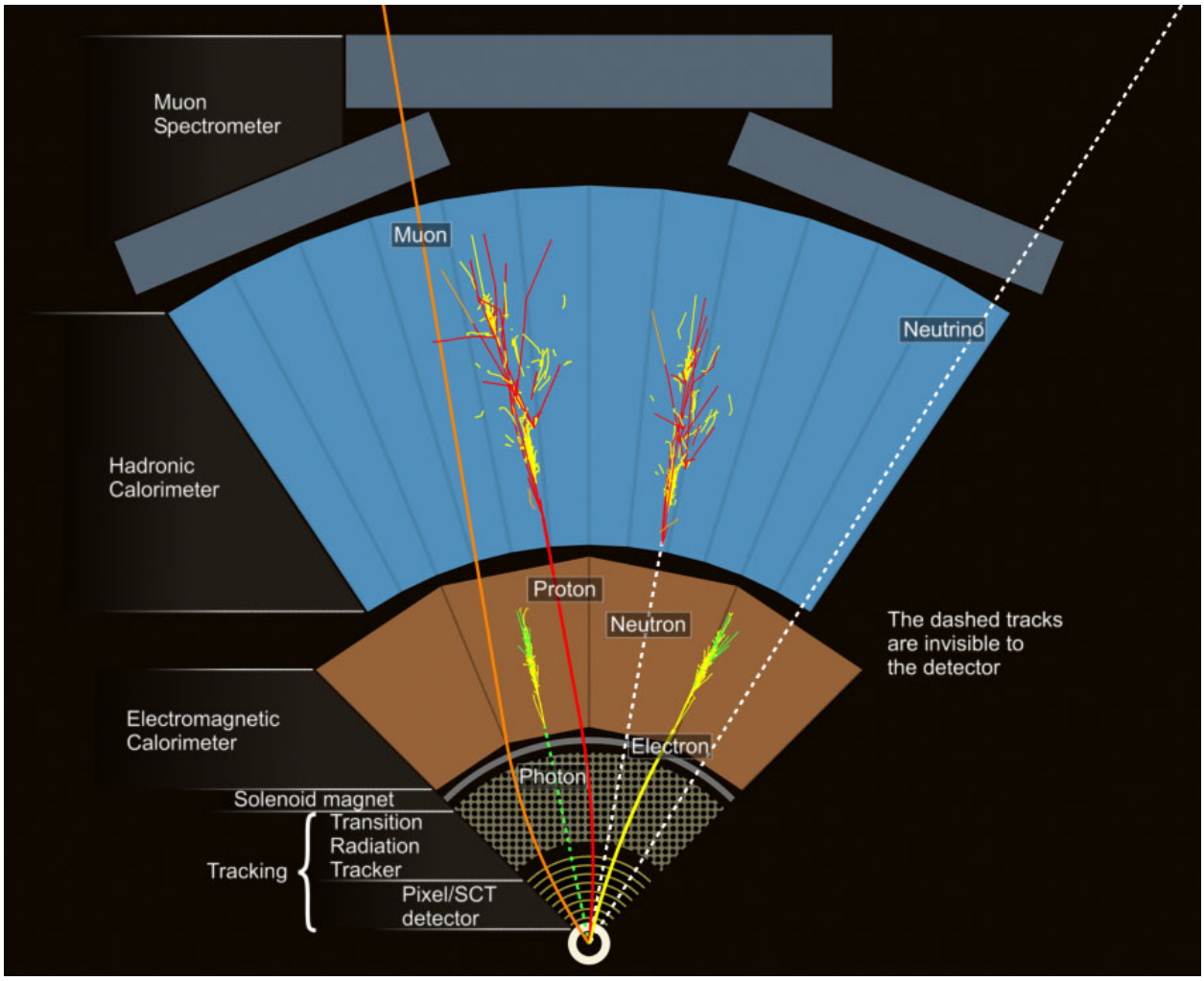

Figure 4.4: The ATLAS detector is built to measure the properties of all "stable" (meaning the ones that have a lifetime long enough to be detected) particles originating from a collision. The innermost part of ATLAS is called the inner detector (ID) and it measures the momentum and position of all charged particles. Outside the ID is the electromagnetic calorimeter (ECAL). Particles that interact primarily through the electromagnetic forces (i.e. electrons, positrons and photons) lose all their energy here. The ECAL measures the energy with good precision, and the precision actually increases with higher particle energies. Outside the ECAL is the hadronic calorimeter (HCAL), which is designed to measure the energy of the hadrons, like protons and neutrons. The outermost region is called the Muon System (MS), and it measures the momentum and position of muons. Of all the SM particles, only muons and neutrinos get through to the MS. The neutrino is not detected at all, but its existence will be inferred from the missing momentum ($\not{E}_T$).

The ID The inner detector (ID) is responsible for measuring the momenta of charged particles. It is able to do this because of the magnetic field provided by the solenoid magnet lying between the ID and the calorimeter. Charged particles will have their trajectories bent in magnetic fields. The amount of bending depends on the momenta and the magnetic field strength, and the direction depends on their charge q

$$\mathbf{F} = q\mathbf{v} \times \mathbf{B}$$

where $\mathbf{F}$ is the force felt by the charged particle with charge q going through a magnetic field $\mathbf{B}$ with velocity $\mathbf{v}$. Particles going slow bend more than particles going fast. Because of this the resolution gets worse with increasing momenta.
The ID is depicted in the lower part of figure 4.4 where the charged particles (muons, proton and electron) are visible. The photon and neutrino are illustrated with dotted lines, meaning their presence is not directly measured, but inferred: the photon energy is measured in the electromagnetic calorimeter, while the neutrino is never actually measured, only set equal to the missing momentum.

The ECAL The electromagnetic calorimeter (ECAL) records the energy of the particles going through it. It is split in two parts - the electromagnetic and the hadronic calorimeter, often referred to as the ECAL and the HCAL respectively. The ECAL measures the energy of particles that have electromagnetic interaction (mainly electrons, positrons and photons). These particles initiate an electromagnetic shower (see section 3.3) that is fully contained in the ECAL. This is illustrated in the brown colored part of figure 4.4.

The HCAL Particles with strong interactions (i.e. hadrons, like protons, neutrons and $\pi^{\pm}$) pass through the ECAL without losing much energy[2], but when entering the much denser hadronic calorimeter (HCAL) they will initiate a hadronic shower. This shower is very much like its electromagnetic counterpart, only with lighter hadrons (like $\pi^{\pm}$) being produced instead of electrons and photons (see section 3.5). This is illustrated in the blue area of figure 4.4.

The MS The muon is an evasive particle that deposits a minimum of energy (about 3 GeV) in the calorimeters before it is registered in the muon system (MS) (see section 3.4). The MS is the outermost part of the ATLAS detector, and is the uppermost, dark blue structure in figure 4.4.

Missing $\not{E}_T$ The ghostly neutrino travels through the whole detector without leaving any trace at all. We can only deduce its presence by using the law of conservation of momentum. It is not the protons themselves that collide, it is the particles inside the protons, valence quarks, sea quarks, gluons, each carrying a fraction of the proton momentum. The fraction of momentum carried by each parton is goverened by statistics and is not a priori known. As a result we can not assume that the momentum in the z direction is conserved. However, the partons have next to none transverse momentum in the lab frame, because the protons are going at nearly the speed of light. This means

[2]Some hadrons, like the neutron, have no net electrical charge. Others, like the proton, has a charge, but the probability of sending out bremsstrahlung (which is what happens in an electromagnetic shower) goes as the inverse square of the particle mass.

that the total transverse momentum in the collision should be zero. Therefore, if the sum om the $p_T$measured in the ECAL, HCAL and MS is non-zero, this is a signature of one or more neutrinos or of a non-interacting non-SM particle.

$$\sum_{\text{visible}} p_T + \sum_{\text{invisible}} p_T = 0 \rightarrow \sum_{\text{invisible}} p_T = -\sum_{\text{visible}} p_T$$

It is the $\sum_{\text{invisible}} p_T$ that is known as the missing E_T, $\not{E}_T$.

The above is true for all "stable" particles, meaning particles that have lifetimes long enough to leave the detector before decaying. The presence of any other particle (like Z^0, π^0 and τ) is inferred. Usually from invariant mass distributions showing a resonance (see section 5.1).

The ATLAS general performance goals are summarized in Table 4.2. An important thing to notice is that the relative resolution for the calorimeters *increases* with increasing energies, while the tracking relative resolution (ID and MS) *decreases* with increasing p_T.

Component	**Resolution**	η **coverage**	
		Measurement	Trigger
Tracker	$\sigma_{p_T}/p_T = 0.05\% p_T \oplus 1\%$	± 2.5	
EM calorimeter	$\sigma_E/E = 10\%/\sqrt{E} \oplus 0.7\%$	± 3.2	± 2.5
Hadronic calorimeter			
barrel and end-cap	$\sigma_E/E = 50\%/\sqrt{E} \oplus 3\%$	± 3.2	± 3.2
forward	$\sigma_E/E = 100\%/\sqrt{E} \oplus 10\%$	$3.1 < \lvert\eta\rvert < 4.9$	$3.1 < \lvert\eta\rvert < 4.9$
Muon spectrometer	$\sigma_{p_T}/p_T \approx 10\%$ at $p_T = 1$TeV	± 2.7	± 2.4

Table 4.2: From [25], the general performance goal of ATLAS. E and p_T must be in units of GeV.

4.2.3 The magnets

The ATLAS magnet system, see figure 4.5 consists of a solenoid aligned on the beam axis, providing the inner detector (see section 4.2.4) with at 2 T magnetic field, and a barrel toroid and two end-cap toroids, creating magnetic fields for the muon system (see section 4.2.6) of 0.5 T and 1 T in the barrel and end-cap region, respectively.

4.2.4 The inner detector

The innermost part of the ATLAS detector is called the inner detector (ID). It is a cylinder extending out 6.2 m along the beam axis with a radius of 1.05 m. It is responsible for measuring the trajectories (containing information about the momentum and the sign of the charge) of charged particles, with a little help from the magnet system (section 4.2.3). A track must have $p_T$above a certain threshold (usually 0.5 GeV, to reduce the number of low

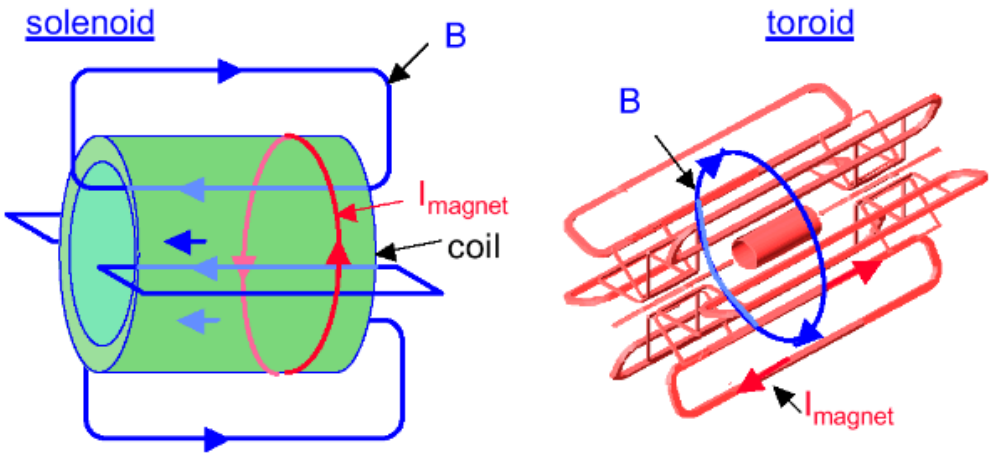

Figure 4.5: Schematic of the magnet system. On the left is the central solenoid, creating the 2 T magnetic field for the inner detector. On the right of this is the barrel toroid and the two end-cap toroids delivering the magnetic field of 0.5 T and 1 T, respectively, to the muon chambers.

$p_T$tracks.) and pseudorapidity in the range $\eta = \langle -2.5, 2.5 \rangle$ for the ID to be able to measure it. In addition to this it can find the impact parameter, and so-called secondary vertices from heavy particles decaying, like the bottom quark.

The inner detector consists of three sub-detectors - the pixel detector, the semiconductor tracker (SCT) and the transition radiation tracker (TRT), see figure 4.6. These are concentric cylinders in the barrel region and the end-cap parts are disks perpendicualar to the beam axis.

The Pixel detector

The barrel part of the pixel detector is composed of three cylindrical layers at approximately 5 cm, 9 cm and 12 cm (see figure 4.6(b)), with 22, 38 and 52 staves respectively. Each stave is composed of 13 pixel modules. The end-caps consists of three disks perpendicular to the beam axis. Each disk has 8 sectors with 6 modules per sector.

A pixel module is approximately 6 cm long and 21 cm wide with 46080 pixels. In total there are about 80.4 million radout channels. The pixel detector covers the region $|\eta| < 2.5$. In the barrel part, the intrinsic measurement accuracies are 10 μm in the R-ϕ and 115 μm in the z direction, and in the end-cap disks they are 10 and 115 μm in R-ϕ and R respectively.

Both the pixel detector and the SCT (see next subsection) are silicon semiconductor detectors. Semiconductors are materials whose outer shell atomic levels have a distict energy band structure and with a large forbidden energy gap (meaning without any allowed energy levels). On opposite sides of this forbidden gap is the conduction (highest energy level) band and the valence band. When an electron is in the conduction band, it can be considered free, and it flows when an electric field is applied. When a charged paticle traversese the semi-

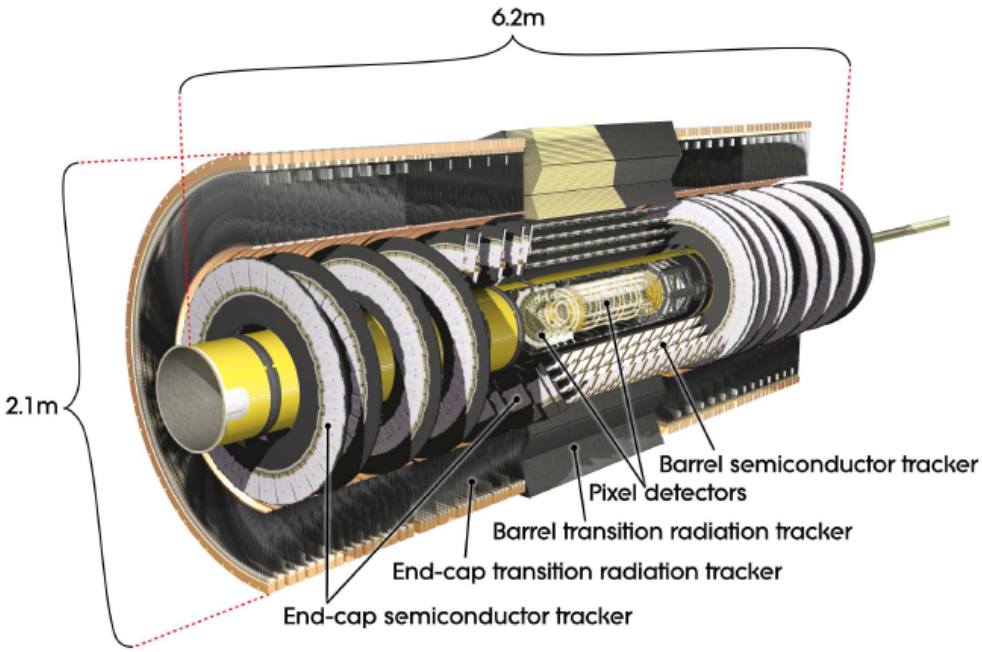

(a) Cut-away view of the ATLAS inner detector.

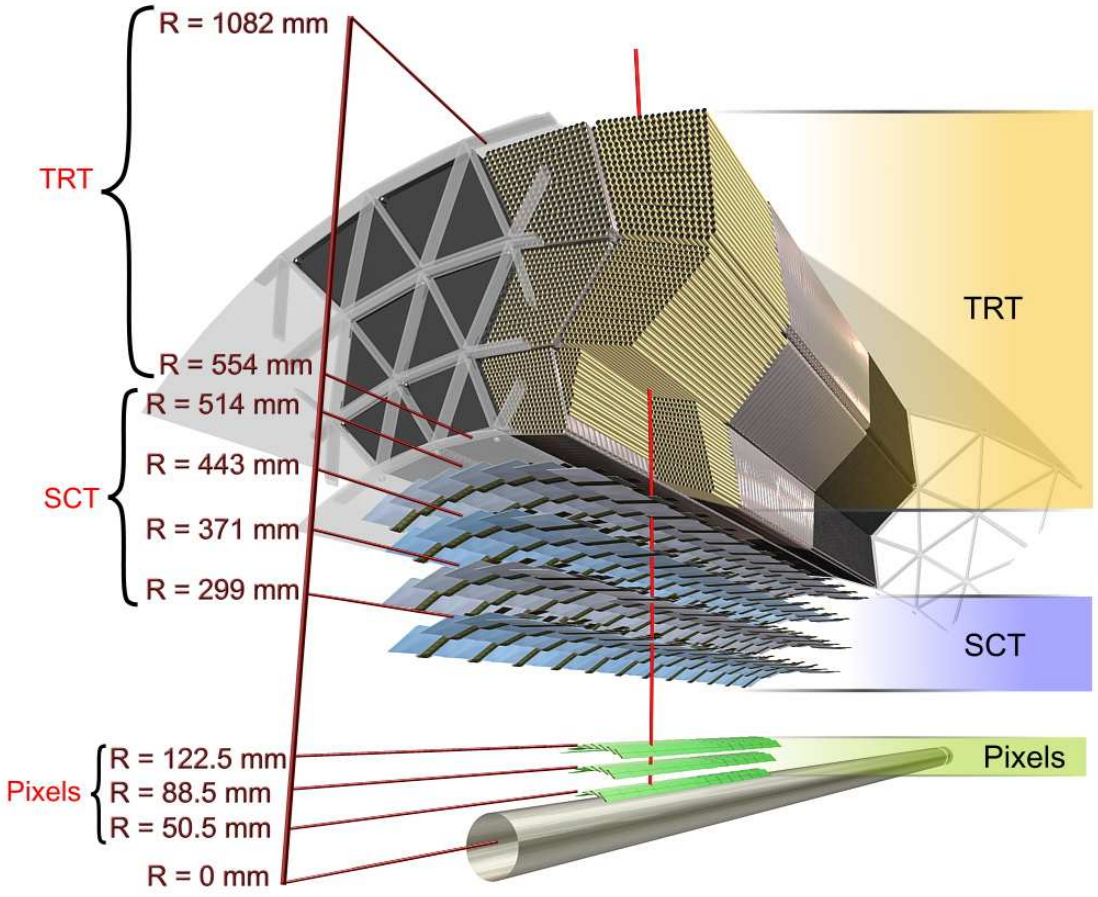

(b) Schematic illustration of the ATLAS inner detector.

Figure 4.6: The ATLAS inner detector (ID).

conductor, electrons are kicked into the conduction band and the current can be detected and measured.

The SemiConductor Tracker

In SCT, which is the layer outside the pixel detector, tracks have to cross eight strip layers. This contributes to the measurement of momentum, impact parameter and vertex position.

The barrel part of SCT is made of concentric cylinders mounted at radii of 30, 37, 45 and 52 cm from the interaction point. In total the barrel has 2112 silicon modules. Each module is made up of 2 pairs of identical silicon micro-strip sensors glued back to back. Each pair forms a 126 mm long strip with a total of 768 readout channels, resulting in a total of 1536 readout channels per module.

The two end-caps are made up of 9 disks each with a total of 1976 modules, all with two sensors each. Thus, in total the SCT has about 6.3 million readout channels.

The intrinsic accuracies are 17 μm (R-ϕ) and 580 μm (z) per module in the barrel, and 17 μm in the R-ϕ plane and 580 μm in the R direction in the end-cap disks.

The Transition Radiation Tracker

The TRT is the outermost part of the inner detector made of straw drift-tube detector covering up to $|\eta| = 2$. The barrel contains 52544 straws[27] going along the beam pipe and the two end-caps each have 18 wheels containing 319488 radial straws alltoghether, see figure 4.6(b).

A wire is strung in the middle of each straw. When a charged particle passes through the straws, the Coulomb interaction between the particle and electrons in the gas will free some of those electrons. Holding the outer wall at high negative voltage, the wire in the middle will act as the anode and the outer wall as the cathode, separating the now freed electrons from the ionized gas. If electrons are freed close to the wire, they will be seen almost immediately. If not, they will have a drift time of at most 40 ns[28]. The drift time is used to infer the distance from the wire.

The straws, which are 4 mm in diameter, are filled with a xenon-gas[3] so that some particle identification possibilites are added. When a relativistic particle comes across some inhomogeneity[4] it can radiate energy in the form af photon (see section 3.7 for more information on the physical process). This emission of photons depends on the relativistic velocity, p/m, of the particle and only happens for $\beta\gamma >\sim 1000$. In practice this is used to distinguish between electrons and hadrons.

It is only possible to get R-ϕ information from the TRT. Each straw has an intrinsic mea-

[3] 70% Xe, 20%CO_2, 10% CF_4

[4] Like the boundary between xenon gas filled area and something else.

surement accuracy[5] of 130 μm per straw. The approximate number of readout channels is 351000, each providing a drift-time measurement and two independend thresholds, allowing the detector to differentiate between tracking hits (low threshold, $\sim$ 200 eV) and transition radiation hits, passing the higher one ($\sim$ 5 keV). The electrons typically produce more high threshold hits than heavier particles at the same energies. Muons with $p_T >$ 100 GeV will also produce transition radiation.

4.2.5 The calorimeters

The ATLAS calorimeter is made up of multiple parts, see figure 4.7, placed outside the inner detector and the solenoid magnet. The two main parts are the electromagnetic calorimeter and the hadronic calorimeter, also called ECAL and HCAL respectively. Their main purpose is to measure the energies and directions of electrons/photons (ECAL) and hadrons (HCAL). The calorimeters cover the range $|\eta| < 4.9$, which is essential for missing E_T ($\not{E}_T$) measurements.

It is important that each calorimeter separately contains the whole electromagnetic or hadronic showers such as to limit punch-through into the muon system. The ECAL is thus $22 - 33$ radiation lenghts (X_0) (the exact number depends on the η of the module), and the HCAL is 9.7 interaction lengths (λ) in the barrel part and 10 λ in the end-caps. A radiation or interaction length is the average distance a particle travels before interacting inelastically through strong and electromagnetic interactions, respectively.

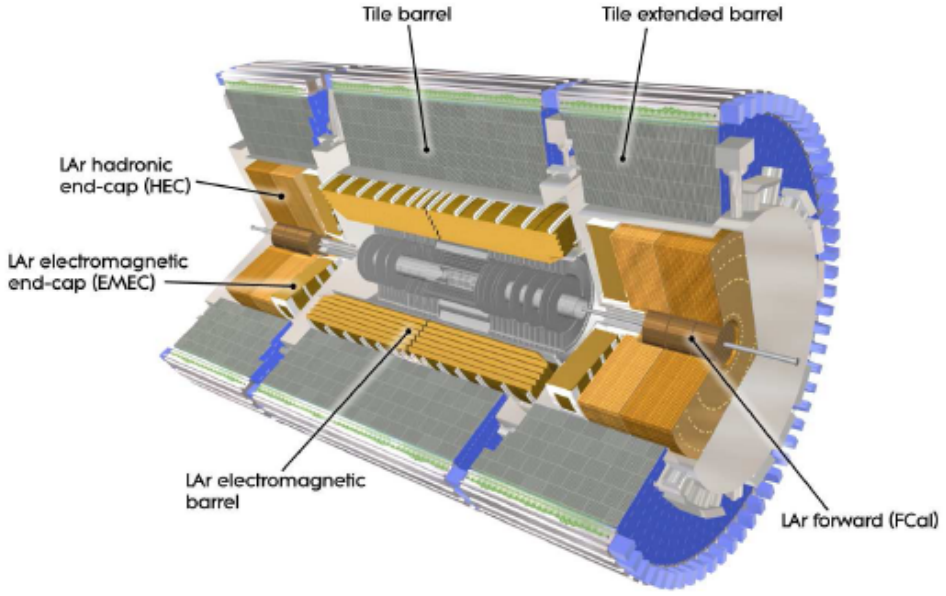

Figure 4.7: The ATLAS calorimeter system [25]

[5] According to [29] this number should be 170 μm.

LAr electromagnetic calorimeter

The aim of the ECAL is to measure the energy of electrons, positrons and photons. When an electron or positron enters the ECAL, it interacts electromagnetically in the detector material (see section 3.3 for more information on the physical process), initiating an electromagnetic shower starting from bremsstrahlung. Similarly, a photon entering the ECAL initiate a shower starting with e^+e^- pair production.

More technically, the ECAL is a lead-liquid Argon (LAr) calorimeter with Kapton[6] electrodes in an accordion shape sandwiched between lead absorber plates over $0 < |\eta| < 3.2$. The two parts of the EM calorimeter are the barrel part, covering $|\eta| < 1.475$, and the two end-cap components covering $1.375 < |\eta| < 3.2$. There are three sampling layers in the precision-measurement region, $0 < |\eta| < 2.5$ and two in the rest, covering $2.5 < |\eta| < 3.2$.

The barrel is itself divided in two half-barrels separated by a crack of 4 mm at $z = 0$. The end-caps are also divided in two parts, one inner part covering $2.5 < |\eta| < 3.2$ and an outer part covering $1.375 < |\eta| < 2.5$. The ECAL covers the entire ϕ angle.

Hadronic calorimeters

The HCAL is quite dense, so as to ensure that the entering hadrons come close enough to the nucleons to interact strongly with them (see section 3.5). When this happens, more particles are created. The hadronic shower is more complicated than the electromagnetic one, because leptons and neutrinos resulting from hadronic decays can also be created, making it hard to get a good measurement of the energy of the incoming particle.

The HCAL is composed of three sub-detectors: the tile calorimeter, the LAr hadronic end-cap calorimeter (HEC) and the LAr forward calorimeter (FCal).

The tile calorimeter is situated right outside the EM calorimeter, starting at a radial position of 2.28 m and extending out to 4.25 m ($\sim$7.4 λ). It covers the region $|\eta| < 1.7$.

The HEC starts just outside the electromagnetic end-cap calorimeter and is composed of two wheels at each end-cap. The wheels have an outer radius of $\sim$ 2 m. The HEC covers the range $1.5 < |\eta| < 3.2$

The forward calorimeters are situated close to the beam axis around 4.7 m from the interaction point and cover the range $3.1 < |\eta| < 4.9$.

4.2.6 Muon system

The muon system (also referred to as the muon spectrometer), see figure 4.8, aims at measuring the momenta and the coordinates of the only visible particles that manage to go through the calorimeters, namely the muons. The momentum is measured in the same way as the

[6]Polyamide film. Stable in the temperature range 0 to 673 K.

ID tracker does it - with magnetic fields. In the range $|\eta| < 1.4$ the bending is done by the large barrel toroid (see section 4.2.3), while for $1.6 < |\eta| < 2.7$ this is performed by two smaller end-cap magnets. In the so-called "transition region", $1.4 < |\eta| < 1.6$, a combination of barrel and end-cap magnets is used. With this magnet-constellation the magnetic field is almost always normal to the muon trajectory (the magnetic field makes circles around the beam axis). The muon system is designed to trigger on (see next subsection for more information) particles in the region $|\eta| < 2.4$, and the transverse momentum resolution is designed to be approximately 10% for a 1 TeV muon.

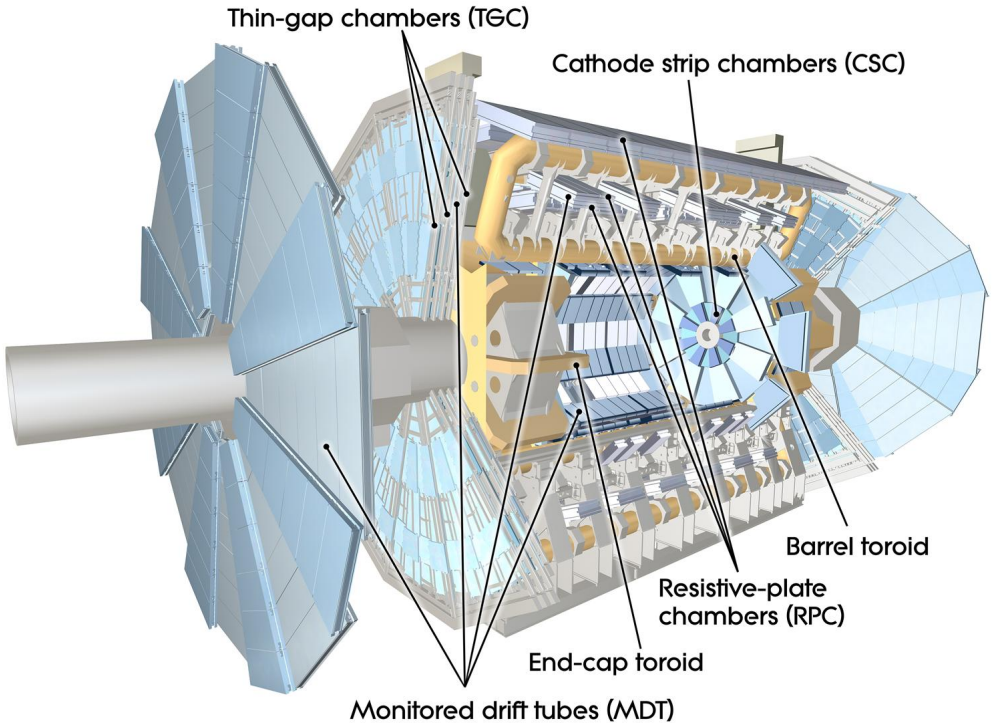

Figure 4.8: Cut-away view of the ATLAS muon system [26]

The actual muon chambers in the barrel section are composed of three concentric cylinder shells (with the beam axis going through the middle) with radii of $\sim$ 5, 7.5 and 10 m. In the end-caps the muon chambers are large wheels normal to the beam axis at distances of $\sim$ 7.4, 10.8, 14 and 21.5 m from the interaction point.

As can be seen from figure 4.8 the muon system is made up of four sub-detectors, the Monitored Drift Tube chambers and the Cathode-Strip Chambers take care of the tracking, and the Resistive Plate Chambers and the Thin Gap Chambers are triggers. The variuos chambers are described below.

The Monitored Drift Tube Chambers

The Monitored Drift Tube (MDT) chambers are responsible for the precision measurement of momentum. This is done by measuring the coordinate in the bending plane (η plane) when

the particle traverses the layers. The chambers are made of small tubes with a diameter of $\sim$ 30mm, filled with Ar/CO_2-gas, and work the same way as all drift-tube detectors (like the TRT for example, see section 4.2.4), i.e. a charged particle (here, the muon) passes through a straw, ionizing the gas. The freed electrons drift toward the wire (here, a 50 μm diameter thungsten-rhenium wire) in the center of the drift tube and are registered there, see figure 4.9.

The chambers consist of three to eight layers of drift tube, with an average resolution of 35 μm per chamber, and cover the range $|\eta| < 2.7$, except for the innermost layer in the end-cap, which is covered by the CSC (see below).

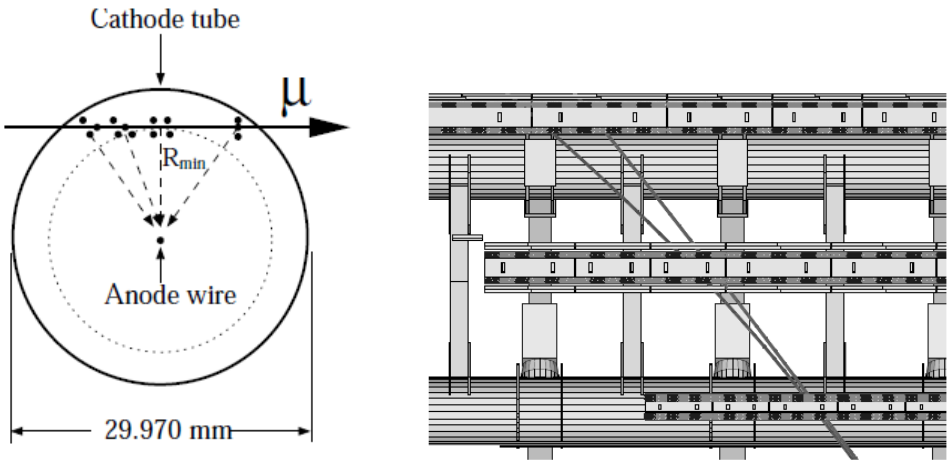

Figure 4.9: Left: Cross-section of a MDT tube, showing the ionization of the gas in the tube when a charged particle (i.e. a muon) traverses the medium. The freed electrons drift toward the positively charged wire and are registered there.
Right: The trajectories through the barrel muon spectrometer of muons with momenta of 4 (bent/left track) and 20 GeV (straight/right track) in the η plane. Tracks usually cross 2×4 inner, 2×3 middle and 2×3 outer layers of MDT tubes. For $|\eta| > 2$, the hits in the inner MDT are replaced by four hits in CSC[25].

.

The Cathode-Strip Chambers

In the range $2 < |\eta| < 2.7$ the Cathode-Strip Chambers (CSCs) aids the innermost layer in the end-cap region of the MDT. This part of the detector are subject to some of the highest doses of radiation, and the CSCs are more radiation hard than the MDTs. In addition to this they have better time resolution.

The CSC (see figure 4.10) is a multiwire proportional chamber (MWPC) with usual cathode plates segmented into strips. It is similar to the drift-tube chamber (see section 4.2.4), except that the cathode strips (planes for the generic MWPCs), not the outside of the tubes, are

held at high negative voltage, with anode wires going orthogonal to the strips. This way both coordinates - η and ϕ - can be measured from the induced-charge distribution.

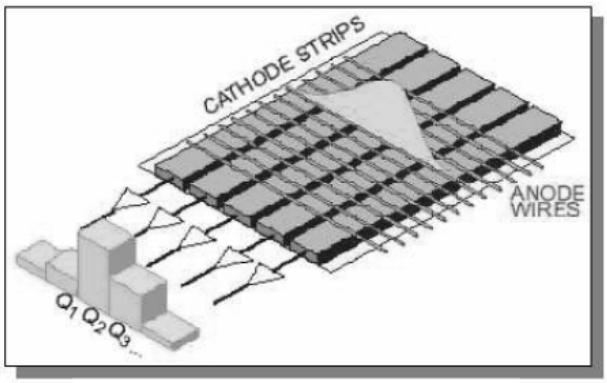

Figure 4.10: The ATLAS CSC is a multiwire proportional chamber with the usual cathode plate segmented into strips[25]. The cathode strips are held at a high negative voltage, and the anode wires at a high positive voltage. When a muon traverses the chamber, the η and ϕ coordinates are inferred from the induced-charge distribution.

The Resistive Plate Chambers and the Thin Gap Chambers

It is very important to be able to trigger on muon tracks. This is the job of the Resistive Plate Chambers (RPC) in the barrel region, $|\eta| < 1.05$, and the Thin Gap Chambers (TGC) in the end-cap region, $1.05 < |\eta| < 2.4$. When a muon crosses the TGC or the RPC, signals are delivered within a few tens of nanoseconds.

Other important tasks are to decide what bunch crossing the muon belongs to (bunch-crossing identification), and to measure the coordinate in the non-bending (ϕ) plane, compensating for the fact that the MDT can only measure the η coordinate.

The RPC, which is a gaseous parallel electrode-plate detector, consists of three concentric cylinders centered at the beam axis. Each RPC unit consists of two resistive plates parallel to each other, one being held at high voltage and the other at ground, separated by 2 mm insulation. The passage of a tracked particle (i.e. muon) causes ionization. In the electric field between the plates, an avalanche is created as the electrons head for the anode, ionizing more gas on their way.

The TGC's are a type of MWPC, but with the wire-to-cathode distance (1.4 mm) smaller than the wire-to-wire distance (1.8 mm), see figure 4.11.

Two of the RPC layers are close to the middle MDT layer and the third layer is close to the outer MDT layer. In the endcap, one TGC layer is in front of the second MDT wheel and two are behind, and the fourth layer is in front of the innermost tracking layer.

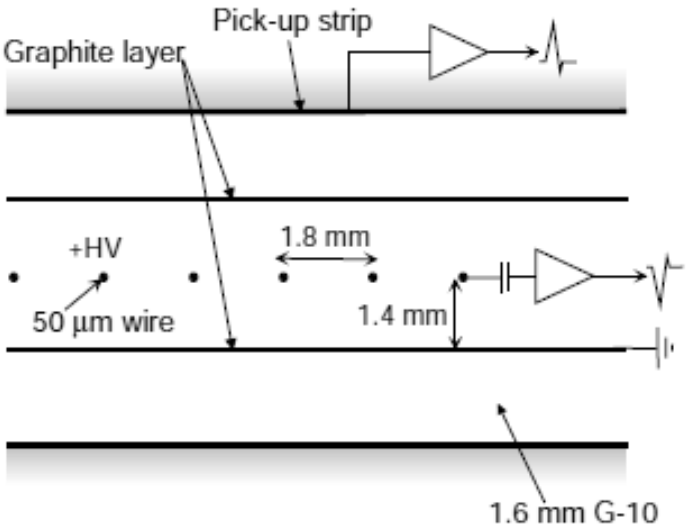

Figure 4.11: Structure of the Thin Gap Chambers.

4.3 Triggers

At the design luminosity of $10^{34}\,\mathrm{cm}^{-2}\mathrm{s}^{-1}$, decisions of keeping the events or not must be taken every 25 ns. Every bunch crossing contains, on average, more than 20 interactions. This of course can not be done manually, and three levels of triggers are designed to do this for us, getting the rate down from 40 MHz to 200 Hz. The goal is to keep all the interesting cases and discard all the not-so-interesting stuff. As can be seen from figure 4.12 the interesting processes are totally swamped by background. The total inelastic cross-section (at 14 TeV center of mass) is of the order of some tens of mb (10^{-3} b). The $b\bar{b}$ is then found a bit below that, at about 700 μb (10^{-6} b), and the SM Higgs to two photons is way down at a few hundred fb (10^{-15} b).

4.3.1 The Level 1 trigger

The Level 1 (L1) trigger system is the first to encounter the data, see figure 4.13. It uses activity in the different sub-detectors to search for high p_T particles (muons, electrons, photons, jets and τ decaying into hadrons) as well as events with large missing transverse energy $\not{E}_T$ and total transverse energy E_T. Within 2.5 μs L1 has to decide whether or not to keep the event, reducing the output rate from 40 MHz down to 75 kHz.

The L1 trigger consists of two separate parts - the L1 Calorimeter trigger (L1Calo) and the L1 Muon trigger (L1Muon). L1Muon searches for high p_T muons, while L1Calo looks for the rest listed above. L1Calo and L1Muon send their information to the Central Trigger Processor (CTP), which makes the final decision. At last the decision is broadcasted by the Timing, Trigger and Control (TTC) system.

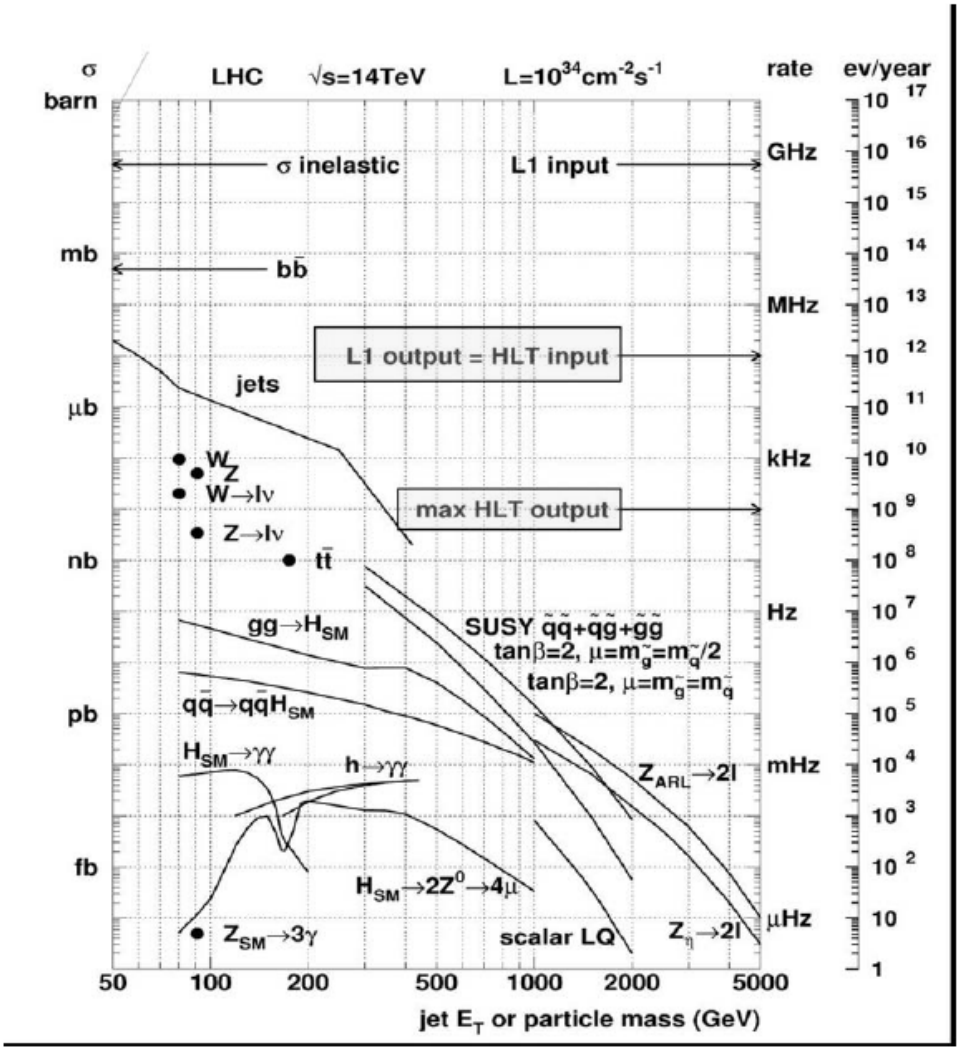

Figure 4.12: The cross-section of processes expected at the LHC energies. The interesting physics is swamped by background made up primarily of low energy QCD jets. The Level 1 trigger output is marked, as well as the HLT output. The high-level triggers (HLTs) are the Level 2 trigger and the event filter combined.[30]

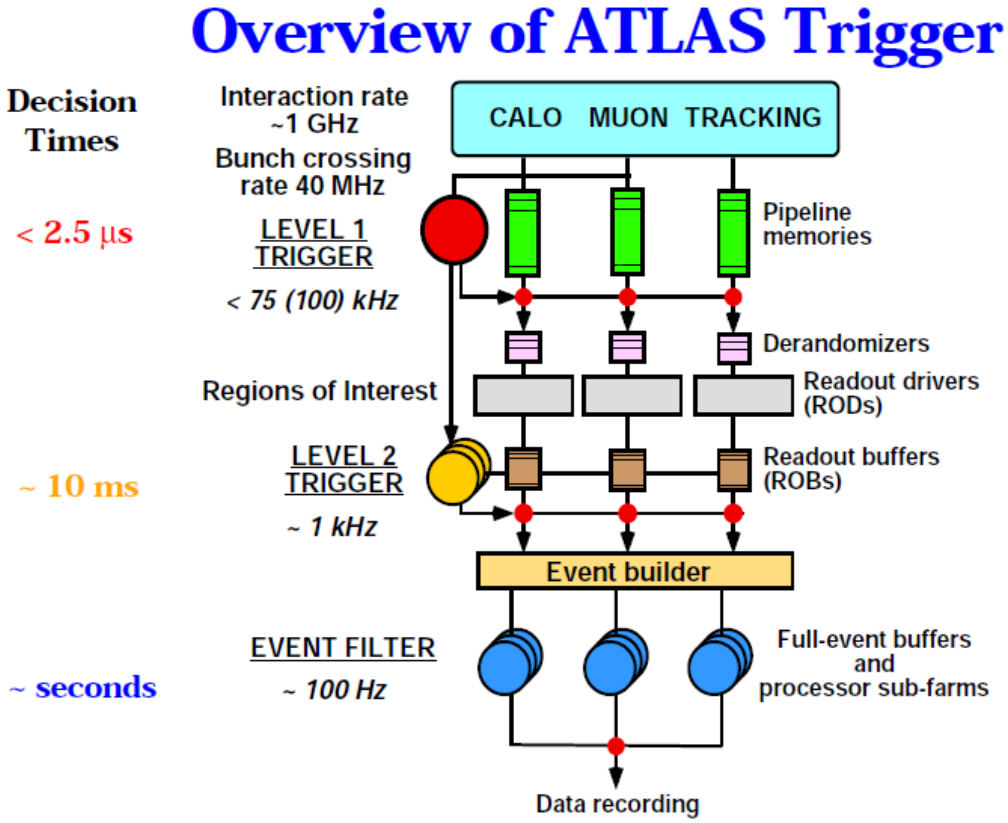

Figure 4.13: The three level trigger system used by the ATLAS detector. The L1 trigger is completely hardware based. It searches for high $p_T$particles and events with a lot of missing momentum or high transverse momentum. Based on this the L1 trigger defines Regions-of-Interests (RoIs) that seed the L2 trigger. The L2 trigger is software based and uses speed-optimized algorithms to reduce the event rate. The RoIs that get through the L2 trigger are seeds for the event filter (EF).

4.3.2 High-level triggers

The combined L2 trigger and Event Filter (EF) are known by a common name - The high-level trigger (HLT), see figure 4.13. They are both software based, in constrast to L1 which is completely hardware based. Both are seeded by the previous step in the chain, i.e. L2 trigger will only consider the regions marked as interesting by the L1 trigger (so called RoIs, Regions-of-Interest). Similarly, the EF will bee seeded by the L1 or L2 trigger.

Both the L2 trigger and EF base their decision on specialised algorithms. The L2 trigger's algorithm is optimized for speed while the EF uses a more complex algorithm to reject a larger fraction of the uninteresting events. The EF uses basically the same algorithms as is used offline, enabling the use of e.g. vertex reconstruction and track fitting.

The L2 trigger reduces the event rate from 75 kHz to 3.5 kHz, using approximately the order of ms on each decision. The EF then reduced the event rate down to 200 Hz, using up to 4 seconds per event.

4.3.3 Triggers in simulated data

The different triggers are simulated in the Monte Carlo data. If one does not require a trigger, there will be discrepancies between real and simulated data. How large that difference is depends on the required trigger. When searching for a very clean signal, as one gets from a Z' for example, the trigger efficiencies will be close to 100% and the offline analysis will probably have stricter cuts than the required trigger uses ($p_T$cuts for example).

4.4 Event reconstruction

After all trigger decisions have been made, the events that are kept must be reconstructed. The specific reconstruction algorithms not discussed here, but the the algorithms of interest are mentioned in due time, see for example section 5.4.1 and 5.4.2.

The data stream coming from the EF will be the basis for the reconstruction algorithms. The output from the reconstruction suitable for calibration is the Event Summary Data (ESD), and for analysis it is the Analysis Object Data (AOD) set. The AODs are reduced in size by a factor 5 in comparison to the ESDs. The ESDs and AODs are both object-oriented, meaning that the data is stored as "electron candidates" and "muon candidates", not as the detector responses delivered by the EF to the reconstruction software. To enable quick searches through all the events, thumbnail information about all the individual events are stored in so-called TAG data. The average size of the TAG data is only 1 kB per event.

The ESDs and AODs are produced centrally, but physics groups and individuals can then go even further and produce smaller datasets called Derived Physics Data (DPD). For all of these datasets one needs to use the Athena framework[7], which uses quite a lot of computing

[7]Athena is the framework used in all levels of data processing within ATLAS, from high-level trigger to

and storage resources. For easier access and faster analysis one makes ntuples (D3PDs) from ESDs, AODs or DPDs and run the analysis within, for example, ROOT[8].

4.5 Data flow

The raw data from the EF is sent to the Tier-0 facility located at CERN. Express and calibration streams are prepared quickly so that problems with the detector, calibration and so on can be caught early on. This is also the place where the first reconstruction is done, creating the ESD, AOD and TAG datasets. After reconstruction the datasets are distributed to 10 larger computer centers around the world known as Tier-1s.

The 10 Tier-1s have two copies of all the ESDs, AODs and TAG samples. The newest ones should be stored on a medium with short latency, while the previous versions may have higher latency (for example, it may be stored on tape). In addition each facility stores about 1/10th of the RAW data, and also do the reprocessing of its share about one to two months after the arrival of the data, when better calibration is provided.

The ATLAS data is made available to physicists worldwide by more than 30 Tier-2 facilities. This is also where all MC samples are generated.

4.6 Summary

In this chapter we have introduced a few important concepts for colliders in general, such as luminosity and event rate, and the ATLAS specifically (i.e. nomenclatur). The layout of the ATLAS detector is described, with all the different subdetectors and their purpose. The topics of trigger system and event reconstruction is briefly visited at the end.

In the next chapter we perform a feasibility study of a new neutral gauge boson, Z', at 10 TeV center of mass collisions.

event simulation.

[8]From http://root.cern.ch/drupal/content/about: "The ROOT system provides a set of OO [Object Oriented] frameworks with all the functionalities needed to handle and analyze large amounts of data in a very efficient way."

Chapter 5

Feasibility study at 10 TeV

In this part we review various aspects of the Z' seen from an experimental point of view - how to discover it through its decay into a pair of leptons (electrons or muons) (section 5.1), what the background is (section 5.2), which cuts to apply to reduce the background (sections 5.5 and 5.6), the angular distribution of the signal and background after all cuts (section 5.7) and finally how much data we need to discover it at different masses (section 5.8). Also the important topics of event generation and particle definitions are covered in sections 5.3 and 5.4 respectively.

5.1 The Z' in the detector

When talking about discoveries in particle physics it is easy to imagine discovering *particles*, but for an experimentalist the Z' is nothing but a high mass resonance, basically meaning a peak in an invariant mass (see equation (5.1)) histogram. It can be found via a simple counting game. In a given channel ($Z' \to e^+e^-$ or $Z' \to \mu^+\mu^-$), one gets a hold of all the candidate Z'-events (for a more precise definition, see section 5.5). Then one finds the so-called invariant mass of the two leptons:

$$M_i = \sqrt{\left(\sum_j E_j\right)^2 - \left(\sum_j \mathbf{p}_j\right)^2}, \quad i = 0, \ldots, N \tag{5.1}$$

where N is the total number of Z' candidates and $\sum_j E_j$ and $\sum_j \mathbf{p}_j$ are the sum of the energy and momentum of the decay products (here, two electrons or muons). The invariant mass is called "invariant" because it is the same in all frames of reference.

Then one divides the whole mass-range into bins and counts how many events fall into each bin, i.e. makes a histogram. Figure 5.1 provides an example of an invariant mass distribution. If a resonant structure emerges we say there is an intermediate particle present. The maximum of the resonance is interpreted as the particle mass and the width of the resonance Γ as the inverse of the lifetime of the intermediate particle, $\tau = \hbar/\Gamma$.

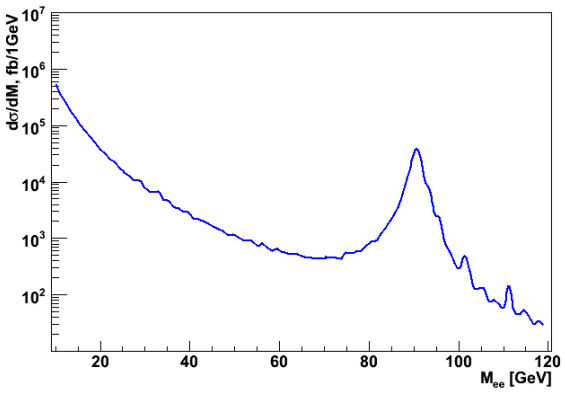

Figure 5.1: Plot of the invariant mass of the dielectrons from the process $q\bar{q} \to Z^0, \gamma \to e^+e^-$. The plot is obtained by drawing numbers from the theoretical distribution. Produced by CompHEP.

This simple histogram represents the partial cross-section of the process we are studying, $q\bar{q} \to Z' \to l^+l^-$ (the "partial" part refers to the specific final state). The partial scattering cross-section of a process tells us something about the probability of a specific subprocess happening when colliding two particles. In general a multitude of things can happen. For example, when colliding protons, there can be elastic scattering ($pp \to pp$) or inelastic scattering ($pp \to$ hadrons), and if a quark and an antiquark collide they can produce many different final states, the most probable being dijets ($q\bar{q} \to q\bar{q}$). The probability for the specific process $q\bar{q} \to l^+l^-$ to happen also varies with the energy of the collision, and a resonance in the cross-section simply means that at some specific energy this probability reaches a maximum. And now we have reached the second possible interpretation of the resonant structure. Instead of interpreting it as a particle one can think of it as just a variation in the likelihood of a specific process happening.

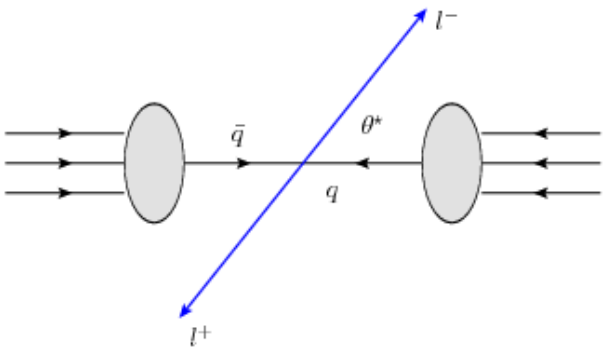

Figure 5.2: A quark and an antiquark colliding. $\theta^\star$ denoting the angle between the incoming quark and the outgoing l^-.

If an electrically neutral resonance is found, the first thing to check is the spin of the resonance. This can in principle easily be determined by looking at the angular distribution

(distribution of the decay angle) in the center of mass of the dilepton. Denoting the angle between the incoming quark and the outgoing negatively charged lepton $\theta^\star$ (see figure 5.2), the distribution for particles with spin 0, 1 and 2 have different forms , see figure 5.3. Of course, if it is not spin 1, it is not a Z'.

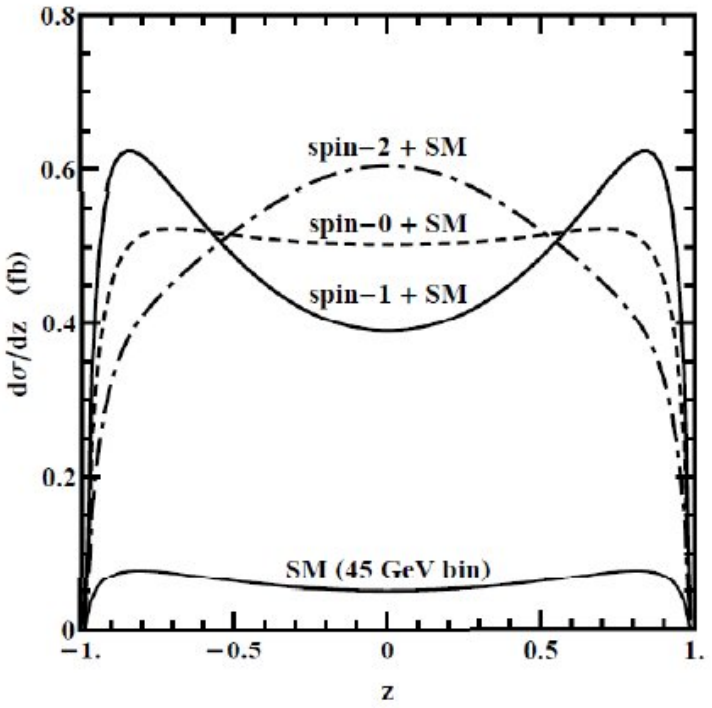

Figure 5.3: The theoretical angular distribution ($z = \cos\theta^\star$) of particles with spin 2, spin 1 and spin 0[31]. Spin 0 and 2 particle correspond to hypothetical particles - the Higgs boson and the graviton respectively. The SM gauge bosons ($W^\pm$, Z^0, gluons and photons) and the hypothetical Z' are all spin 1.

Sadly it might not be as easy as it sounds to find the angular distribution. At LHC the particles being sent around the 27 km ring at nearly the speed of light are protons. What collides however is a different matter. The protons are not elementary particles, they consist of valence quarks (two up quarks and a down quark), sea quarks and gluons. The three valence quarks are surrounded by gluons (known as the color field). The gluons are not at all stable and will split into a quark and a antiquark. These virtual quarks are known as sea quarks.

The momentum carried by a valence quark or a gluon or a sea quark is only a fraction of the total momentum of the proton. This fraction is modelled by the parton distribution functions (PDF), see figure 5.4. A PDF is a probability density for finding a parton with the longitudinal momentum fraction x at a certain momentum transfer μ^2. Note that the valence quarks (u_v and d_v in the figure) have a much higher probability of carrying a large fraction (above 10%) of the total momentum than the sea quarks do.

Because the proton consists of partons, we can not know a priori the direction of the quarks and antiquarks colliding to make a Z' in proton-proton collisions. The Z' can be produced

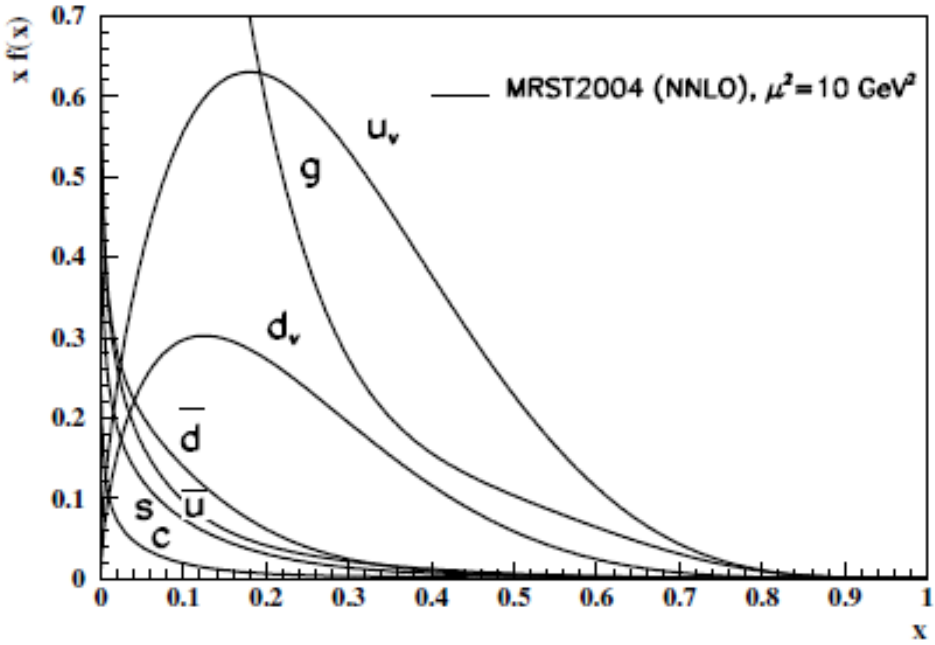

Figure 5.4: The parton distribution functions at $\mu^2 = 10\text{GeV}^2$ for gluons (g), valence up and down quarks (u_v, d_v) and sea up (u), down (d), strange (s) and charm (c) quarks in the proton [4]. The plot shows the product of the longitudinal momentum fraction carried by a parton (x) and the respective distribution functions versus x.

by a collision between a valence quark or a sea quark from one proton and a sea antiquark from the other proton, see figure 5.2. As mentioned above, in the protons it will statistically speaking be the valence quarks that have most energy compared to the sea quarks. Thus when a valence quark collides with a sea antiquark to produce a Z' we can assume that the Z' gets a boost in the direction that the valence quark was going. When two sea quarks collide we can make no such assumption. Due to this and also the fact that sometimes sea antiquarks will have more energy than the valence quark, the angular distribution will be quite diluted in its form.

After confirming that the spin of the newly found resonance is actually 1, one wants to find out what theory it belongs to. And as mentioned earlier (section 2.3), there are actually heaps of theories predicting a Z'. To distinguish between the different models one can use the resonance shapes (figure 5.5(a)) or the forward-backward asymmetry A_{FB} (the difference in the number of particles going in a "forward" direction N_{F} in contrast to a "backward" direction N_{B}) in the Z' center of mass frame, figure 5.5(b)

$$\text{A}_{\text{FB}} = \frac{\text{N}_{\text{F}} - \text{N}_{\text{B}}}{\text{N}_{\text{F}} + \text{N}_{\text{B}}} \tag{5.2}$$

This has not been done here, only the benchmark model, the Sequential Standard Model (SSM), is considered.

The signal can be swamped with other processes mimicking the signal. Luckily many of these are so-called *reducible* backgrounds. The ones belonging to the group of *irreducible*

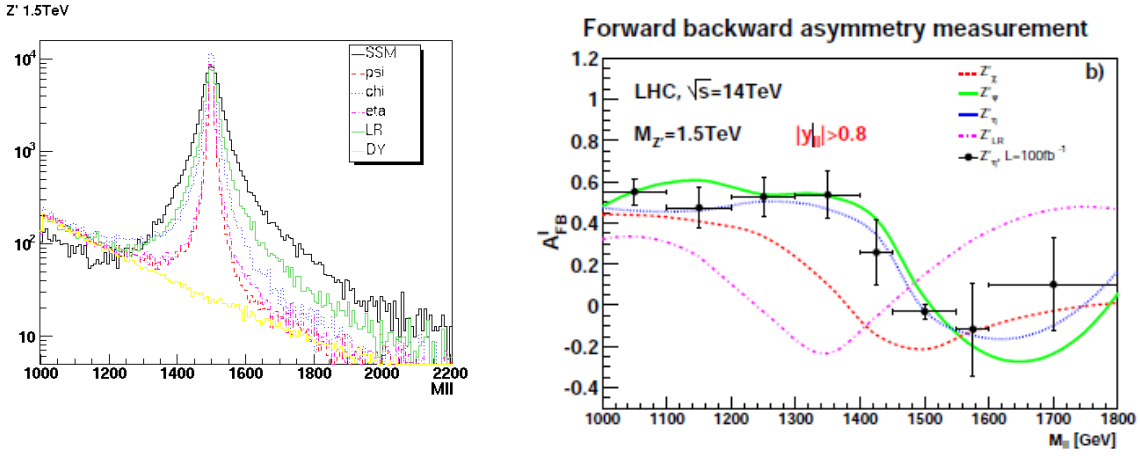

(a) Resonance shapes for different Z' models for a 1.5 TeV Z'.

(b) The forward-backward asymmetry (A_{FB}) for different Z' models near 1.5 TeV

Figure 5.5: The left figure[17] shows the Z' resonance (1.5 TeV) for a variety of models. The resonance shapes can be used to differentiate between these models. The right figure[17] shows the forward-backward asymmetry (equation (5.2)) for the same models. The difference between the models is clearly visible.

background one just has to endure. For more in-depth information about this, see section 5.2.

5.2 Backgrounds

All processes giving two or more leptons and/or photons and/or jets are background for the process $p\bar{p} \rightarrow Z' \rightarrow l^+l^-$. The only irreducible background is the high mass Drell-Yan process ($q\bar{q} \rightarrow \gamma/Z^0 \rightarrow l^+l^-$), see Feynman graph 5.6(a). In the low mass range a simple cut on the invariant mass will remove the majority of the DY, but one still has to consider the high mass region, where an off-shell Z^0 decays to electrons or muons[1].

The reducible backgrounds are dibosons (ZZ, ZW, WW, Zγ, Wγ, $\gamma\gamma$), $t\bar{t}$, dijets, γ+jets, W+jets, DY decaying to tauons ($pp \rightarrow Z^0/\gamma \rightarrow \tau^+\tau^-$ when the τs decay leptonically. DY with jets, when one of the leptons from the photon or Z^0 boson is not reconstructed and a jet fakes a lepton, can also be placed in this group.

[1]We have considered the Drell-Yan as a separate background for simplicity. In reality the γ, Z^0 and Z' are all produced by the same process and interfere with each other.

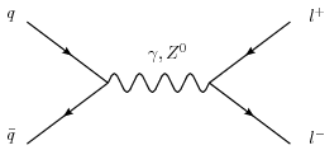

(a) Drell-Yan

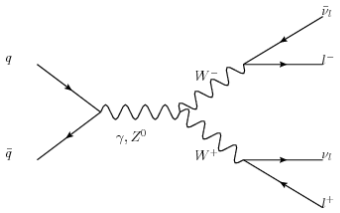

(b) WW

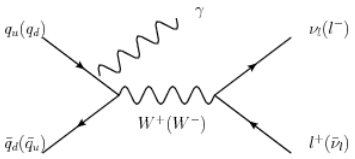

(c) Wγ

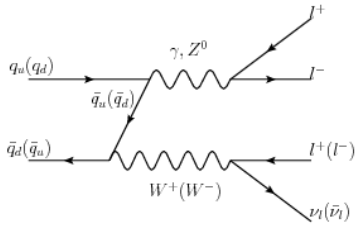

(d) WZ, Wγ

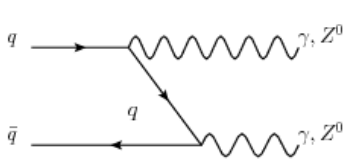

(e) ZZ,Zγ,$\gamma\gamma$

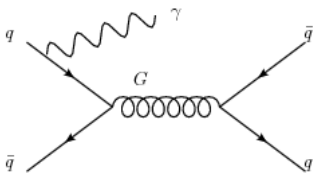

(f) Dijets (without the external photon line),γ+jets

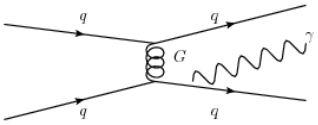

(g) Dijets (without the external photon line),γ+jets

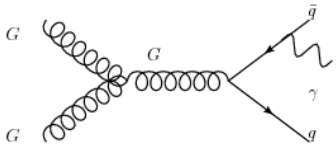

(h) Dijets (without the external photon line),γ+jets

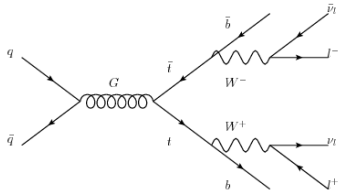

(i) $t\bar{t}$

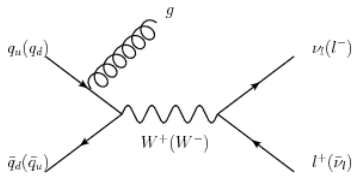

(j) W+jets

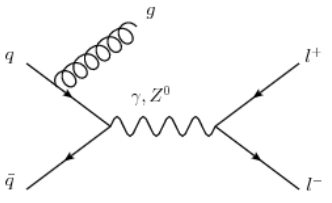

(k) Z+jets

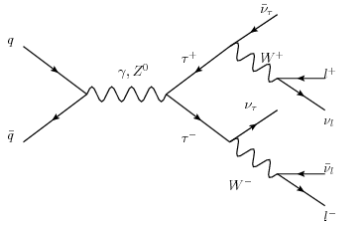

(l) DY to tauons to leptons

Figure 5.6: The SM backgrounds for Z' are DY, diboson (ZZ, ZW, WW, Zγ, Wγ, $\gamma\gamma$), $t\bar{t}$, dijets, γ+jets, Z+jets, W+jets and $\tau^+\tau^-$. Examples of Feynman diagrams for these processes to the leading order are shown here.

5.2.1 Dibosons

WW (graph 5.6(b) is a background when both W bosons decay leptonically, $W^{\pm} \to l^{\pm}\nu_l$. W bosons decay leptonically 33% of the time. For WW to be a background both must decay leptonically, and to the same flavour. These events will be characterized by a large amount of missing E_T from the neutrino, and, therefore, can be reduced by requiring little missing energy.

ZZ (graph 5.6(e) is a background when one or both Z bosons decay leptonically, $Z \to l^+l^-$. The branching ratio to leptons is approximately 10%. If both Zs decay to leptons the ZZ background is easily reduced by requiring exactly two electrons or muons with opposite sign. If only one Z decays to electrons or muons, it can be reduce by vetoing jets (for $Z^0 \to q\bar{q}$) or requiring low missing E_T (from $Z^0 \to \nu_l\bar{\nu}_l$). We expect this to be a non-dominating background because of the low cross-section and branching ratio.

WZ (graph 5.6(d)) must be considered as a background in addition to the usual $Z \to l^+l^-$ (DY), because one of the leptons from the Z can be paired with a lepton from the W when it decays leptonically. These events are expected to be easy to reduce by requiring exactly two high p_T leptons, or, in events where only two leptons are reconstructed, by requiring low missing E_T.

$\gamma\gamma$ (graph 5.6(e)) contributes to the dielectron background by fake electrons in the calorimeter. This is easily reduced by requiring well identified electrons (see section 5.4.1).

Wγ contributes when the W decays leptonically and the photon fakes a lepton in the calorimeter, see graphs 5.6(c) and 5.6(d). Given the missing E_T from the neutrino in the W decay, this contribution is also reducible.

Zγ (graph 5.6(e))) contributes to the dilepton background when the the Z^0 decays leptonically. The dilepton invariant mass is the Z^0 mass and this background is therefore not expected to be dominant.
In addition Zγ contributes to the dielectron background when the photon fakes an electron and the Z^0 decays to electrons where only one electron is reconstructed. In the last scenario, the event features $\not{E}_T$ from the lepton that was not reconstructed.

5.2.2 QCD dijets

QCD dijets (here, all $q\bar{q}$ events up to and including $b\bar{b}$) are why hadron colliders are "messy" - the cross-section is huge, mainly because the strong coupling constant is larger than the other coupling constants making these multi-particle processes all the more likely. The main processes are gluon-gluon fusion and quark collisions mediated by the strong force, see graphs 5.6(f), 5.6(g), 5.6(h). The processes contribute to the dilepton spectrum because occasionally there are real leptons in jets, and to the dielectron background because there may be quite a few fake electrons in jets[2]. This background is expected to be reduced by requiring isolated

[2]This is usually not the case in the dimuon spectrum, as the hadronic calorimeter is designed to stop everything, except for muons, and neutrinos of course. Fake muons can come from punch through (jets that penetrate through the HCAL) or kaon or pion decays in jets (which in this analysis are considered "fake")

leptons (leptons in jets are surrounded by lot of activity in contrast to what is expected for the isolated leptons coming from a Z').

5.2.3 $t\bar{t}$

The $t\bar{t}$ case is treated by itself because of the top quark's very high mass. Almost 100% of the time the top quark decays into a W boson and a bottom quark, $t \to Wb$. The $t\bar{t}$ background thus almost exclusively creates two b jets and two W bosons. One can imagine a multitude of combinations yielding dileptons, see graph 5.6(i). Luckily it can be reduced the same way as the W and dijet backgrounds (missing E_T and isolation).

5.2.4 Boson plus jets

W+jets (graph 5.6(j)) contributes to the dilepton background in a manner similar to what we have seen previously, i.e. when the W decays to electron and neutrino and a jet is reconstructed as a lepton. And just as before this it easy to reduce, becuase there is missing energy and the lepton from the jet (either fake or real) will be surrounded by a lot of activity (non isolated leptons).

$\gamma +$ jets (graphs 5.6(f), 5.6(g) and 5.6(h)) contributes whenever there are two reconstructed leptons, fake or not. But again this is easy to reduce, requiring good, isolated electrons.

5.2.5 $\tau^+\tau^-$

The DY process can lead to a pair of taus (graph 5.6(l)). This is a background for the signal whenever the taus both decay leptonically, $\tau^\pm \to W^\pm + \nu_\tau \to \nu_\tau + e^\pm + \nu_l$. One tau decays to a muon or an electron 17% of the time. The probability for a background for the signal is thus $2(17\%)^2 \approx 5.8\%$ whenever a photon or a Z^0 decays to taus.

5.3 Simulated data

This section is based on references [32], [33] and [34].

The foundation for a feasibility study such as this analysis is Monte Carlo, simulated data. One believes that this simulated data reproduces Nature to a high degree, which is also what is seen when comparing Monte Carlo simulated data to real data as we will show in chapter 6.

The road to a MC data sample has basically three steps. First there is the event generation, where the proton-proton collision is initiated and immediate decays are handled. Second

comes the detector simulation, where the particles generated in the event generation propagates through the detector and interact with it. The last step is the digitization of the energy deposited in the detector (i.e. signals) from the last step, converting the hits in the detector to voltages and currents. The resulting "data" looks exactly like the real data, except for the fact that it contains truth information as well, i.e. information from the event generation about what actually happened. Because simulated and real data are identical in every way that matters they can be run through the same ATLAS trigger, reconstruction and analysis software.

5.3.1 Event generation

As an oversimplified example consider the creation and decay of a Z^0 from two up quarks to two down quarks, $u\bar{u} \to Z^0 \to d\bar{d}$. We start from the differential cross-section

$$d\sigma(u\bar{u} \to Z^0 \to d\bar{d}) = \frac{1}{2\hat{s}} \left|\mathcal{M}(u\bar{u} \to Z^0 \to d\bar{d})\right|^2 \frac{d\cos\theta d\phi}{8(2\pi)^2} \tag{5.3}$$

where $\hat{s}$ is the center of mass energy of the collision squared, $\mathcal{M}$ is the Feynman amplitude and θ and ϕ are the azimuthal and polar decay angles of the down quark.

The next step now is to sample the phase space, that is the two dimensional space $-1 < \cos\theta < 1$, $0 < \phi < 2\pi$. This just means drawing two angles from flat distributions, giving a flat distribution in the phase space. This defines the so-called candidate event. This candidate event's differential cross section (also referred to as the *event weight*) can be calculated from equation (5.3) above. The average differential cross section, $\langle\sigma\rangle$, approximates the integral $\int d\sigma$ (this is the standard Monte Carlo integration) and converges to the cross section of the process.

The candidate events yield nothing more than the cross-section before they are further processed. They are distributed flat in phase space, containing no information of anything physical. There are two ways to go from there. The first path to follow is quite simple, the other more complex.

Take a distribution, say the invariant mass of the two down quarks, and just fill an invariant mass histogram with the event weights of all the candidate events (there should be many). The result is the distribution predicted by the differential cross section of equation (5.3). The programs using this technique are called *cross section integrators*.

The other way to go is to *unweight* the events. After this is done the events themselves are distributed according to theoretical predictions - each event is a simulation of the experiment. The programs using this technique are called *event generators* (this is the kind of program used to produce simulated data).

A much used technique for unweighting events is the hit-and-miss Monte Carlo. For each event one calculates the ratio of the event weight to the maximum event weight [3] $d\sigma/d\sigma_{\max}$

[3] $d\sigma_{\max}$ can be found by scanning the whole space, or in some cases analytically. In our example $d\sigma_{\max}$ occurs when one of the final state quarks is collinear (goes in the same direction in the center of mass frame) with one of the initial state quarks.

and compares it to a random number between 0 and 1 drawn from the flat distribution. If the ratio of the event weight to the maximum event weight is larger than the random number the event is kept. If it is smaller the event is rejected (thrown away). After looping over all the (many) events the ones that are kept will contain physics information according to the cross section equation[4].

Returning to real life we remember that we can't collide quarks directly. The quarks are confined in protons, forever hidden from us. We must describe them via the parton distribution functions (PDFs) and they do not always collide head on (then the Z^0 would always have zero transverse momentum). What must be added, in addition to the PDFs, is a non-constant particle number - the initial, intermediate and final state particles must be allowed to radiate new particles. This in fact addresses both problems. The radiation of new particles means that the quarks can remain hidden, eventually giving bound, observables states (hadronization). The emission of new particles also means that the produced particle may have non-zero transverse momentum (when one of the colliding quarks emits a gluon). In addition, the non-constant particle number enables us to make quantum field calculations in higher orders as well, taking into account quantum corrections.

There are a few different ways of adding these new features. To make higher order calculations one can use

exact calculations to leading order for a small number of emissions. As an example, consider the Alpgen generator[5]: when generating a dataset for, say, γ+jets, Alpgen calculates to leading order the explicit Feynman diagram for γ+Njets, $N = 0, 1, \ldots 4$ etc separately. The results are then passed on to the HERWIG generator[6] for hadronization.

estimation of dominant effects to arbitrary orders in perturbation theory. There are two main methods to do this. The first one is called *resummation* and is a way to sum perturbative series to all orders. The other method is the one used by most event generators and is called the *parton shower approach*.

To describe hadronization one can use

the factorization theorem which is what cross section integrators use.

phenomenological models used by most event generators. The most widespread model is based on parton shower techniques.

[4]This is equivalent to sampling from a distribution. Imagine a simple distribution, say $f(x) = x$. To do a hit-and-miss means to do the following: Draw a number from the flat distribution between $x_{\min}$ and $x_{\max}$ and calculate the value at this point, f(drawn number). Draw another random number from the flat distributon beween zero and maximum function value. Compare this number to the calculated function value. If it is smaller, accept the number, if it is larger reject it. The idea is that if enough numbers are drawn from flat distributions all the points in the square $x_{\min} \leq x \leq x_{\max}, y_{\min} \leq y \leq y_{\max}$ are covered, and only the "events" that are under the curve we want to sample from are accepted.

[5]http://mlm.home.cern.ch/mlm/alpgen/

[6]http://hepwww.rl.ac.uk/theory/seymour/herwig/

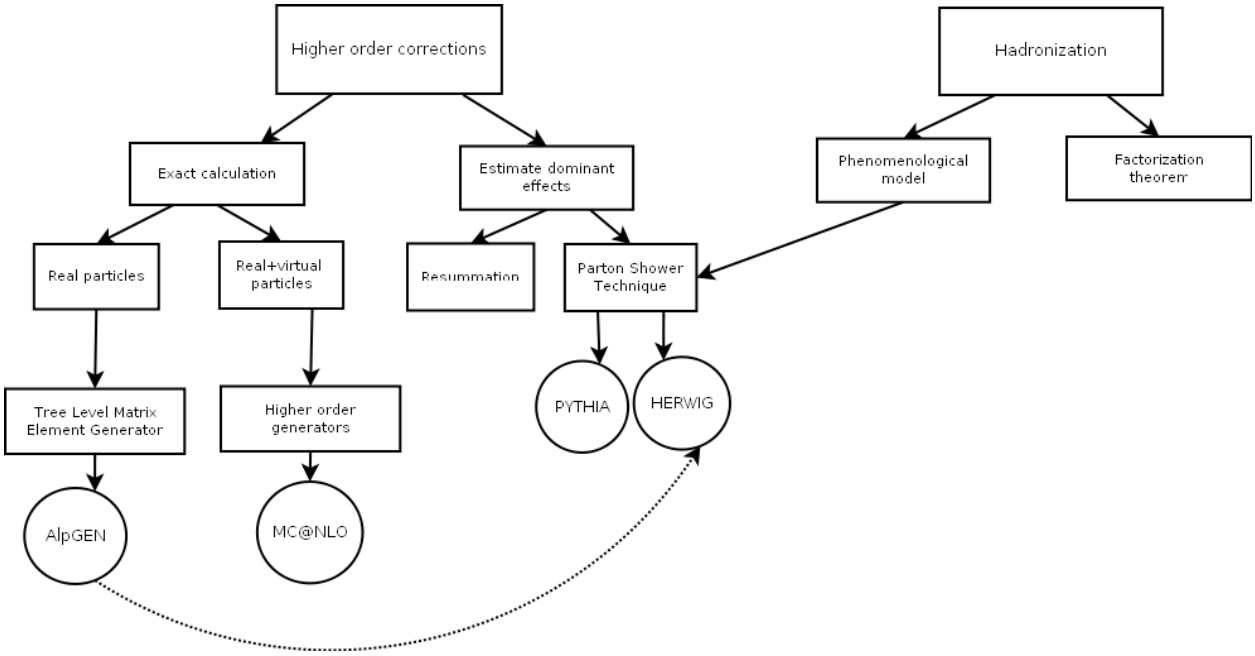

Figure 5.7: A somewhat simplified, schematic view of two important properties of event generators when dealing with higher order corrections: exact calculations and estimating dominant effects.

As discussed above, both hadronization and higher order corrections (both sketched in figure 5.8) can be addressed using the parton shower technique. It begins with a hard subprocess to leading order, and the process is allowed to evolve using parton showers, where partons are allowed to split into new partons[7]. This so-called *branching* continues until all the partons are confined in colorless hadrons. After hadronization is done the underlying event is generated, including beam remnants and interactions of the other partons. See figure 5.8 for the general structure of a parton shower.

Of course there can also be other particles in the final state (leptons and gauge bosons), not just quarks (even though the QCD jets are what is seen most often). These are handled in much the same way, except that hadronization is no longer needed.

Particles with decay length $c\tau$ above 10 mm (like the τ lepton) are considered stable by the event generator and are handled by the detector simulation. Particles with decay lengths less than 10 mm are handled directly by the event generator. This leads us to the next step, which is detector simulation.

5.3.2 Detector simulation and digitization

The ATLAS detector simulation is done with a particle simulation toolkit know as GEANT4[8]. This is the most time-consuming part of the chain. GEANT is provided with the information

[7]Gluons can split to quarks or gluons ($g \to q\bar{q}$, $g \to gg$) or quarks can emit a gluon ($q \to gq$, $\bar{q} \to g\bar{q}$)
[8]http://geant4.cern.ch/

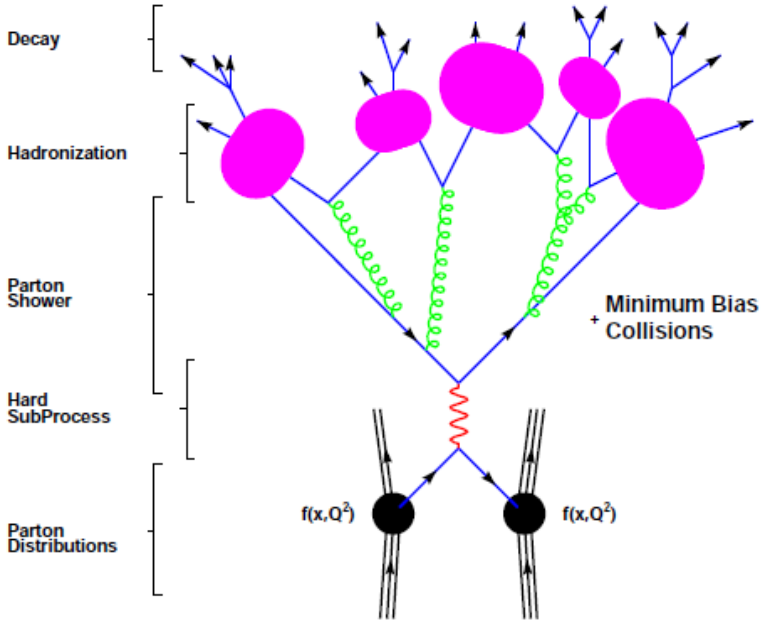

Figure 5.8: Schematic view of the Parton Shower technique[32], showing (from bottom up) the hard collision of two partons, the parton shower followed by hadronization, and finally decay of the colorless hadrons.

about the detector (the detectors, subdetectors, material, misalignment, etc). All "stable" particles are propagated through the full ATLAS detector. Energies deposited are recorded as "hits" and are written to the simulation output file (called a hit file) with the total energy deposition, position in space and the time of the hit. Also at this stage the truth information is kept for all events.

After the detector responce is simulated, the energy deposits must be converted to a form similar to what is read out from electronics in an actual experiment, so-called "digits". A digit is for example when a current in a redout channel rises above a threshold. It might even be more complex, and for example, include the shape of a signal over time.

The digitization process may also add for example detector noise simulation, beam halo events and pile-up events.

After digitization the events must be reconstructed before they are stored and accessible for analysis. The reconstruction procedure is discussed briefly in section 4.4.

5.3.3 Dataset used

The datasets used in this (10 TeV) analysis are collected in table 5.1.

There are 4 Z' samples generated by the Pythia generator[10] two masses (1.0 and 1.5 TeV)

[10]http://home.thep.lu.se/∼torbjorn/Pythia.html

Dataset	Dataset number	Generator	Recon.tag	No. of MC events	X-section[9] $\sigma_{\mathrm{LO}} \times \epsilon$ [fb]
Signal datasets					
$Z' \to e^+e^-, \quad m'_Z = 1.0$TeV	105603	Pythia	r808_r838	41996	254.0
$Z' \to \mu^+\mu^-, \quad m'_Z = 1.0$TeV	105601	Pythia	r808_r838	29964	254.0
$Z' \to e^+e^-, \quad m'_Z = 1.5$TeV	105624	Pythia	r808_r838	14973	76.1182
$Z' \to \mu^+\mu^-, \quad m'_Z = 1.0$TeV	105625	Pythia	r808_r838	14993	77.7981
Background datasets					
$Z, \gamma \to ee, \quad M_{ee} > 200$GeV	105121	Pythia	r808_r838	14981	1622.0
$Z, \gamma \to \mu\mu, \quad M_{\mu\mu} > 200$GeV	105122	Pythia	r808_r838	15000	1620.5
$Z, \gamma \to \tau\tau, \quad M_{\tau\tau} > 200$GeV	105123	Pythia	r808_r838	24971	1644.2
$Z \to ee$, 1 lepton,	106050	Pythia	r808_r838	999126	1097.8
$Z \to \mu\mu$, 1 lepton,	106051	Pythia	r808_r838	477770	1097.8
$WW \to l\nu_l + X$	105985	Herwig	r808_r838	49932	1.55736×10^4
$ZZ \to l^+l^- + X$	105986	Herwig	r808_r838	49953	1353.6
$WZ \to l + X$	105987	Herwig	r808_r838	99803	4855.0
$W \to l\nu_l + \gamma$	006540	Pythia	r474	78800	5.23208×10^4
$Z \to l^+l^- + \gamma$	105120	Pythia	r808_r838	23989	1.10935×10^4
$\gamma\gamma, M_{\gamma\gamma} > 15$GeV	105964	Pythia	r808_r838	99939	1.197029×10^5
$t\bar{t}$ (leptonic)	105200	MC@NLO	r808_r838	983206	$2.05480\times10^5*$
$t\bar{t}$ (hadronic)	105204	MC@NLO	r808_r838	184116	$1.68120\times10^5*$
$J0$	105009	Pythia	r808_r838	399704	1.17×10^{13}
$J1$	105010	Pythia	r808_r838	977225	8.67×10^{11}
$J2$	105011	Pythia	r808_r838	926193	5.6×10^{10}
$J3$	105011	Pythia	r808_r838	1393401	3.28×10^9
$J4$	105011	Pythia	r808_r838	985870	1.52×10^8
$J5$	105011	Pythia	r808_r838	1195459	5.12×10^6
$J6$	105011	Pythia	r808_r838	366536	1.12×10^5
$J7$	105011	Pythia	r808_r838	376320	1.08×10^3
$J8$	105011	Pythia	r585	241475	1.112
$W \to e\nu_e +$ jets	106020	Pythia	r808_r838	1740936	1.035×10^7
$W \to \mu\nu_\mu +$ jets	106021	Pythia	r808_r838	1220067	1.035×10^7
$W \to \tau\nu_\tau +$ jets	106022	Pythia	r808_r838	495701	1.021×10^7
$\gamma +$ 1jet	106123	Alpgen	r808_r838	99835	5.13×10^{10}
$\gamma +$ 2jets	106124	Alpgen	r808_r838	98802	1.54×10^{10}
$\gamma +$ 3jets	106125	Alpgen	r808_r838	99781	5.31×10^9
$\gamma +$ 4jets	106126	Alpgen	r808_r838	99835	1.97×10^9

Table 5.1: These are the MC datasets used in the analysis. The cross-sections are as reported in http://ami.in2p3.fr/opencms/opencms/AMI/www/. The cross-sections are reported as the leading order physical cross-section multiplied with a number called "GenFilter efficiency", i.e. $\sigma_{\mathrm{LO}} \times \epsilon$. The GenFilter efficiency is different from 1 if a selection criteria is used, for example $t\bar{t}$ decaying to at least one electron. A star ($*$) next to the cross-section means that it is the next to leading order cross-section.

and two channels (electron and muon). Pythia is a general-purpose detector which is often used when only generating leading order[11].

Pythia was also used to generate the DY datasets ($Z^0, \gamma \rightarrow l^+l^-$, $l = e, \mu, \tau$), the diboson dataset ($\gamma\gamma$, Wγ and Zγ), the dijet datasets (J0-J8[12]) and the W ($W \rightarrow l\nu_l$, $l = e, \mu, \tau$) datasets.

The diboson datasets WW, WZ and ZZ are generated by Herwig, another general-purpose generator.

$t\bar{t}$ is generated by the MC@NLO generator[13], which calculates the process with full QCD next-to-leading order corrections. MC@NLO generates events with event weights that are either $+1$ or -1, depending on whether the Feynman amplitude is positive or negative. The numbers of MC events cited in table 5.1 are the weighted number of $t\bar{t}$ events (this is the number used when scaling the histograms to an integrated luminosity). The unweighted numbers are 1332858 and 249710 for leptonic and hadronic $t\bar{t}$ decays respectively.

Alpgen generated the γ+jets dataset. This generator is often used when the final states have large jet multiplicities.

Taking a closer look at table 5.1, we see a problem: some of the processes (e.g dijets, γ+jets) have very high cross-sections, which means that the number of generated events must be equally high to ensure smooth distributions. For example, the J3 sample has a cross-section of 3.28×10^9 fb. At at integrated luminosity of $1\,\text{fb}^{-1}$ we thus expect 3.28×10^9 events from this dataset, but only 1.5×10^6 are generated. To make the problem worse, only a small fraction of these events pass all the cuts, thus introducing even more fluctuations in the distribution.

The high dijet cross-sections in particular means that these backgrounds should be estimated using data driven methods. Background estimation in this analysis is, however, based on MC.

5.4 Particle definitions

This section is based on references [30] and [35].

In theory a particle is well-defined with well-known properties. It is not this simple from an experimental point of view. Consider a muon; originating from the interaction point in the middle of the detector it propagates outwards, leaving some traces along its way. What should the criteria be for calling it a muon? A few hits in the muon chamber? Maybe combined with a few hits in the inner detector? How well must the hits in the ID match the ones in the muon spectrometer? Or take electrons with energy deposits in the calorimeter

[11] Although some next-to-leading order effects are added.

[12] The number X in JX points to how large the energy transfer in the hard process is. 0 means little, 8 means much.

[13] https://www.hep.phy.cam.ac.uk/theory/webber/MCatNLO/

- is it an electron or is the electromagnetic shower initiated by a photon? There are many possible definitions, and we will go through the main ones.

5.4.1 Electron reconstruction and identification

For electrons there is only one possible collection to import to the analysis, namely ElectronAODCollection. The reconstruction is performed by one of two algorithms - one for high and one for low p_T electrons [30].

The reconstruction

The calorimeter-seeded algorithm is the standard reconstruction algorithm for electrons. The track-based algorithm is used in special cases, when the transverse momentum of the electron is low, for example in J/ψ decays.

The algorithm is seeded by an electromagnetic tower (in the second layer of the ECAL) with transverse energy above 2.5 GeV. In the region $|\eta| < 2.5$ (covered by the tracking detectors) a track in the inner detector is searched for. If no track is found within a certain $\eta - \phi$ separation, the electron candidate is ignored. If more than one track is found, the one with the smallest difference $\Delta R = \sqrt{\Delta\eta^2 + \Delta\phi^2}$ between its impact point on the ECAL and the seed cluster is chosen. Tracks without hits in the SCT or pixel are considered as more likely to have come from conversion and have lower priority than tracks with hits in these subdetectors.

Both prompt electrons and converted photons have an electromagnetic cluster with a track pointing at it. Because of this the electron container is significantly contaminated with converted photons at this point, but high efficiency is assured. The contamination will be dealt with later, when adding electron identification (see the "Electron identification" subsection).

The track-based algorithm starts with a track that is extrapolated into the electromagnetic calorimeter. The transverse momentum of the electron must be higher than 2 GeV (the algorithm can handle tracks with as little p_T as 0.5 GeV, but to enhance the rejection of fakes 2 GeV is used as a lower limit) and $|\eta| < 2$. The limit 2 on the pseudorapity is used because the transition radiation tracker (covering up to $|\eta| = 2$) is crucial both for preselection of tracks and for reconstruction. The requirements include at least 9 hits in the pixel and SCT combined and 20 in the TRT. The tracks passing these criteria are then extrapolated out to the electromagnetic calorimeter where some additional refinement is performed before the electron candidate is confirmed.

Electron identification

After reconstruction, identification criteria are applied. There are three standard sets of cuts with increasing background rejection power: loose, medium and tight (table 5.2).

Loose cuts uses information from the middle layer of the EM calorimeter (i.e. shower shapes and shower width) and hadronic leakage variables. Electron candidates are also required to be within the geometrical acceptance of the detector ($|\eta| < 2.47$). The loose requirements have high selection efficiency, but low background rejection.

Medium cuts include the loose definition and use additional information from the first layer of the calorimeter, track quality requirements and track-cluster matching.

Tight cuts include the medium identification and requirements on E/p and b-layer, information from the TRT and tighter track matching.

Type	Description	Variable name
	Loose cuts	
Detector acceptance	$\|\eta\| < 2.47$	
Hadronic leakage	For $\|\eta\| > 0.8$ and $\|\eta\| < 1.27$ only:	
	E_T(first layer of HCAL)/E_T(EM cluster)	R_{had1}
	E_T(HCAL)/E_T(ECAL)	R_{had}
Second ECAL layer	Ratio in η of cell energies in 3×7 versus 7×7 cells	R_η
	Lateral shower width	w_{η^2}
	Medium cuts (includes Loose)	
First ECAL layer	Total shower width	w_{tot}
	$(E_2 - E_1)/(E_2 + E_1)$, where E_2 is the largest energy deposit and E_1 the smallest	E_{ratio}
Track quality	Number of hits in the pixel detector (≥ 1)	
	Number of hits in pixels and SCT detectors (≥ 7)	
	Transverse impact paramter (< 5 mm)	d_0
Track matching	$\Delta\eta$ between cluster and track (< 0.01)	$\Delta\eta_1$
	Tight cuts (includes Medium)	
b-layer	Number of hits in the innermost layer of pixel (≥ 1)	
Track matching	$\Delta\phi$ between cluster and track (< 0.02)	$\Delta\phi_2$
	Ratio of the cluster energy to the track momentum. The cut value is η and E_T dependent and ranges from 0.7 to 5.0.	E/p
	$\Delta\eta$ between cluster and track tightened (< 0.005)	$\Delta\eta_1$
Track quality	Transverse impact parameter tightened (< 1 mm)	d_0
TRT	Total number of hits in the TRT. The difference between measured and expected average number of hits is required to be less than 15.	
	N(high threshold hits)/N(total number of hits) The cut value is η dependent and ranges from 0.08 to 0.155	
Conversions	Electron candidates matched to reconstructed electrons from photon conversions are rejected	

Table 5.2: Electron identification variables[35].

5.4.2 Muon reconstruction

Muons are subject to one or more of three possible identification and reconstruction algorithms - standalone, combined and tagged muons. These strategies are grouped into two families, and each family contains one algorithm for each strategy. These families are called by the names of the combined algorithms: Staco[25, p.165] and Muid[25, p.165]. Staco is currently the default for physics analysis.

Standalone muons

Only the muon spectrometer is used to find tracks and then extrapolate these to the beam line. In the Staco family, this is done by Muonboy[30, p.166], and in the Muid family it is done by Moore[30, p.166]. The extrapolation to the beam line can be quite tricky as it must account for multiple scattering and energy loss. Because standalone algorithms only uses the muon spectrometer they cover pseudorapidities up to 2.7, compared to what the inner detector is capable of ($|\eta| < 2.5$). There are holes near 0.0 and 1.2 where different detector parts are merged, see for example figure 5.16(d). In addition low momentum muons ($p < 3$ GeV) will not penetrate through the detector and reach the muon spectrometer. Muons with p_T less than and up to 6 GeV are hard to reconstruct. Also, non-prompt ("fake") muons from decay of particles like $\pi^{\pm}$ and $K^{\pm}$ in the calorimeter will often be found in the standalone reconstruction.

Combined muons

The general idea is to pair tracks found in the muon spectrometer to tracks in the inner detector and use the combined results. What defines a "good fit" is the χ^2 of the match

$$\chi^2 = \sum_N \frac{1}{\sigma_i^2}[y_i - f(x_i)]^2$$

where N is the number of degrees of freedom (here 5: p_T, η, ϕ, z_0 (longitudinal impact parameter) and d_0 (transverse impact parameter)); y_i is the measurement in the inner detector and $f(x_i)$ is the measurement in the muon spectrometer extrapolated to the inner detector.

Two different algorithms for finding combined muons, called Staco and Muid, were mentioned above. They have different strategies when finding the track, but the differences are not really important here.

Tagged muons

The two muon spectrometer tagging algorithms, called MuTag[30, p.166] (belonging to Staco) and MuGirl[30, p.166] (belonging to Muid), both extrapolate all inner detector tracks (with momentum over a certain limit) out to the first of the three stations of the muon spectrometer and look around there for traces of passing muons. Both use some sort of definition of how close the extrapolated track needs to be to be associated the muon hit. If a muon is found close enough, the inner detector track is tagged as corresponding to a muon. The big difference between MuTag and MuGirl is that MuGirl tries to find all muons, while MuTag only looks at the inner detector track not already used by Staco. These algorithms are meant for the low-p_T regime and are thus not of any interest to us.

5.5 Preselection of particles

In the analysis code used here some preselection is employed when running through all the events in a sample. The point of this is to make smaller samples from the AODs (see section 4.4), so-called ntuples with the necessary information (i.e. four-momentum, energy, etc of specific particles in the event, typically the ones with highest p_T). We do not want to lose any interesting events on this first run-through, so the cuts are not tight. The event selection is shown in table 5.3 and the electron and muon preselection requirements are as listed in tables 5.4 and 5.5.

1. Trigger (`e20_loose`, `e10_medium`, `e25_tight` or `mu10`)
2. At least two electrons or muons with $p_T > 30$ GeV

Table 5.3: Event preselection. The requirements on the electrons and muons are given in tables 5.4 and 5.5.

1. $\|\eta\| < 2.5$. ($\eta = 2.5$ corresponds to $\theta \approx 10°$.)
2. Ignore region $\|\eta\| > 1.37$ and $\|\eta\| < 1.52$. This is the region where the barrel part and end-cap part of the electromagnetic calorimeter meet, and all the cabling and material in the area creates a small dead region (known as "the crack").
3. "Loose" electrons (see table 5.2 for definition).
4. Author is 1 or 3 (meaning it should be reconstructed by the calorimeter-seeded algorithm or both the track-seeded and the calorimeter-seeded algorithm (see section 5.4.1).

Table 5.4: Electron preselection requirements. All events are also required to pass the event selection in table 5.3.

1. $\|\eta\| < 2.5$
2. Combined muon with $\chi^2 < 100$ (see section 5.4.2).
3. Longitudinal impact parameter $\|z_0\| < 200\,\text{mm}$

Table 5.5: Muon preselection requirements. All events are also required to pass the event selection in table 5.3.

A Z' boson never decays into only one lepton. There are cases where only one of the leptons is properly reconstructed, but this is not an event we are eager to keep. For this reason we require at least two leptons right from the beginning.

The most probable p_T of these two leptons will be 500 GeV for a Z' with mass 1 TeV. We are therefore not interested in low-p_T leptons and require a p_T of a least 30 GeV.

Loose electrons (see section 5.4.1) are chosen to to keep the selection efficiency high (see section 5.5.2). The loose identification is part of the standard electron selection in the dilepton sub-working group as of July 2010.

Figure 5.9(a) shows the χ^2 distribution for the combined muon fit (see section 5.4.2) and figure 5.9(b) the longitudinal impact parameter z_0 of the muons. About 0.6% and 0.7% of the muons from a 1.0 TeV and a 1.5 TeV Z' respectively are cut away when requiring $\chi^2 < 100$ for the fit between the inner detector and muon spectrometer measurement. The wide cut on the impact parameter, $|z_0| < 200\,\text{mm}$, reflects the fact that the bunches of protons colliding are elongated in the direction of the beam axis. Some 0.1% of the muons from both the 1.0 TeV and the 1.5 TeV Z' are cut away.

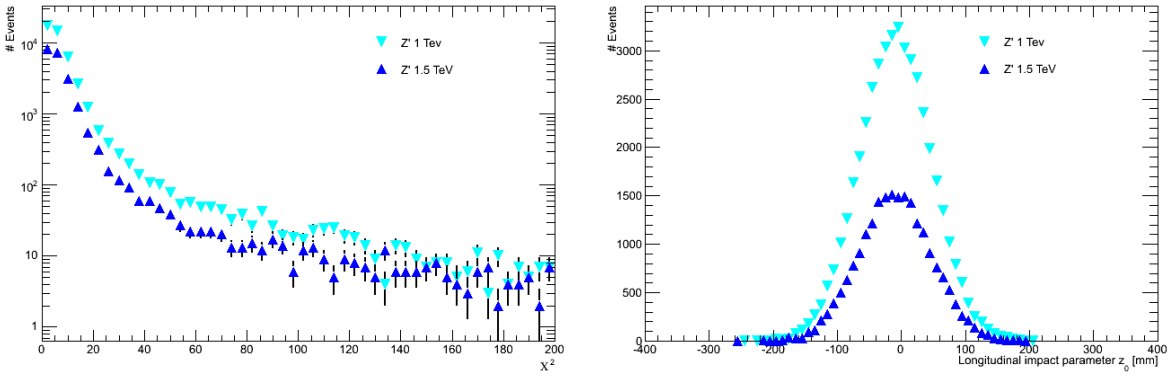

(a) The χ^2 of the fit between the measurements made in the inner detector and the muon spectrometer (see section 5.4.2).

(b) The longitudinal impact parameter z_0.

Figure 5.9: χ^2 and longitudinal impact parameter z_0 distributions for Z' with mass 1.0 TeV and 1.5 TeV.

Figure 5.10 shows the invariant mass distributions for Z' with masses 1.0 TeV and 1.5 TeV in the electron and muon channel. We see, in addition to the expected resonances at the Z' masses, a structure at 500 GeV. This is due to a 500 GeV cut in the invariant mass applied at the generator level. Between 500 GeV and the Z' mass we see the effect of the interference between Z'/Z^0 and the photon - the falling distribution. Had there not been a cut at 500 GeV, we would have seen an ever-growing distribution towards lower invariant masses. The reason for doing it this way is to gather enough statistics close to the Z' peak without having to generate all the events at lower invariant mass. Remember that the current lower limit on the Z' we are investigating here is above 900 GeV.

Figures 5.11(a) and 5.11(b) show the invariant mass distributions after preselection (tables 5.4 and 5.5). The two highest p_T leptons are chosen when more than two leptons pass the preselection. We see that there are some differences between the channels. The most

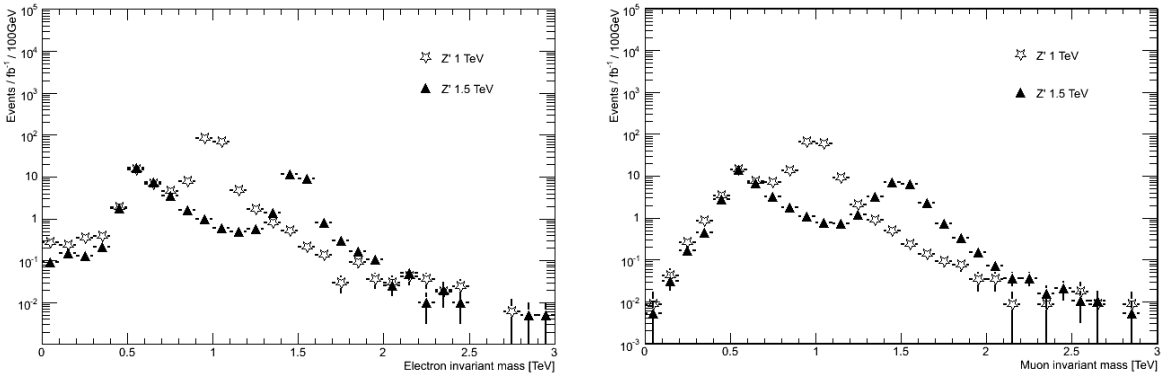

(a) Electron channel (b) Muon channel

Figure 5.10: The invariant mass distribution in the electron channel (left) and muon channel (right) of Z' particles of masses 1.0 TeV and 1.5 TeV.

striking one is the dijet cross-section - in the electron channel it is quite dominating. Also the diboson and W+jets cross-sections are noticeably lower in the muon channel. This is due to the fact that jets and photons can fake electrons in the ECAL.

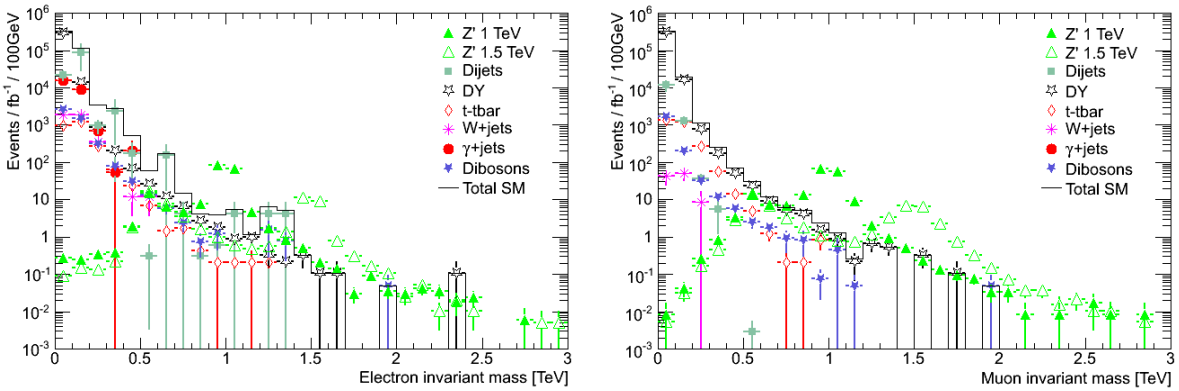

(a) Electron channel (b) Muon channel

Figure 5.11: Dilepton invariant mass for Z' signal and Standard Model backgrounds in the electron (5.11(a)) and muon (5.11(b)) channels after preselection (tables 5.4 and 5.5). The "dijets" include all dijets up to and including jets from b-quarks, and the "diboson" includes WW, WZ, ZZ, Wγ, Zγ and $\gamma\gamma$. The DY background and the $W \to l + \nu_l$ are both including jets.

The diboson contribution is composed of many smaller parts. In figure 5.12 the individual parts are shown for the electron channel (5.12(a)) and muon channel (5.12(b)). We see that the contributions from the massive dibosons (WW, WZ and ZZ) and Zγ are about the same in both channels, as expected, because they lead to two or more real leptons. The difference

in the diboson contribution for the two channels becomes noticeable when looking at the contributions from Wγ and $\gamma\gamma$ - it is almost negligible in the muon channel and prominent in the electron channel. This is because the photons are reconstructed as electrons.

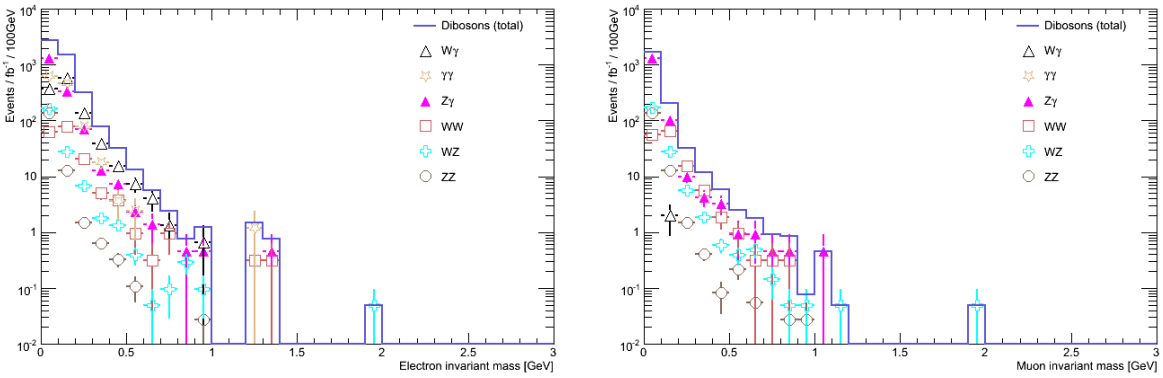

(a) Electron channel

(b) Muon channel

Figure 5.12: Dilepton invariant mass distributions for the different diboson datasets. Only preselection cuts are employed.

The p_T of the two leading leptons is shown in figure 5.13. We see that the signal E_T or p_T is peaked at half the Z' mass, as it should be. The lepton p_T is correlated to the invariant mass, which can be seen in figure 5.14. This means that a cut in the lower range of the p_T spectrum cuts away invariant masses in the lower spectrum as well.

One might notice that there is not much statistic in the higher invariant mass regions for datasets other than the Z'. This is merely because the probability for such high p_T leptons are very low. The most important background is expected to be Drell-Yan, and because the Pythia 105121 and 105122 datasets (table 5.1) have an invariant mass cuts at 200 GeV at the generator level (similar to the 500 GeV cut in the Z' datasets), more statistics at higher invariant masses are gathered. To account for lower invariant masses, we combined those datasets with another set of Pythia DY datasets (106050 and 106051) by removing all events with dilepton masses above 200 GeV.

5.5.1 Trigger

The electrons are required to pass either `e20_loose`, `e10_medium` or `e25_tight`[14], and the muons are required to pass `mu10`. They all require one electron or muon passing a threshold of 20, 10, 25 and 10 GeV respectively[15]. The "loose", "medium" and "tight" refer to the same

[14] Two of the datasets used (J8 and Wγ) do not exist with the same reconstruction tag as the other datasets for some reason, and they have no triggers in common. The trigger `e25_tight` was added for these two datasets.

[15] Although the threshold might be a little different in reality, these are the nominal thresholds.

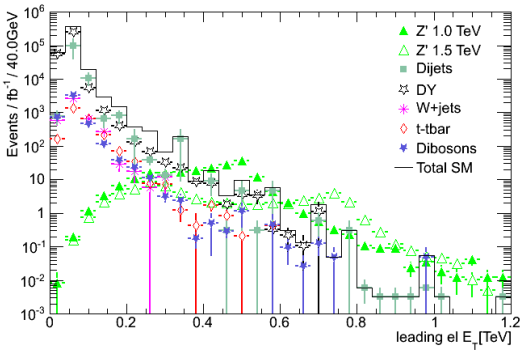

(a) Leading electron

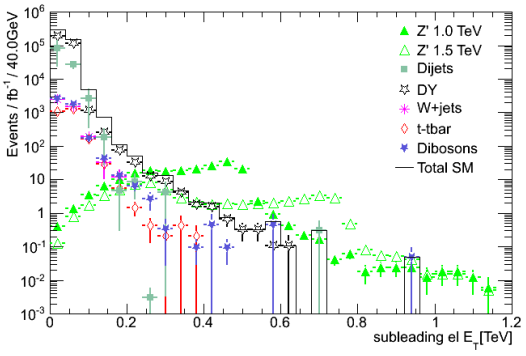

(b) Subleading electron

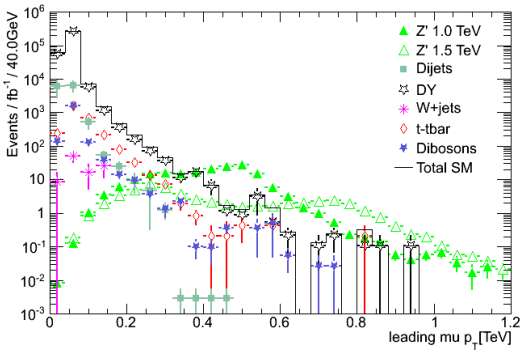

(c) Leading muon

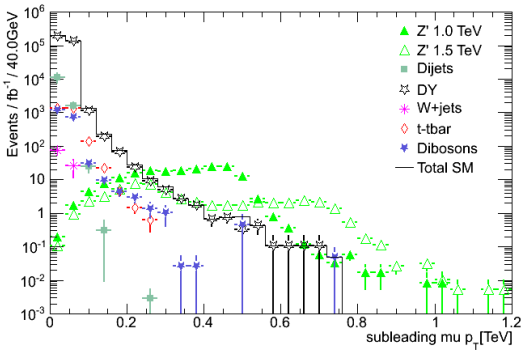

(d) Subleading muon

Figure 5.13: The E_T and p_T distributions for the two leading electrons (top) and muons (bottom) respectively after preselection (tables 5.4 and 5.5).

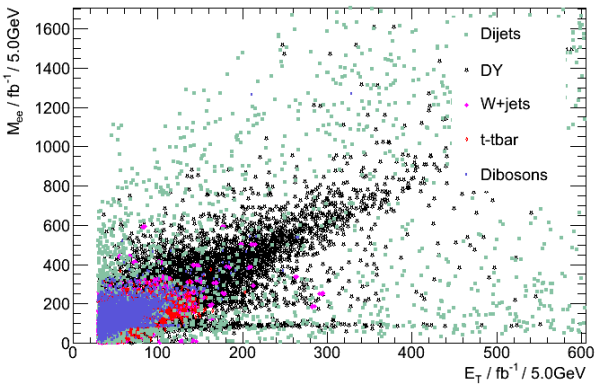

(a) Electron channel

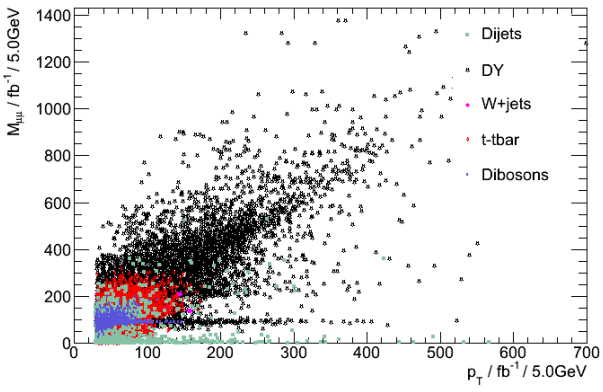

(b) Muon channel

Figure 5.14: 2 dimensional histogram of the p_T of the electrons or muons versus their invariant mass M_{ll}. We see a correlation between the two variables p_T and M_{ll}.

electron identification as is used in offline analysis (see Section 5.4.1). At a luminosity of $10^{31}\,\mathrm{cm}^{-2}\mathrm{s}^{-1}$ none of them are prescaled[16].

The reason for using triggers in MC is to mimic what actually happens in the detector with real data. We don't want to store all the uninteresting events, so we require a trigger to go off, alarming us of something possibly exciting happening. The triggers will not manage to fire at all the events, thus reducing the total number of events recorded by a percentage.

Another very important thing is to find a trigger that lets as much as possible of the signal through. For Z' this is not very hard to find, as the signal (two isolated, high p_T leptons) is very easy to trigger on. We will now dive very briefly and superficially into the intricate world of trigger efficiency analysis.

Trigger efficiencies

The trigger efficiency is defined as the number of events passing preselection and trigger divided by the number of events after preselection, where the preselection criteria are listed in tables 5.4 for electrons and 5.5 for muons.

$$\epsilon_{\text{trigger}} = n_{\text{preselection+trigger}}/n_{\text{preselection}} \tag{5.4}$$

An event is said to have triggered if it triggers either of the triggers `e20_loose`, `e10_medium` or `e25_tight` in the electron channel and the `mu10` in the muon channel. The percentages quoted are not single lepton efficiencies as all events have two or more leptons that can fire the trigger.

The efficiencies listed in table 5.6 are very high, and nearly no signal events are lost. This is hardly surprising; as mentioned before, the signal is easy to trigger on.

Errors on efficiencies

One thing worth noticing is the error on the efficiency; special care has to be taken when calculating these[36]. The denominator in the efficiency calculation, $\epsilon = m/N$, can hardly be thought of as having any uncertainty: If we first choose a number of Monte Carlo events to generate and then want to check how many of them pass some requirement, there is no uncertainty in the number of MC events[17]. The number of events passing trigger, m, is binomially distributed (each event can either pass or not pass) with variance $V[m] = N\epsilon(1-\epsilon)$.

An estimator of the efficiency is $\hat{\epsilon} = m/N$, and the variance of the estimator is

$$V[\hat{\epsilon}] = V\left[\frac{m}{N}\right] = \frac{1}{N^2}V[m] = \frac{\epsilon(1-\epsilon)}{N}$$

[16]Pre-scaling is a way of reducing the output rate of the trigger. If prescaled by a factor 100, 99 out of 100 events will automatically be thrown away. This leads to the loss of many interesting events.

[17]According to reference [36] this is the best way to do it even if N has some uncertainty

where one has to use the estimator of the efficiency, $\hat{\epsilon}$ in the expression above.

Note that $\epsilon = 0$ and $\epsilon = 1$ are special cases where the variance of the estimator of the efficiency is zero. This does not mean that the error is zero, just that m happened to be equal to N in this specific case (in analogy to the error on a bin with no entries).

Also note that the number N should be the *unnormalized* number of events.

Dataset	Electron channel			Muon channel		
	Preselection	Trigger	$\epsilon_{\text{trigger}}$ [%]	Preselection	Trigger	$\epsilon_{\text{trigger}}$ [%]
Z' 1 TeV	33120	33103	99.9±1.5e-6	22151	21658	97.7± 9.8e-5
Z' 1.5 TeV	11394	11387	99.9±8.8e-3	10623	10377	97.7±2.1e-4

Table 5.6: Calculation of trigger efficiencies. Triggers used are `e20_loose`, `e10_medium` and `e25_tight` in the electron channel and `mu10` in the muon channel. Note that these are not single lepton efficiencies, as all events are required to have at least two high p_T electrons or muons. The numbers quoted are the total number of generated Monte Carlo events, not normalized to any cross-section.

5.5.2 Reconstruction efficiency

We chose to require only loose electrons. This is what is agreed on in official ATLAS Z' analysis, but there are some discussions going on about the benefits of using medium electrons. This would remove a large fraction of fake electrons that one has to remove later when using loose electrons, with cuts like isolation.

We will now have a quick look at the reconstruction efficiency for loose, medium and tight electrons, and combined muons.

To get the reconstruction efficiency we use truth matching on Z' datasets. An electron or muon is considered reconstructed if the distance betwen a truth lepton and a reconstructed lepton is less than 0.2 in the $\eta - \phi$ plane, $\Delta R = \sqrt{(\Delta\phi)^2 + (\Delta\eta)^2} < 0.2$. Figure 5.15 shows the difference in the p_T of the truth and reconstructed electron (5.15(a)) and muon (5.15(b)). We see that we do not need an additional requirement on Δp_T, the requirement on ΔR is sufficient. Only the two leading (in terms of p_T) leptons are considered - it will be shown later (figure 5.17) that there are rarely more than 2 high p_T electrons (muons) in a Z' to electrons (muons) sample.

We note that the Δp_T distributions in figure 5.15 are asymmetric, especially in the electron channel. Leptons with are reconstructed with smaller p_T more often than with higher p_T. We contribute this effect to bremsstrahlung that went unnoticed by the reconstruction software.

Figures 5.16(a), 5.16(c) and 5.16(e) show the reconstruction efficiency of two the highest p_T electrons for loose, medium and tight identification in a 1 TeV $Z' \rightarrow e^+e^-$ sample normalized to truth electrons with $p_T > 30\,\text{GeV}$ and $|\eta| < 2.5$ as a function of p_T and η. Figures 5.16(b), 5.16(d) and 5.16(f) show the corresponding variables for all reconstructed and combined muons.

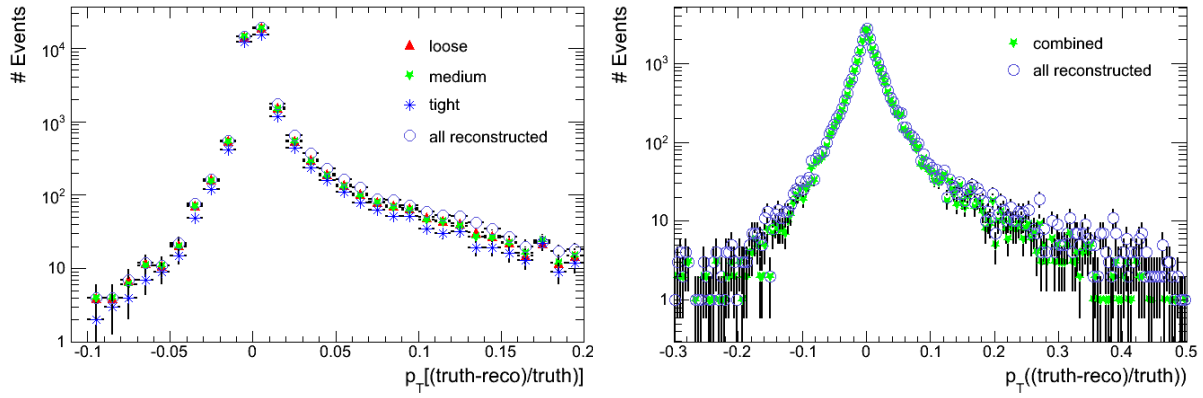

(a) Electron channel

(b) Muon channel

Figure 5.15: The difference in p_T of the truth lepton and reconstructed lepton from a 1.0 TeV Z' when the difference between them in the $\phi - \eta$ plane is less than 0.2.

We see that for loose and medium electrons the efficiency as a function of p_T is quite flat (figure 5.16(a)). It starts out at about 90% for low p_T, but then rises quickly to above 95%. It's important to keep in mind that the statistics are best for electron p_T around 500 GeV. Above that and at very low values there are hardly any events at all. Another thing is that the error on the efficiency is zero when the efficiency is 100% or zero, as we discussed in section 5.5.1. We see about the same in the muon channel (figure 5.16(b)), except that the efficiency starts out at higher values.

When looking at the efficiency as a function of η in the electron channel(figure 5.16(c)) we see three dips, one at $\eta = 0$ and two at $|\eta| \approx 1.3$. The first dip is caused by the previously mentioned crack in the ECAL (where the two barrel parts are joint), and the latter is the crack where the end-cap and the barrel of the ECAL are joint together. A similar pattern happens for muons (figure 5.16(d)), where the dip at $|\eta| = 1$ is where the end-cap and barrel parts of the muon system meet, and the one at $\eta = 0$ is caused by a a crack between the two barrel parts of the MS.

The efficiencies in ϕ (figures 5.16(e) and 5.16(f)) are reasonably flat, as expected. The variation seen in muons is due to cabling and support structure (the "feet" of the MS[25, p.317]). The overall reconstruction efficiencies are given in table 5.7 for electrons and muon. The electron efficiency is only 2% lower for medium electrons than for loose - the best choice is not obvious and should be studied (not done here). We use loose in this analysis, as mentioned before.

5.6 Event selection

The number of events before and after preselection (tables 5.4 and 5.5) are listed in column 2 of tables 5.8 and 5.9 for the electron and muon channels respectively. The cuts in the

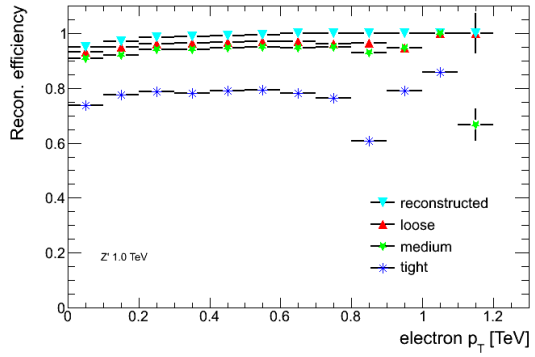

(a) Electron p_T

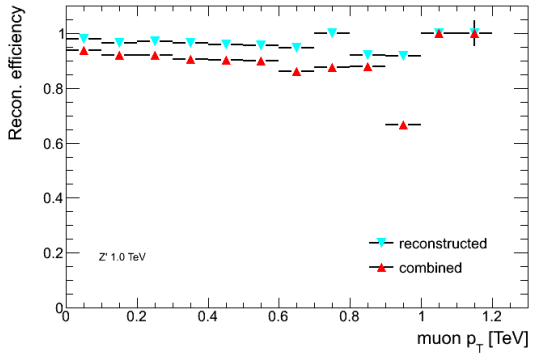

(b) Muon p_T

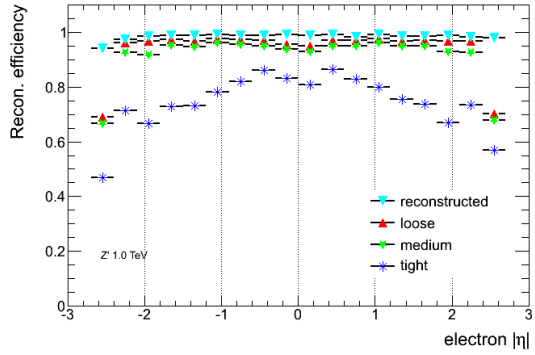

(c) Electron $|\eta|$

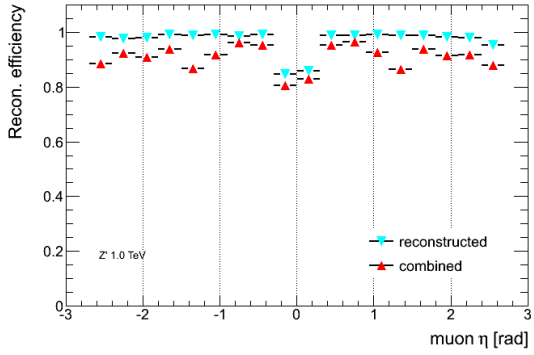

(d) Muon $|\eta|$

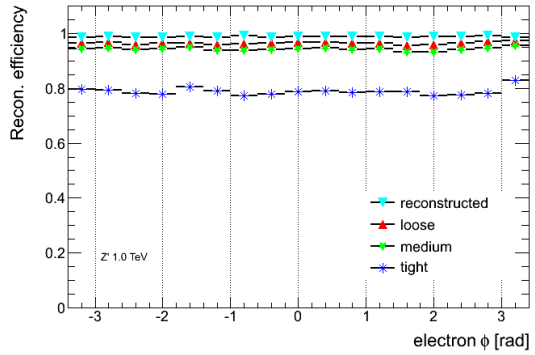

(e) Electron ϕ

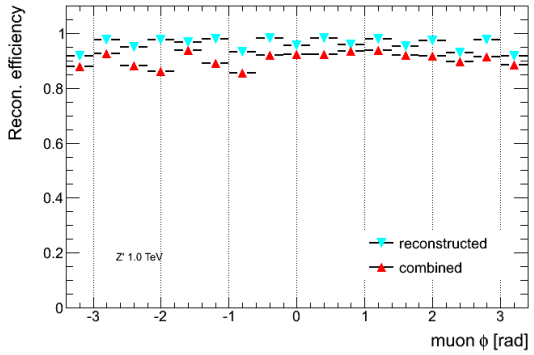

(f) Muon ϕ

Figure 5.16: Reconstruction efficiencies in 1 TeV $Z' \rightarrow e^+e^-$ and $\mu^+\mu^-$ samples as functions of p_T, η and ϕ for all recontructed, loose, medium and tight electrons and all reconstructed and combined muons, normalized to the number of truth particles with p_T greater than 30 GeV and $|\eta|$ smaller than 2.5.

Channel	Type	Efficiency
El	Reconstructed	0.99
	Loose	0.96
	Medium	0.94
	Tight	0.79
Mu	Reconstructed	0.96
	Combined	0.91

Table 5.7: Overall reconstruction efficiencies for electrons and muons.

remaining columns are explained in the following subsections.

The goal now is to reject as much background as possible while keeping as many Z' events as affordable. After all cuts are applied, the discovery reach can finally be calculated (section 5.8).

	No cuts	Pre	$+E_T$-cone/p_T	$+\Delta\phi$	$+p_T$ balance	+lepton fraction
Z' 1 TeV	505	198±1.1	193±1.1	176±1.0	166±1.0	164±0.99
Z' 1.5 TeV	154	57.9±0.54	56.2±0.53	51.1±0.51	48.4±0.50	47.3±0.49
DY	2.20e6	3.09e5±582	2.52e5±525	1.84e5±449	1.65e5±425	4.36e4±218
$W \to l\nu$+jets	3.09e7	4.26e3±183	1.30e3±97.5	333±51	181±37	29.7±13
γ+jets	7.40e7	2.50e4±2.68e3	5.39e3±1.28e3	2.49e3±951	2.23e3±935	689±537
$t\bar{t}$	3.74e5	3.44e3±27.5	2.08e3±20.9	424±9.4	190±6.3	5.0±1.0
Dijets	1.26e13	1.13e5±6.14e4	327±218	163±154	4.3±4.3	4.3±4.3
$Z\gamma$	1.109e4	1.75e3±28.5	1.44e3±25.8	620±17	385±13	78.2±6.0
$W\gamma$	5.23e4	1.17e3±27.9	1.17e3±27.9	372±16	227±12	66.4±6.6
ZZ	1.35e3	151±2.0	123±1.8	21.5±0.76	10.5±0.53	1.2±0.2
WW	1.56e4	174±7.4	122±6.2	38.4±3.5	25.6±2.8	9.7±1.7
WZ	4.87e3	202±3.1	164±2.8	29.9±1.2	14.9±0.85	1.9±0.3
$\gamma\gamma$	1.20e5	1.19e3±37.8	925±33	623±27	555±26	149±13

Table 5.8: Cut flow table in the electron channel. Expected number of electron pairs passing various requirements per 1 fb^{-1} are given together with the uncertainties.

	No cuts	Pre	+Charge	$+E_T$-cone/p_T	$+\Delta\phi$	$+p_T$ balance	+lepton fraction
Z' 1 TeV	505	184±1.2	184±1.2	176±1.2	161±1.2	153±1.1	148±1.1
Z' 1.5 TeV	154	53.8±0.53	53.8±0.53	51.9±0.52	47.0±0.49	44.6±0.48	42.7±0.47
DY	2.20e6	3.26e5±864	3.25e5±863	3.18e5±853	2.35e5±734	2.25e5±717	5.33e4±348
$W \to l\nu$+jets	3.09e7	102±15	93.3±28	0	0	0	0
γ+jets	7.40e7	0	0	0	0	0	0
$t\bar{t}$	3.74e5	3.75e3±28.6	3.09e3±26	2.15e3±21.2	420±9.4	255±7.3	5.85±1.1
Dijets	1.26e13	1.29e4±4.17e3	9.09e3±3.4e3	0	0	0	0
$Z\gamma$	1.109e4	1.44e3±25.8	1.44e3±25.8	1.37e3±25.2	582±16	461±15	64.3±5.5
$W\gamma$	5.23e4	2.0±1.2	1.3±0.94	0	0	0	0
ZZ	1.35e3	154±2.0	151±2.0	142±2.0	26.9±0.85	17.7±0.70	1.07±0.17
WW	1.56e4	146±6.7	146±6.7	142±6.7	41.8±3.5	32.7±3.2	12.2±1.9
WZ	4.87e3	205±3.1	191±3.1	182±3.0	32.4±1.3	22.4±1.0	1.76±0.29
$\gamma\gamma$	1.20e5	0	0	0	0	0	0

Table 5.9: Cut flow table in the muon channel. Expected number of muon pairs passing various requirements per 1 fb^{-1} are given together with the uncertainties.

5.6.1 Number of leptons per event

Figure 5.17 shows the number of electrons or muons per event for signal and background. One might quickly notice that not much background is cut by requiring exactly two leptons. As a matter of fact, in the electron channel 2.2% of the signal events are cut away, but only 0.11% of the background. In the muon channel the corresponding numbers are 0.032% and 0.028%.

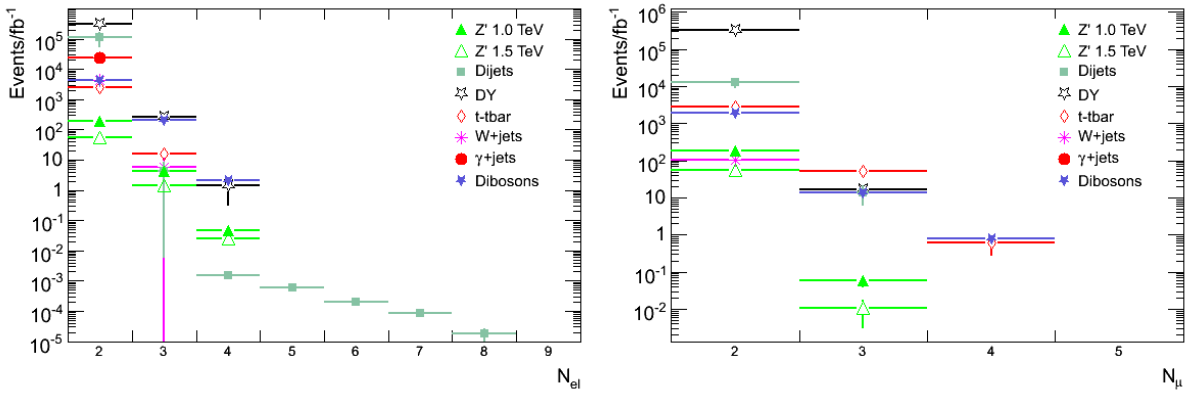

(a) Electron channel

(b) Muon channel

Figure 5.17: The number of electrons or muons per event after preselection (tables 5.4 and 5.5).

Even though lepton multiplicity is not a good cut variable, we need to look at the statistics. In the electron channel 2% of the events contain more than two electrons - are we picking out the right ones when using the two highest p_T electrons? Also, there might be some events where only one lepton from the Z' (or even none) is reconstructed properly, in which case at least one of the selected leptons stems from the underlying event. Let us have a closer look at the Z' Monte Carlo samples.

Figure 5.18 and table 5.10 show the number of electrons and muons in MC Z' samples after preselections (tables 5.4 and 5.5) but without the requirement on the number of leptons (i.e two leptons are *not* required). We consider the channels separately:

	Mass [TeV]	0	1	2	3	4
el	1.0	1.51±0.060	19.7±0.22	77.0±0.43	1.75±0.065	0.01904±0.0067
	1.5	1.82±0.11	22.2±0.20	74.1±0.70	1.82±0.11	0.0334±0.015
mu	1.0	2.45±0.090	23.6±0.20	73.9±0.50	0.023±0.0088	0
	1.5	2.83±0.14	26.3±0.42	70.8±0.68	0.0133±0.0094	0

Table 5.10: The multiplicity of electrons (muons) in MC samples of $Z' \to e^+e^-$ ($Z' \to \mu^+\mu^-$) for Z' masses 1.0 TeV and 1.5 TeV. All numbers are given in percent.

Electron channel For the 1.0 TeV (1.5 TeV) Z' we see that the distribution is peaked at 2 electrons per event, which is what we expected. In addition we see that in 21% (24%)

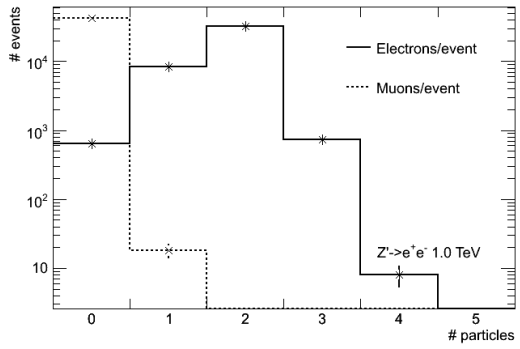

(a) 1 TeV Z' -> ee

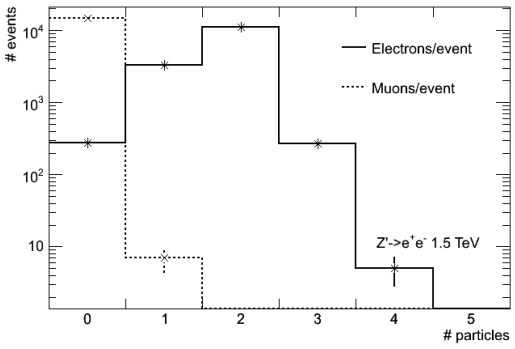

(b) 1.5 TeV Z' -> ee

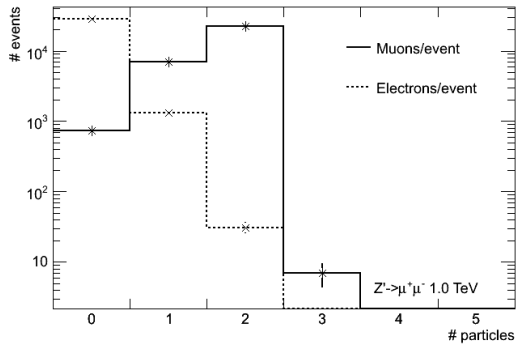

(c) 1 TeV Z' -> $\mu\mu$

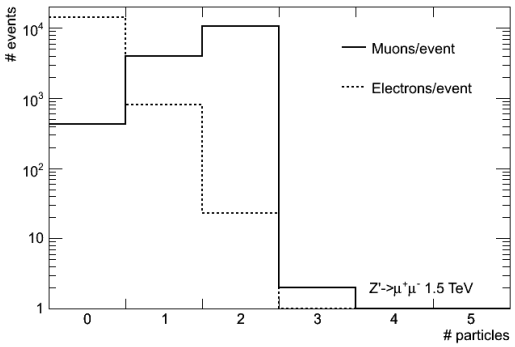

(d) 1.5 TeV Z' -> $\mu\mu$

Figure 5.18: The number of electrons and muons per event passing preselection when a 1.0 TeV or a 1.5 TeV Z' decays to muons. See also table 5.10.

of the events, one or no electron is reconstructed. 1.8% (1.9%) of the events contain 3 or more reconstructed electrons.

Muon channel For the 1.0 TeV (1.5 TeV) Z' the distribution is peaked again at 2 muons per event. 26% (29%) of the events have one or no muon reconstructed, while only 0.023% (0.0133%) have 3 or more reconstructed muons.

We now return to the two percent of events in the electron channel that contain three or more electrons to see if we pick out the electrons originating from the Z' when we choose the two electrons with highest p_T. We number the electrons from 1 to 3, where 1 is the leading electron and 3 is the one with the third highest p_T. According to figure 5.19 we find that for the 1.0 TeV (1.5 TeV) Z' the two leading electrons come from the Z' in 68.2±3.2% (68.7±5.3%) of the events. So, although the fraction of 3 electrons is relatively high as compared to the muon case, the two leading electrons stem from the Z' 69% of the time.

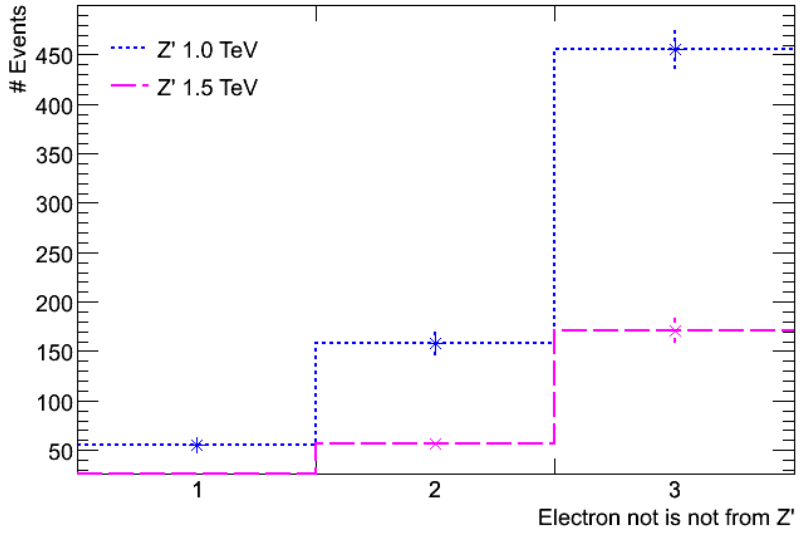

Figure 5.19: The three reconstructed electrons with the highest p_T are matched with truth electrons. The histogram shows how often the highest, second highest and third highest p_T electron does *not* match an electron coming from the Z'. Reconstructed electrons are required to pass preselection (table 5.4).

5.6.2 Charge

An obvious cut seems to be to require that the leptons have opposite electric charge, but first we must investigate the charge misidentification rates.

The electron charge is measured only in the inner detector where the charge misidentification probability is quite high. Figure 5.20(a) and 5.20(c) show that the probability grows with increasing p_T and η, with a mean charge misidentification probability of 5.3%.

The charge misidentification probability is only 0.02% for muons coming from 1.5 TeV Z' decays. It is much lower than for electrons because muon tracks are measured in both ID and in MS and the information from the two subdetectors is combined.

Based on these considerations we require the muons to have opposite charges, but not the electrons. This is also the strategy taken by the ATLAS exotics group. However, studies are ongoing to understand the charge misidentification in view of searches for same sign leptons.

Figure 5.21 and table 5.11 show the number of events where the two highest p_T leptons have opposite charge or same charge. Requiring opposite sign electrons would reduce the Z' signal by 10%. The corresponding loss is negligible in the muon case. The reason for the higher probabilities compared to figure 5.20 is that the previously quoted numbers were for single leptons. The charge misidentification probability for *two* leptons is $2p(1-p)$, where p is the probability for one lepton being tagged with the wrong charge. The background reduction through the opposite charge requirement is 29% in both channels.

	$Z' \to e^+e^-$		$Z' \to \mu^+\mu^-$	
Mass [TeV]	1.0	1.5	1.0	1.5
Charge misId [%]	10.3	10.4	0.00923	0.0386

Table 5.11: The charge misidentification rate in Z' to electrons and muons after preselection (tables 5.4 and 5.5). No truth matching is applied here.

As can be seen from column 3 in the cut flow table 5.9 the charge requirement in the muon channel removes a non-negligible fraction of $t\bar{t}$, W+jets and diboson events, whereas only 2% of the ZZ events are reduced.

5.6.3 Isolation

Leptons coming from a Z' are in the vast majority of events isolated. This is not expected to be the case for leptons within jets[18]. Thus we try to reduce these backgrounds using a cut based on the activity in the vicinity of the leptons. To do this we use the variable called E_T-cone. It is defined as the sum of the transverse energy in the calorimeters within a circle in the $\eta - \phi$ plane,

$$E_T^{\Delta R<X} \equiv \sum_{\Delta R<X} E_T, \quad \Delta R = \sqrt{(\Delta\eta)^2 + (\Delta\phi)^2} \tag{5.5}$$

For $X = 0.3$ this leads to the E_T-cone variable E_T-cone30 shown in figure 5.22 for the signal and background datasets for the two leptons with highest p_T[19].

[18] $t\bar{t}$ is special: the top quark decays to a b quark and a W boson, and when the W bosons from both top and anti-top decay leptonically this results in two isolated leptons in the event.

[19] The E_T-cone variable actually comes with different radii in the $\eta - \phi$ plane, $\Delta R = 0.20$, 0.30 and 0.40. A comparison of these was made and no essential difference was found. Studies have been made[35] showing that the E_T-cone30 is best in the sense that it combines high discrimination power and robustness against pile-up.

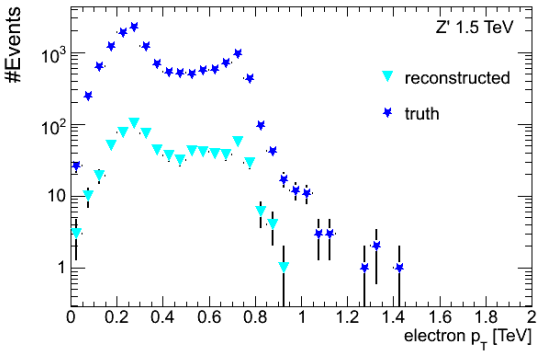

(a) Electron p_T

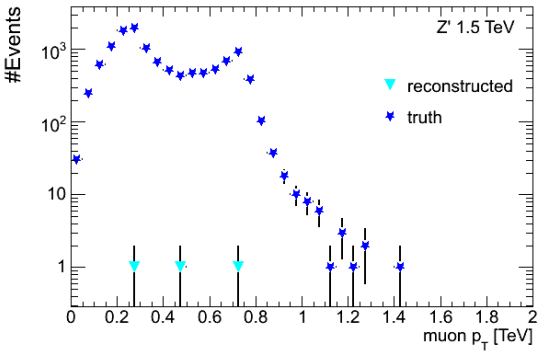

(b) Muon p_T

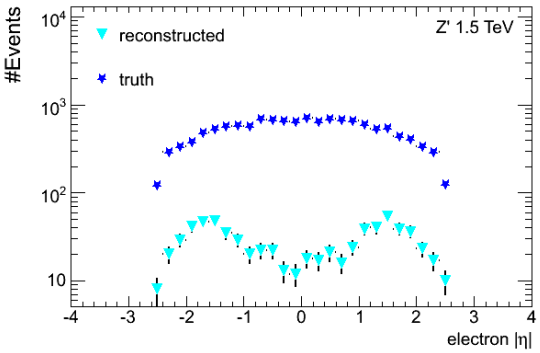

(c) Electron η

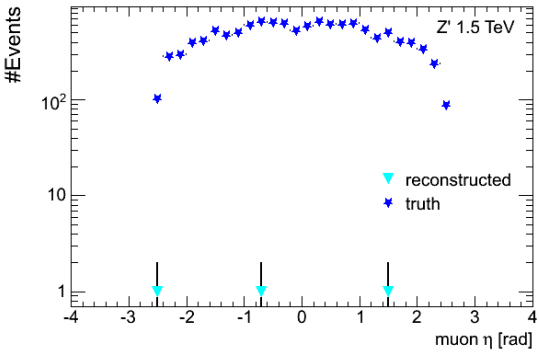

(d) Muon η

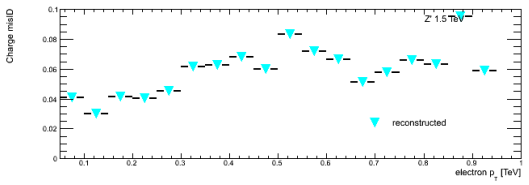

(e) Electron p_T

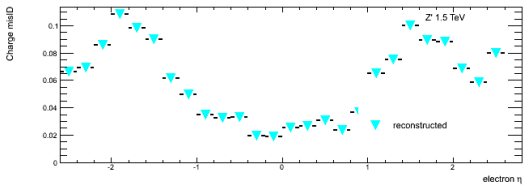

(f) Electron η

Figure 5.20: Plotted are the total number of leptons and the number that has the opposite charge as compared to the corresponding truth particle as functions of p_T and η for electrons (5.20(a) and 5.20(c)) and muons (5.20(b) and 5.20(d)). 5.20(e) and 5.20(f) show the ratio of these number for electrons. Reconstructed leptons from 1.5 TeV Z's are matched to truth leptons using the algorithm described in appendix C.2. Mean charge misidentification is 5.3% for electrons and 0.02% for muons.

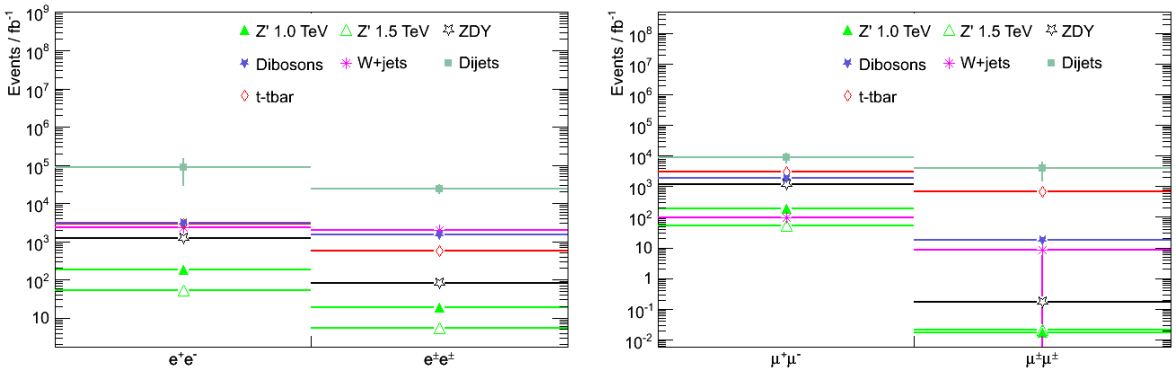

(a) Electron channel

(b) Muon channel

Figure 5.21: Total number of events passing preselection with opposite charge and same charge dielectrons (5.21(a)) and dimuons (5.21(b)). See table 5.11 for charge misidentification probability for dielectrons/-muons from Z'.

A p_T-dependent E_T-cone variable is obtained by dividing the E_T-cone variable by the lepton p_T

$$E_T^{\Delta R<X}/p_T = \sum_{\Delta R<X} E_T/p_T, \quad \Delta R = \sqrt{(\Delta\eta)^2 + (\Delta\phi)^2} \tag{5.6}$$

This takes into account that high p_T leptons have a higher probability to emit bremsstrahlung than leptons with lower p_T. Effectively we accept more activity around high p_T leptons than around lower p_T leptons because much of this activity is due to bremsstrahlung. This variable is plotted in figure 5.23 for the two leading electrons and muons. It is interesting to see that the shapes of the curves are different in the electron and muon channels. This difference is caused by the fact that electrons have a much higher probability of emitting bremsstrahlung than muons. Bremsstrahlung emission is also the reason why there is much more activity around the second highest p_T leptons (photon emission makes the lepton p_T lower than that of the other lepton).

Comparing the E_T-cone and the E_T-cone/p_T plots it becomes clear that the best variable to cut on is the latter as it discriminates better the various backgrounds. Furthermore, a large fraction of the dijet background can be cut away in both the electron and muon channel. Comparing to the invariant mass distributions in figure 5.11 we see that this is good news in the electron channel as the dijet background is quite prominent in the signal regions, but that the dijets are mainly at lower invariant masses in the muon channels. The isolation cut also removes parts of the other backgrounds.

Some samples have low statistics, making it difficult to optimize the isolation. We opted for E_T-cone30/p_T < 0.1, for both electrons and muons. This keeps the signal efficiency above 97% in all cases and the reducible background (total SM background excluding DY) rejection above 70%, see table 5.12.

The consequence of requiring E_T-cone30/p_T < 0.1 is seen in the cut flow tables 5.8 and 5.9

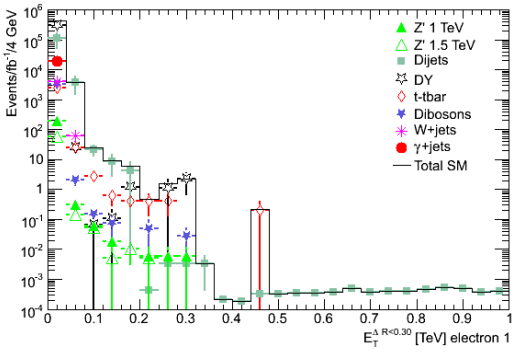

(a) E_T-cone30 - electron 1

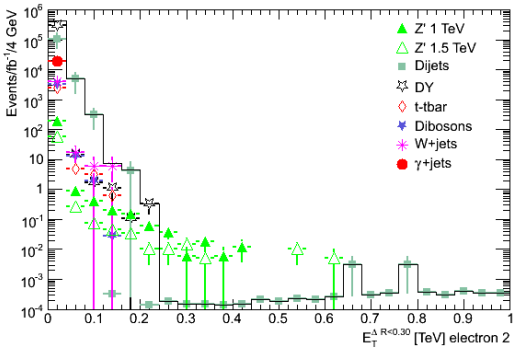

(b) E_T-cone30 - electron 2

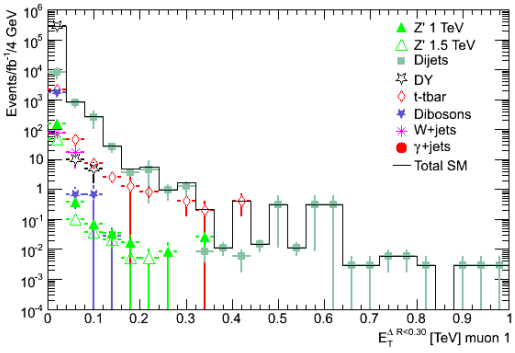

(c) E_T-cone30 - muon 1

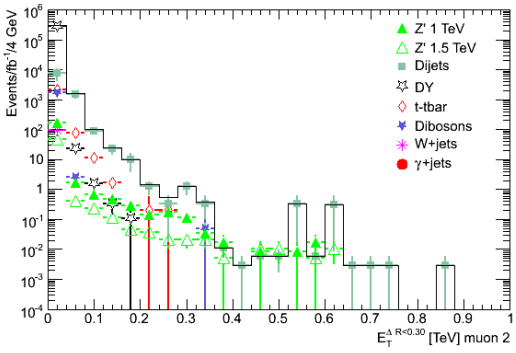

(d) E_T-cone30 - muon 2

Figure 5.22: The variable E_T-cone30 (Equation (5.5)) for the leading electron (5.22(a)) and subleading electron (5.22(b)), and leading and subleading muons (5.22(c) and 5.22(d), respectively) after preselection and muon charge requirement.

	Mass [TeV]	Cut	r_{bkg}^{SM} l_1	r_{bkg}^{SM} l_2	$r_{bkg}^{reducible}$ l_1	$r_{bkg}^{reducible}$ l_2	ϵ_{signal} l_1	ϵ_{signal} l_2
el	1.0	0.1	0.276	0.263	0.799	0.755	0.998	0.990
	1.5	0.1					0.997	0.989
mu	1.0	0.1	0.0310	0.0365	0.698	0.716	0.997	0.974
	1.5	0.1					0.997	0.978

Table 5.12: Signal efficiency and total SM background rejection rate for the isolation cut E_T-cone30/p_T < 0.1 in the electron and muon channel for a 1.0 TeV and a 1.5 TeV Z'. l_1 and l_2 are the two highest p_T leptons. r_{bkg}^{SM} and $r_{bkg}^{reducible}$ are the fractions of rejected events for total SM background and the reducible background (total SM minus DY) respectively. ϵ_{signal} is the fraction of signal events that remains after the cut.

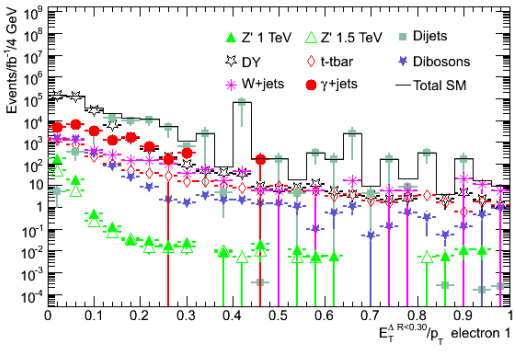

(a) E_T-cone30/p_T - electron 1

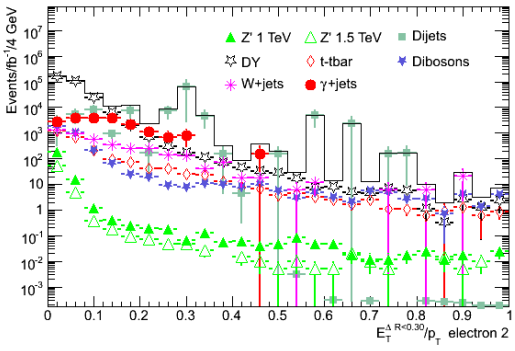

(b) E_T-cone30/p_T - electron 2

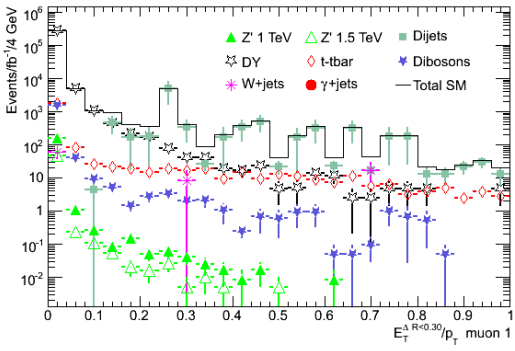

(c) E_T-cone30/p_T - muon 1

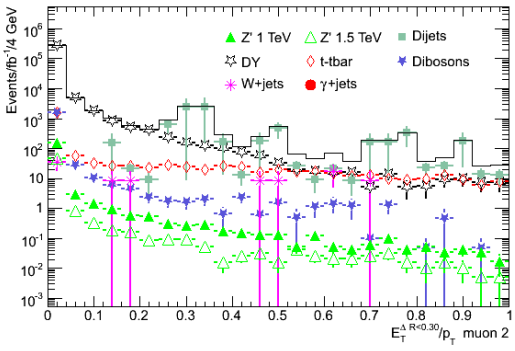

(d) E_T-cone30/p_T - muon 2

Figure 5.23: The p_T normalized variable E_T-cone30 (Equation (5.6)) for the leading electron (5.23(a)) and subleading electron (5.23(b)), and muons (5.23(c) and 5.23(d)) after preselection and charge requirement (muon channel only).

in the electron and muon channels respectively. The results are as summarized below:

Electron channel 97% of signal events remain. The best reduction is in the dijet channel, where 99.7% of the events are removed.

Muon channel 96% of signal events remain. The highest reduction is in W+jets, γ+jets, Wγ and dijets, where close to 100% of the MC events are removed.

The effect of the isolation cut is summarized in table 5.13.

Channel	Z' 1.0 TeV	Z' 1.5 TeV	DY	W+jets	γ+jets	$t\bar{t}$
El	2.53	2.94	18.4	69.5	78.4	39.5
Mu	4.35	3.53	2.1	100	100	30.4

Channel	dijets	Zγ	Wγ	ZZ	WW	WZ	$\gamma\gamma$
El	99.7	17.7	0	18.5	30.0	18.8	23.3
Mu	100	4.86	100	5.96	2.74	4.71	-

Table 5.13: The reduction (in percent) achieved by the cut E_T-cone30$/p_T < 0.1$. A "-" means the background was 0 before the cut.

Figure 5.24 shows the invariant mass distributions in the electron (5.24(a)) and muon (5.24(b)) channels after requiring E_T-cone30$/p_T < 0.1$. Comparing to the invariant mass distributions before requiring isolation (figure 5.11) we see that in the muon channel most of the reduced background was at low invariant mass, but that the isolation cut removed some from the signal region. In the electron channel we see a similar reduction at low invariant mass, but also a sizeable fraction of dijets and $t\bar{t}$ events are eliminated in the vicinity of the signal resonances.

5.6.4 Opening angle in the transverse plane

In the rest frame of the Z' the two leptons will be back to back. A particle as heavy as the Z' will often decay at or almost at rest. This means that the angle between the two muons or electrons in the transverse plane is expected to be quite close to 180° in the laboratry frame as well. This is not necessarily expected for the SM backgrounds.

A cut on the opening angle in the transverse plane also ensures that the colliding quarks are not heavily affected by initial state radiation (ISR), which makes it more difficult to differentiate between different models. Section 5.7 gives more information on this.

Figure 5.25 shows the opening angle in the transverse plane, $\Delta\phi$ for the electron (5.25(a)) and muon (5.25(b)) channels. We see that the DY and Z' are peaked at $\Delta\phi = \pi$ while distributions are flatter for the reducible backgrounds.

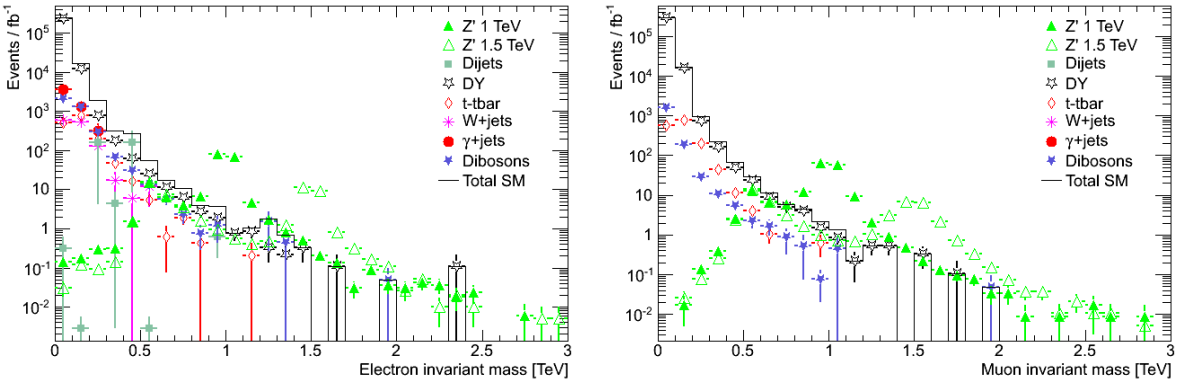

(a) Electron channel (b) Muon channel

Figure 5.24: The invariant mass distributions of the two highest p_T leptons after preselection, trigger and requiring an isolation cut E_T-cone30/p_T < 0.1 for all leptons and opposite charge requirement for muons.

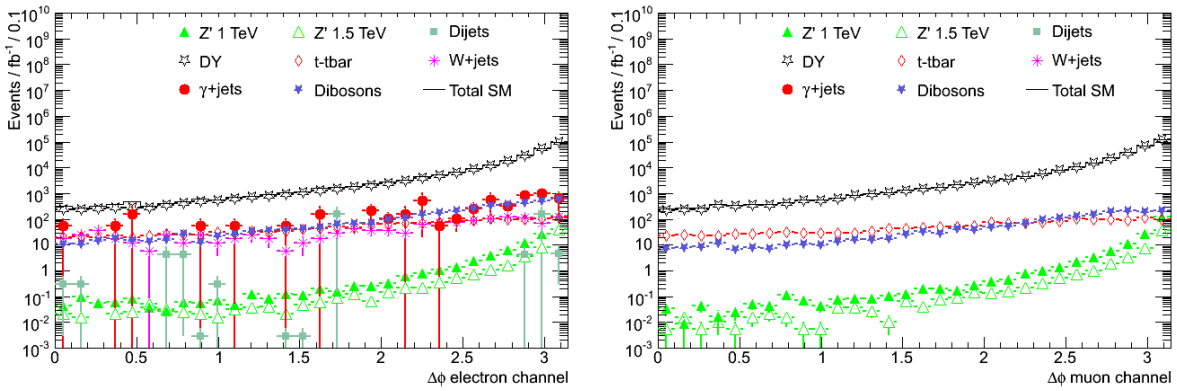

(a) Electron channel (b) Muon channel

Figure 5.25: The opening angle between the two highest p_T leptons in the transverse plane ($\Delta\phi$) after preselection, trigger requirement and isolation cuts.

Instead of choosing the cut value by eye, we optimize the cut by maximizing the product of a signal efficiency ϵ_{signal} and background rejection r_{bkg}. Signal efficiency is defined as the fraction of the signal events passing a specific cut

$$\epsilon_{signal} = \frac{n^{\text{signal}}_{\text{after}}}{n^{\text{signal}}_{\text{before}}} \tag{5.7}$$

and background rejection as the fraction of the background events rejected by the cut

$$r_{\text{bkg}} = 1 - \frac{n^{\text{bkg}}_{\text{after}}}{n^{\text{bkg}}_{\text{before}}} \tag{5.8}$$

The results are shown in figure 5.26 in the electron (5.26(a)) and muon (5.26(b)) channels. The background rejection factors are shown for both total SM background ($r^{\text{SM}}_{\text{bkg}}$) as well as reducible background ($\text{r}^{\text{reducible}}_{\text{bkg}}$, total SM background minus DY). We see that the background rejection factor for the total SM is dominated by DY, which means that the cut on $\Delta\phi$ must be very close to π to reject a large fraction. We therefore chose to base the maximization on the reducible background.

The optimal cut as defined above is $\Delta\phi > 2.85$ in both channels, which corresponds to a background rejection factor and a signal acceptance of 86%. We chose to cut on $\Delta\phi > 2.8$. While this reduces the background rejection by 4%, it increases the signal acceptance above 90% (table 5.14).

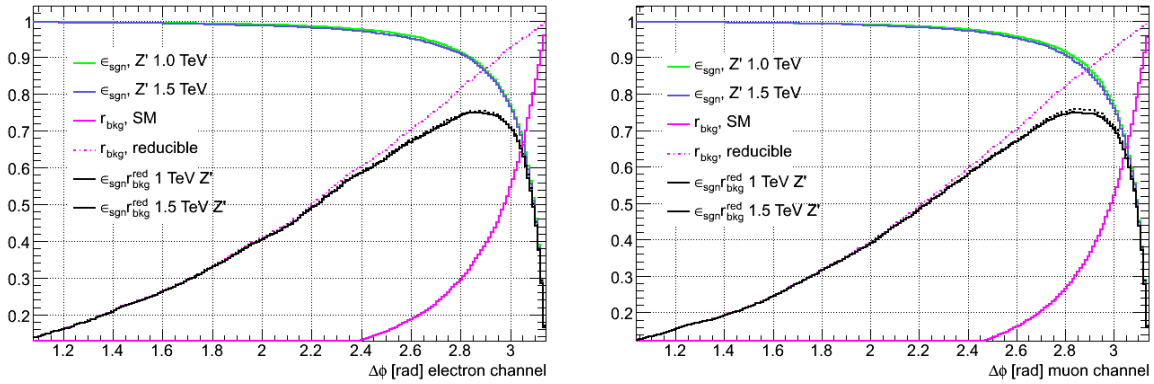

(a) Electron channel

(b) Muon channel

Figure 5.26: We optimize the cut on $\Delta\phi$ using the signal efficiency ϵ_{sgn}(equation (5.7)) and the background rejection r_{bkg}(equation (5.8)). Background rejection curves for both total and reducible background (everything except for DY) backgrounds are shown.
Leptons are required to pass preselection (5.4 for electrons and 5.5 for muons), trigger and isolation cuts.

Column 5 (6) of table 5.8 (5.9) show the effect of the cut on the signal and background datasets in the electron (muon) channel. Table 5.15 illustrates the situation in a slightly different way, giving the effect of the cut for the various datasets. The main results are:

	Mass [TeV]	$\Delta\phi_{\text{min}}$	$r_{\text{bkg}}^{\text{SM}}$	$r_{\text{bkg}}^{\text{reducible}}$	ϵ_{signal}
el	1.0	2.8	0.296	0.815	0.914
	1.5	2.8			0.910
mu	1.0	2.8	0.266	0.820	0.916
	1.5	2.8			0.906

Table 5.14: Signal efficiency and background rejection (total SM and reducible) for the cut on the angle between the two highest p_T leptons ($\Delta\phi > 2.8$) in the transverse plane in the electron and muon channel for a 1.0 TeV and a 1.5 TeV Z'.

Electron channel The signal is reduced by 9%. The greatest background reduction is achieved for the $t\bar{t}$ channel with 86%.

Muon channel The signal is reduced by 9%, and the greatest background reduction is achieved for the Zγ channel with 88%.

Comparing the invariant mass distributions after requiring $\Delta\phi > 2.8$ to the invariant mass distributions before (figure 5.24) we see that the cut removed mostly events at low invariant mass. Because of low statistics most distributions do not extend out to higher invariant masses, making the estimation of the optimal value of the cut hard to make. Still we know that the distributions would be smooth given enough statistics and that the cuts we consider would indeed remove a fraction of the background events.

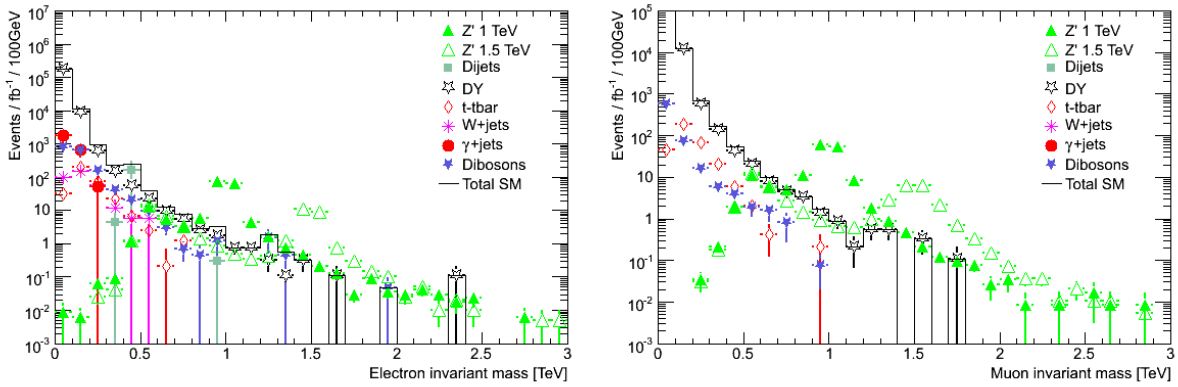

(a) Electron channel

(b) Muon channel

Figure 5.27: The invariant mass distributions of the two highest p_T electrons (5.27(a)) and muons (5.27(b)) after preselection, lepton isolation (E_T-cone30/p_T < 0.1, section 5.6.3) and $\Delta\phi > 2.8$ (section 5.6.4).

5.6.5 p_T balance

In Z' decays we expect two isolated leptons approximately back-to-back in the transverse plane, as discussed in section 5.6.4. The two leptons have the same energy in the Z' center

Channel	Z' 1.0 TeV	Z' 1.5 TeV	DY	W+jets	γ+jets	$t\bar{t}$
El	8.81	8.92	27.0	74.4	53.8	86.2
Mu	8.52	9.44	26.1	-	-	80.5

Channel	dijets	Zγ	Wγ	ZZ	WW	WZ	$\gamma\gamma$
El	50.2	56.9	68.2	82.5	68.5	81.8	32.6
Mu	-	87.5	-	81.1	21.8	30.9	-

Table 5.15: The reduction (in percent) achieved by the cut $\Delta\phi > 2.8$. A "-" means the background was 0 before the cut.

of mass frame, and also in the lab frame when the Z' decays at rest. Another possible cut is thus the p_T balance, $p_{T,1}/p_{T,2}$. For a Z' one expects the lepton p_T ratio to be close to one, and in general greater than one for backgrounds.

The p_T balance is shown in figures 5.28(a) and 5.28(b) for electrons and muons respectively. The ratio falls off very steeply for Z' and DY, and not so much for the other backgrounds.

A optimal cut is found by maximizing the product $r_{\text{bkg}}\epsilon_{\text{signal}}$ (equations (5.8) and (5.7)). The plots of the signal efficiencies and background rejection (for the whole SM and the reducible background (total SM minus DY)) are shown in figure 5.29. Because the DY background resembles the signal in the p_T balance variable, we optimize with respect to the total SM background minus the DY background.

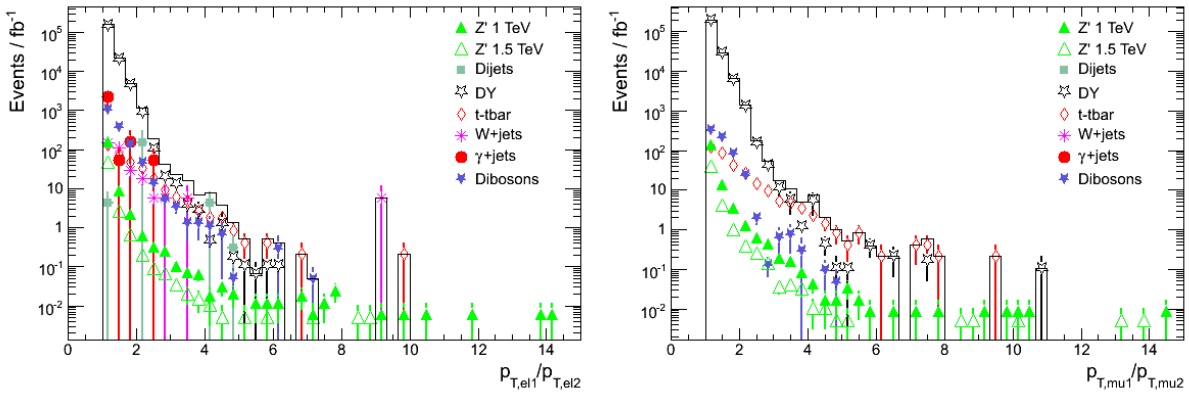

(a) Electron channel

(b) Muon channel

Figure 5.28: The p_T balance distributions of the two highest p_T leptons requiring all particles passed preselection, having E_T-cone30$/p_T < 0.1$ and $\Delta\phi > 2.8$ (see sections 5.6.4 and 5.6.3).

The optimal cut in the electron (muon) channel is 1.22 (1.28). This gives a signal efficiency of 86% (78%) and a background rejection of 77% (72%). However, we opt for a slightly different value to cut on to preserve a larger fraction of the signal, namely the one corresponding to a signal efficiency at about 95%, which is $p_{T,el1}/p_{T,el2} < 1.4$ ($p_{T,mu1}/p_{T,mu2} < 1.6$) (table 5.16).

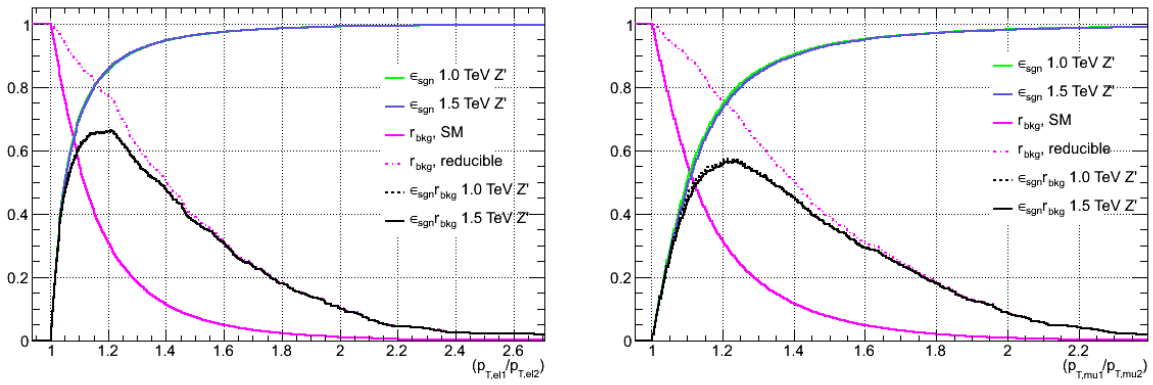

(a) Electron channel

(b) Muon channel

Figure 5.29: We optimize the cut on the p_T balance of the leptons using the signal efficiency ϵ_{sgn}(equation (5.7)) and the background rejection r_{bkg}(equation (5.8)). Background rejection curves for both total and reducible (everything except for DY) are shown. Leptons are required to pass preselection (5.4 for electrons and 5.5 for muons), trigger and cuts on isolation and $\Delta\phi$.

	Mass [TeV]	$(p_{T,1}/p_{T,2})_{\text{max}}$	$\text{r}_{\text{bkg}}^{\text{SM}}$	$\text{r}_{\text{bkg}}^{\text{reducible}}$	ϵ_{signal}
el	1.0	1.39	0.103	0.477	0.950
	1.5	1.40	0.105	0.482	0.950
mu	1.0	1.59	0.0493	0.311	0.950
	1.5	1.60	0.0459	0.305	0.950

Table 5.16: Signal efficiency and background rejection (total SM and reducible) for the cut on the p_T balance, $p_{T,1}/p_{T,2}$, of the leptons in the electron and muon channel for a 1.0 TeV and a 1.5 TeV Z'.

Column 6 in the cut flow table 5.8 for the electron channel and column 7 in table 5.9 for the muon channel show the effect of the p_T balance cut. The percentages of removed events for signal and background are listed in table 5.17. The main results are:

Channel	Z' 1.0 TeV	Z' 1.5 TeV	DY	W+jets	γ+jets	$t\bar{t}$
El	5.68	5.28	10.3	45.6	10.4	55.2
Mu	5.00	5.1	4.26	-	-	39.3

Channel	dijets	Zγ	Wγ	ZZ	WW	WZ	$\gamma\gamma$
El	97.4	37.9	39.0	51.2	33.3	50.2	10.9
Mu	-	20.8	-	34.2	21.8	30.9	-

Table 5.17: The reduction (in percent) achieved by requiring the p_T balance to be smaller than 1.4 (1.6) in the electron (muon) channel. A "-" means the background was 0 before the cut.

Electron channel A reduction in the signal by 6% (5%) for the 1.0 TeV (1.5 TeV) Z'. Dijets are reduced by 97%.

Muon channel 5% reduction of signal events. The greatest reduction of 39% is achieved for the $t\bar{t}$ background.

Figure 5.30 shows the invariant mass distributions in the electron (5.30(a)) and muon (5.30(b)) channels. Comparing to the invariant mass distributions before the p_T balance cut (figure 5.27) we see a reduction in events at low invariant masses. As mentioned before the statistics are too low too conclude at higher invariant masses.

The $\Delta\phi$ requirement of the previous subsection cuts away a large fraction of the events where the Z' is heavily affected by ISR, but it does not affect the events where the decay angle is 0 or π, i.e. the events where the Z' decays to leptons going paralell and anti-paralell to the Z' direction of motion. The p_T balance requirement, however, removes those events.

5.6.6 Lepton fraction

Z' decaying into leptons is expected to be a very clean event, and there should not be many other high energy particles. We define the lepton fraction, which is the fraction of the total transverse p_T carried by the dileptons, as

$$\frac{p_{T,1} + p_{T,2}}{\not{E}_T + \sum p_T} \tag{5.9}$$

where $p_{T,1}$ and $p_{T,2}$ are the p_T of the two leptons, $\not{E}_T$ is the missing E_T and $\sum p_T$ is the total p_T of the event. Note that these are scalar sums.

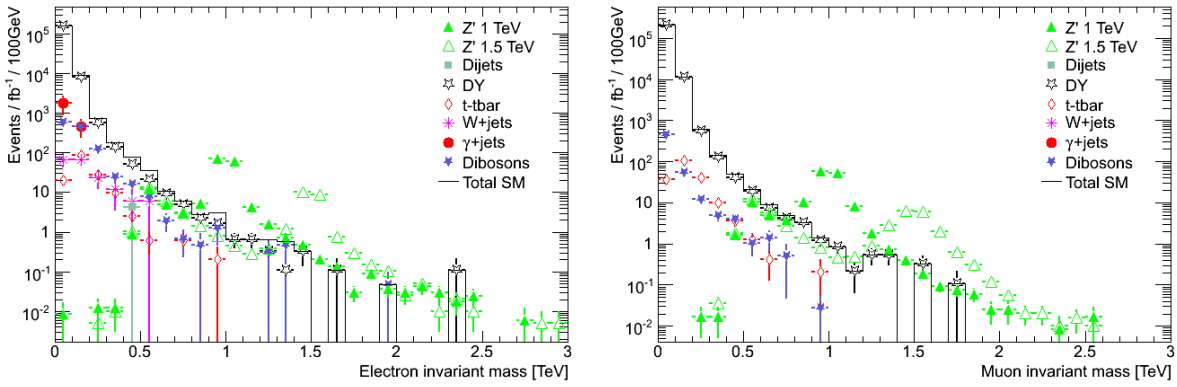

(a) Electron channel (b) Muon channel

Figure 5.30: The invariant mass distributions of the two highest p_T electrons (5.30(a)) and muons (5.30(b)) after preselection, lepton isolation (E_T-cone30/p_T < 0.1, section 5.6.3), $\Delta\phi > 2.8$ (section 5.6.4) and the p_T balance cuts $p_{T,el1}/p_{T,el2} < 1.4$ (electron channel) and $p_{T,\mu 1}/p_{T,\mu 2} < 1.6$ (muon channel).

We expect the lepton fraction to be close to one for Z' events, larger than 1 for SM backgrounds. This is confirmed by figure 5.31 for both electrons (5.31(a)) and muons (5.31(b)).

Note that when considering cuts on $\Delta\phi$ (figure 5.28) and p_T balance (figure 5.25) the DY distribution was similar in shape to the Z' distributions, while here the DY shows a different pattern as it has its most probable lepton fraction value at about 0.3. Hence we expect a cut on the lepton fraction will remove a larger fraction of DY than of Z'. The fraction of DY removed is, however, most probably be at low invariant mass.

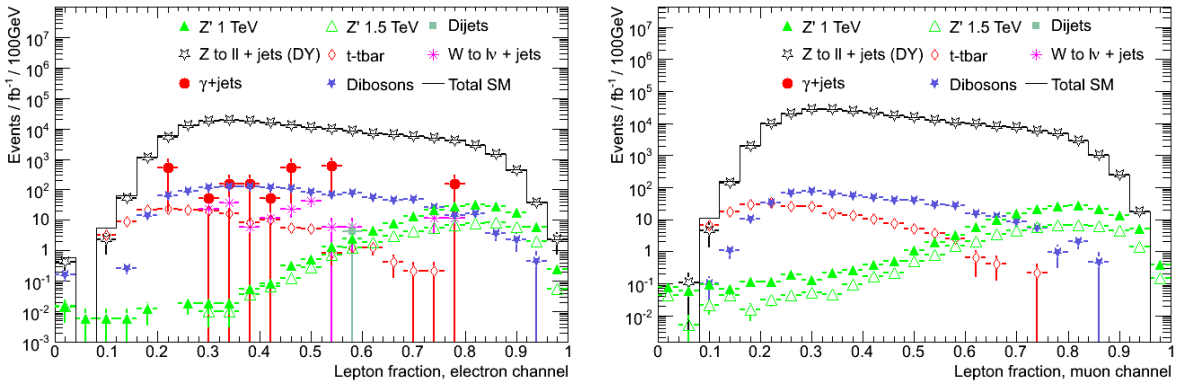

(a) Electron channel (b) Muon channel

Figure 5.31: The lepton fraction as defined in equation (5.9), requiring that all particles have passed preselection, $\Delta\phi > 2.8$, the isolation cuts from section 5.6.3 and the p_T balance cuts from section 5.6.5.

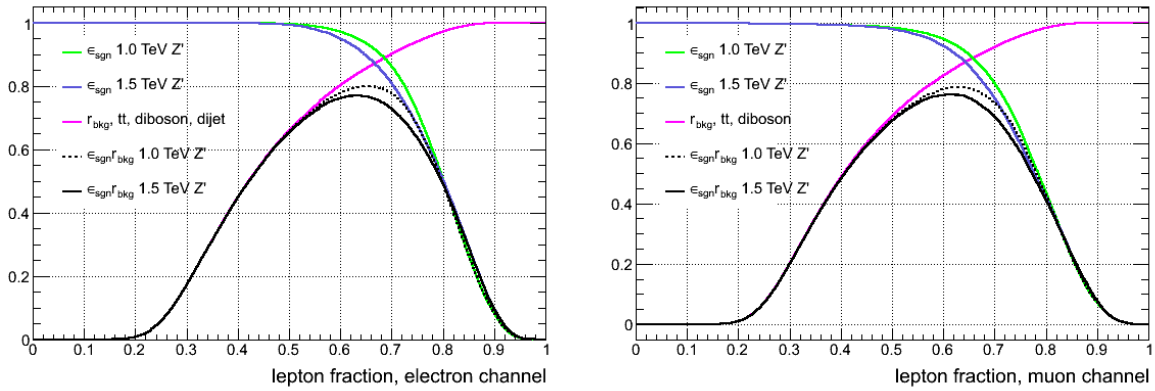

(a) Electron channel

(b) Muon channel

Figure 5.32: We optimize the cut on the lepton fraction (equation (5.9)) using the signal efficiency ϵ_{sgn}(equation (5.7)) and the background rejection r_{bkg}(equation (5.8)). Background rejection curves for both total and reducible background (everything except for DY) are shown.
Leptons are required to pass preselection (tables 5.4 for electrons and 5.5 for muons), trigger and cuts on lepton isolation, $\Delta\phi$ and p_T balance.

The backgrond rejection factor and signal efficiency curves are shown in figure 5.32. From the signal efficiency curves we see that the one corresponding to the 1.5 TeV Z' falls more steeply than the one for the 1.0 TeV Z'. If this is a general tendency, the curve falls even more steeply for higher masses. We therefore chose a wide cut at lepton fraction 0.55. Table 5.18 shows that 75% of the SM background is removed by the cut while the keeping between 96% and 99% of the signal depending on the channel and mass.

	Mass [Tev]	cut (lepton fraction$_{\text{min}}$)	$r_{\text{bkg}}^{\text{SM}}$	$r_{\text{bkg}}^{\text{dijet,diboson,t}\bar{\text{t}}}$	ϵ_{signal}
el	1.0	0.55	0.735	0.771	0.988
	1.5	0.55			0.978
mu	1.0	0.55	0.763	0.884	0.970
	1.5	0.55			0.959

Table 5.18: Signal efficiency and background rejection (for total SM and the combined dijet, diboson and $t\bar{t}$) for the lepton fraction < 0.55 cut in the electron and muon channel for a 1.0 TeV and a 1.5 TeV Z'. All leptons are required to pass preselection and cuts on lepton isolation, $\Delta\phi$ and p_T balance

.

The last columns of the cut flow tables 5.8 (electron channel) and 5.9 (muon channel) show the number of events remaining per $1\,\text{fb}^{-1}$ after the lepton fraction cut. Table 5.19 shows the reduction in percent for signal and background. The main results are the following:

Electron channel 1% (2%) of the events from the 1.0 TeV (1.5 TeV) Z' are cut away. The largest reduction is in the $t\bar{t}$ background (97.4%).

Muon channel 3% (4%) of the events from the 1.0 TeV (1.5 TeV) Z' are cut away. The largest reduction is as for the electrons in the $t\bar{t}$ (97.7%)

Channel	Z' 1.0 TeV	Z' 1.5 TeV	DY	W+jets	γ+jets	$t\bar{t}$
El	1.20	2.27	73.6	83.6	69.1	97.4
Mu	3.27	4.26	76.3	-	-	97.7

Channel	dijets	Zγ	Wγ	ZZ	WW	WZ	$\gamma\gamma$
El	0	79.7	70.7	88.6	62.1	87.2	73.2
Mu	-	86.1	-	93.5	62.7	92.1	-

Table 5.19: The reduction (in percent) achieved by requiring the lepton fraction (equation (5.9)) to be larger than 0.55. A "-" means the background was 0 before the cut.

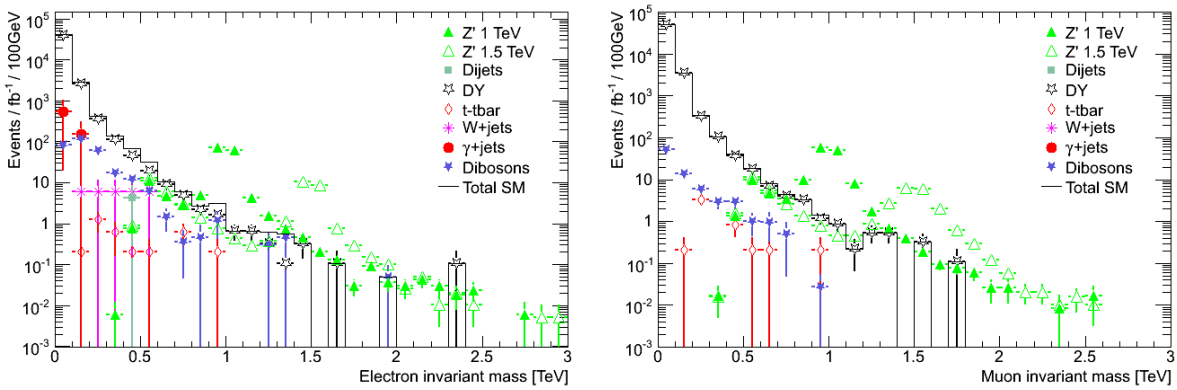

(a) Electron channel

(b) Muon channel

Figure 5.33: The resulting invariant mass distributions of the two highest p_T electrons (5.33(a)) and muons (5.33(b)) after all cuts of table 5.20 have been applied.

5.6.7 Summary of cuts used

Table 5.20 summarizes all the cuts made up to this point. The resulting invariant mass distributions are shown in figure 5.33.

Cut variable	Comment	El channel	Mu channel	Section
Charge	Require opposite charges	No	Yes	5.6.2
p_T	Lepton transverse momentum	> 30 GeV	> 30 GeV	5.5
Isolation	E_T-cone30$/p_T$	< 0.1	< 0.1	5.6.3
p_T balance	$p_{T,l1}/p_{T,l2}$	< 1.4	< 1.6	5.6.5
lepton fraction	$(p_{T,1} + p_{T,2})/(\not{E_T} + \sum p_T)$	> 0.55	> 0.55	5.6.6

Table 5.20: Cuts after preselection (tables 5.4 for electrons, 5.5 for muons) used in the 10 TeV analysis.

5.7 Angular distribution and forward-backward asymmetry

This section is based on reference [37].

It is usual that after the observation of a resonance we determine its spin. This is done using the lepton angular distribution in the center of mass of the dileptons and comparing to figure 5.3. As discussed in section 5.1 we assume that the colliding quark travels in the same direction as the Z'. We define two quantities:

θ^* as the angle between the outgoing e^-/μ^- and the incoming quark in the Z' rest frame, and

$\theta^\otimes$ as the angle between the outgoing e^-/μ^- candidate and the direction of the reconstructed Z'

Figure 5.34 shows the correlation between $\cos\theta^*$ and $\cos\theta^\otimes$. We see that the approximation is valid.

In general, initial state radiation (ISR) modifies the Z' axis with respect to the quark axis, introducing a greater uncertainty on the estimator $\cos\theta^\otimes$ for the size $\cos\theta^*$.

Figure 5.35 shows the angular distribution for total signal and background in a mass window ± 200 GeV around the resonance for a 1.0 TeV (5.35(a)) and a 1.5 TeV (5.35(b)) Z'. By comparison to figure 5.3 we recognize the signal as being compatible with a spin-1 particle. Further the curves should be fit with the theoretical predictions for signal and backgrond. This is not done here. Also note that more than 1 fb^{-1} might be needed to differentiate between different spins, especially for the 1.5 TeV Z' where the expectation value per bin subceeds 1 event for some values of $\cos\theta^*$.

The resulting the forward-backward asymmetry A_{FB} (equation (5.2)) can be used to differentiate different models, see figure 5.5(b). Figure 5.36 shows the A_{FB} distribution in the electron and muon channels as a function of the invariant mass for the 1.0 TeV Z'. The blue curve shows the A_{FB} for the signal only. We see what we expected - it is zero exactly at the particle mass and positive/negative below/above that point. The green curve shows the signal and the background together. This is what we would actually see in the detector - a somewhat washed out version of the blue curve. But at the Z' pole the A_{FB} is dominated by the signal, hopefully enough to make it possible to differentiate between Z' models.

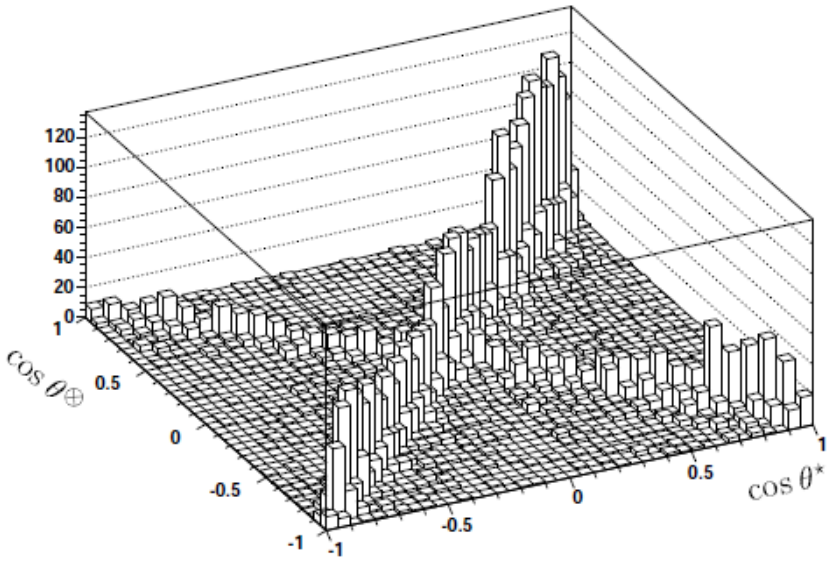

Figure 5.34: $\cos\theta^*$ vs $\cos\theta^{\otimes}$ for a (SSM) Z' of mass 1.5 TeV[37].
$\cos\theta^*$ is the angle between the outgoing electron and the incoming quark in the Z' rest frame, while $\cos\theta^{\otimes}$ is the angle between the outgoing electron candidate and the direction of the reconstructed Z'. We see that the assumption that the Z' continues in the direction of the quark is well motivated for most θ^*s, the exception being at values of $\cos\theta^*$ close to one, where the uncertainty on the quark direction is close to 50%.

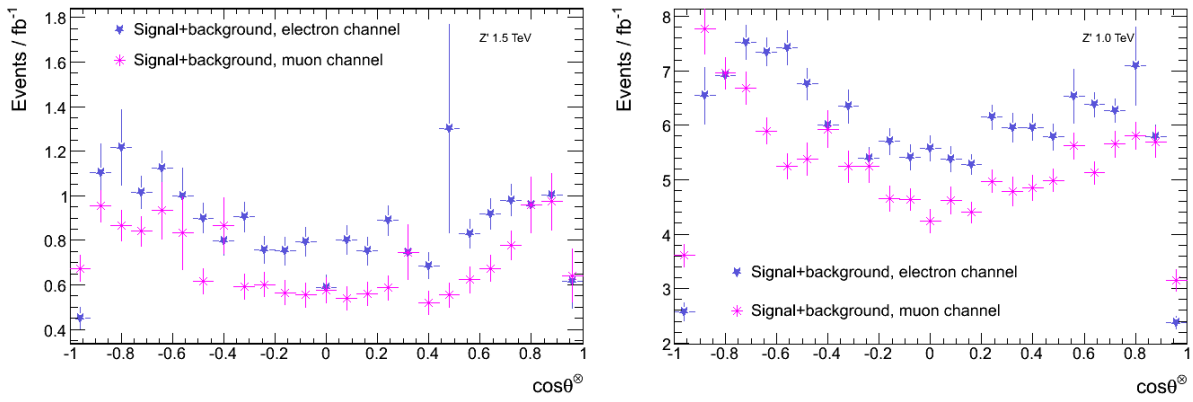

(a) Z' 1.0 TeV (b) Z' 1.5 TeV

Figure 5.35: The reconstructed angular distribution in the center of mass of the dileptons for the combined signal and background in a mass window of ±200 GeV around the resonance.

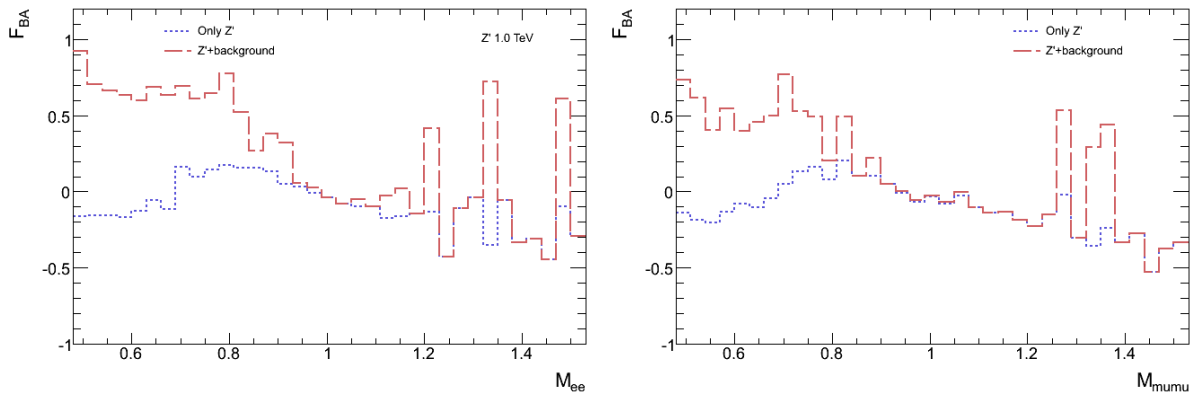

(a) Electron channel

(b) Muon channel

Figure 5.36: The reconstructed forward backward asymmetry (equation (5.2)) for signal only and background and signal.

5.8 Discovery reach

After the background reduction in the previous sections 5.5 and 5.6 we now set out to find the discovery reach.

5.8.1 Significance

In the ATLAS experiment (and in all high energy collider experiments) the probability of finding a signal in one bunch crossing is close to zero (recall figure 4.12). The nature of the signal is dependent on the search - in the case of Z', the signal is two high p_T leptons.

The probability of seeing two high p_T leptons is considered constant in time, and an event of this kind are independent of all the other events of the same kind. Hence we can consider the creation of a signal event as a Poisson process.

The creation of two high p_T electrons or muons will either happen, or not. This means that the number of such events is binomially distributed; the probability of getting k events (successes) in n trials when the probability of success is p is

$$f(k;n,p) = \frac{n!}{k!(n-k)!}p^k(1-p)^{n-k}$$

Because the probability of this happening is so small and the total number of trials is so enormous, the binomial distribution can be approximated with a Poisson distribution - the probability of getting k successes when the expectation value is λ is

$$f(k;\lambda) = \frac{\lambda^k e^{-\lambda}}{k!}$$

The expected number of events is given by theory.

All collected data from the LHC is considered as being *one* sampling from this distribution. If we expect for example 10 events and we observe 15 events, the p-value is the probability of getting the value 15 when sampling from the f(k,10) distribution. The *significance* is defined as the number of standard deviations (σ) from the mean in a standard normal distribution giving that p-value.

A significance of 3 is referred to as *evidence* and 5 as a *discovery* ("5 sigmas"). In addition to requiring 5 sigma it is customary not to claim a discovery based on a few signal events only, but wait until there are at least 10.

5.8.2 Z' discovery reach

Various formulas are used as an estimate of the significance, depending on the situation. We make use of the following expression that fits the situation with small background and large signal[38]

$$S = \sqrt{2[(s+b)\ln(1+s/b) - s]} \tag{5.10}$$

We define a *signal region* by defining a lower limit on a mass window. An upper limit is for simplicity neglected as it will not affect the result, the reason being that the cross-section falls rapidly at high masses. The lower limit is found by optimizing the significance. This results in $M_{ll} > 0.90\,\text{TeV}$ and $M_{ll} > 1.4\,\text{TeV}$ for Z' mass of 1.0 TeV and 1.5 TeV respectively using the combined electron and muon channels. Counting the events in this mass window we find the numbers quoted in table 5.21 for the expected number of events for $1\,\text{fb}^{-1}$ integrated luminosity.

Channel	Mass [TeV]	s	b	S
El	1.0	140	6.15	25.4
	1.5	20.4	0.590	10.4
Mu	1.0	119	4.02	24.6
	1.5	15.3	0.432	9.07

Table 5.21: The expected number of signal (s) and background (b) events per 1 fb^{-1} in a mass window $M_{ll} > 0.9\,\text{TeV}$ and 1.4 TeV for the 1.0 and 1.5 TeV Z' respectively. S is the significance given by equation (5.10).

We now nvert the numbers and find which integrated luminosity is needed to discover Z' of various masses via the relation $N = \sigma \times \epsilon \int Ldt$, where ϵ is an efficiency depending on the invariant mass cut and $\sigma \times \epsilon$ is the cross section. The results are listed in table 5.22. We see that we need approximately 42 pb^{-1} to achieve a 5σ discovery of a 1.0 TeV Z', or

71 pb^{-1} requiring 10 events as well, which is often used as an additional requirement. The odds get even better when combining the two search channels. About 38 pb^{-1} are required to discover a 1.0 TeV Z', and 252 pb^{-1} to discover a 1.5 TeV Z'. See figure 5.37 for a visual representation of the results.

Channel	Mass [TeV]	$\int L$dt [fb^{-1}] (S>5)	$\int L$dt [fb^{-1}] (S>5 and s>10)
El	1.0	0.0388	0.0715
	1.5	0.229	0.490
Mu	1.0	0.0414	0.0841
	1.5	0.304	0.655
Combined	1.0	0.0200	0.0386
	1.5	0.131	0.280

Table 5.22: The amount of collected data (in units of fb^{-1}) one needs to discover a Z' with mass 1.0 TeV and 1.5 TeV. The results from the two channels are also combined, improving the significance. See figure 5.37 for a visual representation of this result.

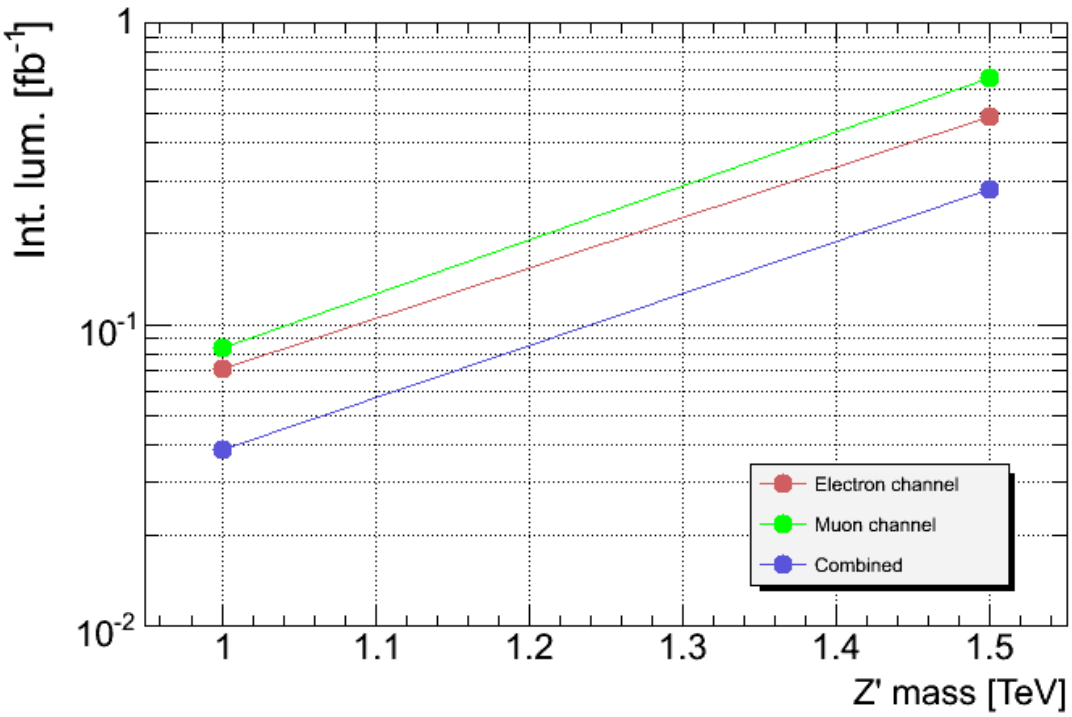

Figure 5.37: The integrated luminosity needed to discover a 1.0 and a 1.5 TeV Z'. Electron and muon channels are given in addition to the result from these channels combined.

5.9 Summary

This chapter was a feasibility study of a hypothetical new neutral gauge boson Z'at 10 TeV center of mass energy. We was how it is detected in the detector through decays to e^+e^- or $\mu^+\mu^-$ and what processes are considered as backgrounds. The topics of simulated data and particle identification are discussed brifly. Then the analysis is described, i.e. what cuts are used to remove as much as possible of the background while keeping signal events. Finally we calculate how much data needs to be collected to discover a $Z'$of mass ranging from 1.0 TeV to 1.5 TeV, the results being that 38.6 pb^{-1}(280 pb^{-1}) is needed to discover a 1.0 TeV (1.5 TeV) SSM Z'.

The ATLAS detector has been taking data from March to November 2010 at 7 TeV center of mass energy. In the next chapter we analyse this data with focus on the Z^0 resonance.

Chapter 6

Z^0 analysis on 2010 data

Before claiming any discovery of new physics it is of the outmost importance to make sure we understand the detector. It should be an easy task to rediscover the known SM particles. That is surely what is done in figure 6.1. The figure shows the di-muon invariant mass spectrum for `L1_MU10` (see section 4.3) triggered events with at least two combined (section 5.4.2) muons. The trigger itself applies a p_T threshold of approximately 10 GeV. The data used are from period A to G and constitute a total of 8.96 pb^{-1}.

Compared to official ATLAS plots (see figure C.3) we see a big difference, the Z^0 peak is much more prominent in the version showed here. The reason for this is different cuts. We require at least two combined muons with $p_T > 9$ GeV, and then combine all opposite sign dimuon candidates with $p_T > 2$ GeV each. In addition we require all events to be `L1_MU10` triggered. They require all events to be triggered by `L1_MU6`, which means they apply a p_T threshold of about 4 GeV lower then here. They require opposite sign, combined muons, but their offline p_T requirement is 4 GeV on the leading muon and 2.5 GeV on the subleading. We use 9 pb^{-1} while they use only 3 pb^{-1}, which means we have three times the statistics on the Z^0 peak.

We see multiple resonances. From left to right we have a combined ρ and ω at $\approx$ 800 MeV, ϕ at just above 1 GeV, J/ψ at a bit above 3 GeV and its first excited state, ψ', at $\approx$ 3.7 GeV. Υ shows up at just under 10 GeV, and finally the Z^0 at about 90 GeV. Comparing to table 6.1 giving the most current values[4] of the particle masses we see that the resonances in figure 6.1 show up exactly where they are expected.

Particle	Constituents	Mass [MeV]
ρ^0	$u\bar{u}$, $d\bar{d}$	775.49±0.24
ω^0	$u\bar{u}$, $d\bar{d}$	782.65±0.12
ϕ	$s\bar{s}$	1019.455±0.020
J/ψ	$c\bar{c}$	3096.916
ψ'	$c\bar{c}$	3686.09±0.04
Z^0	-	91187.6±2.1

Table 6.1: The most recent values for the resonances shown in figure 6.1[4].

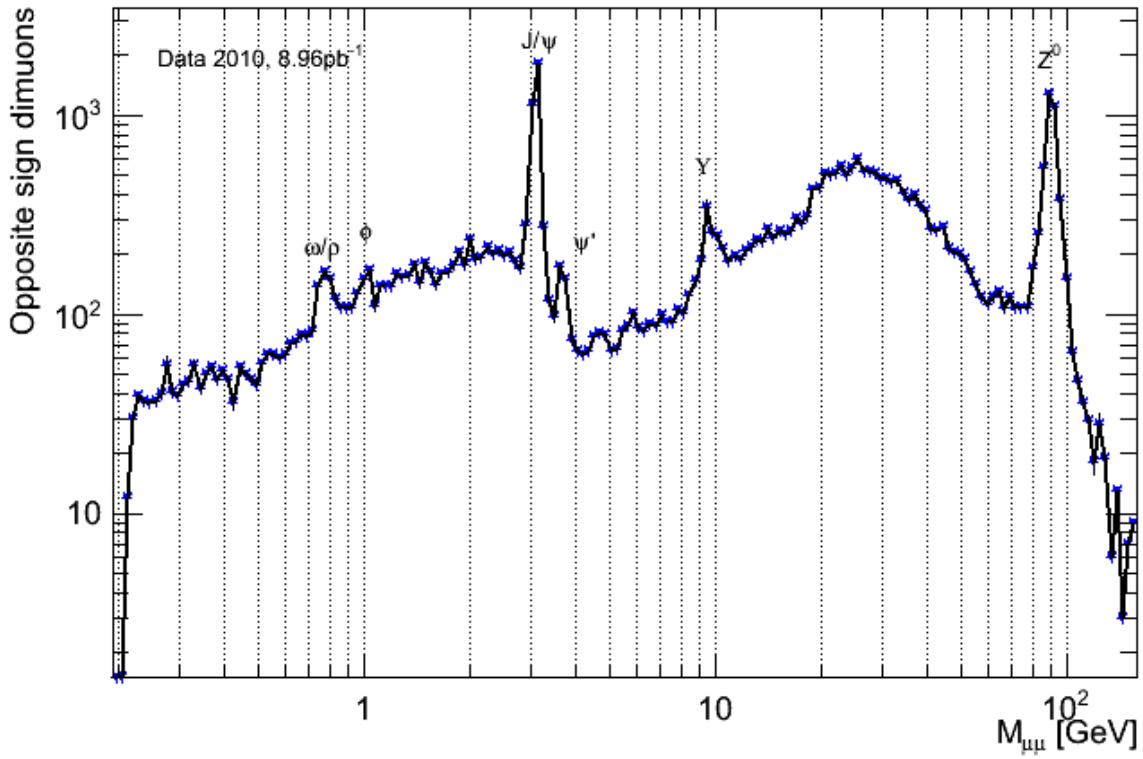

Figure 6.1: Di-muon invariant mass spectrum from the ρ^0 resonance at 800 MeV to the Z boson at 91 GeV. The data are 9 pb^{-1} of `L1_MU10` triggered events. All events are required to containt at least two combined muons with $p_T > 9$ GeV. All opposite sign muon candidates with $p_T > 2$ GeV are added to the plot.

The di-muon spectrum gives a rough insight into the performance of the detector, but we need to dig deeper. LEP measured the Z^0 properties to a very high degree of accuracy. Because we believe we know the mass and width of the SM Z boson so well, we can use it to not only check the performance of the detector, but also *calibrate* it. For example if the Z^0 mass is a bit off, then there is probably something that needs tuning (see section 6.3.1).

With this in mind we will now take a look at the Z^0 resonance. This analysis follows the cuts used in reference [39].

6.1 MC datasets for signal and background

The background sources for the Z^0 signal are the same as for the Z', except that, due to the lower mass of the Z^0, the background rate is larger. We have not considered all of them here, only the main ones (when comparing to data later we will see that we are not mistaken in doing so). The backgrounds considered are W+jets, $Z^0 \rightarrow \tau\tau$, $t\bar{t}$ and QCD dijets[1], see section 5.2, and the actual background samples as well as some information are listed in table 6.3.

As we noted in the 10 TeV analysis (section 5.3.3) the cross-section of some of the processes are huge in comparison to the number of generated events. For example in 40 pb^{-1} of data we expect 4×10^{11} J0 events (dijets events with little energy transfer between the partons), and the number of generated events is only 1.4×10^6. Data driven methods are usually applied to estimate the dijet background. This is not done here.

The Alpgen Z^0/γ datasets were added for the sole purpose of being a low mass sample. Pythia Z^0/γ is divided into 11 mass bin samples, ranging from 75 GeV to 2000+ GeV. Alpgen has an invariant mass cut $M_{ll} > 60\,\text{GeV}$ at generation level and we added an invariant mass cut of $M_{ll} < 75\,\text{GeV}$.

Except for datasets generated by MC@NLO, the cross-sections are calculated to leading order[2] at generation time. Wherever next to next to leading order (NNLO) cross-section are stated, k-factors are used. The k-factor used for the Pythia Z^0/γ samples with mass bins are mass dependent and given in table 6.2. For the remaning samples with NNLO cross-section, a flat k-factor was used[39].

6.2 Event selection

All data were taken at a center of mass energy of 7 TeV between April and November 2010 (period A to I), giving a grand total of 39.0 pb^{-1} in the electron channel and 41.8 pb^{-1} in

[1]Only the J0 to J6 are considered as the cross-sections for J7 and J8 (which have the highest momentum transfer in the hard scattering of the partons involved) are so low that less than one event is expected for $40\,\text{pb}^{-1}$.

[2]Pythia adds a few important NLO effects, but the cross-section is still considered to be leading order accuracy.

Mass bin [GeV]	K-factor
75-120	1.155
120-250	1.150
250-400	1.114
400-600	1.086
600 - 800	1.054
800-1000	1.029
1000-1250	0.997
1250 -1500	0.951
1500-1750	0.891
1750-2000	0.825

Table 6.2: (http://www-personal.umich.edu/∼qianj/DrellYanStudySlides.pdf)

the muon channel.

We will now go through the event selection. This is common for both channels. Table 6.4 gives a quick overview of the requirements. Unless steted otherwise, all plots are normalized to the cross-section.

6.2.1 MET cleaning

Analysis of minimum bias events[40] showed that data are sometimes contaminated with very localized high-energy calorimeter deposits that do not come from the collision of protons, but rather from beam-gas collisions (collision of one proton beam with gas coming from the imperfect vacuum in the beam pipe), muons or pions travelling in the halo of the beam (beam halo events, where an outlier particle hits some part of the detector) or from cosmic ray muons emitting bremsstrahlung. To reject events like these, dedicated cleaning requirements are used (cutting away events that are not well timed with collision events). It has been shown in Monte Carlo simulations that these cleaning cuts remove $< 0.1\%$ of minimum-bias events, 0.004% of $W \to l\nu_l$ and 0.01% of dijet events.

In addition to the cosmic cleaning there are cleaning requirements that remove noise from both the electromagnetic calorimeter and the end-cap of the hadronic calorimeter. Jets with an electromagnetic fraction over 95% and a jet quality[3] of more than 0.8 are considered noise in the ECAL. Jets with over 80% of their energy in the hadronic end-cap that deposit 90% of their energy in less than 6 cells, are considered noise in the hadronic end-cap.

[3]The fraction of LAr cells that have a so-called Q-factor larger than 4000. The Q-factor is a measure of the difference between the measured and the expected pulse shape. See https://twiki.cern.ch/twiki/bin/view/AtlasProtected/HowToCleanJets#Bad_jets

Dataset	Dataset number	Generator	Recon.tag	No. of MC events	Cross-section $\sigma \times \epsilon$ [fb]
Signal datasets					
$Z' \to ee, \quad m'_Z = 2.0$TeV	105409	Pythia	r1303_r1306	19998	2.55284 (LO)
$Z' \to ee, \quad m'_Z = 1.75$TeV	105554	Pythia	r1303_r1306	19997	5.9892 (LO)
$Z' \to ee, \quad m'_Z = 1.5$TeV	105624	Pythia	r1303_r1306	19996	15.3947 (LO)
$Z' \to ee, \quad m'_Z = 1.25$TeV	105549	Pythia	r1303_r1306	19997	40.9309 (LO)
$Z' \to ee, \quad m'_Z = 1.0$TeV	105603	Pythia	r1303_r1306	19995	129.074 (LO)
$Z' \to \mu\mu, \quad m'_Z = 2.0$TeV	105349	Pythia	r1303_r1306	19998	2.57953 (LO)
$Z' \to \mu\mu, \quad m'_Z = 1.75$TeV	105544	Pythia	r1303_r1306	19995	6.00179 (LO)
$Z' \to \mu\mu, \quad m'_Z = 1.5$TeV	105625	Pythia	r1303_r1306	19995	15.0779 (LO)
$Z' \to \mu\mu, \quad m'_Z = 1.25$TeV	105534	Pythia	r1303_r1306	19995	41.8832 (LO)
$Z' \to \mu\mu, \quad m'_Z = 1.0$TeV	105601	Pythia	r1303_r1306	19996	128.932 (LO)
Background datasets					
$Z^0/\gamma \to ee, \quad 75 < M_{ee} < 120$GeV	105466	Pythia	r1303_r1306	19990	948000 (NNLO)
$Z^0/\gamma \to ee, \quad 120 < M_{ee} < 250$GeV	105467	Pythia	r1303_r1306	19998	9990 (NNLO)
$Z^0/\gamma \to ee, \quad 250 < M_{ee} < 400$GeV	105468	Pythia	r1303_r1306	19997	461 (NNLO)
$Z^0/\gamma \to ee, \quad 400 < M_{ee} < 600$GeV	105469	Pythia	r1303_r1306	19999	72.9 (NNLO)
$Z^0/\gamma \to ee, \quad 600 < M_{ee} < 800$GeV	105470	Pythia	r1303_r1306	19998	11.8 (NNLO)
$Z^0/\gamma \to ee, \quad 800 < M_{ee} < 1000$GeV	105471	Pythia	r1303_r1306	19998	2.8 (NNLO)
$Z^0/\gamma \to ee, \quad 1000 < M_{ee} < 1250$GeV	105472	Pythia	r1303_r1306	19995	0.912 (NNLO)
$Z^0/\gamma \to ee, \quad 1250 < M_{ee} < 1500$GeV	105473	Pythia	r1303_r1306	19998	0.235 (NNLO)
$Z^0/\gamma \to ee, \quad 1500 < M_{ee} < 1750$GeV	105474	Pythia	r1303_r1306	19999	0.0687 (NNLO)
$Z^0/\gamma \to ee, \quad 1750 < M_{ee} < 2000$GeV	105475	Pythia	r1303_r1306	19997	0.0217 (NNLO)
$Z^0/\gamma \to ee, \quad 2000 < M_{ee}$GeV	105476	Pythia	r1303_r1306	19995	0.015 (NNLO)
$Z^0/\gamma \to ee, \quad 75 < M_{\mu\mu} < 120$GeV	105477	Pythia	r1303_r1306	19994	948000 (NNLO)
$Z^0/\gamma \to \mu\mu, \quad 120 < M_{\mu\mu} < 250$GeV	105478	Pythia	r1303_r1306	19996	9990 (NNLO)
$Z^0/\gamma \to \mu\mu, \quad 250 < M_{\mu\mu} < 400$GeV	105479	Pythia	r1303_r1306	19997	461 (NNLO)
$Z^0/\gamma \to \mu\mu, \quad 400 < M_{\mu\mu} < 600$GeV	105480	Pythia	r1303_r1306	19996	72.9 (NNLO)
$Z^0/\gamma \to \mu\mu, \quad 600 < M_{\mu\mu} < 800$GeV	105481	Pythia	r1303_r1306	19993	11.8 (NNLO)
$Z^0/\gamma \to \mu\mu, \quad 800 < M_{\mu\mu} < 1000$GeV	105482	Pythia	r1303_r1306	19946	2.8 (NNLO)
$Z^0/\gamma \to \mu\mu, \quad 1000 < M_{\mu\mu} < 1250$GeV	105483	Pythia	r1303_r1306	19992	0.912 (NNLO)
$Z^0/\gamma \to \mu\mu, \quad 1250 < M_{\mu\mu} < 1500$GeV	105484	Pythia	r1303_r1306	19995	0.235 (NNLO)
$Z^0/\gamma \to \mu\mu, \quad 1500 < M_{\mu\mu} < 1750$GeV	105485	Pythia	r1303_r1306	19987	0.0687 (NNLO)
$Z^0/\gamma \to \mu\mu, \quad 1750 < M_{\mu\mu} < 2000$GeV	105486	Pythia	r1303_r1306	19991	0.0217 (NNLO)
$Z^0/\gamma \to \mu\mu, \quad 2000 < M_{\mu\mu}$GeV	105487	Pythia	r1303_r1306	19990	0.015 (NNLO)
$Z^0/\gamma \to ee, \quad M_{ee} > 60$GeV	106046	Pythia	r1303_r1306	2488763	989000 (NNLO)
$Z^0/\gamma \to \mu\mu, \quad M_{\mu\mu} > 60$GeV	106047	Pythia	r1303_r1306	2499086	989000 (NNLO)
$Z^0/\gamma \to ee$, 0 jets	107650	Alpgen	r1303_r1306	304216	857.6e3 (NNLO)
$Z^0/\gamma \to ee$, 1 jets	107651	Alpgen	r1303_r1306	63440	150.2e3 (NNLO)
$Z^0/\gamma \to ee$, 2 jets	107652	Alpgen	r1303_r1306	19497	45.4e3 (NNLO)
$Z^0/\gamma \to ee$, 3 jets	107653	Alpgen	r1303_r1306	5499	14.3e3 (NNLO)
$Z^0/\gamma \to ee$, 4 jets	107654	Alpgen	r1303_r1306	1499	3.73e3 (NNLO)
$Z^0/\gamma \to ee$, 5 jets	107655	Alpgen	r1303_r1306	500	0.971e3 (NNLO)
$Z^0/\gamma \to \mu\mu$, 0 jets	107660	Alpgen	r1303_r1306	303947	856.3e3 (NNLO)
$Z^0/\gamma \to \mu\mu$, 1 jets	107661	Alpgen	r1303_r1306	62996	171.6e3 (NNLO)
$Z^0/\gamma \to \mu\mu$, 2 jets	107662	Alpgen	r1303_r1306	18993	52.1e3 (NNLO)
$Z^0/\gamma \to \mu\mu$, 3 jets	107663	Alpgen	r1303_r1306	5497	14.4e3 (NNLO)
$Z^0/\gamma \to \mu\mu$, 4 jets	107664	Alpgen	r1303_r1306	1499	3.74e3 (NNLO)
$Z^0/\gamma \to \mu\mu$, 5 jets	107665	Alpgen	r1303_r1306	499	0.977e3 (NNLO)
$Z^0/\gamma \to \tau\tau$, 0 jets	107670	Alpgen	r1303_r1306	303359	854.6e3 (NNLO)
$Z^0/\gamma \to \tau\tau$, 1 jets	107671	Alpgen	r1303_r1306	63481	172.7e3 (NNLO)
$Z^0/\gamma \to \tau\tau$, 2 jets	107672	Alpgen	r1303_r1306	19492	52.0e3 (NNLO)
$Z^0/\gamma \to \tau\tau$, 3 jets	107673	Alpgen	r1303_r1306	5497	14.2e3 (NNLO)
$Z^0/\gamma \to \tau\tau$, 4 jets	107674	Alpgen	r1303_r1306	1499	3.6e3 (NNLO)
$Z^0/\gamma \to \tau\tau$, 5 jets	107675	Alpgen	r1303_r1306	499	1.26e3 (NNLO)
$J0$	105009	Pythia	r1303_r1306	1.40e6	9.753e12 (LO)
$J1$	105010	Pythia	r1303_r1306	1.40e6	673.0e9 (LO)
$J2$	105011	Pythia	r1303_r1306	1.40e6	41194.7e6 (LO)
$J3$	105012	Pythia	r1303_r1306	1.40e6	2193.25e6 (LO)
$J4$	105013	Pythia	r1303_r1306	1.40e6	87.85e6 (LO)
$J5$	105014	Pythia	r1303_r1306	1.39e6	2.32856e6 (LO)
$J6$	105015	Pythia	r1303_r1306	1.35e6	33.8461e3 (LO)
$t\bar{t}$ (leptonic)	105200	MC@NLO	r1303_r1306	999387	80.031e3 (NLO)
$t\bar{t}$ (hadronic)	105204	MC@NLO	r1303_r1306	149899	64.169e3 (NLO)
$WW \to l\nu_l + X$	105985	Herwig	r1303_r1306	249837	11.50e3 (LO)
$ZZ \to l^+l^- + X$	105986	Herwig	r1303_r1306	249725	0.976e3 (LO)
$WZ \to l + X$	105987	Herwig	r1303_r1306	249830	3.48e3 (LO)
$W \to e\nu_e +$ jets	106043	Pythia	r1303_r1306	2.49e6	10454.0e3 (NNLO)
$W \to \mu\nu_\mu +$ jets	106044	Pythia	r1303_r1306	2.50e6	10454.0e3 (NNLO)
$W \to \tau\nu_\tau +$ jets	106022	Pythia	r1303_r1306	999874	10454.0e3 (NNLO)

Table 6.3: The Monte Carlo datasets used in this analysis. "LO" means the cross-section is leading order, "NLO" next-to-leading order and "NNLO" next to next-to-leading order.

#	Cut	Notes
0	Skimming	At least 2 loose electrons with $E_T > 10$ GeV, author 1 or 3 or at least 2 combined muons with $p_T > 10$ GeV
1	GRL	Using only runs flagged as good for physics
2	Good PV	At least one good primary vertex (PV) (longitudinal coordinate no more than 15 cm from nominal interaction point and at least three tracks)
3	Trigger	Event must be triggered. Table 6.5 gives the triggers used.
4	MET Cleaning	Removing cosmics and noise in the calorimeters

Table 6.4: Event selection for Z^0 analysis. These requirements are used for both channels (electron and muons). For electron (muon) selection, see table 6.6 (6.8). Author 1 or 3 means reconstructed by the calorimeter-seeded algorithm, see section 5.4.1). Combined muons are defined in section 5.4.2

6.2.2 Primary vertex

Only collisions having at least one good primary vertex are selected. A primary vertex is considered "good" if it has at least three tracks associated with it (to help reject cosmics), and it is no further away in the longitudinal (z) direction from origo than 15 cm[4].

6.2.3 Good Runs List

Only runs for which LHC declared stable beams are used. In addition only lumi blocks[5] flagged for "physics" are considered. This data quality requirement is executed by the Good Run Lists (GRLs, for completeness we use WZ GRLs). They are based on data quality (DQ) status flags, which are indicators of data quality. DQ flags are set by each sub-detector and the combined performance groups on every luminosity block in every run.

There are multiple levels of flags. The lowest one is filled automatically and is based on detector control conditions (DCS), including parameters such as temperature and humidity. Higher levels include which detectors and magnets are on during a run, if the triggers are working, etc.

6.2.4 Trigger

All events are required to be triggered. Whenever possible an unprescaled trigger is used, and one typically goes for the unprescaled trigger with the highest rate so as to keep as many

[4]The RMS of this distribution is 6.2 cm. It is not as odd as it sounds, in fact, that the collision happens so far from the nominal position. What collides is in fact long bunches of protons, much longer in the z-direction than in the transverse plane.

[5]A lumi(nosity) block (also know as LB) is a time interval over which the luminosity can be considered to be constant

of the interesting events as possible. The triggers used in the analyses of chapters 6 and 7 are listed in table 6.5.

	Period	Trigger
El	A-E8	L1_EM14
	E9-I	EF_e20_loose
	MC	L1_EM14
Mu	A-E4	L1_MU10
	E5-G5	EF_mu10
	G6-I1	EF_mu13
	I1-I2	EF_mu13_tight
	MC	L1_MU10

Table 6.5: The triggers used in the electron and muon channels and in MC. For general information on triggers, see section 4.3.

The number in the trigger gives the nominal threshold in GeV. All the triggers used here require only one electron or muon. General information on triggers is given in section 4.3.

6.3 Lepton selection

After the initial event selection, we go on to selecting good electron and muon candidates.

6.3.1 Electron selection

In all calculations and cuts involving electrons, the calo cluster variables are used (E_{cl}, $E_{T,\mathrm{cl}}$, η_{cl}, ϕ_{cl}), except in the calculation of invariant mass M_{ee} where we use calo cluster energy and track quantities to define direction. This is according to the ATLAS SM working group recommendations.

We will now go through the cuts used on all electron candidates. Table 6.6 gives a quick overview of these.

Electron candidates are required to be identified as "medium" (see section 5.4.1)[6], which is what is agreed on in the SM working group within ATLAS, have a ECAL cluster energy of at least 20 GeV, $E_T > 20$GeV, have author 1 or 3 (see section 5.4.1), and are within the geometrical acceptance, $|\eta| < 2.47$, but excluding the crack, $1.37 < |\eta| < 1.52$. These requirements are basic and need no further explanation.

[6]This is in reality a new definition, called "robust medium". It is equal to the medium definition except for different (looser) values on two of the cut variables. The reason for redefining this identification variable was that some of its components were badly simulated. See appendix C.1.

#	Cut	Notes
5	Electron author	Author 1 or 3
6	η	η within the geometrical acceptance, $\|\eta\| < 2.47$, but excluding the crack $1.37 < \|\eta\| < 1.52$
7	p_T	p_T at least 20 GeV
8	OTx	Not located in a dead region of the ECAL
9	Electron ID	Identified as "medium"
10	# of electrons	Exactly 2 electrons
11	Charge	Opposite charge electrons
12	Invariant mass	At the Z^0 peak, $66\,\text{GeV} < M_{ee} < 116\,\text{GeV}$

Table 6.6: All electron candidates are required to pass the cuts 5 up to and including 9. Events are required to pass cuts 10 up to and including 12. All events have passed the event selection as listed in table 6.4.

Object Quality Maps - OTx cut

Due to dying optical readout links, non-nominal high voltage on modules, etc, we make use of so-called Object Quality (OQ) Maps in the electron channel. They are essentially maps in ϕ and η showing the bad areas of the calorimeter. If an electron candidate passing the author and medium cuts is located in any of these regions, it is rejected.

One might imagine that this cut is best placed at the end when one is left with exactly two medium electrons. Employing the cut at this point in time would ensure that the event as a whole was cut. Using this cut (OTx) as a part of the electron selection on the other hand, might give unwanted results. Consider the following: after all selection cuts (but before requiring exactly two) are made we are left with three good electrons. Two of these are from the Z^0, one comes from another process. If one of the electrons from the Z^0 happens to be in a dead zone of the ECAL and the two other electrons pass the OTx cut, we will end up combining one electron from the Z^0 and one from another source. We estimate the probability of this happening to be very small (confirmed by the electron multiplicity distribution in figure 6.2), and will therefore use this cut as part of the electron selection, which is also what is usually done within the ATLAS EGamma working group.

ECAL calibration

It became clear that the ECAL was not properly calibrated. When looking at the Z^0 peak, it was shifted towards lower energies, i.e. the Z^0 mass was found to be a bit low, about 89 GeV. To correct for this, the energy of the electrons as measured in the calorimeter is adjusted, $\text{E} \rightarrow \text{E}/(1+\alpha)$, where α takes on different values in the barrel and end-caps, see table 6.7.

	α_{B}	α_{EC}
Value	-0.0096	0.0189

Table 6.7: The ECAL is calibrated in a less than perfect way. The electron energy must be modified by a factor $1/(1+\alpha)$. The value of α is different in the endcaps (EC) and in the barrel (B).

Electron multiplicity

Furthermore, events containing more than two medium electrons are vetoed. Figure 6.2 shows the lepton multiplicity (for values larger than 1). In comparison to keeping all events with two or more electrons, this cut rejects 0.33% of total SM background and keeps 99.9% of data and DY MC.

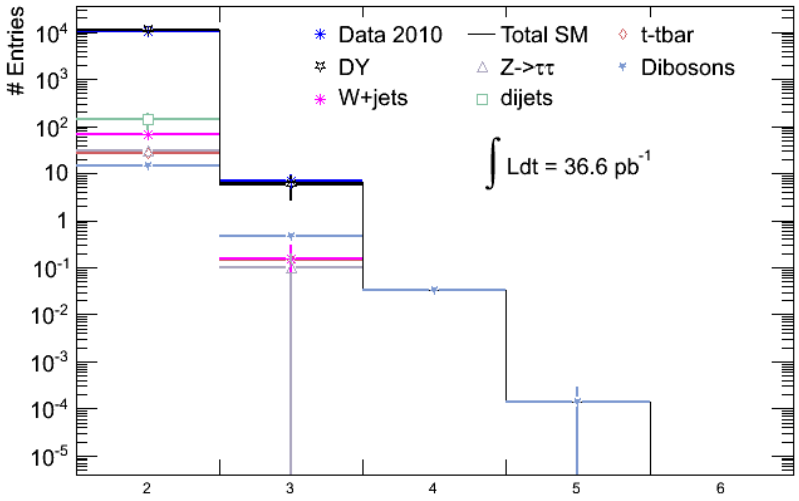

Figure 6.2: The electron multiplicity distribution for values larger than 1. Only events with exactly two electrons are used in the Z^0 analysis.

Charge

Leptons coming from the neutral Z^0 have opposite charge, and an opposite charge requirement arises rather naturally. Before it is imposed it is important to check how large the charge misidentification in the inner detector is in the relevant mass range.

To check this we use Z^0 simulated data and the truth information. The two highest p_T reconstructed electrons (passing all Z^0 cuts up to and including number 9, see table 6.9) are matched with a truth particle by a simple truth matching algorithm checking if their separation in the η-ϕ plane, ΔR, is less than 0.2. For more information on this, see appendix C.2. If the reconstructed lepton has the opposite charge of the corresponding truth lepton, it is tagged as charge misidentified.

Figures 6.3(a) and 6.3(b) shows the number of electrons with wrong charge compared to the corresponding truth particle and the ratio of these numbers as a function of p_T and η respectively. Note that only dielectrons with invariant masses between 66 GeV and 116 GeV are considered. We see that the charge misidentification seems to get higher with growing p_T, which is what we expect (higher p_T means larger bending radius, which means it is more likely to misidentify the charge). We also see that the probability to misidentify the charge is η dependent - it is close to zero at $\eta = 0$ and grows to 10% at high $|\eta|$. This is also according to expectations (the bending power decreases as with increasing η, which means that tracks at larger η bend less, and also there are more material in the ID in the forward regions). The mean charge misidentification ratio is 1.6% for single electrons.

Figure 6.4 shows the number of opposite and same sign dielectron pairs as a function of M_{ee}, and the ratio of these. Because of the correlation between p_T and invariant mass it comes as no surprise that the charge misidentification grows with growing invariant mass. The total misidentification is 3.1%. The higher value here is obviously because there are *two* electrons that each have 1.6% probability of being measured with the wrong charge - $2 \cdot 0.016 \cdot (1 - 0.016) = 0.031$.

Figure 6.5 shows the number of events after cuts 1 to 9 (table 6.9) with opposite and same sign dielectrons. Requiring opposite charge electrons cuts away 5.5% of data events. According to MC it rejects 28.6% of the total SM background and keeps 97.0% of the DY.

6.3.2 Muon selection

In all calculations and cuts involving muons we use the p_T measurement from the MS only p_T^{ME} (where "ME" means the MS measurement extrapolated to the perigee) and otherwise the combined variables. This is what is agreed upon within the dilepton working subgroup in ATLAS.

We will now go through the muon selection used in the Z^0 analysis. Table 6.8 gives an overview of the cuts used.

First of all, muons are required to be combined (to reduce the rate of fake muons from decay of particles like pions or punch through) and to have $p_T > 20\,\mathrm{GeV}$ and $|\eta| < 2.4$.

The p_T resolution of the muon system is a bit worse than expected, leading to a narrower p_T distribution in simulated data than what is observed in real data. To resolve this problem within the current release of simulated data the p_T measurement in the MS is smeared. The exact formula used is

$$q/p_{T,\mathrm{smeared}} = q/p_T + q/p_T \cdot 0.02 \cdot X_1 + 0.13 \times 10^{-6} \cdot X_2 \tag{6.1}$$

where X_1 and X_2 are two independent random numbers drawn from the standard normal distribution, N(0,1).

The requirement on the transverse momentum is set at 20 GeV because at lower values of the p_T the background is large and not well understood. The requirement on η is to ensure that

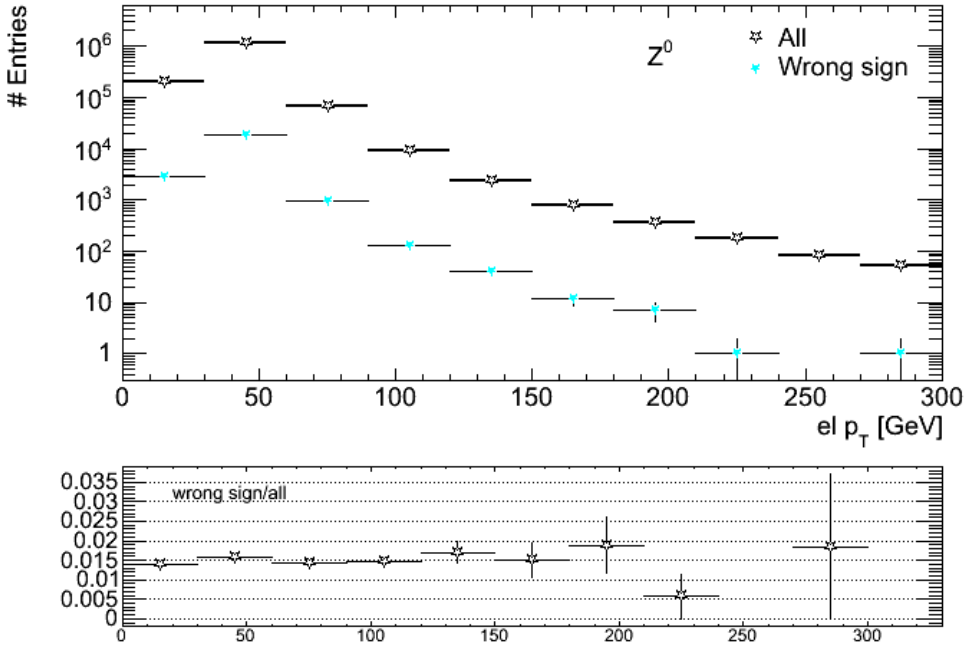

(a) Charge misidentification as a function of p_T

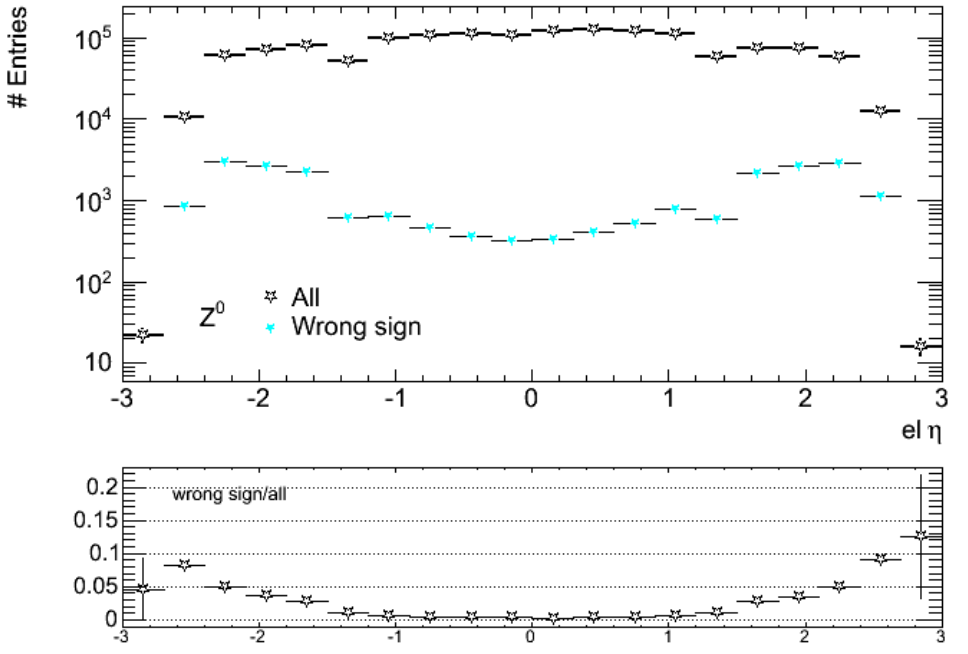

(b) Charge misidentification as a function of η

Figure 6.3: The charge misidentification of electrons as a function of p_T (top) and η (bottom). Plotted are the total number of truth-matched reconstructed electrons and the number that have opposite charge compared to the truth electron. The mean charge misidentification ratio is 1.6% for a single electron

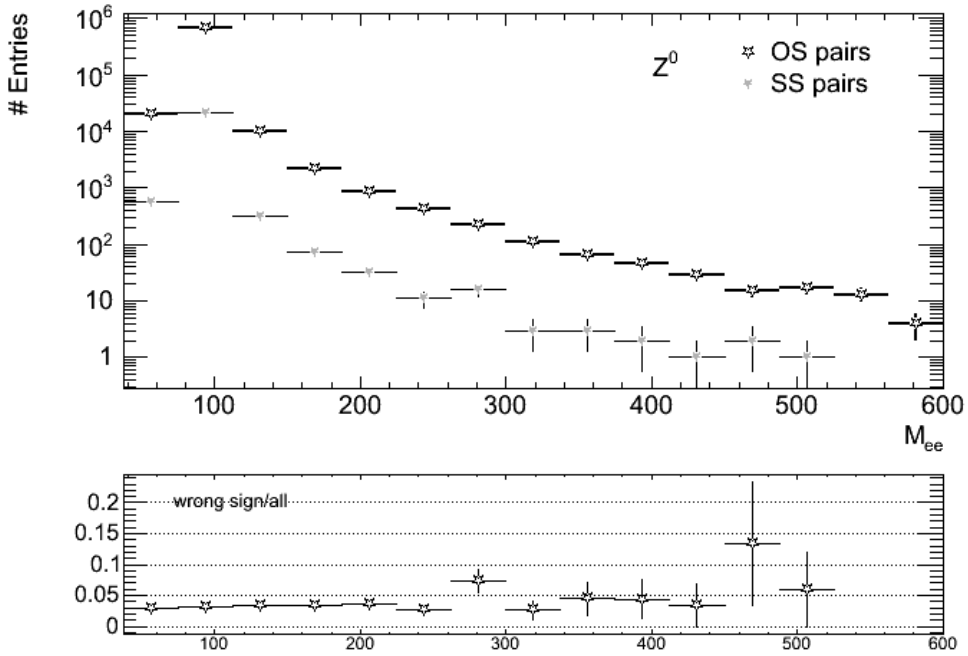

(a) Charge misidentification as a function of M_{ee}

Figure 6.4: The charge misidentification of dielectrons as a function of M_{ee}. The plot shows the total number of truth-matched reconstructed dielectrons and the number of events where the dielectrons have same charge. The mean charge misidentification ratio is 3.1%.

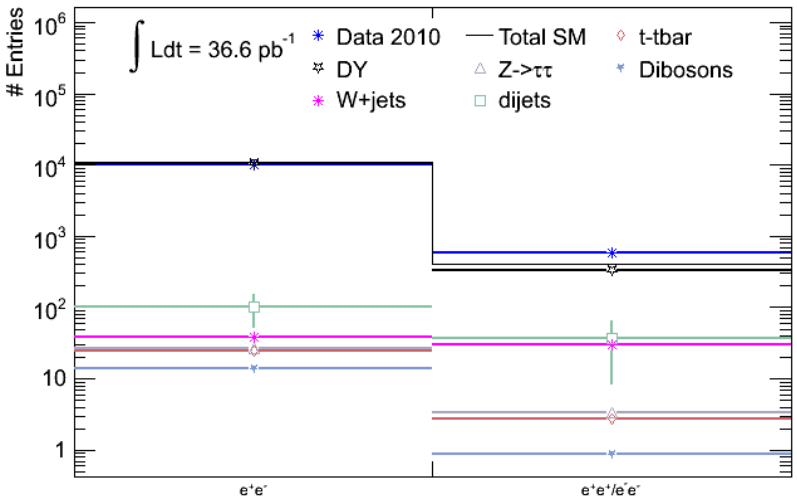

Figure 6.5: The number of events in data and MC containing opposite and same sign dielectrons.

#	Cut	Notes
5	p_T and η	p_T above 20 GeV, within $\eta < 2.4$
6	Combined	Combined muon (see section 5.4.2 for more information)
7	p_T difference	Difference in p_T measurement in inner detector and muon spectrometer (extrapolated to ID) less than 15 GeV, $\lvert p_T^{\mathrm{ID}} - p_T^{\mathrm{ME}} \rvert < 15$ GeV
8	z_{PV} difference	Difference in z coordinate of primary vertex and muon track extrapolated to the beam line less than 1 cm, $\lvert \Delta z_{\mathrm{PV}} \rvert < 1$ cm
9	MS track	Track in MS with at least 10 GeV, $p_T^{\mathrm{MS}} > 10$ GeV
10	Isolation	Normalized p_T-cone40 less than 0.2, $p_T^{\Delta R<0.4} < 0.2$
11	Charge	Opposite charge
12	Invariant mass	At the Z^0 peak, $66\,\mathrm{GeV} < M_{\mu\mu} < 116\,\mathrm{GeV}$

Table 6.8: All muon candidates are required to pass the cuts listed here. All events have passed the event selection as listed in table 6.4.

the muons are within the geometrical acceptance of the detector. Using combined muons (see section 5.4.2) is a way of reducing the contribution from fake muons (both from highly energetic jets and from heavy flavour decay) - a real muon should leave a track in the inner detector as well as in the muon system.

There is no cut on the χ^2 at this point. The muons with badly matched tracks will be cut away later using cuts on the differences in p_T (see next subsection) and the longitudinal position of the primary vertex as measured in the ID and extrapolated to the beam line (see section 6.3.2).

p_T difference in ID and MS

The difference in the measured p_T in the inner detector and muon spectrometer (taking into account the energy loss of the muon going through the detector, which is of order 3 GeV) is required to be less than 15 GeV,

$$\left| p_T^{\mathrm{ID}} - p_T^{\mathrm{MS,\ extrapolated}} \right| < 15 \text{ GeV}$$

This cut is meant to help ensure the combination of the right tracks (to avoid combining tracks in the MS and ID from two different particles). Figure 6.6 shows a plot of this difference. The agreement between data and MC is quite good. The distribution seems narrower in MC than in data, also after the p_T smearing. The dominant contribution is from DY. The agreement between data and MC is quite good as it is, but we suspect it would be even better with a data driven QCD background estimation.

A cut of 15 GeV keeps 97.3% of the muons in the data stream. According to MC, only 1.4% of muons coming from the Z^0 are rejected. From the cut flow table 6.10 we see that 93.2%

of the events are left after requiring at least two muons with a p_T difference less than 15 GeV. The reason for the big difference in the numbers 93.2% and 97.6% is that we require at least two muons when counting the number of $Z^0 \to \mu^+\mu^-$ candidate events.

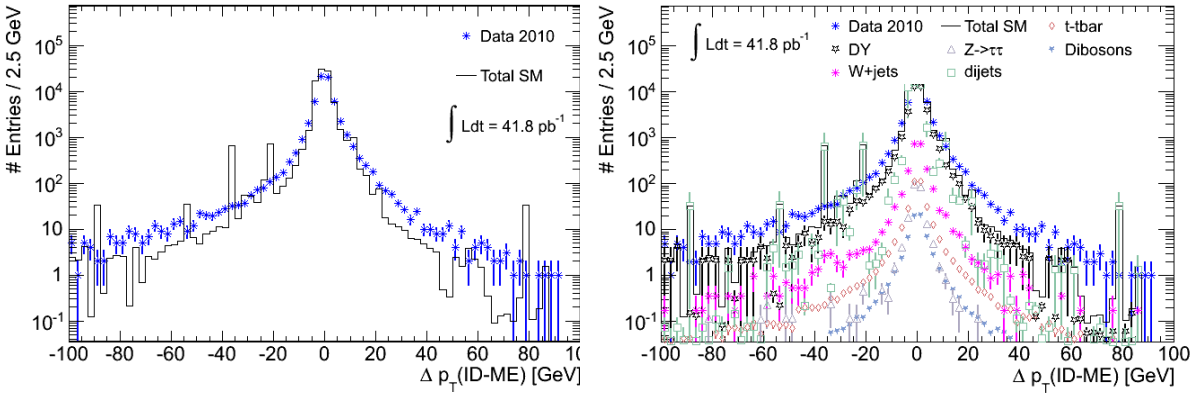

(a) Total SM and data

(b) SM contributions and data

Figure 6.6: The difference $\Delta p_T(|\mathrm{ID} - \mathrm{ME}|)$ All muons are required to be combined and to have a p_T of at least 20 GeV and $|\eta| < 2.4$ (cuts 1 up to and including 6 in table 6.8).

Primary vertex

To reject muons that do not originate from the primary vertex, like cosmic muons, a cut is applied on the difference Δz_{PV} in the z-component of the primary vertex and the muon track extrapolated to the beam line. This difference is required to be less than 1 cm.

In addition to rejecting the events from cosmics, this cut also ensures that all muons come from the *same* primary vertex. This is an issue from this point in time (October 2010 with ($\mathcal{L} \approx 10^{32}\,\mathrm{cm}^{-2}\mathrm{s}^{-1}$), with 3.8 events on average (each giving one primary vertex) per collision.

Figure 6.7 shows the Δz_{PV} distribution for combined muons with $p_T > 20$ GeV, $|\eta| < 2.4$ and $|\Delta p_T\,(\mathrm{ID} - \mathrm{ME})| < 15$ GeV. 99.6% of the muons in real data are within $|\Delta z_{\mathrm{PV}}| < 1$ cm. DY peaks at zero as expected. Over the whole range, QCD is dominating. The shape of the distribution seems to fit quite nicely with MC, especially if we overlook the QCD MC fluctuations due to a lack of statistics. As before we suspect that data driven QCD estimation would improve the situation.

Nearly 100% of the SM background and DY MC remain after the cut. From the cut flow table 6.10 we see that 0.5% of the total candidate $Z^0 \to \mu\mu$ events are rejected by this cut when also requiring at least two muons.

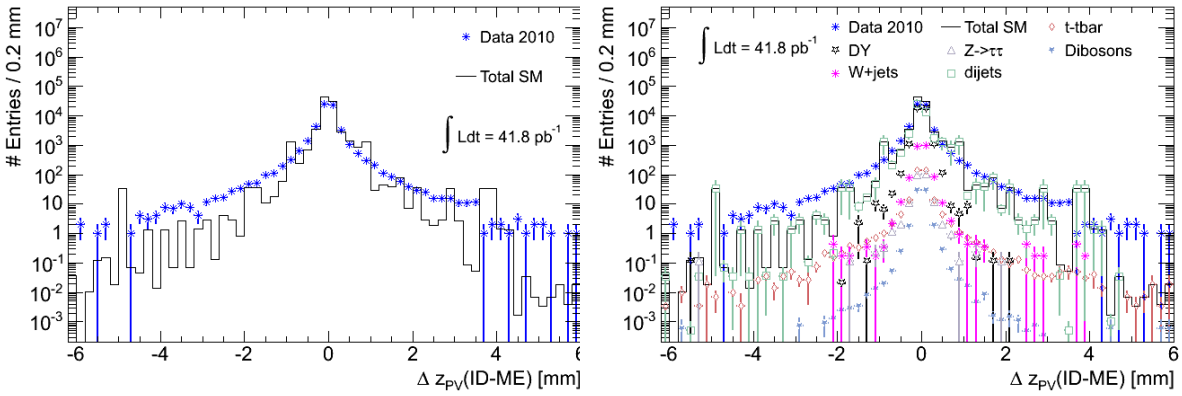

(a) Total SM and data

(b) SM contributions and data

Figure 6.7: The difference in the z-position of the primary vertex and the muon track extrapolated to the beam line. All combined muon candidates are required to have a p_T of at least 20 GeV, $|\eta| < 2.4$, and $\Delta p_T(|\mathrm{ID} - \mathrm{ME}|) < 15\,\mathrm{GeV}$ (cuts 1 up to and including 7 in table 6.8).

MS track

Furthermore, muons are required to have a muon spectrometer track with a p_T of at least 10 GeV. We already require all muons to have a p_T of at least 20 GeV (measured at the perigee) and this cut aims at removing events that are assigned a p_T in the MS at least 10 GeV less than the p_T at perigee.

Figure 6.8 shows this distribution. Data/MC agreement is quite good. Still the agreement would be better with a data driven QCD estimate in the regions where the QCD contribution is large. All muons pass this cut, and from the cut flow table 6.10 we see that all data events remain as well.

Isolation

The muon isolation cut used is defined as follows: the sum of p_T of all the tracks in a cone in η-ϕ ($\Delta R < 0.4$) normalized to the muon p_T should be less than 0.2, that is $p_T^{\Delta R<0.4}/p_T < 0.2$.

The distribution for the normalized p_T-cone is shown in figure 6.9 for all muons that passed all the previuos cuts. DY is the dominant contribution at $p_T^{\Delta R<0.4}/p_T$ approximately smaller than 0.1. Above that the dijet background dominates completely.

Cutting on 0.2 rejects 36.6% of all muons from data. Looking at DY MC we see that 99.4% of all muons from the Z^0 remain after the cut, while 64.2% of all background events are rejected. From table 6.10 we see that 15.1% of data events are rejected.

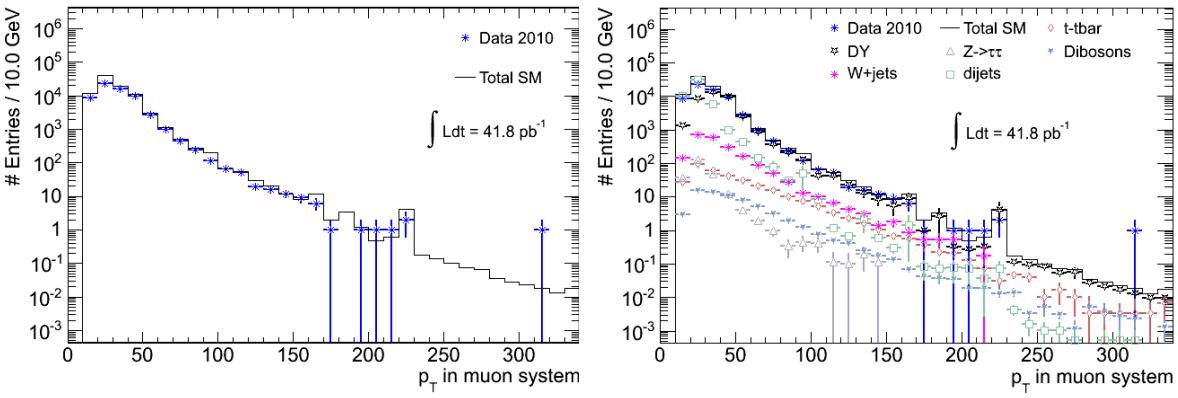

(a) Total SM and data

(b) SM contributions and data

Figure 6.8: The p_T of the combined muon track in the muon system requiring all combined muon candidates to have a p_T of at least 20 GeV, $|\eta| < 2.4$, having $\Delta p_T(|\mathrm{ID} - \mathrm{MS}|) < 15\,\mathrm{GeV}$ and $|\Delta z_{\mathrm{PV}}| < 1\,\mathrm{cm}$ (corresponding to cuts 1 up to and including 8 in table 6.8).

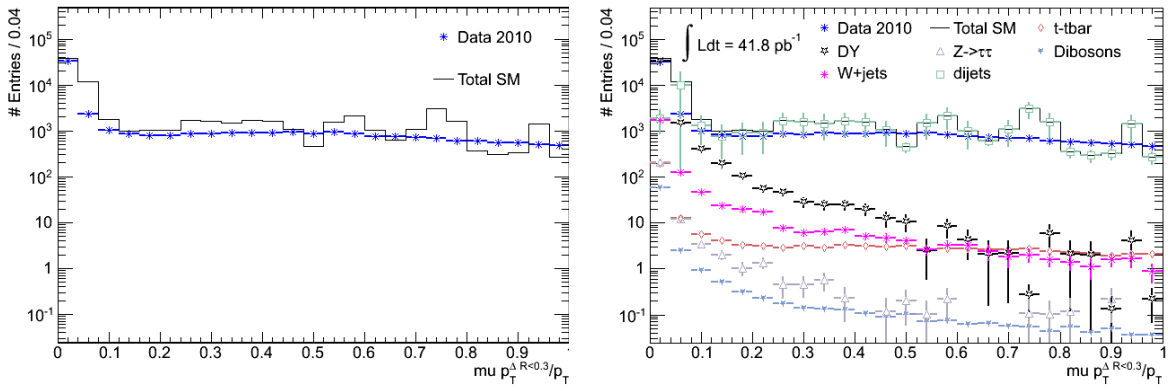

(a) Total SM and data

(b) SM contributions and data

Figure 6.9: The normalized isolation variable $p_T^{\Delta R<0.4}/p_T$ shown for all combined muons requiring a p_T of at least 20 GeV within $|\eta| < 2.4$, having $\Delta p_T(|\mathrm{ID} - \mathrm{MS}|) < 15\,\mathrm{GeV}$, $|\Delta z_{\mathrm{PV}}| < 1\,\mathrm{cm}$ and $p_T^{\mathrm{MS}} > 10\,\mathrm{GeV}$ (corresponding to cuts 1 up to and including 9 in table 6.8).

Charge

From the 10 TeV analysis (specifically section 5.6.2) we remember that the charge misidentification for muons was not an issue. For completeness we repeat the study here.

Reconstructed muons (passing all cuts in table 6.10) are truth-matched using the same algorithm as in section 6.3.1. Figure 7.8 shows that the charge misidentification ratio is basically zero.

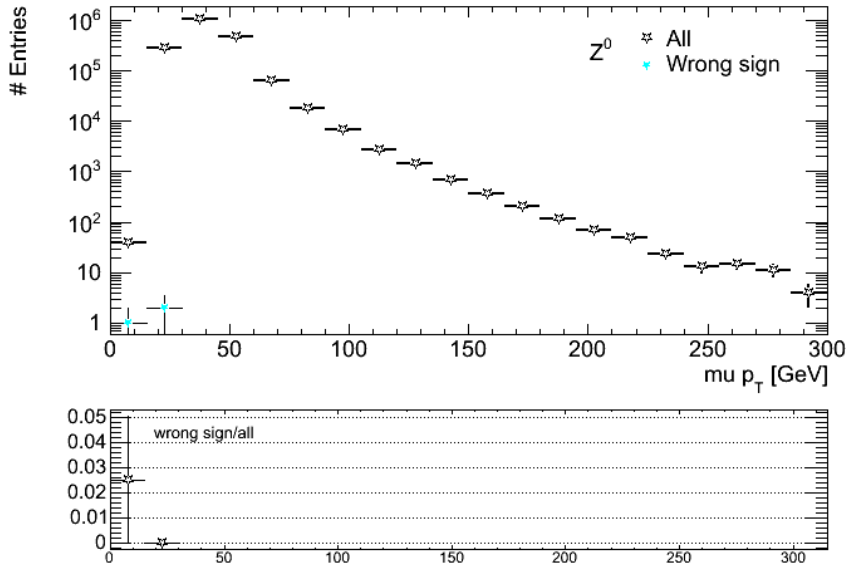

Figure 6.10: The charge misidentification of muons as a function of p_T. Plotted are the total number of truth-matched reconstructed muons and the number that have opposite charge compared to the truth muon. The mean charge misidentification ratio is 0% for a single muon.

The number of events after cuts 1 up to and including 10 from table 6.8 with opposite and same sign dimuons is shown in figure 6.11. 99.95% of data remains after this cut. Close to 100% of MC DY also remains, while 3.75% of the SM background is rejected.

6.4 Z^0 candidates after final selection

The cut flow tables 6.9 and 6.10 summarize the number of $Z^0 \to l^+l^-$ left after each cut from sections 6.3.1 (electron channel) and 6.3.2 (muon channel) respectively. Note that we require all electrons and muons to pass the corresponding lepton selection, and that we in addition require at least two electrons or muons at each step in the event selection.

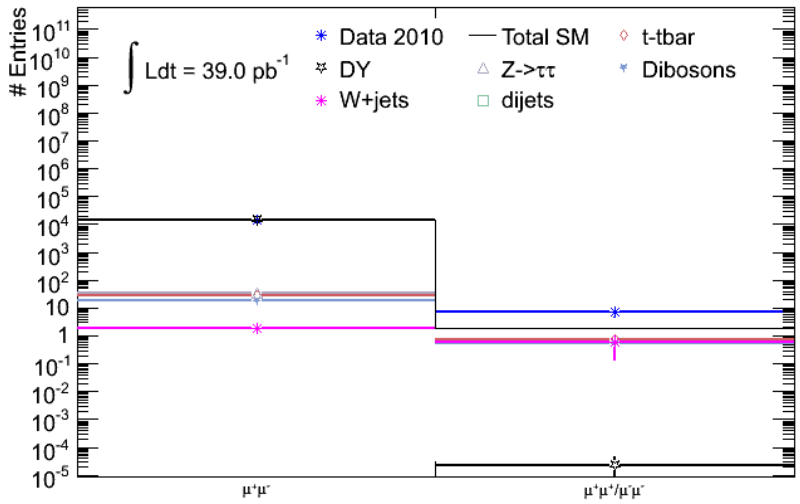

Figure 6.11: The number of events in data and MC containing opposite and same sign dimuons.

No.	Cut	Events
0	Skimming	1172671
1	GRL	977181
2	Good PV	966153
3	Trigger	240204
4	MET Cleaning	240204
5	$N_{el} > 1$ and Electron author	240070
6	$N_{el} > 1$ and η	229540
7	$N_{el} > 1$ and p_T	54445
8	$N_{el} > 1$, OTx	47548
9	$N_{el} > 1$ and Electron ID	10551
10	# of electrons	10544
11	Charge	9963
12	Invariant mass	9143

Table 6.9: The number of candidate $Z^0 \rightarrow e^+e^-$ events in data (calo stream), periods A to I. Total integrated luminosity is 36.6 pb^{-1}. Cuts used are described in tables 6.4 (cut 0 to 4) and 6.6 (cut 5 to 12).

No.	Cut	Events
0	Skimming	178623
1	GRL	170046
2	Good PV	167824
3	Trigger	113512
4	MET Cleaning	113512
5	$N_\mu > 1$ and p_T, η	18389
6	$N_\mu > 1$ and Combined	18389
7	$N_\mu > 1$ and p_T difference	17145
8	$N_\mu > 1$ and z_{PV} difference	17067
9	$N_\mu > 1$ and $p_T^{MS} > 10$ GeV	17067
10	$N_\mu > 1$ and Isolation	14487
11	$N_\mu > 1$ and Charge	14480
12	$N_\mu > 1$ and Invariant mass	13524

Table 6.10: The number of candidate $Z^0 \to \mu^+\mu^-$ events in data (muon stream), periods A to I. Total integrated luminosity is 41.8 pb^{-1}.

6.4.1 Electron channel

In addition to the cuts from section 6.3.1 we use a cut on the invariant mass, 66 GeV $< M_{ee} <$ 116 GeV and require exactly two electrons with opposite charge. After all cuts we are left with 9143 $Z^0 \to e^+e^-$ candidates.

The p_T and η distributions for electrons are plotted in figure 6.12. Data fits extraordinarily well with what we expect from Monte Carlo simulation, both in shape and number - DATA/MC = 94.0%. The η distribution is almost perfect over the whole range, while data follows expectations closely in the p_T distribution up to 200 GeV. Above 200 GeV the expectation value for the SM background per bin falls to below 1, and the data points seem scattered.

This is really an amazing result - not only is the shape of the distributions well modelled, the number of data events are only 6% off.

The η distribution is actually not symmetric. This can barely be seen on a log scale, but on a linear scale it becomes visible, see figure 6.13. The cause of this is the OTx cut (see section 6.3.1).

Figure 6.14 presents the invariant mass distribution in the electron channel. 6.14(a) shows M_{ee} from 60 GeV to 600 GeV, which is around the place where the last data point is. 6.14(b) shows the Z^0 peak only, from 66 GeV to 116 GeV. Here, the data deficit is 9.7%..

Comparing our results to the most recent results from ATLAS[41], we see that the number of Z^0 candidates is about the same, they have 9170 with 37 pb^{-1}, we have 9143 with 36.6 pb^{-1}.

Comparing 6.14(d) to C.4(a) we see that the shape of the invariant mass distributions are nearly identical in shape. We believe the slight differences migh be due to ECAL energy

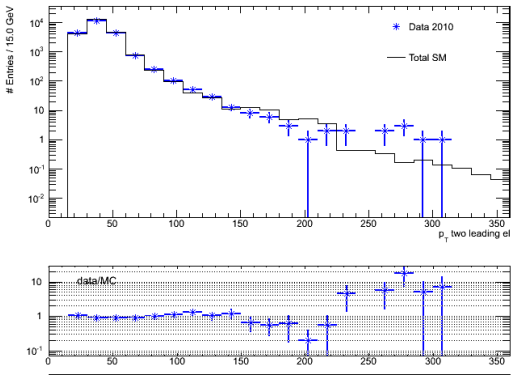

(a) Electron p_T

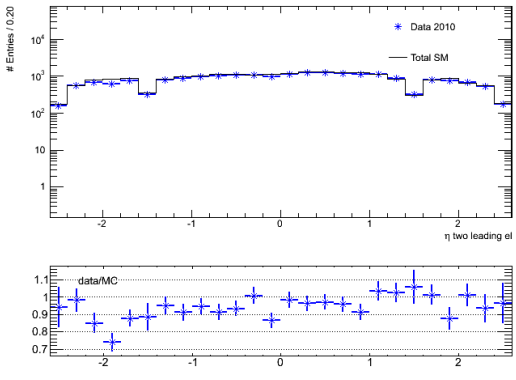

(b) Electron η

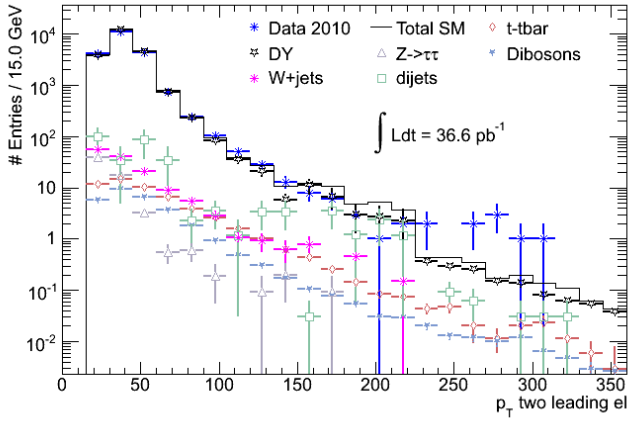

(c) Electron p_T. The SM background is divided into constituents.

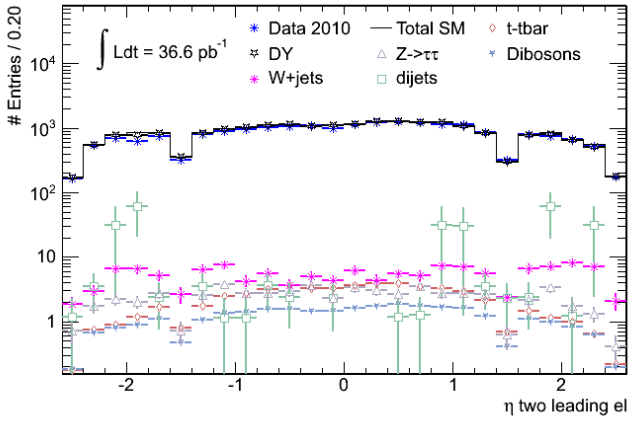

(d) Electron η. The SM background is divided into constituents.

Figure 6.12: The p_T and η distributions for the two electrons after cuts 1 up to and including 10 (table 6.9). The datapoints account for 94.0% of MC.

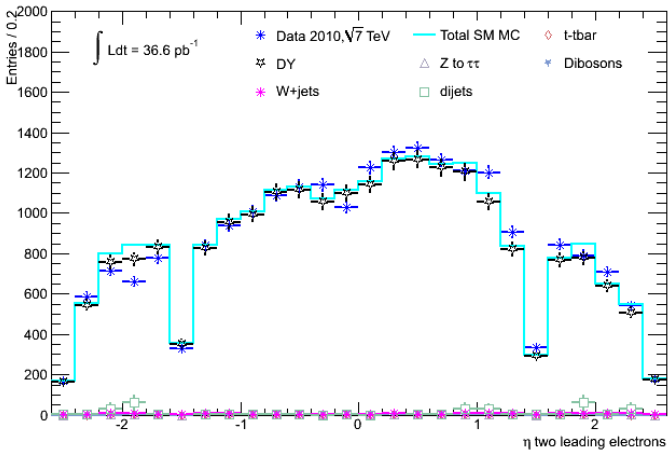

Figure 6.13: The η distribution is slightly asymmetric. This is due to the OTx cut. Cuts used are 1 up to and including 10 from table 6.9.

corrections. They do not state what is used. Also note that the normalization of MC is different - they normalize to the number of data entries.

6.4.2 Muon channel

In the muon channel as well we require opposite signs and make a cut on the invariant mass 66 GeV $< M_{\mu\mu} <$ 116 GeV. We do however not require exactly two muons. When there are more than two, we pick out the ones with highest p_T.

After all the cuts are implemented we are left with 13524 dimuon events passing all the cuts. Figure 6.15 shows the p_T and η ditributions for MC and data for the two leading (in terms of p_T) muons. Again we see that the shape fits the theoretical expectations, and the number of events are within reason (data deficit is 10.6%).

The dimuon invariant mass distribution is shown in figure 6.16 from 50 to 350 GeV (top), and on the Z^0 peak (bottom). The shape of the data distribution is very similar to the MC distribution. There is a data deficit of 4.9% on the Z^0 peak.

Again we compare our result to the most recent ATLAS results[41]. They report 42 pb^{-1}, we have 41.8 pb^{-1}. Comparing 6.16(d) to C.4(b) we see that our invariant mass distribution appears broader than the official distribution. We found this to be because we use the MS measurement of the p_T only, while they use the combined p_T (combined measurements from ID and MS). This is also the reason for the discrepancy in the number of $Z^0 \to \mu^+\mu^-$ events. They report 13858, we find 13524. However, if we use the combined p_T measurement, we find 13745, which is reasonable.

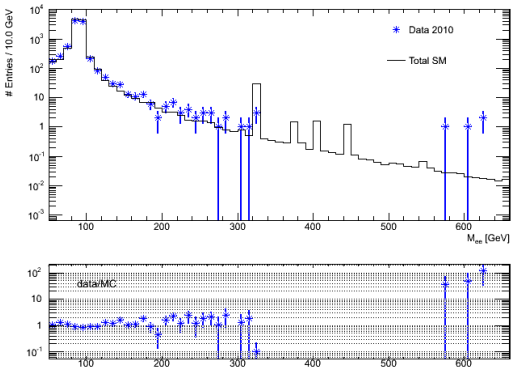

(a) Dielectron invariant mass.

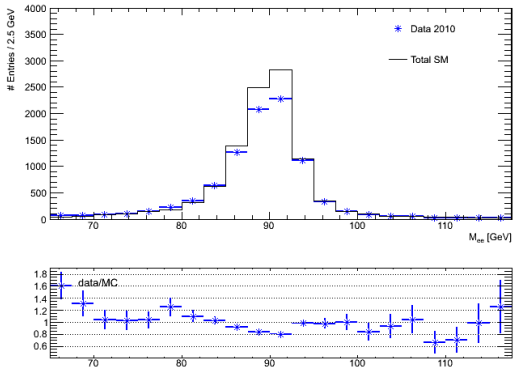

(b) Dielectron invariant mass on the Z^0 peak.

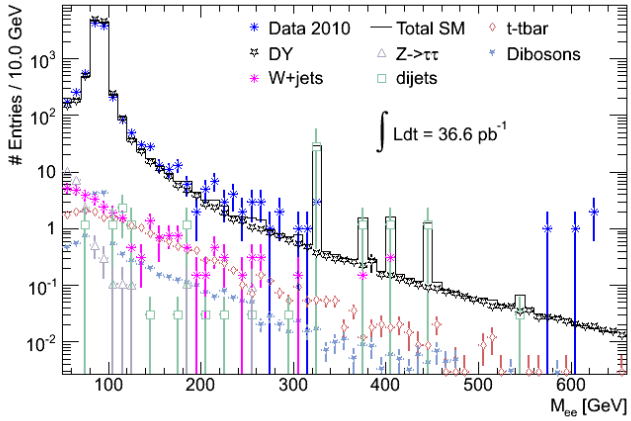

(c) M_{ee} with the SM contribution is divided into its constituents.

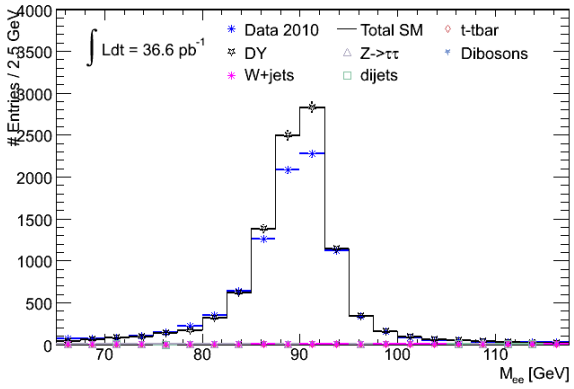

(d) M_{ee} with the SM contribution is divided into its constituents.

Figure 6.14: The invariant mass distribution in the electron channel after all cuts (table 6.9) The datapoints account for 90.3% of MC on the Z^0 peak.

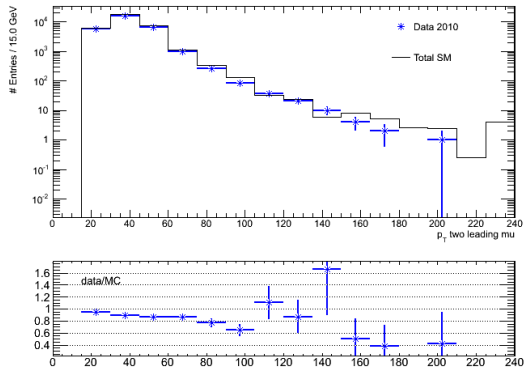

(a) Muon p_T

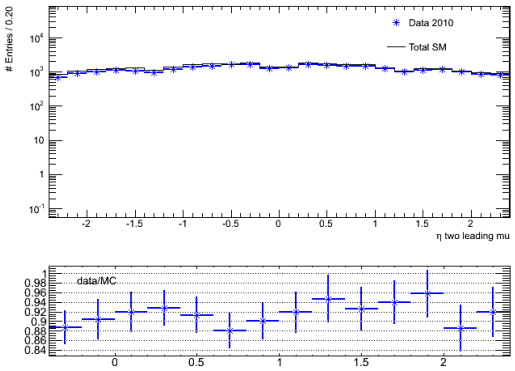

(b) Muon η

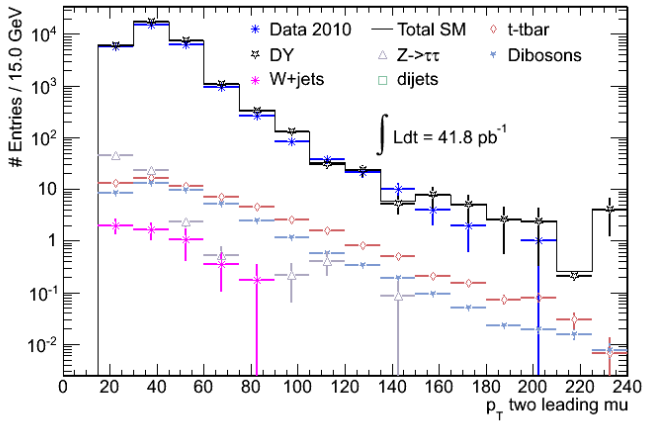

(c) Muon p_T. The SM background is divided into its constituents.

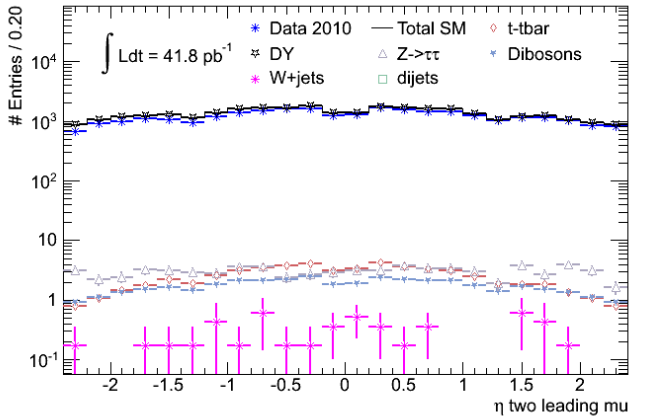

(d) Muon η. The SM background is divided into its constituents.

Figure 6.15: The p_T and η distributions for the two highest p_T muons after cuts 1 up to and including 10 (table 6.10). There is a data deficit of 10.6%.

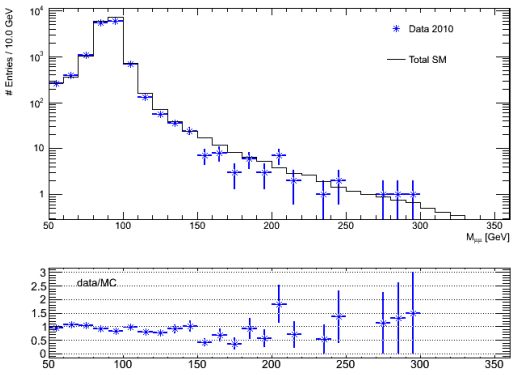

(a) Dimuon invariant mass.

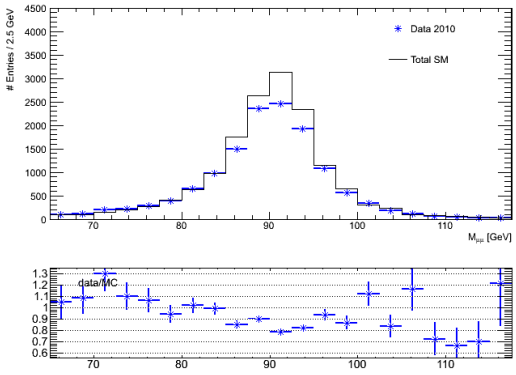

(b) Dimuon invariant mass on the Z^0 peak.

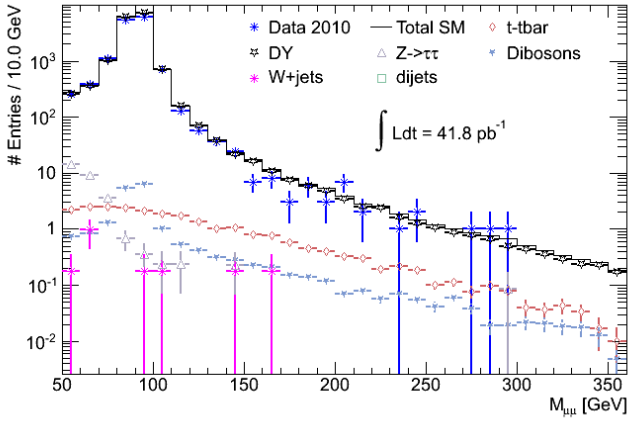

(c) $M_{\mu\mu}$ with the SM contribution is divided into its constituents.

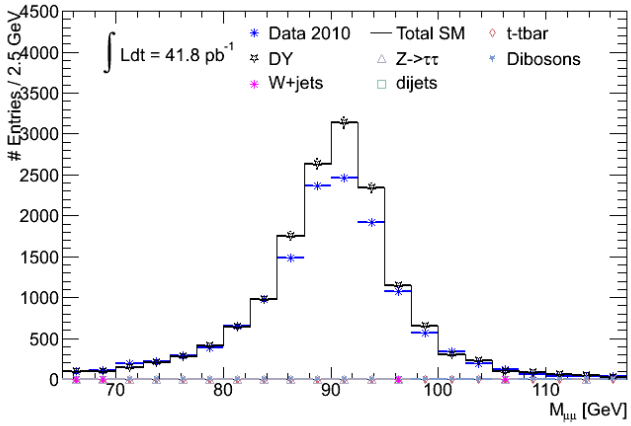

(d) $M_{\mu\mu}$ with the SM contribution is divided into its constituents.

Figure 6.16: The invariant mass distribution in the muon channel after all cuts (6.10). The datapoints account for 88.8% of MC on the Z^0 peak.

6.5 Fitting the invariant mass distributions

The Breit-Wigner distribution is often used to model resonances. It has the probability density function (PDF)

$$f(E) \sim \frac{\Gamma}{(E-M)^2 + \Gamma^2/4} \tag{6.2}$$

where M is the mass and Γ is the with of the resonance.

In addition to a Breit-Wigner PDF, the invariant mass distributions of figures 6.14 and 6.16 are influenced by the errors of the measurement. This error is assumed to be Gaussian.

To fit the curves we therefore use a convolution of a Breit-Wigner and a Gaussian PDF. A convolution of two distributions f and g, written $f * g$, is given by

$$(f * g)(y) \equiv \int_{-\infty}^{\infty} f(x)g(y-x)dx \tag{6.3}$$

It provides an answer to the question "What is the probability that the sum of two variables following the distributions f and g, is y?" This is exactly what we want - the invariant mass distribution is a convolution of the real invariant mass PDF[7] of the Z^0 which means that the measurement error PDF from the detector, and the measured invariant mass is the sum of a variable following a Breit-Wigner distribution with a width Γ and mass M equal to the width and mass of the Z^0 respectively and a Gaussian with a width corresonding to the detector resolution. Ideally all three of these variables could be estimated from one fit. In reality we need to fix one or two of the parameters and extract the other(s).

Table 6.11 shows the result of the fitting. Note that the width of the Breit-Wigner is fixed to the full width of the Z^0, 2.4952 GeV, and that the mass is fixed to 91.1876 GeV in rows 2 and 4.

	Mass [GeV]	σ [GeV]	Notes
M_{ee}	89.61	2.68	Standard $Z^0 \to e^+e^-$ cuts
	fixed	2.18	
$M_{\mu\mu}$	90.25	4.26	Standard $Z^0 \to \mu^+\mu^-$ cuts
	fixed	4.26	
	90.22	3.54	Standard $Z^0 \to \mu^+\mu^-$ cuts with $\lvert\eta\rvert < 1.05$
	fixed	3.37	

Table 6.11: The result of fitting the Z^0 peak to a Breit-Wigner distribution (equation 6.2) convoluted with a gaussian. The standard $Z^0 \to e^+e^-$ ($Z^0 \to \mu^+\mu^-$) cuts are given in table 6.9 (6.10).

We see that the result is less than perfect. Where the mass is not fixed, it is off by 1.58 GeV in the electron channel and 0.938 GeV in the muon channel. The detector resolution in the electron channel is 2.68 GeV, and in the muon channel 4.26. The results are shown in figure 6.17.

[7]To be exact, a PDF always has an area of 1, while our distributions are normalized to the number of events. We still use the term "PDF" however.

Fixing the mass in addition to the width makes no difference for the result on the detector resolution in the muon channel, but enhances the result a bit in the electron channel (from 2.68 to 2.18).

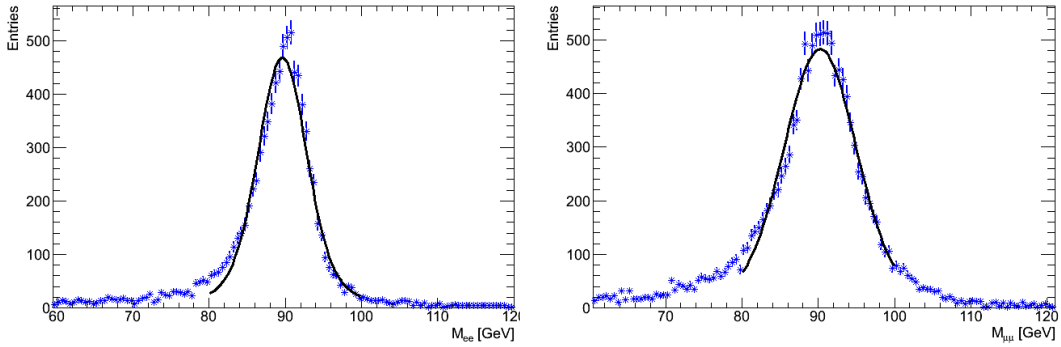

(a) M_{ee} (b) $M_{\mu\mu}$

Figure 6.17: Fitting data to a Breit-Wigner distribution (equation 6.2) modelling the shape of the resonance, convoluted with a gaussian which models the detector resolution. The Z^0 width is fixed to the nominal value of 2.4952 GeV, while the Breit-Wigner mass and the Gaussian width are free parameters.

Figure C.5 and C.6 are the official ATLAS plots showing the detector resulution in the electron and muon channels respectively. We see that the dielectron invariant mass fit is much better than what we have. They have used the Crystall Ball function, consisting of a Gaussian core portion and a power-law tail, below a certain threshold. It is often used to account for radiative losses, lik bremsstrahlung. They report a resolution (Crystall ball σ) of 1.73 ± 0.08 GeV, which is lower than what we got (2.18). We believe the difference lies in the fact that we use a Gaussian to model the resolution.

We get comparable results to the official ATLAS results in the muon channel. They report on a detector resolution of 3.27 ± 0.07 GeV when using measurements from the MS only. We get 3.37 GeV fixing both the mass and width of the Z^0 to the nominal values.

6.6 Summary

The LHC collected data for proton-proton collisions at 7 TeV center of mass energy from March 2010 to November 2010. In this chapter we analysed this data with focus on the Z^0 resonance. Using the standard set of cuts agreed upon by the ATLAS SM working group[39] we found 9143 $Z^0 \to e^+e^-$ candidates and 13524 $Z^0 \to \mu^+\mu^-$ candidates with 37 pb^{-1} and 42 pb^{-1} of data respectively. Data fits simulations well and the results are in agreement with official results[41]. We conclude that the ATLAS detector performs well. The next chapter focuses on cuts designed to optimize the discovery potential of the hypothetical Z' particle.

Chapter 7

Z' analysis on 2010 data

In chapter 5 we performed a feseability study for a possible SSM Z' discovery at LHC with ATLAS at 10 TeV center of mass energy. The collision energy was later decided to be 7 TeV, and ATLAS has been taking data at this energy since 30 March 2010, collecting approximately 45 pb^{-1}. In chapter 6 we investigated the performance of the detector by reconstructing the Z^0 resonance through its decay into e^+e^- and $\mu^+\mu^-$. The ATLAS detector is in excellent shape, and we are now ready to redo the analysis in the search for new neutral gauge bosons Z'.

It is natural that some cuts are revised when starting the search for the Z', as the decay products generally have a much higher p_T. After some preliminary studies, the exotic dilepton subgroup within ATLAS converged towards a set of common cuts. Improvements are under constant consideration, but the cuts used here as of January 2011 have not changed much the last few months.

Data presented here is based on reconstruction R15. The autumn reprosessing of data and MC (R16) did not become available in time for this analysis. R16 comes with many improvements, especially regarding the energy measurements in the ECAL and the alignment of the MS.

The standard event selection routine (section 6.2) no longer includes the MET Cleaning but is otherwise identical. In practice the difference in negligible - as we remember from section 6.4 this cut did not remove any events. Anyhow, this cut is more important for searches involving missing E_T, when noise in the calorimeters disturbs the $\not{E}_T$ measurement.

Table 7.1 summarizes the event selection.

7.1 Electron selection

There are not many changes in the electron channel compared to the Z^0 analysis. The p_T cut is increased to 25 GeV, while the η cut, author, OTx (section 6.3.1) and electron identification ("medium") stays the same. The changes lie mostly in that the cut on the

#	Cut	Notes
0	Skimming	At least 2 loose electrons with $E_T >$ 10 GeV, author 1 or 3
1	GRL	Using only runs flagged as good for physics
2	Good PV	At least one good primary vertex (PV) (longitudinal coordinate no more than 15 cm from interaction point and at least three tracks)
3	Trigger	Event must be triggered. Table 6.5 gives the triggers used.

Table 7.1: Event selection for Z' analysis. These requirements are used for both channels. For electron (muon) selection, see table 7.2 (7.3).

number of electrons is loosened (we only require at least two electrons, not exactly two, so that when more than two electrons pass selection, the two with highest p_T are chosen) and that the charge requirement is removed (see next subsection). See table 7.2 for a list of cuts.

#	Cut	Notes
4	Electron author	Author 1 or 3, meaning reconstructed by the calorimeter-seeded reconstruction algorithm
5	η	η within the geometrical acceptance, $\lvert\eta\rvert < 2.47$, but excluding the crack $1.37 < \lvert\eta\rvert < 1.52$
6	p_T	p_T at least 25 GeV
7	OTx	Not located in a dead region of the ECAL
8	Electron ID	Identified as "medium"
9	Invariant mass	Invariant mass of electron pair above 75 GeV, $M_{ee} >$ 75 GeV

Table 7.2: All electron candidates are required to pass the cuts listed here. All events have passed the event selection as listed in table 7.1.

7.1.1 Charge

In section 6.3.1 we saw that the charge misidentification probability in the electron channel for electrons coming from the Z^0 was about 1.3%. The electron charge is measured in the ID by checking which way the track bends. The tracker's p_T resolution decreases with increasing p_T, which means that the charge misidentification rate is expected to increase.

Figure 7.1 shows the charge misidentification for a 1.0 and a 2.0 TeV Z' as a function of p_T and η. We see the same patterns as for the Z^0, namely that the probability is largest at high p_T and $|\eta|$, but the mean value is higher than before, 4.8% and 7.0% for the 1.0 and the 2.0 TeV Z' respectively. This translates to a mean charge misidentification of 9.26% and 13.2% respectively on event basis (requiring at least two electrons).

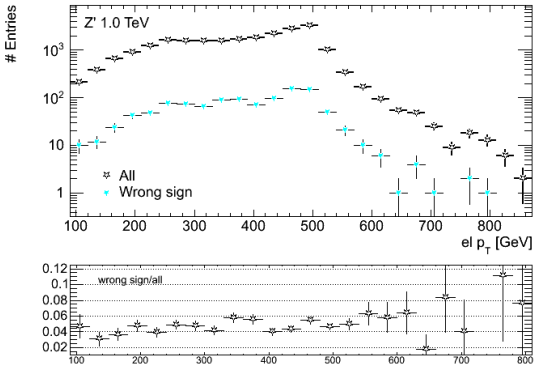

(a) Charge misidentification as a function of p_T for a 1.0 TeV Z'

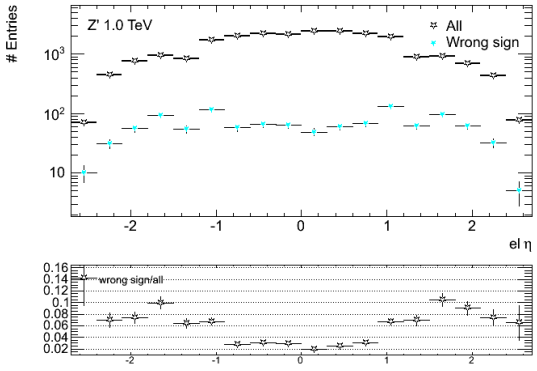

(b) Charge misidentification as a function of η for a 1.0 TeV Z'

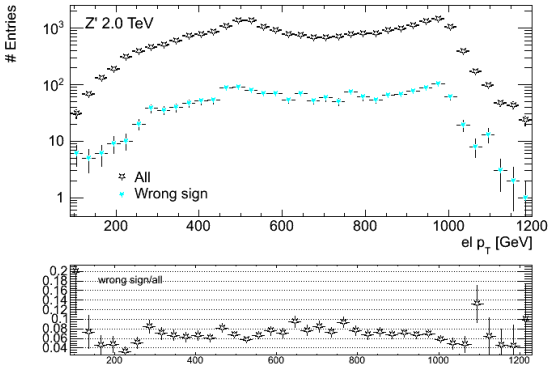

(c) Charge misidentification as a function of p_T for a 2.0 TeV Z'

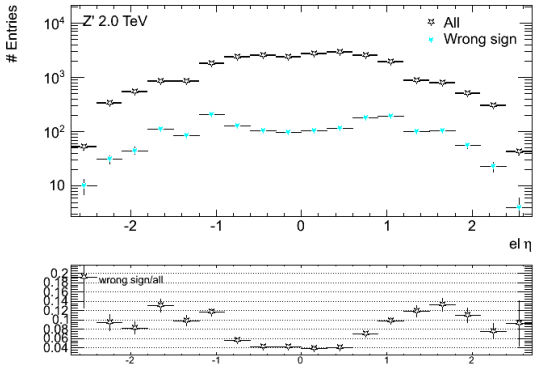

(d) Charge misidentification as a function of η for a 2.0 TeV Z'

Figure 7.1: The charge misidentification of electrons as a function of p_T (left) and η (right). The plot shows the total number of truth-matched reconstructed electrons and the number that have opposite charge compared to the truth electron, and the ratio of these numbers. The mean charge misidentification is 4.8% (7.0%) for a single electron coming from a Z' of 1.0 (2.0) TeV.

Discussions are ongoing about the opposite charge requirement. The argument against it is the loss of 10% of all Z' events. However, some believe we would be very hesitant with claiming discovery if a large fraction of the candidate Z' events had same sign electrons.

7.2 Muon selection

In the muon channel the p_T cut is also raised to 25 GeV and all muons are required to be combined, as before. In this analysis we chose to rely solely on p_T measurements from the MS, p_T^{ME} (recall from section 6.3.2 that "ME" means MS measurement extrapolated to the perigee), and restrict the pseudorapidity to the barrel section only ($|\eta| < 1.05$) because of misalignment issues in the ID. A lot of work has been invested to understand the misalignment. As a result, reconstruction R16 is very much improved in this sense, and combined p_T measurements can be used and the whole pseudorapidity range up to $|\eta| < 2.4$ can be included again.

An overview of the muon selection cuts is given in table 7.3.

#	**Cut**	**Notes**
5	Combined	Combined muon (see section 5.4.2 for more information)
6	p_T and η	p_T^{ME} above 25 GeV, within $\|\eta\| < 1.05$
7	MS Hits	At least 3 hits in each of the 3 barrel MDT stations, veto hits in BIS78 and BEE. At least 1 phi hit in at least two RPC layers.
8	ID Hits	At least 4 SCT hits and 1 pixel hits, and the sum of hits in SCT and pixel must be greater than 6.
9	IP	Longitudinal and transverse impact parameters (z_0^{exPV} and d_0^{exPV}) with respect to primary vertex are required to be less than 1 and 0.2 mm respectively
10	Isolation	Normalized p_T-cone30 less than 0.05, $\sum p_T^{\Delta R<0.3}/p_T < 0.05$
11	Charge	Opposite charge
12	Invariant mass	Invariant mass of muon pair above 60 GeV

Table 7.3: All muon candidates are required to pass the cuts listed here. All event have passed the event selection as listed in table 6.4.

7.2.1 Hits in the muon spectrometer

The requirements on hits in the MS is as follows: At least 3 hits in each of the 3 barrel MDT (see section 4.2.6 for general information on the Monitored Drift Tube chambers) stations. Events with hits in BIS78 or BEEE are vetoed. At least 1 phi hit in at least two RPC (section 4.2.6) layers. See figures 7.3 and 7.4.

The purpose of the MDT is to measure the coordinate of the track in the bending plane,and the 3 hits requirement in the BI ("Barrel Inner"), BM ("Barrel Middle") and BO ("Barrel

Outer") chambers are to ensure a good quality muon track. There should be no hits in BEE ("Barrel End-cap Extra" chambers) because the BEEs measure tracks passing from the barrel to the end-cap. Also hits in BIS78 (small chamber in sector 7, the 8th in line, of the inner cylinder of the barrel) are vetoed because of bad alignment.

The MDT is divided into multiple chambers[25]. The naming conventions are as follows: the first letter gives the placement in barrel (B) or end-cap (E) and the second letter whether the chamber is in the inner (I), middle (M) or outer (O) chamber layer. The third letter is L if it is a small sector, or S if it is a small sector. The first number gives the sector number (1-16), and the second gives the sequence number of the chamber in a row of chambers in a sector. In addition a few extra chambers are, like the BEE chamber, where the "E" stands for "extra". The BEEs are located on the top boundary of the end-cap toroid.

Figure 7.2 shows a cross-section of the muon system in the transverse plane (left) and in the longitudinal plane, with the location of the different chambers.

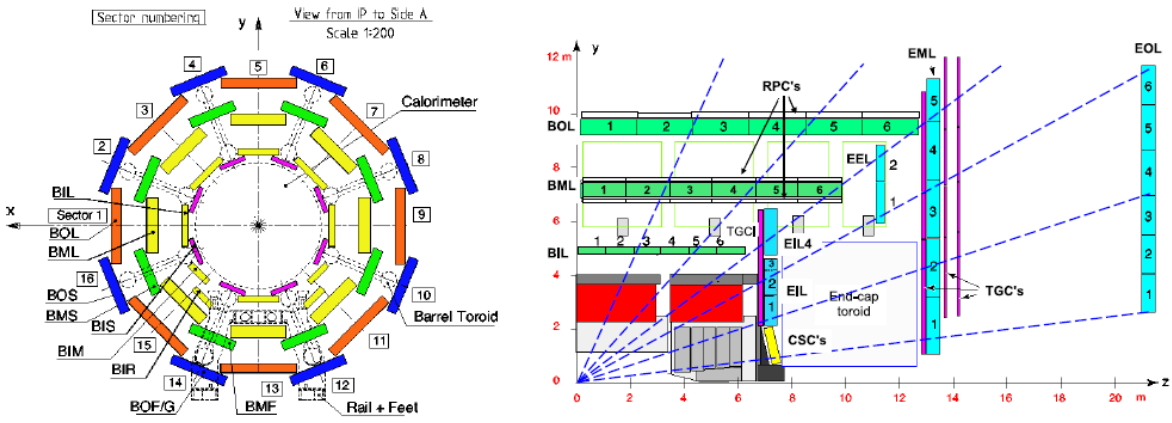

Figure 7.2: Left: Cross-section of the barrel part of the MS in the transverse plane[25], with three concentric cylindrical layers with eight large and eight small chambers.
Right: Cross-section of the muon system in the longitudinal plane[25].

The trigger chambers (RPC for $|\eta| < 1.05$, for general information see section 4.2.6) measures the η and ϕ coordinates of a track. To ensure a high quality track, 1 hit in at least 2 of the 3 concentric layers (ϕ layers) are required.

Figures 7.3 and 7.4 show the number of hits in the different MDT and RPC stations. The agreement between data and MC is not perfect, but OK. We believe a data driven estimate of the QCD background would help. Table 7.4 lists the relevant numbers associated with these cuts. We are not trying to reject the background by these cuts, only get high quality muon tracks. It is of vital importance, naturally, that the signal is not cut, and it is surely not.

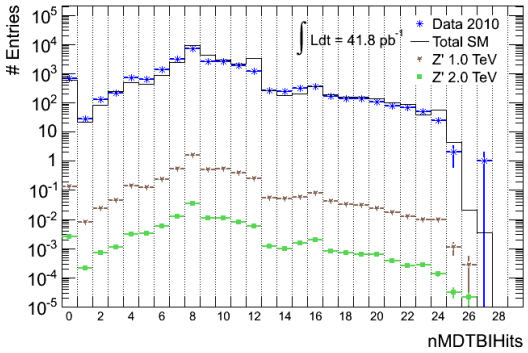

(a) MDT BI

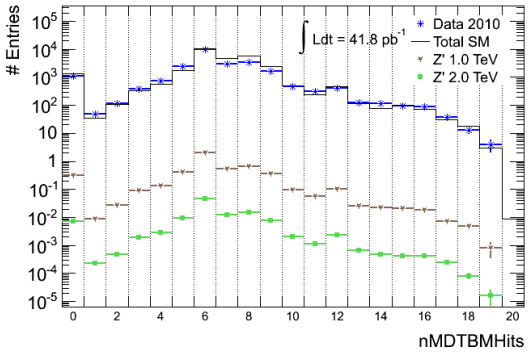

(b) MDT BM

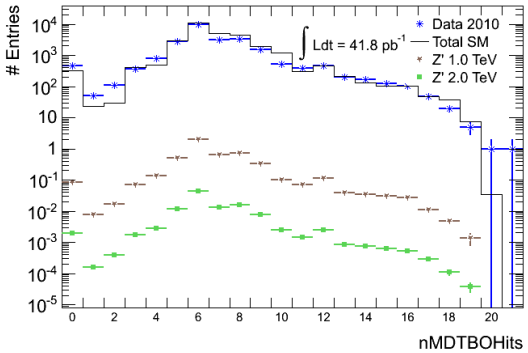

(c) MDT BO

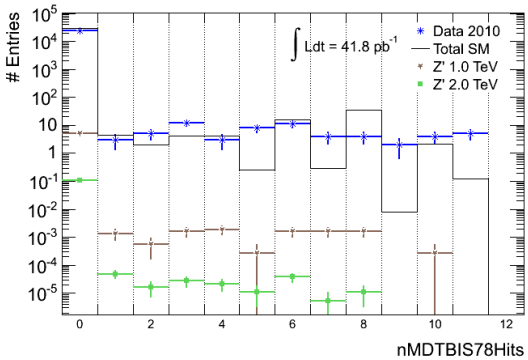

(d) MDT BIS78

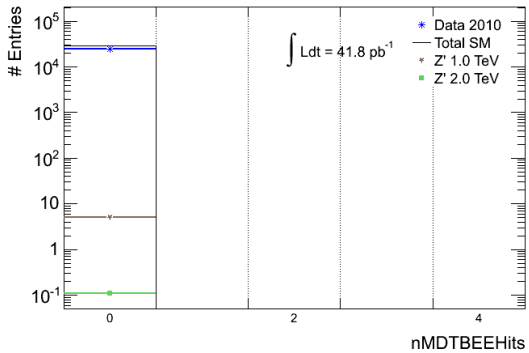

(e) MDT BEE

Figure 7.3: The number of hits in various MDT chambers. At least 3 hits are required in each of the 3 barrel MDT stations and no hits in BIS78 or BEE. All muons are required to pass cuts 1 to and including 6 from table 7.3.

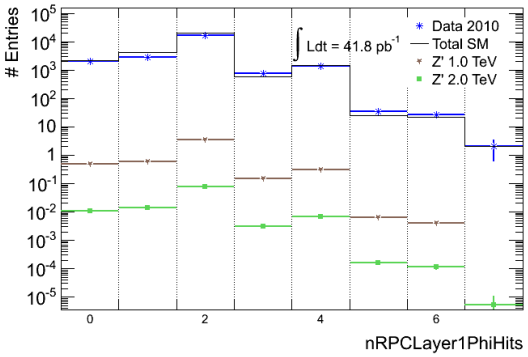

(a) RPC Layer 1

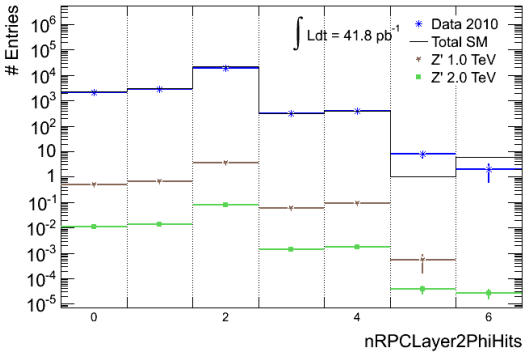

(b) RPC Layer 2

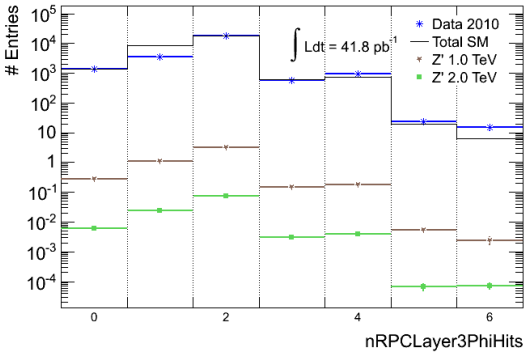

(c) RPC Layer 2

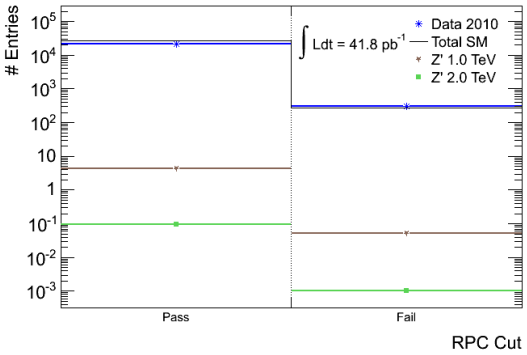

(d) RPC Cut

Figure 7.4: The number of hits in various RPC layers. The requirements are at least 1 hit in at least 2 RPC layers. 7.4(d) show the number of events that pass or fail the requirement. All muons are required to pass cuts 1 to and including 6 from table 7.3.

Cut	Data	SM	Z' 1.0 TeV	Z' 2.0 TeV	Description
MDT BI	96.6	97.5	96.8	96.8	At least 3 hits
MDT BM	94.8	94.8	92.8	92.9	At least 3 hits
MDT BO	97.4	98.7	97.8	97.7	At least 3 hits
MDT BIS78	99.7	99.8	99.8	99.8	No hits
MDT BEE	100	100	100	100	No hits
RPC Layer	98.6	99.0	98.8	98.8	At least 1 phi hit in at least 2 RPC layers
SCT	100	100	100	100	At least 4 SCT hits
Pixel	99.9	100	100	100	At least 1 pixel hit
SCT+Pixel	100	100	100	100	The sum of hits in SCT and pixel greater than 6
d_0^{exPV}	98.0	99.3	100	100	Less than 0.2 mm
z_0^{exPV}	99.3	100	100	100	Less than 1 mm
Isolation	99.7	69.3	99.6	99.5	$\sum p_T^{\Delta R<0.3}/p_T < 0.05$

Table 7.4: The percentage of events in data, total SM and Z' with mass 1.0 and 2.0 TeV that pass the requirements on MS Hits, ID Hits, impact parameter and isolation. The requirements are described in table 7.3.

7.2.2 Hits in the inner detector

The requirements on hits in the ID are as follows: At least 4 SCT hits and 1 pixel hit, and the sum of hits in SCT and pixel must be greater than 6. These requirements are added to ensure high quality muon tracks in the ID.

Figure 7.5 shows the distribution of the number of hits in data, background and signal (Z' at mass 1.0 and 2.0 TeV) in SCT and Pixel, and also the number of events that pass or fail the requirement on the sum of hits in SCT and Pixel. Table 7.4 summarizes the percentages of events passing or failing the requirements for data, background and signal (1.0 and 2.0 TeV Z').

7.2.3 Impact parameter

Longitudinal and transverse impact parameters with respect to primary vertex are required to be less than 1 mm and 0.2 mm respectively

$$d_0^{\mathrm{exPV}} < 0.2\,\mathrm{mm}, \quad z_0^{\mathrm{exPV}} < 1\,\mathrm{mm}$$

Figure 7.6 shows the distributions for data, background and signal (1.0 and 2.0 TeV Z'), and table 7.4 summarizes the percentages of events passing those cuts.

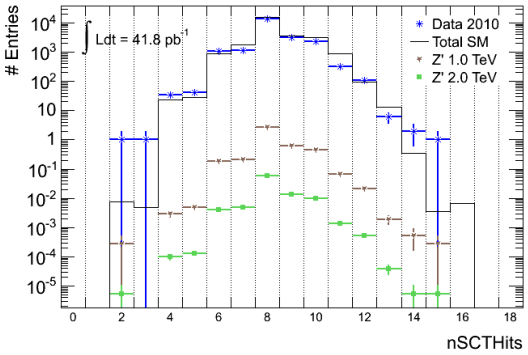

(a) Number of SCT hits

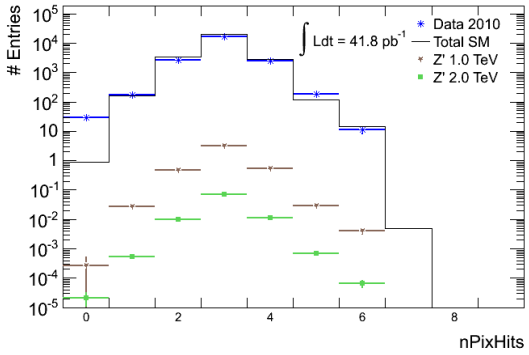

(b) Number of pixel hits

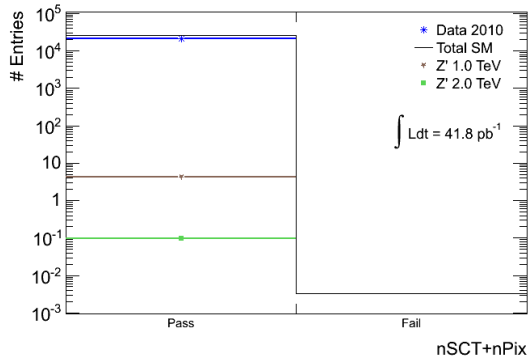

(c) Number of events passing or failing cut (number of SCT hits plus pixel hits at least 6)

Figure 7.5: Number of hits in SCT and pixel are required to be at least 4 and 1 respectively, and the sum of these at least 6. All muons are required to pass cuts 1 to and including 7 from table 7.3.

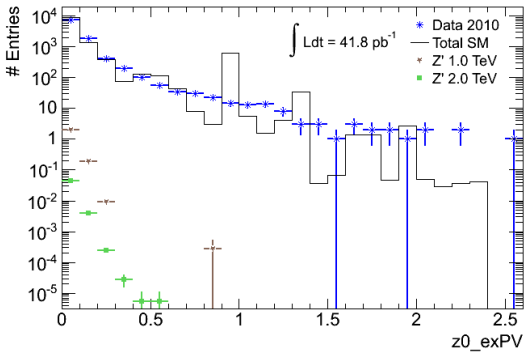

(a) Transverse impact parameter

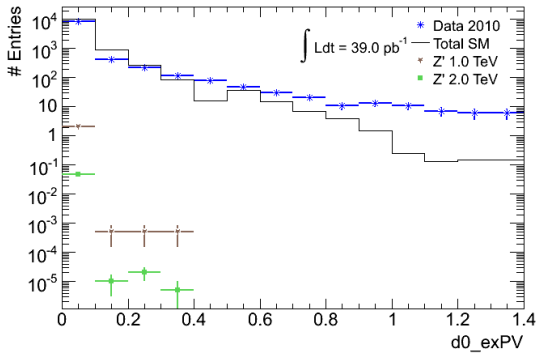

(b) Longitudinal impact parameter

Figure 7.6: Transverse and longitudinal impact paramter wrt primary vertex are required to be less than 0.2 mm and 1.0 mm respectively. All muons are required to pass cuts 1 to and including 8 from table 7.3.

7.2.4 Isolation

The isolation cut has changed and is now $\sum p_T^{\Delta R<0.3}/p_T < 0.05$ (compared to $\sum p_T^{\Delta R<0.4}/p_T < 0.2$, section 6.3.2). The distribution for the normalized p_T-cone30 is shown in figure 7.7.

We see that data fit MC very well at low values. Above 0.1 the QCD contribution dominates completely. The structure in the distribution at values above 0.1 is caused by the QCD being taken from MC instead of data driven methods. Data seems to fit nicely with simulations when disregarding the fluctuations in QCD.

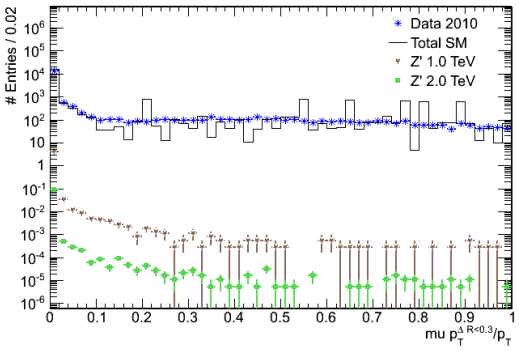

(a) The normalized isolation variable $\sum p_T^{\Delta R<0.3}/p_T$.

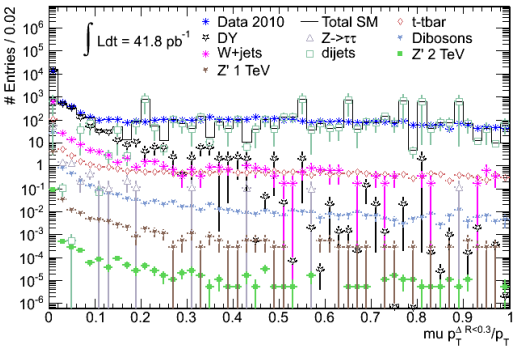

(b) The SM contribution divided into its constituents.

Figure 7.7: The normalized p_T-cone variable $\sum p_T^{\Delta R<0.3}/p_T$ shown for data, background and signal (1.0 and 2.0 TeV Z'). All muons are required to pass cuts 1 to and including 9 from table 7.3.

The cut $\sum p_T^{\Delta R<0.3}/p_T < 0.05$ rejects 31.7% of the SM background. 99.7% of data and 99.6% (99.5%) of the 1.0 TeV (2.0 TeV) Z' events remain.

7.2.5 Charge

We expect the charge misidentification for muons to be low (see sections 5.6.2 and 6.3.2). For completeness we confirm it here. Figure 7.8 shows the number of muons with the same charge and opposite charge compared to the corresponding truth muon (information on the truth-matching algorithm is given in C.2). The mean charge misidentification is 0.25%, and we therefore keep the requirement of opposite charge dimuons.

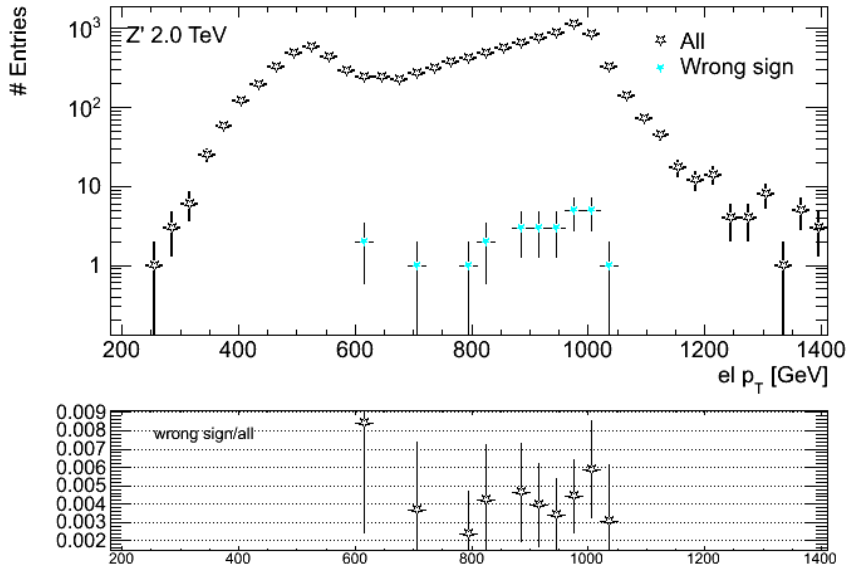

Figure 7.8: The charge misidentification of single muons as a function of the muon p_T. The number of muons with the same charge and opposite charge compared to the corresponding truth muon are shown as well as the ratio of these numbers. The mean charge misidentification is 0.25%.

7.3 Z' candidates after final selection

The cut flow tables 7.5 (electron channel) and 7.6 (muon channel) shows the number of remaining data events after each major cut from sections 7.1 and 7.2 respectively. We see that 8508 electron events from the calo stream are left, and 2886 muon events from the muon stream. The reason for the low number of dimuon events is the tight $|\eta| < 1.05$ cut.

#	**Cut**	**Events**
0	Skimming	1172671
1	GRL	977181
2	Good PV	966153
3	Trigger	240204
4	$N_{el} > 1$ and Electron author	240070
5	$N_{el} > 1$ and η	229540
6	$N_{el} > 1$ and p_T	31395
7	$N_{el} > 1$ and OTx	27361
8	$N_{el} > 1$ and Electron ID	8986
9	$N_{el} > 1$ and Invariant mass	8508

Table 7.5: Cut flow table for the calo stream, periods A to I. The total integrated luminosity is 36.6 pb^{-1}. Tables 7.1 (event selection) and 7.2 (electron selection) describe the various cuts. Note that at least two electrons are required at each cut from 4 up to and including 9.

#	**Cut**	**Events**
0	Skimming	178623
1	GRL	170046
2	Good PV	167824
3	Trigger	113512
5	$N_{\mu} > 1$ and Combined	75283
6	$N_{\mu} > 1$ and p_T, η	4591
7	$N_{\mu} > 1$ and MS Hits	3536
8	$N_{\mu} > 1$ and ID Hits	3521
9	$N_{\mu} > 1$ and IP	3338
10	$N_{\mu} > 1$ and Isolation	2932
11	$N_{\mu} > 1$ and opposite charge	2931
12	$N_{\mu} > 1$ and Invariant mass	2886

Table 7.6: Cut flow table for the muon stream, periods A to I. Total integrated luminosity is 41.8 pb^{-1}. Tables 7.1 (event selection) and 7.3 (muon selection) describe the various cuts. Note that at least two muons are required at each cut from 5 up to and including 12.

7.3.1 Electron channel

All cuts from section 7.1 are used in the final selection. When more than two electron pass the cuts, the leading and subleading electrons (in terms of p_T) are selected. An additional requirement on invariant mass is used, $M_{ee} > 75\,\text{GeV}$. This requirement is imposed because the background is not well understood at lower invariant masses.

Figure 7.9 shows the p_T (7.9(a)) and η (7.9(b)) distributions of the two leading electrons. The structure in the η distribution at $|\eta| \approx 1.4$ is caused by the so-called crack, where the barrel and end-cap sections of the ECAL are joint. The spikes in MC in the p_T spectrum are caused by two effects. The small fluctuations are because of lack of statistics - the distributions would be smooth if the generated number of events were high enough. The spikes at approximately 400 and 900 GeV, however, are caused by the DY being divided into mass bins. Different mass-bins have different cross-sections, and then we can get situations like this, where single events are scaled up.

The agreement between data and MC is good, with a data deficit of 6.2%, about the same as in the Z^0 analysis.

Figure 7.10 shows the invariant mass distribution with data, MC background and signal (1.0 TeV and 2.0 TeV Z'). The spikes are caused by the lacking statistics in the dijet datasets.

The four events at ∼600 GeV in the dielectron invariant mass distribution (7.10) have been discussed, and conclusion are that they are within statistical expectations. The number of background events above invariant mass 570 GeV is 1.59. We find a total of four data events in this region, which means that the number of potential signal events is 2.41. We find the significance is 2.2 using equation (5.10) with $s = 2.41$ and $b = 1.59$.

7.3.2 Muon channel

In the final muon selection, all cuts from section 7.2 are used, and a cut on the invariant mass ($M_{\mu\mu} > 60\,\text{GeV}$) is added (for the same reason as in the previous subsection; poorly understood background). If more than two muons pass the requirement, the two highest p_T muons are chosen.

Figure 7.11 shows the p_T (7.11(a)) and η (7.11(b)) distributions for the two leading muons. Data follows theoretical expections perfectly in η, and also in p_T up to about 200 GeV.

The invariant mass distribution of the two leading muons is shown in figure 7.12 for data, MC background and Z' signals (1.0 TeV and 2.0 TeV).

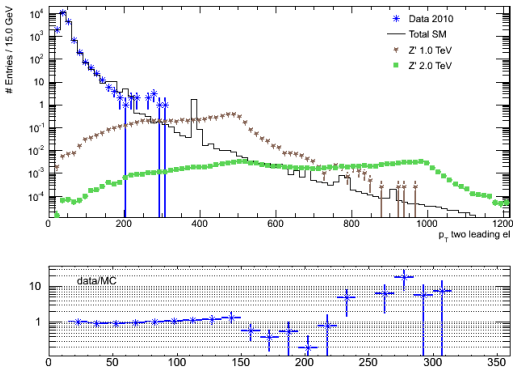

(a) Electron p_T

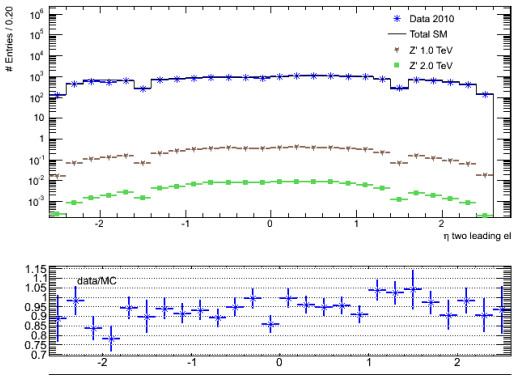

(b) Electron η

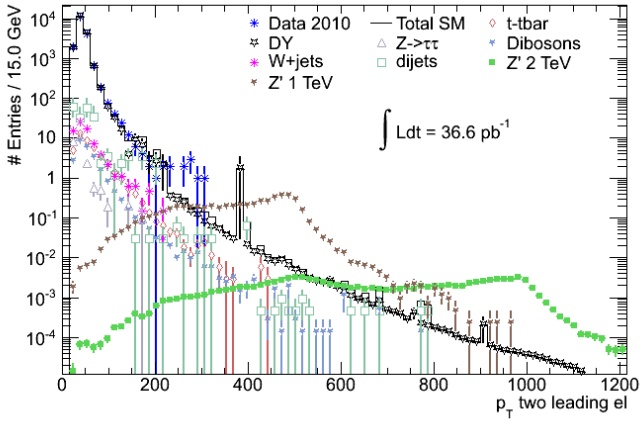

(c) Electron p_T. The SM background is divided into constituents and two Z's are shown (1.0 and 2.0 TeV).

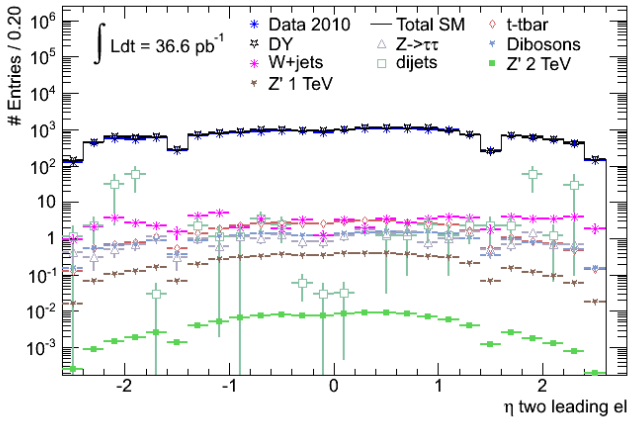

(d) Electron η. The SM background is divided into constituents and two Z's are shown (1.0 and 2.0 TeV).

Figure 7.9: The p_T and η distributions for the two leading electrons after cuts 1 up to and including 8 (table 6.9). The data deficit is 6.2%.

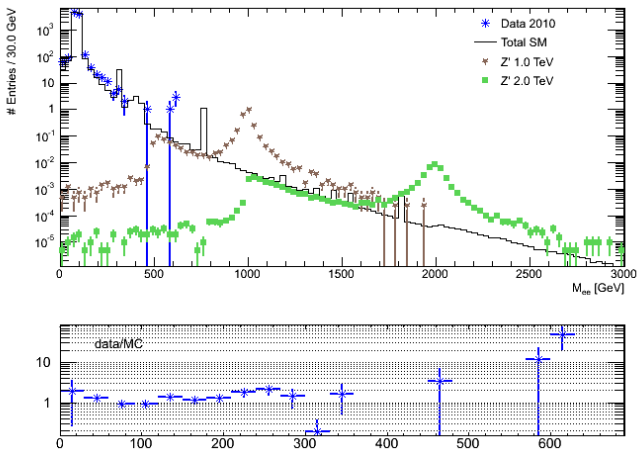

(a) Dielectron invariant mass.

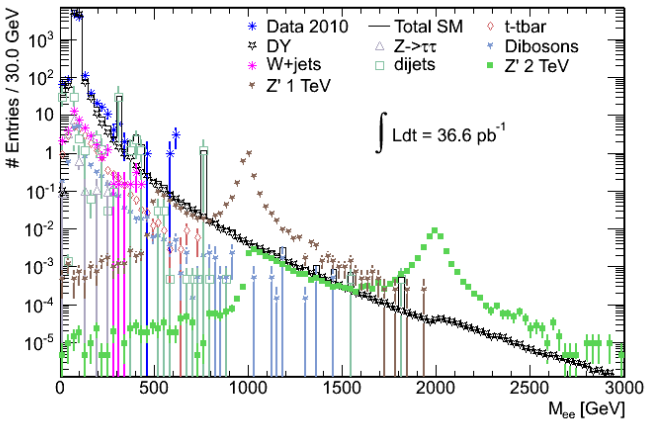

(b) The SM contribution is divided into its constituents.

Figure 7.10: The invariant mass distribution in the electron channel after all cuts (table 6.9). The datapoints account for 92.6% of MC.

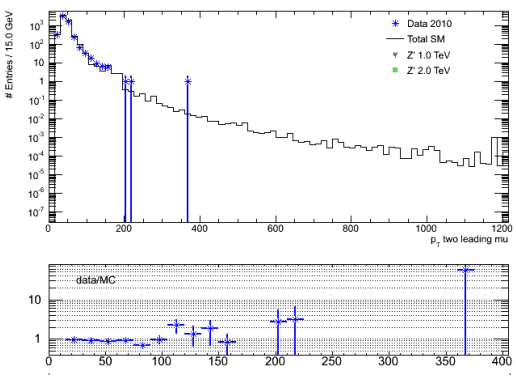

(a) Muon p_T

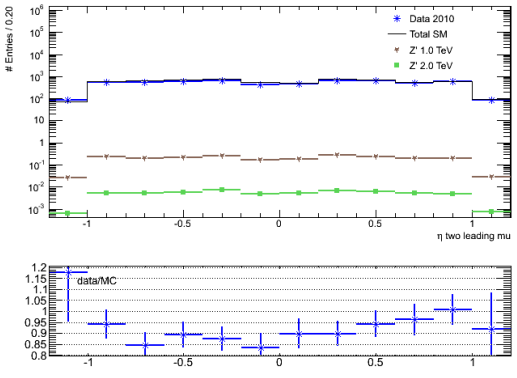

(b) Muon η

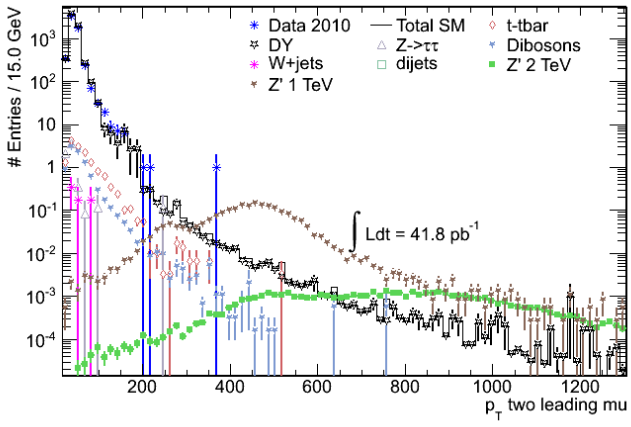

(c) Muon p_T. The SM background is divided into its constituents and two Z's are shown (1.0 and 2.0 TeV).

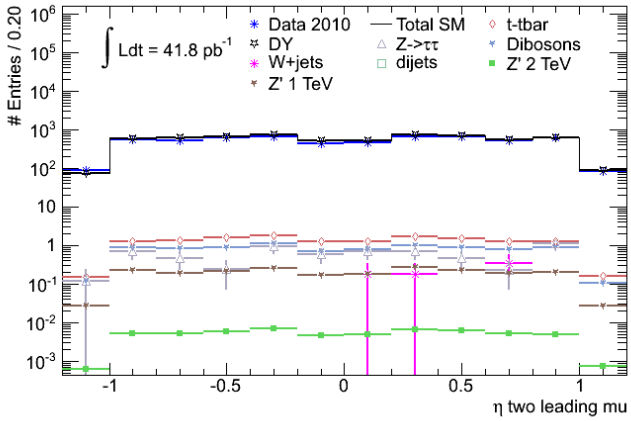

(d) Muon η. The SM background is divided into its constituents and two Z's are shown (1.0 and 2.0 TeV).

Figure 7.11: The p_T and η distributions for the two highest p_T muons after cuts 1 up to and including 10 (table 6.10). The data deficit is 8.8%.

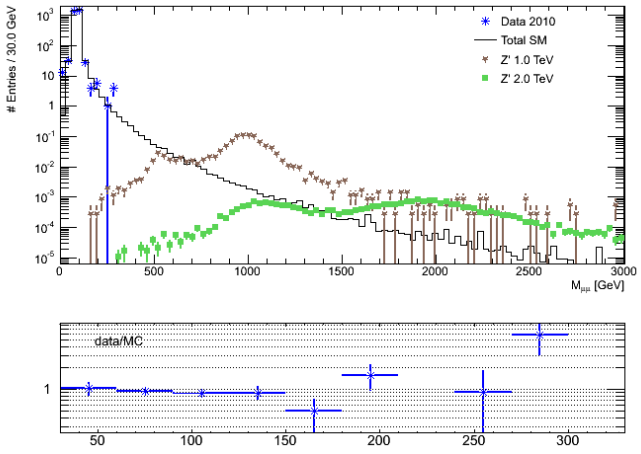

(a) Dimuon invariant mass.

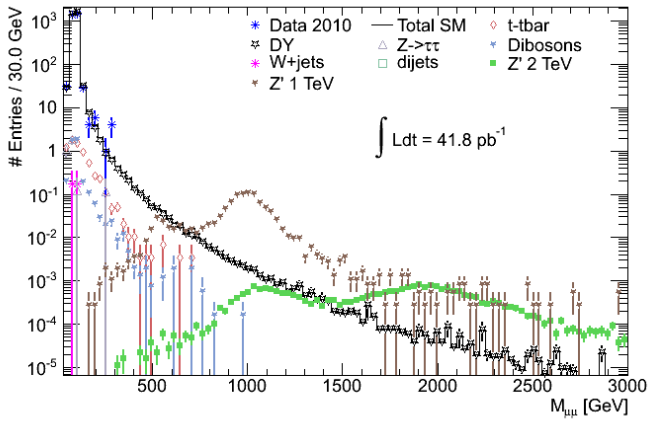

(b) The SM contribution is divided into its constituents and two Z's are shown (1.0 and 2.0 TeV).

Figure 7.12: The invariant mass distribution in the muon channel after all cuts (table 6.10). The datapoints account for 90.7% of MC.

7.4 Discovery reach

As we did for 10 TeV center of mass collisions in section 5.8, we now proceed to find the discovery reach for new neutral gauge bosons at 7 TeV center of mass collisions.

We use the same expression for the significance as we did before (equation (5.10))

$$S = \sqrt{2[(s+b)\ln(1+s/b) - s]} \tag{7.1}$$

We define a signal region using a lower limit of the invariant mass. The mass window is optimized for significance (i.e. the lower limit on the mass window that gives the highest significance, is chosen). The results are listed in table 7.7. When combining the two channels, the mass windows for each channel is used and the number of signal and background events are added.

Z' mass [TeV]	0.75	1.0	1.25	1.5	1.75	2.0
$M_{ee}^{\min}$ [TeV]	0.63	0.92	1.18	1.37	1.61	1.84
$M_{\mu\mu}^{\min}$ [TeV]	0.62	0.85	1.05	1.24	1.43	1.64

Table 7.7: The signal region is defined using a lower limit on the invariant mass. The window is found by maximizing the significance (equation (7.1)). The lower mass limits are given for the electron channel ($M_{ee}^{\min}$) and the muon channel ($M_{\mu\mu}^{\min}$).

Figure 7.13 shows the amount of integrated luminosity needed to discover a Z' with masses ranging form 1.0 TeV to 5.0 TeV. We assume a discovery is made when the significance is at least 5. The figure also shows the discovery reach when requiring 5 sigma *and* at least 10 signal events. Waiting until 10 signal events are accumulated is not a rule, but it is customary not to claim discoery based on a few signal events only.

When requiring only 5 sigma, we see that about 50 pb^{-1}is needed to discover a 1.0 TeV Z' using the combined channels, which means that it is almost within reach today. If Nature chose a 2 TeV Z', we need 4 fb^{-1}. At the end of 2011 we should have collected at least 2 fb^{-1}, meaning we can discover a 1.8 TeV Z'.

Requiring at least 10 signal events means the corresponding numbers are $\sim$100 pb^{-1} and 7-8 fb^{-1} to discover Z's of masses 1.0 TeV and 2.0 TeV respectively, and a 1.65 TeV Z' can be discovered with 2 fb^{-1}.

7.5 Exclusion limits

In section 7.4 we computed the integrated luminosity needed to discover a Z' with a certain mass range from 1 TeV to 2 TeV. We now ask the question of how large a Z' mass we can *exclude*.

To do this we define a null hypothesis "H_0 : Background only" and an alternative hypothesis "H_a : Signal plus background" and use the number of observed events in the signal region

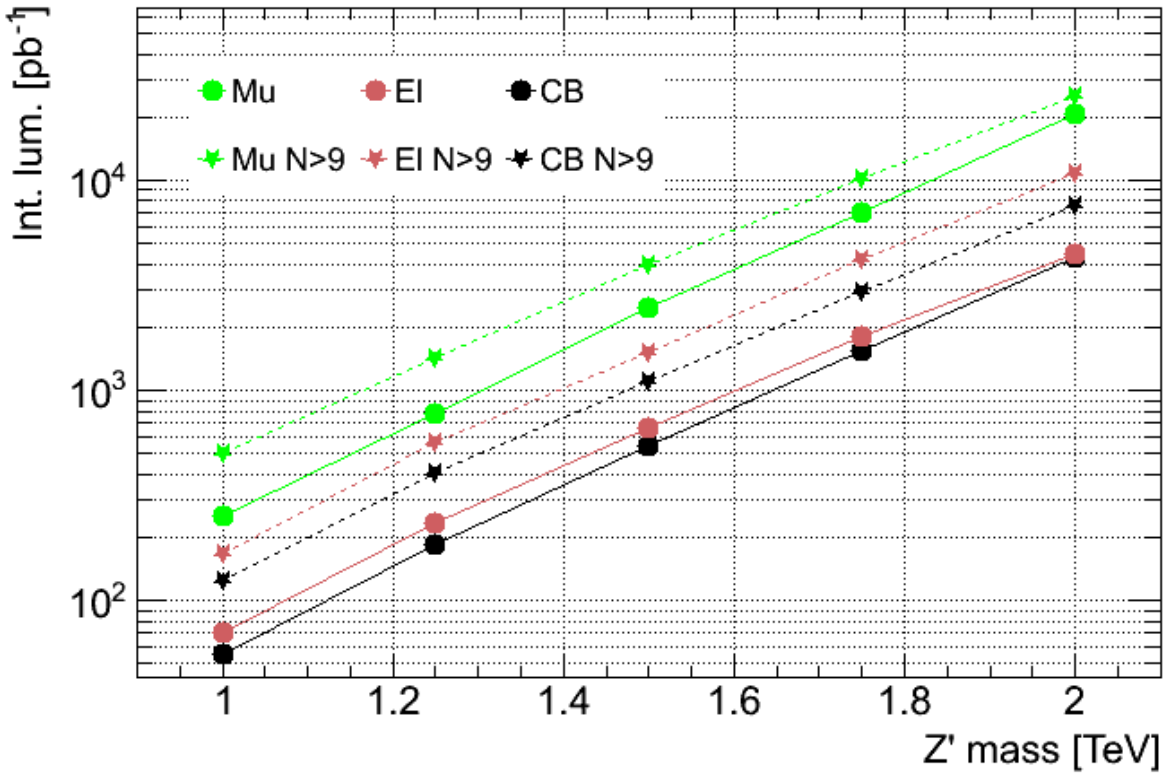

Figure 7.13: The integrated luminosity needed to discover a Z' with mass ranging from 1.0 TeV to 2.0 TeV. Results are shown for electron channel (brown), muon channel (green) and the two channels combined (black). The solid lines are for a significance of 5, and the dotted lines are for 5 sigma *and* at least 10 signal events.

as a test statistic. Remembering from section 5.8 that the number of observed events is distributed according to a Poisson distribution we can calculate the p-value (the blue area in figure 7.14, illustrating the probability of drawing n_{obs} or an even more extreme value from a Poisson distribution with expectation value $s + b$)

$$p = \sum_{k=0}^{n_{\text{obs}}} \frac{(s+b)^k e^{-(s+b)}}{k!} \tag{7.2}$$

H_a can be excluded at a $1 - p$ confidence level (CL). Usually one uses a CL of 95%.

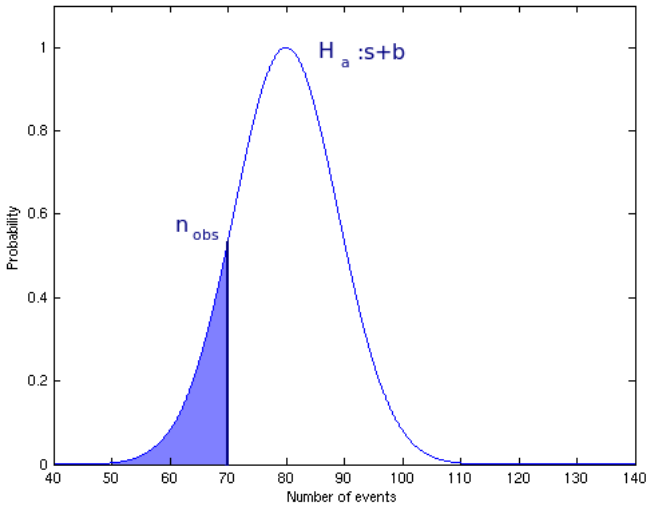

Figure 7.14: The number of events are distributed according to Poisson statistics. In this figure, the most probable value is $n = 80$. If 70 events are observed, we can calculate the probability of $n_{\text{obs}} \leq 70$ given the background plus signal hypothesis H_a using equation (7.2). This probability is illustrated by shaded area in the figure.

A problem appears when the number of observed events is less than what is expected from H_0, the background only hypothesis. If H_0 can be excluded at 95% CL, then *any* H_a predicting a positive number of signal events is excluded with *at least* 95% confidence (see figure 7.15). This is not a good situation. To correct for this, the CL_s method was developed[42].

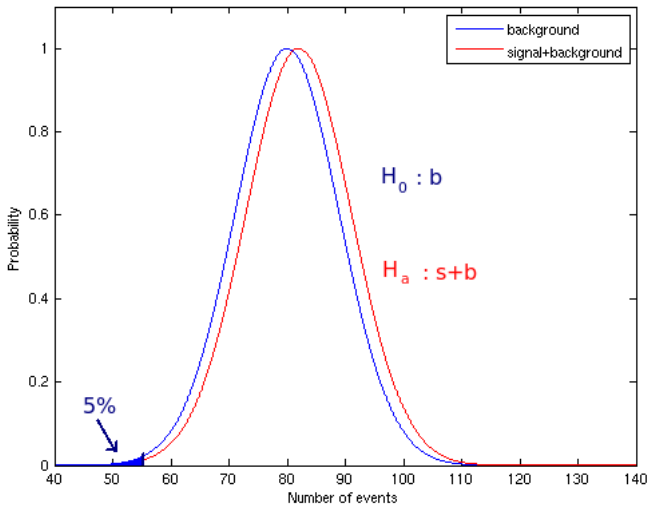

Figure 7.15: If the background only hypothesis (H_0 : b) can be excluded with 95% confidence, *any* hypothesis H_a : s+b predicting a positive number of signal events is excluded with *at least* 95% confidence.

7.5.1 The CL_s method

We now normalize the observed confidence level for alternative the hypothesis H_a : s+b, CL_{s+b}, to the confidence level observed for the null hypothesis H_0 : b, CL_b (see figure 7.16)

$$CL_s \equiv CL_{s+b}/CL_b$$

CL_s is a ratio of confidence, not really a confidence level, but H_a is considered excluded at the confidence level CL when

$$1 - CL_s \geq CL$$

It can be shown that the false exclusion probability is less than $1 - CL$. When encountering the situation described above, with a large downward fluctutation of the background and the expected number of signal events close to zero, the value of CL_s is close to 1, thus avoiding the problem.

7.5.2 Z' exclusion limits

Using the same signal region as in section 7.4 (table 7.7) and the CL_s method, we find the smallest number of events that is excluded at 95% CL[1].

[1] 95% is the usual value one chooses for exclusion.

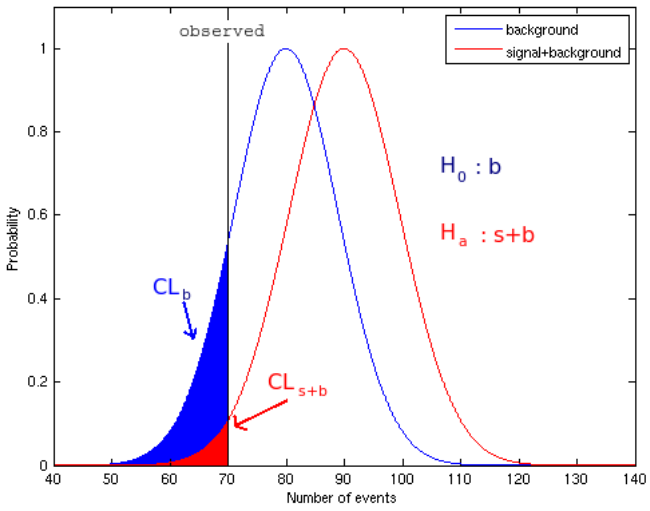

Figure 7.16: The colored areas illustrate the concept of confidence levels, CL_b (blue) and CL_{s+b} (red). A CL is a quantitative way of telling how much confidence we have in a hypothesis.

Finding the smallest number of events that is excluded with 95% confidence can be illustrated by considering figure 7.16: Keep the blue distribution (H_0: b) fixed while varying the red distribution (H_a: s+b) until CL_s reaches 5%. All theories predicting at least s signal events are then excluded.

The result is shown in figure 7.17. SSM Z' with mass up to 995 GeV is thus excluded at 95% CL.

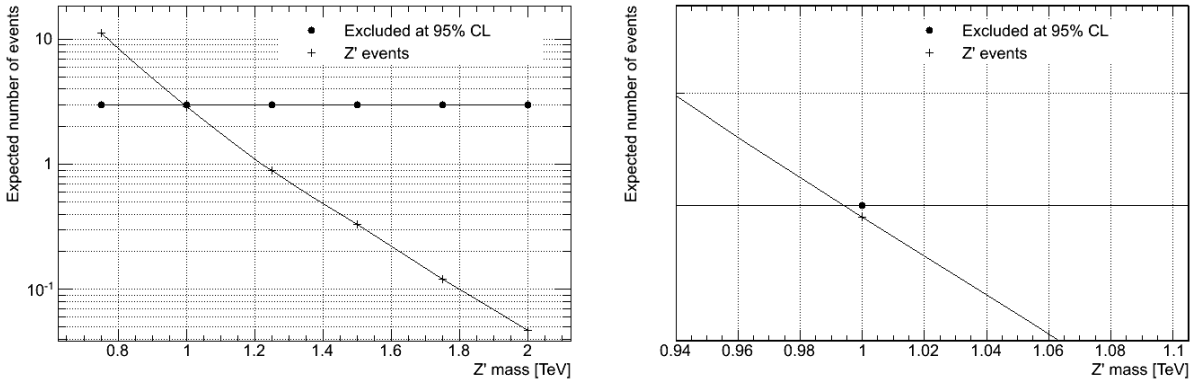

(a) (b)

Figure 7.17: "Z' events" is the number of events from the Z' with a given mass. "Excluded at 95% CL" corresponds to CL_s= 5%.

7.6 Summary

In this chapter we have analysed the 2010 data with focus on the discovery potential for the hypothetical new gauge boson Z'. Using cuts as agreed upon by the exotics dilepton subgroup as of January 2011 we extracted the discovery reach of the Z' with mass ranging from 1.0 TeV to 2.0 TeV, and we used the 2010 data to exclude SSM Z's up to mass 0.995 TeV.

Conclusions and outlook

In this thesis we started with two introductory chapters to the physics the analyses are based on. Chapter 1 described the theoretical framework that the current theory of particle physics is based on, namely that of the Standard Model. Chapter 2 went beyond the Standard Model and introduced a few popular theories, including the theories giving rise to the most common Z' bosons.

The next two chapters, 3 and 4, covered the topics of particle interaction with matter and the ATLAS detector respectively. The former introduced how particles can be detected, and the latter how it was technically done in ATLAS.

In chapter 5 we performed a feasibility study at 10 TeV center of masss collisions for a hypothetical new neutral gauge boson in the model used as a standard candle in many searches, i.e. the Sequential Standard Model (SSM) Z'. This section is based solely on Monte Carlo simulations. We reviewed the SM backgrounds that are expected to be non-negligible and used optimized cuts to suppress them while keeping as much signal as possible. The angular distribution was extracted, and we concluded that more than 1 fb^{-1} was needed to deduce the spin of the resonance. Final conclusions were that 38.6 pb^{-1} was required to discover a 1.0 TeV SSM Z' at 10 TeV center of mass collisions, while the corresponding integrated luminosity for a 1.5 TeV Z' was 280 pb^{-1}. No systematics were taken into account.

The 2010 data were taken at 7 TeV center of mass collisions, and in chapter 6 we analysed this data with focus on the Z^0 resonance using cuts mainly as agreed upon by the ATLAS SM working group. We found 9143 $Z^0 \to e^+e^-$ and 13524 $Z^0 \to \mu^+\mu^-$ candidates in 37 pb^{-1} and 42 pb^{-1} of data respectively. Data were found to be consistent with MC simulations. The invariant mass distributions in both channels were fitted with a Breit-Wigner convoluted with a Gaussian, and the detector resolution was extracted. Our results were found to be in agreement with the public results from the ATLAS collaboration.

In chapter 7 we performed a somewhat different analysis on the same data as in the previous chapter. The cuts used were mainly the ones agreed upon by the ATLAS exotics dilepton subgroup as of January 2011. The agreement between MC and data was enhanced by a few percent. We extracted the discovery reach of the SSM Z', and found that 50 pb^{-1} were needed to discover a 1.0 TeV Z', while 2 fb^{-1} were needed if Nature chose a Z' mass of 2.0 TeV. During 2011 we will collect a minimum of 2 fb^{-1} which means that a discovery of a 2.0 TeV Z' can be made in 2011 already, and that of a 2.0 TeV Z' early in 2012. A SSM Z' with mass below 0.995 TeV was excluded using the CL_s method. Note that no systematics were taken into account.

Outlook

The whole data analysis was performed with reconstruction R15, and as mentioned in chapter 6, reconstruction R16 is now available, offering many improvements, like better alignment and resolution. In light of these improvements, the analysis of chapter 7 should be redone. The biggest improvement would probably come as a result of including the whole pseudo-rapidity range, $|\eta| < 2.4$, for muons. This would give both a higher discovery reach and exclusion limit.

All analysis results in this thesis are too optimistic because systematic uncertainties are not included. There are three main sources of systematics. First of all there is the uncertainty on the luminosity, which is approximately 11%. Secondly, the extrapolation of the Parton Distribution Function to higher momentum transfers (between the partons) than what has been measured before, is associated with an uncertainty. And lastly there is the uncertainty connected to all efficiencies and cuts; for example when requiring isolated leptons, what fraction of leptons from the signal passes the cut.

As higher luminosities are reached, pile-up starts to become an issue, as previously mentioned in section 6.3.2. The analyses of chapter 6 and 7 should be redone with pile-up MC.

In this thesis we only considered the SSM Z'. The time consuming task of comparing different models predicting Z's would be a nice complement to the analyses. To differentiate between models we would need to use a correction on the angular distribution discussed in section 5.7. One such correction is mentioned in reference [37]. The general idea is to extract from MC truth the probability as a function of the rapidity Y, $\epsilon(Y)$, to be wrong when taking the Z' direction as the direction of the incoming quark. Defining N_+ (N_-) to be the number of events with the outgoing l^- in the forward (backward) direction, we write the number of observed $N_\pm^{\text{obs}}$ as a function of the number $N_\pm^{\text{gen}}$ at the generation level and the probability ϵ

$$N_\pm^{\text{obs}} = N_\pm^{\text{gen}}(1 - \langle\epsilon\rangle) + \langle\epsilon\rangle N_\mp^{\text{gen}}$$

where $\langle\epsilon\rangle$ denotes the mean value of ϵ. Using the definition of the forward-backward asymmetry $A_{\text{FB}} = (N_+ - N_-)/(N_+ + N_-)$ we get

$$A_{\text{FB}}^{\text{obs}} = (1 - 2\langle\epsilon\rangle)A_{\text{FB}}^{\text{gen}}$$

Using this knowledge, a corrected forward-backward asymmetry is defined

$$A_{\text{FB}}^{\text{corr}} = \frac{1}{1 - 2\langle\epsilon\rangle}A_{\text{FB}}^{\text{obs}}$$

This method gives good results, as shown in page 21 of reference [37].

Final thoughts

I have learnt a lot during these last couple of years, but there are still things I feel should have been explored. Some examples are listed below:

I never understood why the charge misidentification probability for muons is close to zero. It seems logical at first - the muon spectrometer measures the muon track over a longer distance than the inner detector does. Thus it should be easier to determine the bending of the track. But even when I consider the inner detector track of the muon, the charge misidentification rate is close to zero. It seems apparent that the reconstruction algorithm compares the charge as measured in the muon spectrometer (MS) and inner detector (ID) separately and does something clever. Given more time, this is something I would like to understand.

In chapters 6 and 7 I used solely the MS measurement of the p_T. This is what was agreed on within the ATLAS dilepton working sub-group, but I also used it in the Z^0 analysis. The reason for using the MS measurement only is poor alignment. Thus I should have restricted the pseudorapidity accordingly, using only $|\eta| < 1.05$. Or I could have used the full pseudorapidity ($|\eta| < 2.4$) and the combined p_T measurement. But I should not have combined it the way I did.

Also regarding chapter 6: the SM working group also uses dielectron pairs where one has author 1 or 3 and the other has author 8 (meaning reconstructed by the forward algorithm, allowing pseudorapidities up to 4.8). I did not. Furthermore, when fitting the Z^0 invariant mass distributions I would use a convolution of a Breit-Wigner and a Crystall Ball if given more time.

Last but not least - almost all statistical errors I have presented are based on the Poisson approximation. For example in the cut flow tables. These should have been binomial. The reason being the following: take a $Z' \to e^+e^-$ sample. The probability of observing what we are looking for, dielectrons, in a $Z' \to e^+e^-$ sample is very high. Because the probability of success is high, the Poisson distribution is not a valid approximation - the number of observed events follow the binomial distribution.

Appendix A

Training for SCT shifts

Unless stated otherwise all info is taken from training manuals avaiblable on the ATLAS TWiki.

While the SCT is on, it is continuously under control and monitoring such that any problems can be solved as quickly as possible. This is important not only to ensure good conditions during data taking, but also to ensure the SCT is not damaged in any way.

There are three shifts a day, covering the time slots 7 a.m to 15 p.m, 15 p.m to 11 p.m and then 11 p.m to 7 a.m. Before one is allowed to do shifts, one has to do the SCT shift training. It consists of four parts - DCS (Detector Control System), DAQ (Data Aquisition), DQM (Data Quality Monitoring) and cooling - corresponding to the four somewhat different items one has to monitor during a shift.

Figure A.1 shows me in the ATLAS control room (ACR), on a shadow shift. It was in November 2010, rigth at the end of the heavy ion run.

A.1 Detector Control System

There are two main interfaces to the DCS - the Finite State Machine (FSM) Panel (figure A.2) and the Alarm Panel.

The FSM covers the entire SCT. It is organized in a tree structure. At the top level is ATLAS. The subdetectors, including SCT, are children of ATLAS. Within the SCT there are three so-called TTC (Trigger Timing and Control) partitions - the Barrel, Endcap A and Endcap C.

Within each of these are subsystems controlling all important aspects. The environmental monitoring (ENV) monitors humidities and temperatures around the SCT. The temperatures in question are the mechanical temperatures (of the physical SCT, modules, cables etc), the air temperature (the gas inside SCT) and at the exhaust of the cooling loops. ENV can interlock the system if the exhaust temperature is too high, switching off the affected

Figure A.1: Me in the ACR on a shadow shift in November 2010.

modules to prevent any damage. The power supply (PS) system controls all the power supplies. There are 4088 of them, one per SCT module.

One of the shifters duty is in general to check for alarms using the Alarm panel. If anything is out of the ordinary in the FSM interface, the shifter takes action against it and reports the findings in the ATLAS E-log, an online database of the detector status.

When manipulating the beam in any way there are special procedures to follow. Before beam injection the high voltage (giving the bias to the SCT modules, nominal value 150 V) must be at STANDBY (50 V) and the beam protection must be enabled. When the beam is stable, the background noise is below a certain threshold and the beam is stable, the HV can be ramped up to the nominal value. After this the SCT detector takes "physics quality" data on which offline analyis are run. When the beam is dumped, either planned or unplanned, the SCT will keep the HV on for a few minutes and then ramp down.

A.2 Data Acquisition

The SCT Data Acquisition (DAQ) system is responsible for controlling, configuring and calibrating the 6.3 million silicon strips that are within the SCT. In a physics run it also acts as a communication channel between hit strips and the high level trigger system - if a level 1 trigger has fired, the information reaches the DAQ requesting tracking information from the SCT. The DAQ will then get the tracking information from the silicon strips and pass it onwards to the high level trigger.

The ATLAS DAQ is arranged into different partitions that can run independently of each

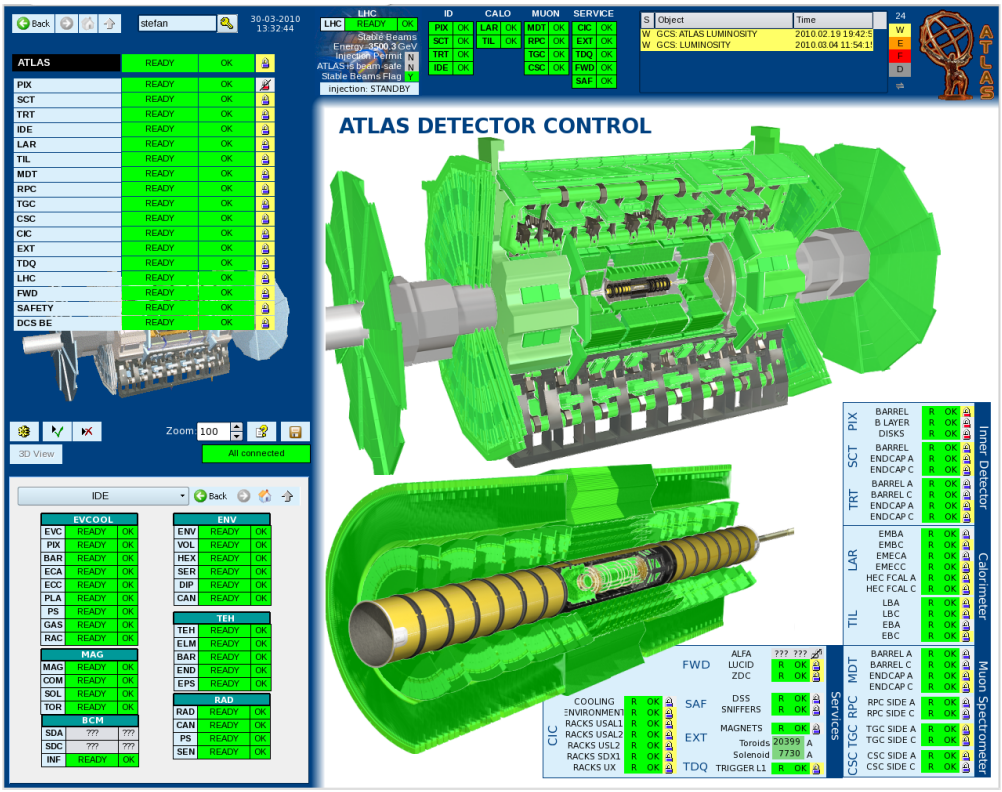

Figure A.2: The Finite State Machine (FSM) that represents the whole ATLAS detector monitors the environmental parameters such as temperature and umidity, and monitors and controls the power supply.

other. A partition can contain the subdetectors (which is the case when ATLAS is taking data), or it can containt only some or one of the subdetectors. This way the SCT can be run completely independently of the rest of the detector and even of the other parts of the inner detector, the Pixel and TRT. This is what is done when calibrating the SCT.

There are multiple tests to run to find out if and how the modules are functioning and to repair them if needed. The interface is shown in figure A.3. For example a 2D optical scan is performed. Out of 2000 triggers sent out, how many are returned when varying the Rx threshold (how much light is needed to detect a signal) and the Rx delay (how long to wait before the signal is received), see figure A.4. The system automagically sets new optimized values if needed.

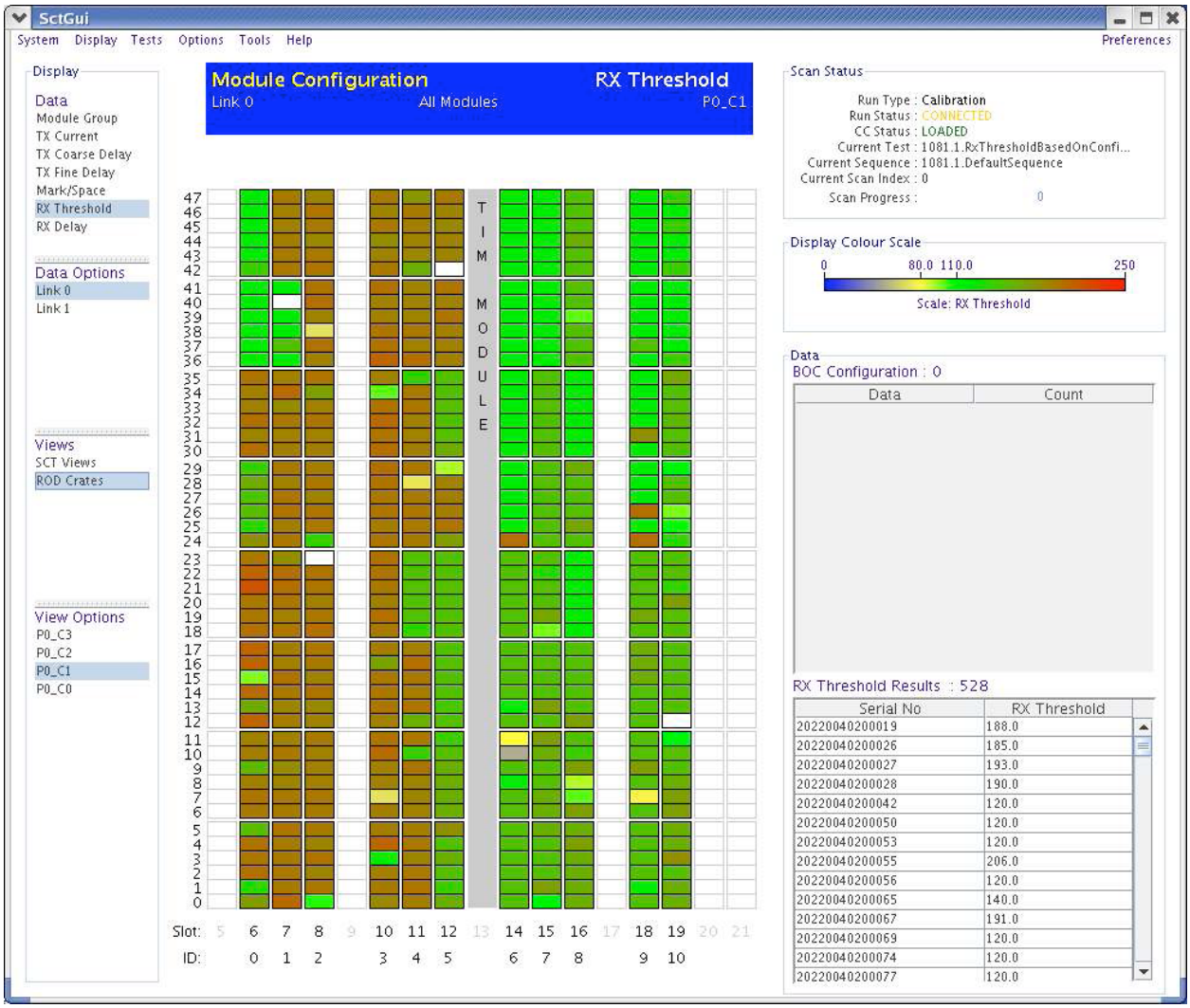

Figure A.3: The main interface to the DAQ, the SCT gui, being used in a calibration run to test the Rx (receiver) threshold, i.e. how much light is needed to detect a signal.

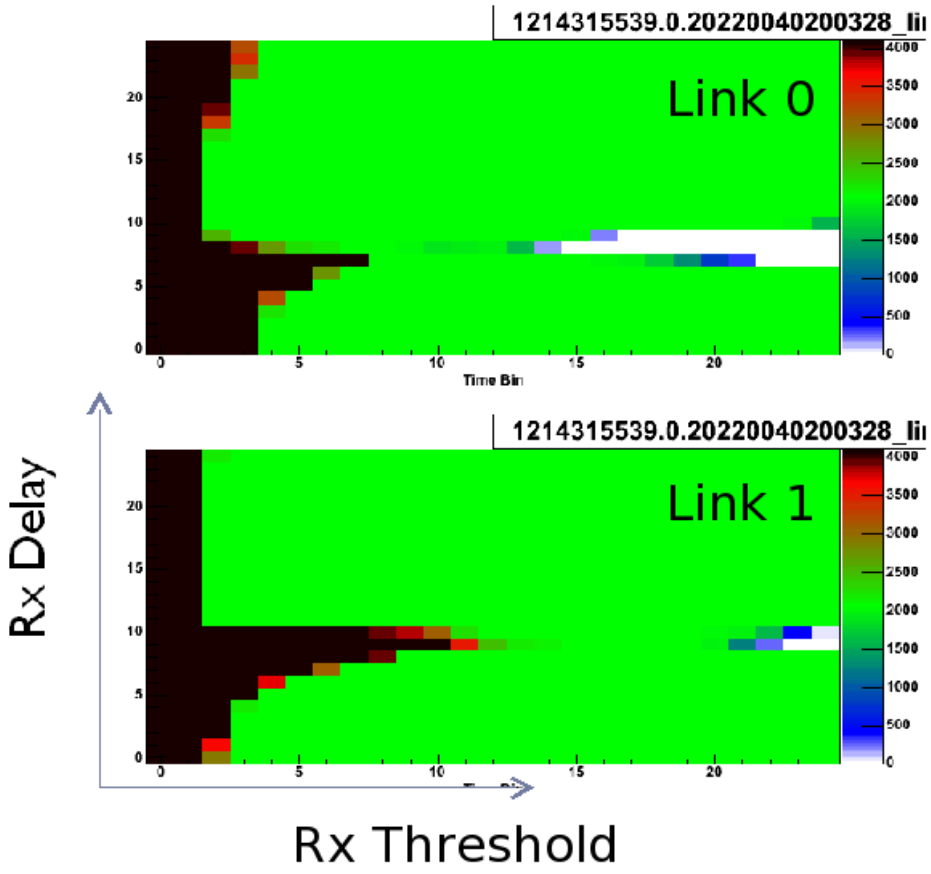

Figure A.4: An example of the 2D optical scan. 2000 triggers (in the form of 2000 zeros and 2000 ones) are sent to the SCT and the number sent back is counted. The green area represents 2000 returning triggers, which is just what we want. The black area means 4000 triggers were sent back. This happens when the Rx threshold is too low. Then even the zeros will be interpreted as triggers. The white area means that 0 triggers are returned. This is the result of an unlucky chosen Rx delay. Imagine a square pulse as a function of time. The readout should not be at the edge of this pulse, then the result will be arbitrary. The two plots represent each of the two Rx (readout) links on the modules.

A.3 Data Quality Monitoring

This part of the SCT shifter duties consists of checking that the data read out from the modules looks sensible. If a problem is spottet, this should be investigated further, reported to the DQM experts, and inserted into the e-log. Every hour one has to check a number of things, for example if there are any noisy or inefficient modules, or modules with error.

As a concrete example, consider the time bin plots (figure A.5): The L1 trigger fires and a request is sent out to the SCT DAQ for the track information, the SCT information is read out for three timebins of length 25 ns. Ideally all SCT signals should be in the timeslot for which the trigger fired, but sometimes it is in the timeslot before or after or even covering two timeslots. Figure A.5 shows a histogram of this type for the barrel. If the signal arrives in the 25 ns timeslot before the trigger fires it will fill the 100 bin. If it arrives in the right timebin it will fill 010, and if it arrives in the timebin after it will fill 001. If the signal extends over the two last timebins, it will fill 011, and so on. The ideal situation is a high peak around 010. As an example, if the trigger occurs 10 ns after the signal there will be about the same number of entries in bins 010, 011 and 001.

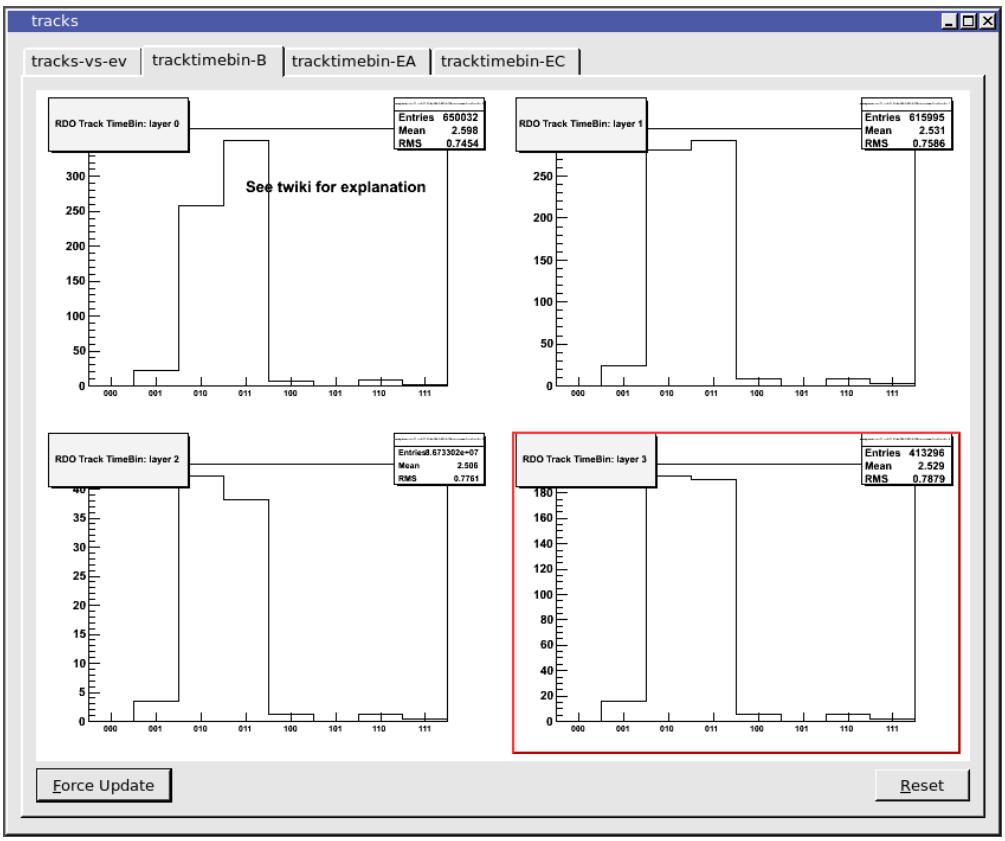

Figure A.5: Binary hit pattern for hits on tracks. Most of the hits should be in the 010 bin. This means that the SCT records hits at the correct time in comparison to the time at which the trigger fired.

A.4 ID General

The fourth and last thing the shifter has to be in control of is the cooling, called the IDE Evaporative Cooling DCS. It monitors and controls the system that cools down the Pixel and the SCT subdetectors. It is composed of 204 independent loops divided in the following way: 88 to cool down the Pixel detector, 44 to cool down the SCT barrel sector and 36 to cool down each of the two SCT endcaps.

Shifter duties include monitoring the level of coolant liquid, checking for communication difficulties between the cooling system and the FSM and checking for general errors, like malfunctioning fan trays and rising temperatures.

Appendix B

Hands on Particle Physics Masterclasses

B.1 International

Hands on Particle Physics Masterclasses are an offer to about 6000 high school students in 23 countries to come to a nearby university or research center to have a look at how a particle physicist works. I assisted at these events in 2009 and 2010.

A few introductory lectures are given first, about particle physics and detection of particles. After the lectures, the students are divided into small groups. Each group is given 100 Z decay events taken from real LEP data as recorded by the DELPHI detector. The idea is to categorize the Z decays into dielectron (e^+e^-), dimuon ($\mu^+\mu^-$), ditau ($\tau^+\tau^-$) and two ($q\bar{q}$), three ($q\bar{q}g$) and four jet decays ($q\bar{q}q\bar{q}$, $q\bar{q}gg$). To do this they are given a graphical user interface (GUI, figure B.1) called WIRED showing the events. The GUI gives information about the center of mass energy in the collision, the number of tracks in the detector and the total reconstructed energy. The students can turn on and off different detector parts to figure out where the energy was deposited and hence what kind of particle it was. As an aid for the eye, neutral "tracks" are also depicted.

After all the groups have gone through their events, all the information is collected and combined and the branching ratios to all the decay modes are calculated.

Given enough time and interest from the students the strong coupling constant α_s is calculated using the Z decays to two and three jets

$$\alpha_s = k\frac{N_{3-\text{jets}}}{N_{2-\text{jets}}} \tag{B.1}$$

where $N_{2-\text{jets}}$ and $N_{3-\text{jets}}$ are the number of two and three jet events respectively, k is a constant that depends on the program grouping particles in jets. The constant k is dependent on another parameter d_{join}, which is reported to be $d = 5 + mathrmGeV/c$ for the events in WIRED. The students can then get the correct value for k by checking agains the graph in figure B.2.

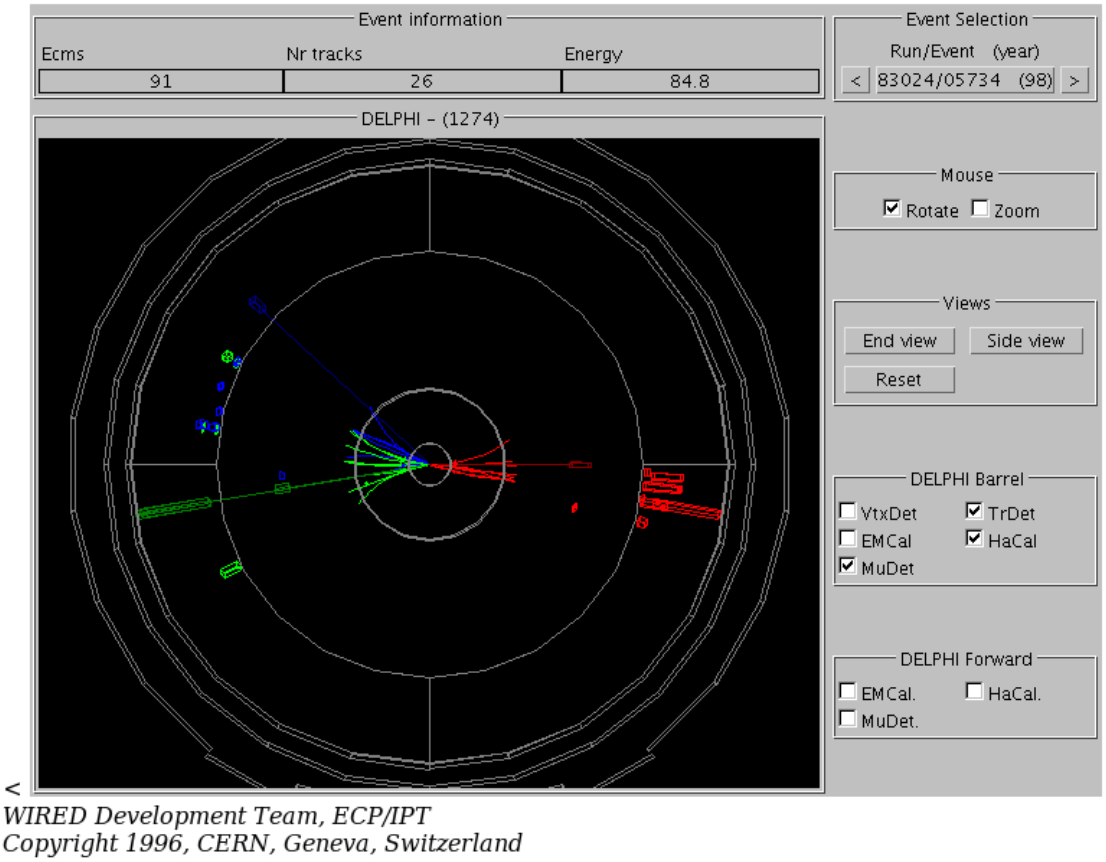

Figure B.1: The graphical user interface (WIRED) showing Z decays to electrons, muons, taus and quarks in the DELPHI detector. Different detector parts can be turned on and off, and the event can be rotated and zoomed.

At the end of the day there is a video conference with CERN, where we together with a few other countries report and discuss our findings. In addition, there is a question session where the students can ask questions about CERN, general particle physics, detectors etc.

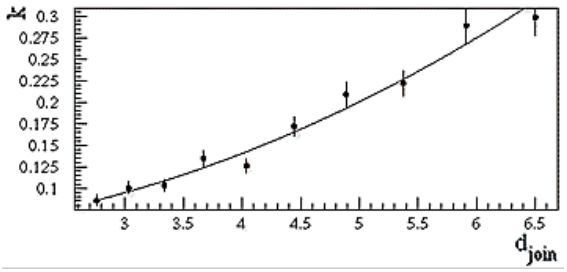

Figure B.2: The value of the constant k (equation (B.1)) depends on the value d, which is 5 GeV/c from the events in WIRED.

B.2 National

In a national masterclass 2010 a similar event took place, but this time with the LHC detector and simulated as well as real collision data.

In the morning the students got an introduction to the Standard Model and the ATLAS detector. The afternoon session consisted of hands-on exercises.

The first part of the practical session was based on simulated W and Z decays as well as one Higgs decay. The events were viewed in the Atlantis event display for ATLAS (figure B.3). After a short introduction to Atlantis, the students were asked to classify the events according to the decay channel, which could be e^+e^- or $\mu^+\mu^-$ for the Z, electron or muon plus missing E_T(due to the neutrino) for the W, 2 e^+e^- and/or $\mu^+\mu^-$ pairs for Higgs, or hadronic decays of the W or Z boson ("background").

We made sure all detector parts were on, but the students could rotate and zoom the events and turn on and off different cuts, for example p_T cuts in the inner detector. After all groups were finished, the results were compared. All groups correctly classified the Higgs event, and got more or less the same answers elsewhere.

In the second part we used, for the very first time, real data (Z decays) from the LHC and the ATLAS detector. We were not allowed to show them the full events, and made snapshots of the Atlantis event display with reasonable cuts turned on (figure B.4). In addition to this we put in a few simulated Z'events. The students went through some tens of events in small groups and punch the relevant numbers (particle type (electron, muon), angles and total reconstructed transverse energy) into an Excel sheet which calculated the invariant mass of the two leptons and put the event into a histogram. The result is showed in figure B.4 for the combined muon and electron channels. We see that the students found the Z^0at the correct mass. A small resonance structure showed up at higher invariant masses (not shown here), and we had a small discussion about the Z'.

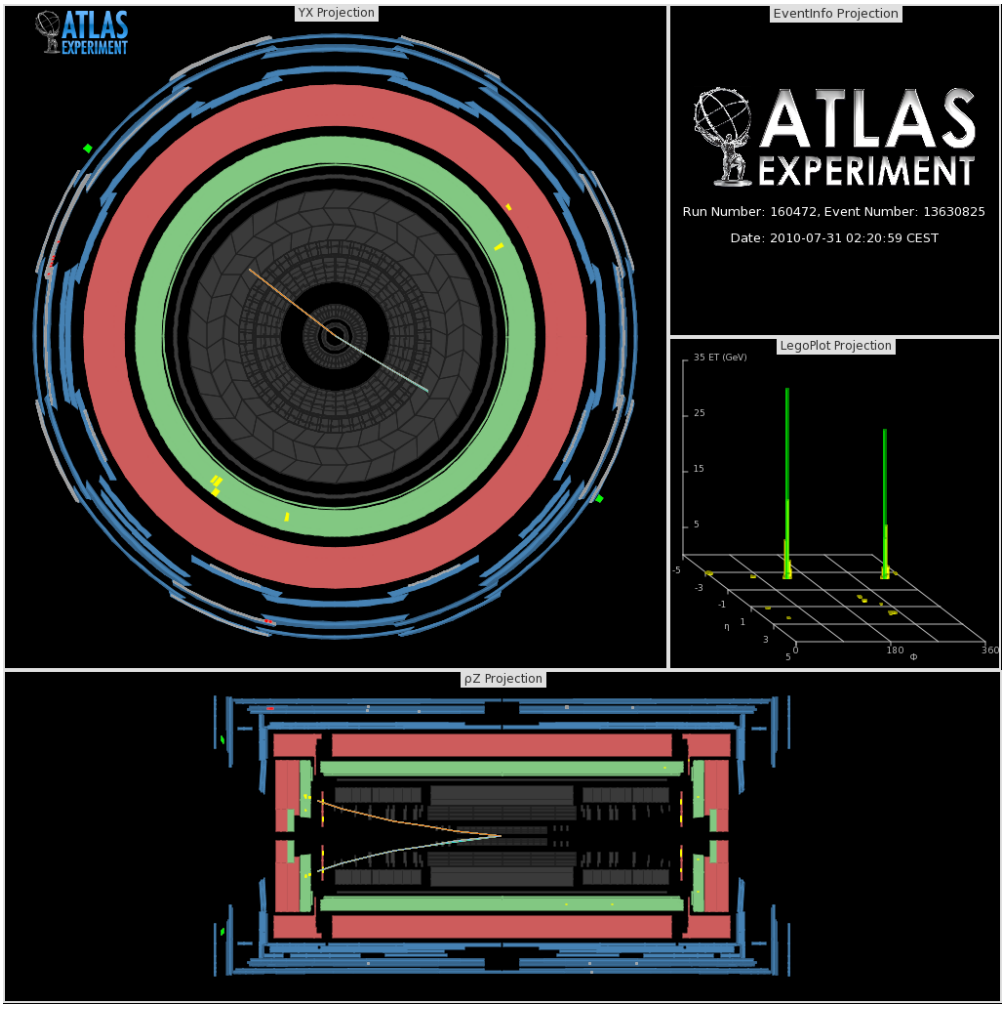

Figure B.3: The Atlantis event display for ATLAS

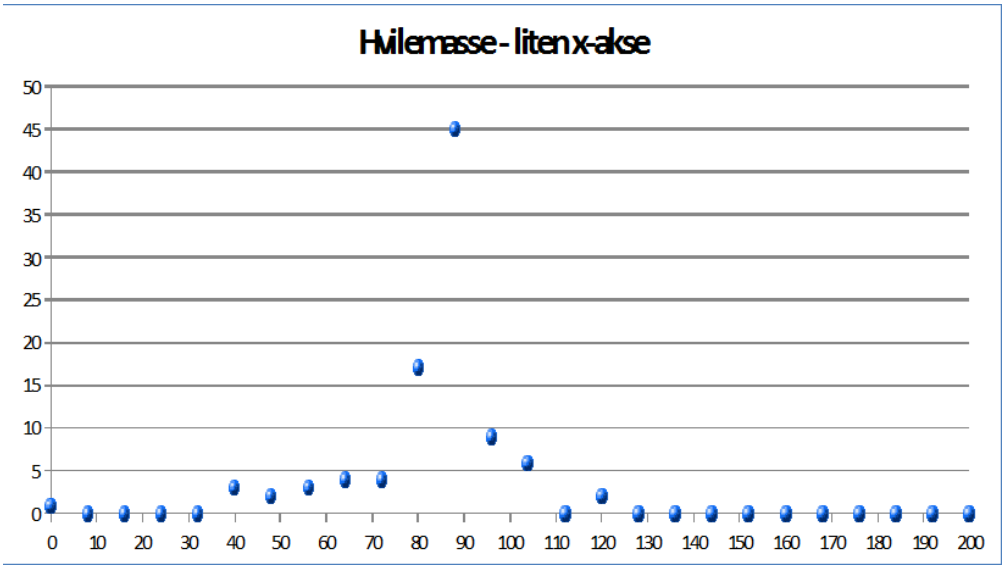

Figure B.4: The invariant mass of the Z.

Appendix C

Additional details

C.1 Old vs new electron identification variables

As we remember from section 5.4.1 the standard electron identification variables are called loose, medium and tight. In october 2010[1] it became clear the electromagnetic showers were broader in data than in the MC. As a result some of the identification variables in the loose identification are not modelled very well by data, giving a shift in the relevant distributions (lateral shower shape R_η and width $w_{\eta 2}$).

As a result up to 10% of the signal is lost in end-cap when using Event Filter (EF) triggers with loose identification. In addition offline analysis using these identification variables show discrepancy between data and MC. This discrepancy became very visible when running on D3PDs that were skimmed[2] on at least one loose electron with $p_T >$ 10 GeV. This removed more data than MC and showed up as a 25% discrepancy in the invariant mass plot in figure C.1

[1] http://indico.cern.ch/getFile.py/access?contribId=46&sessionId=12&resId=0&materialId=slides&confId=66744

[2] Skimming is removing events that does not satisfy certain criteria. An example of a skimming requirement is "at least one electron with $p_T >$ 10 GeV".

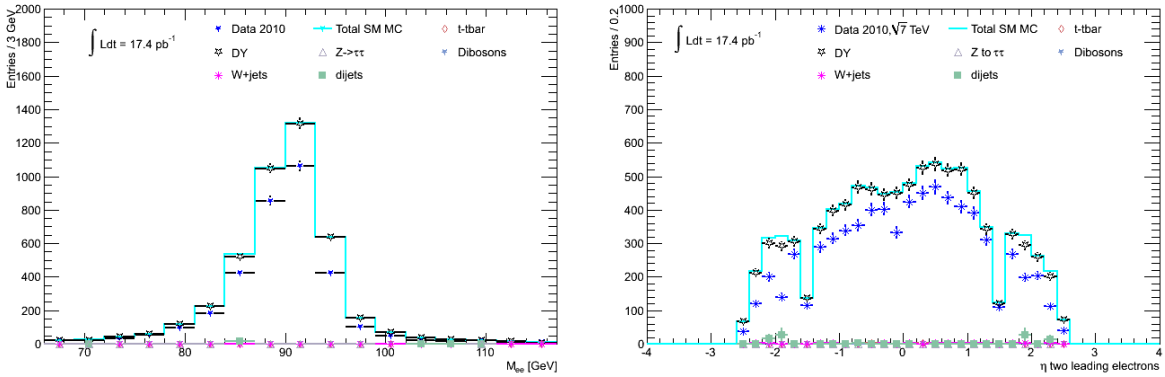

(a) Dielectron invariant mass M_{ee}

(b) η of two leading electrons

Figure C.1: The discrepancy between data and MC is large (MC/data = 0.75). This is caused by badly simulated shower shape variables - the electromagnetic showers turned out to be wider than expected. Thus the relevant variables in MC were too narrow. Because of this, the electron identification cut away more data than MC, giving the discrepancy as seen here.

C.2 Truth matching

The two highest $p_T$reconstructed electrons (passing all Z^0cuts up till number 10, see table 6.9) are matched with a truth particle by a simple truth matching algorithm checking if their separation in the η-ϕ plane, ΔR, is less than 0.2. This is a quite simple algorithm, one could easily imagine that a requirement on the separation in the ϕ and η planes separately was needed and for the difference in $p_T$to be within certain limits, but looking at the plots in figure C.2 of $\Delta\eta$ (C.2(a) and C.2(b)), $\Delta\phi$ (C.2(c) and C.2(d)) and Δp_T (C.2(e) and C.2(f)) we see that the distributions are very much peaked at zero, as they should be for a truth match.

The structure in figures C.2(a) to C.2(d) at $\Delta\eta \approx 0.14$ and $\Delta\phi \approx 0.14$ is caused by 0.14 being the maximum values of these variables in the symmetric $\Delta\eta$-$\Delta\phi$ case - $\sqrt{(2x^2)} \leq 0.2 \Rightarrow x \leq 0.14$.

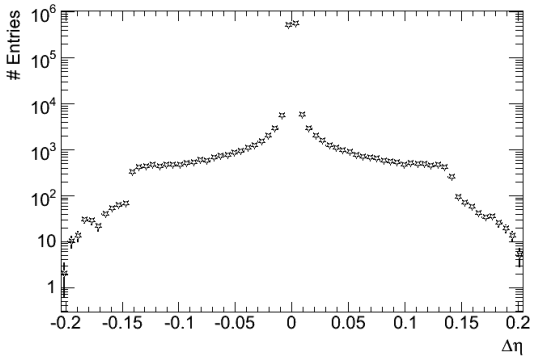

(a) $Z^0 \to e^+e^-$

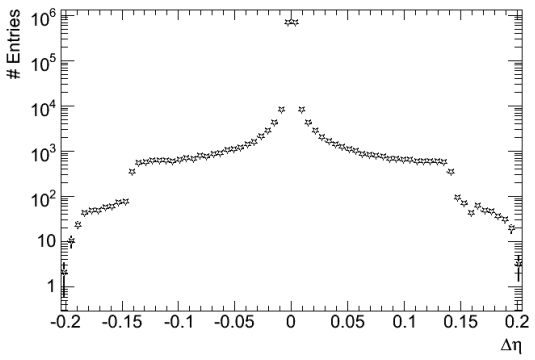

(b) $Z^0 \to \mu^+\mu^-$

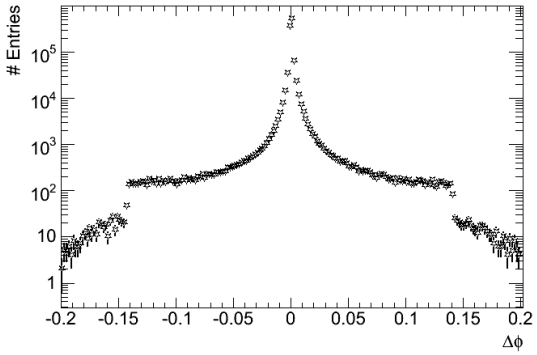

(c) $Z^0 \to e^+e^-$

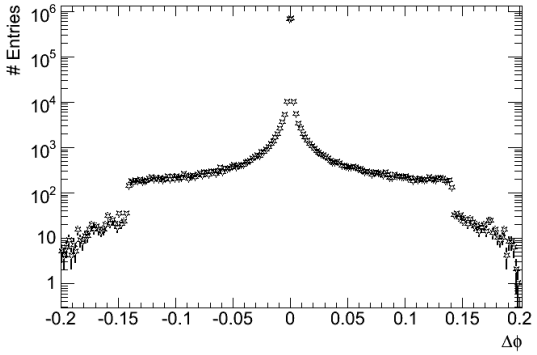

(d) $Z^0 \to \mu^+\mu^-$

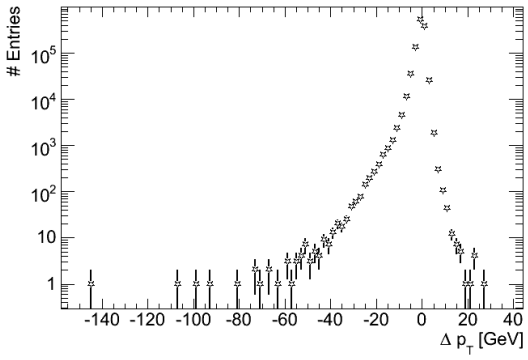

(e) $Z^0 \to e^+e^-$

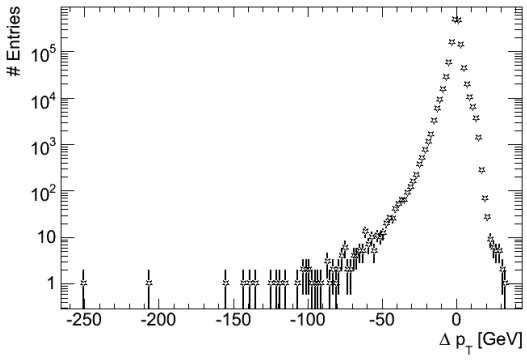

(f) $Z^0 \to \mu^+\mu^-$

Figure C.2: Truth matching is done by requiring the separation in the $\phi - \eta$, ΔR, to be less than 0.2. The figures show that the $\Delta\eta$, $\Delta\phi$ and Δp_T are small for the matches. Thus there is no need for a more complicated algorithm.

C.3 ATLAS plots

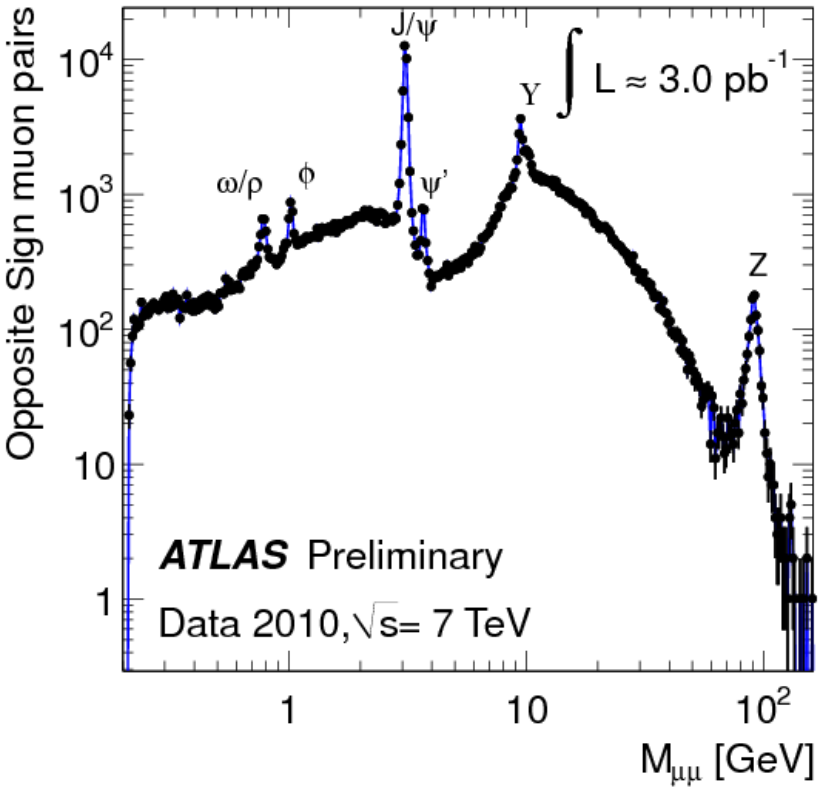

Figure C.3: Official ATLAS plot from the Combined Muon Performance group showing dimuon invariant mass spectrum from about 10 MeV to 100 GeV. 3 pb^{-1}of `L1_MU6` triggered events are used. All opposite sign combined muons passing the requirements of $p_T >$ 4 GeV for leading and $p_T >$ 2.5 GeV for subleading are used.

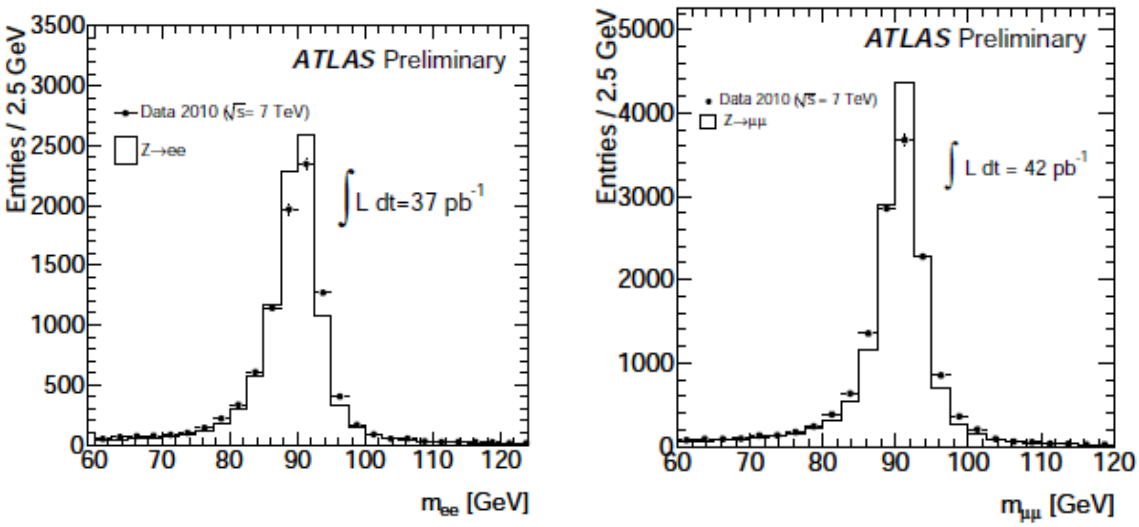

(a) Dielectron invariant mass

(b) Dimuon invariant mass

Figure C.4: Invariant mass of Z^0candidates in the electron (C.4(a)) and muon (C.4(b)) channels[41]. MC is normalized to the number of data entries.

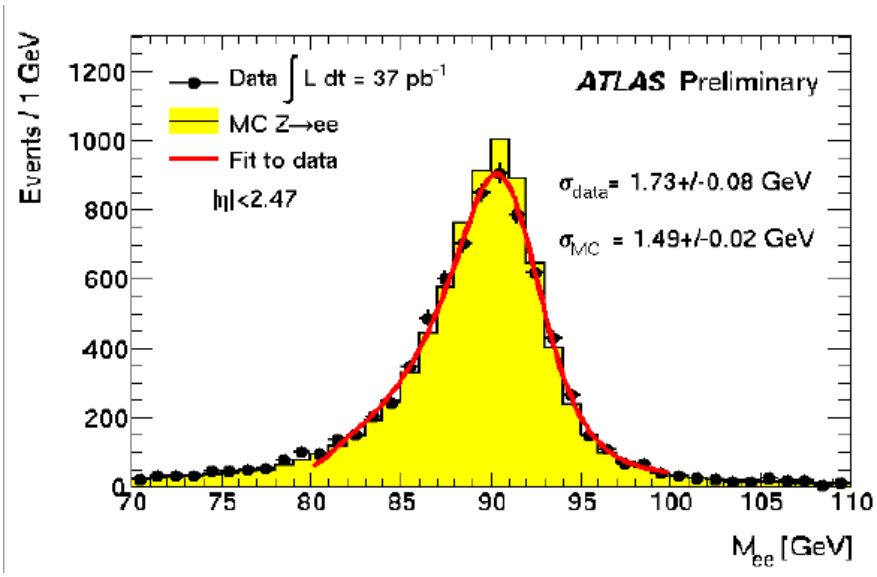

Figure C.5: The dielectron invariant mass distribution is fitted with a Breit-Wigner convoluted with a Crystal Ball[43]. The obtained resolution (σ of the Crystal Ball) is 1.73 ± 0.08. 36.6 pb^{-1}of data is used. Electrons are required to be identified as medium, have E_T>20 GeV and $|\eta| < 2.47$ (excluding the crack $1.37 < |\eta| < 1.52$). Dielectrons with opposite sign and invariant mass between 80 GeV and 100 GeV are used in the fit.

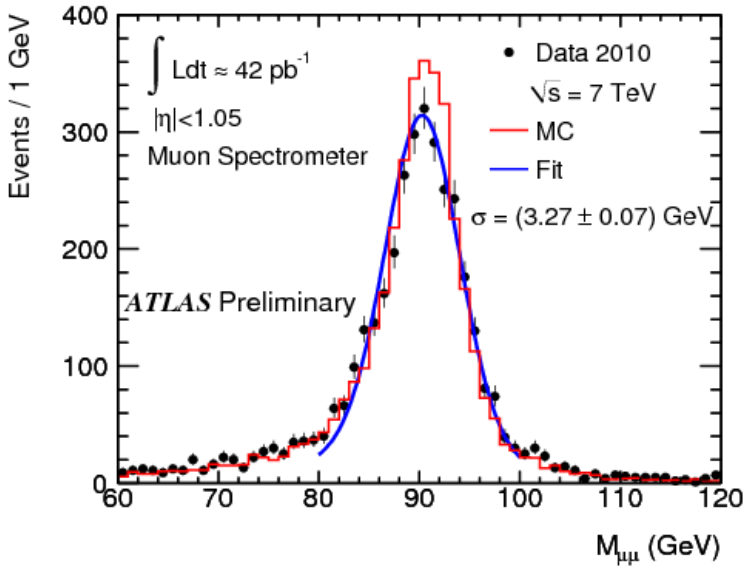

Figure C.6: Dimuon invariant mass distribution for muons measured only with the muon spectrometer is fitted with unknown function (https://twiki.cern.ch/twiki/bin/view/AtlasPublic/MuonPerformancePublicPlots). Oppositely charged, isolated muon pairs with $p_T^{\mathrm{ME}} > 20$ GeV within $|\eta| < 1.05$ are chosen. The isolation criteria is $p_T^{\Delta R<0.4}/p_T < 0.2$. Events are triggered by `EF_mu10` at low luminosity and `EF_mu13` at higher.

Bibliography

[1] F. Englert and R. Brout. Broken symmetry and the mass of gauge vector mesons. *Phys. Rev. Lett.*, 13(9):321–323, Aug 1964.

[2] G. S. Guralnik, C. R. Hagen, and T. W. B. Kibble. Global conservation laws and massless particles. *Phys. Rev. Lett.*, 13(20):585–587, Nov 1964.

[3] A. Quadt. Top quark physics at hadron colliders. *Eur. Phys. J. C*, 48(3):835–1000, 2006.

[4] K Nakamura and Particle Data Group. Review of Particle Physics. *Journal of Physics G: Nuclear and Particle Physics*, 37(7A):075021, 2010.

[5] Sheldon L. Glashow. Partial-symmetries of weak interactions. *"Nuclear Physics"*, 22(4):579 – 588, 1961.

[6] Weinberg, Steven . A Model of Leptons. *Phys. Rev. Lett.*, 19(21):1264–1266, Nov 1967.

[7] Nobel Symposium and Nobelstiftelsen. . *Elementary particle theory. Relativistic groups and analyticity. Proccedings of the Eighth Nobel Symposium held May 19-25, 1968 at Aspenasgarden, Lerum, in the county of Alvsborg, Sweden. Edited by Nils Svartholm* . Almqvist and Wiksell; John Wiley, Stockholm, New York, London [etc.] , 1968 .

[8] Hasert et al. 1973a.

[9] T. Kinoshita, editor. *Advanced Serios on Directions in High Energy Physics - Vol. 7 Quantum Electrodynamics*. Cornell, 1990.

[10] Wu, C. S. and Ambler, E. and Hayward, R. W. and Hoppes, D. D. and Hudson, R. P. Experimental Test of Parity Conservation in Beta Decay. *Phys. Rev.*, 105(4):1413–1415, Feb 1957.

[11] F. Mandl and G. Shaw. *Quantum field theory*. Wiley, Revised Edition edition, 1997.

[12] M. Thomson. Tests of lepton universality from tau decays at LEP. pages 331–338. Editions Frontieres, Gif-sur-Yvette, 1996.

[13] D. Griffiths. *Introduction to Elementary Particles*. John Wiley and Sons Inc, Second Edition edition, 1987.

[14] Paul Langacker and Jens Erler and Eduardo Peinado. Neutrino physics. *Journal of Physics: Conference Series*, 18(1):154, 2005.

[15] S. A. Thomas, F. B. Abdalla, O. Lahav. Upper Bound of 0.28 eV on Neutrino Masses from the Largest Photometric Redshift Survey. *Physical Review Letters*, 105(3):031301–+, July 2010.

[16] Ugo Amaldi, Wim de Boer, and Hermann Fürstenau. Comparison of grand unified theories with electroweak and strong coupling constants measured at LEP. *Physics Letters B*, 260(3-4):447 – 455, 1991.

[17] T. G. Rizzo. Z' Phenomenology and the LHC. *ArXiv High Energy Physics - Phenomenology e-prints*, 2006.

[18] Mirjan Cvetič and Stephan Godfrey. Discovery and Identification of Extra Gauge Bosons. *ArXiv High Energy Physics - Phenomenology e-prints*, 1995.

[19] Pei-Hong Gu. Left-right symmetric model for neutrino masses, baryon asymmetry, and dark matter. 81(9), May 2010.

[20] The LEP Collaborations: ALEPH Collaboration and DELPHI Collaboration and L3 Collaboration and OPAL Collaboration and the LEP Electroweak Working Group . A Combination of Preliminary Electroweak Measurements and Constraints on the Standard Model. *ArXiv High Energy Physics - Experiment e-prints*, December 2006.

[21] The CDF Collaboration. Search for high mass resonances decaying to muon pairs. 2010. CDF/PHYS/EXO/PUBLIC/10165.

[22] The D0 Collaboration. Search for a heavy neutral gauge boson in the dielectron channel with 5.4 fb^{-1} of $p\bar{p}$ collisions at $\sqrt{s} = 1.96$ TeV. *Physics Letters B*, 695:88–94, 2011.

[23] W. R. Leo. *Techniques for Nuclear and Particle Physics Experiments*. Springer, Second Edition edition, 1994.

[24] DONALD E. GROOM, NIKOLAI V. MOKHOV, and SERGEI I. STRIGANOV. MUON STOPPING POWER AND RANGE TABLES 10 MeV-100 TeV. *"Atomic Data and Nuclear Data Tables"*, 78(2):183 – 356, 2001.

[25] G. Aad and others. The ATLAS Experiment at the CERN Large Hadron Collider. *JINST*, 3:S08003, 2008.

[26] CERN Document Server. http://cdsweb.cern.ch/collection/Photos?ln=en.

[27] Capéans-Garrido, M. The transition radiation tracker of the ATLAS experiment. *IEEE Trans. Nucl. Sci.*, 51:994–1000, 2004.

[28] Hance, M. Readout of the ATLAS Transition Radiation Tracker: Timing Parameters and Constraints. Technical Report ATL-INDET-PUB-2008-008. ATL-COM-INDET-2008-002, CERN, Geneva, Sep 2007.

[29] Haywood, S and Rossi, L and Nickerson, R and Romaniouk, A. *ATLAS inner detector: Technical Design Report, 2*. Technical Design Report ATLAS. CERN, Geneva, 1997.

[30] ATLAS Collaboration. *Expected performance of the ATLAS experiment: detector, trigger and physics*. CERN, Geneva, 2009.

[31] P. Osland and A. A. Pankov and A. V. Tsytrinov and N. Paver. Spin identification of the Randall-Sundrum resonance in lepton-pair production at the CERN LHC. 78(3), 2008.

[32] Dobbs. M. A.and Frixione. S.and Laenen. E.and Tollefson. K.and Baer. H.and Boos. E.and Cox. B.and Engel. R.and Giele. W.and Huston. J.and Ilyin. S.and Kersevan. B.and Krauss. F.and Kurihara. Y.and Lonnblad. L.and Maltoni. F.and Mangano. M.and Odaka. S.and Richardson. P.and Ryd. A.and Sjostrand. T.and Skands. P.and Was. Z.and Webber. B. R.and Zeppenfeld. D. Les Houches Guidebook to Monte Carlo Generators for Hadron Collider Physics. *ArXiv High Energy Physics - Phenomenology e-prints*, 2004.

[33] Assamagan, K et al. The ATLAS Monte Carlo Project. Technical Report ATL-SOFT-INT-2010-002, CERN, Geneva, 2010.

[34] CERN. Geneva. LHC Experiments Committee ; LHCC. *ATLAS detector and physics performance: Technical Design Report, 1.* Technical Design Report ATLAS. CERN, Geneva, 1999. Electronic version not available.

[35] Aharrouche, M and Anastopoulos, C and Dao, V and Derue, F and Dudziak, F and Fedin, O and Fournier, D and Froidevaux, D and Hartert, J and Iconomidou-Fayard, L and Kerschen, K and Koenig, S and Koffas, T and Maleev, V and Paganis, E and Pásztor, G and Poveda, J and Robichaud-Véronneau, A and Schaffer, A and Sarangi, T and Sedykh, E and Solovyev, V and Tackmann, K and Theveneaux-Pelzer, T and Urquijo, P and Wielers, M and Wu, S L. Expected electron performance in the ATLAS experiment. Technical Report ATL-PHYS-INT-2010-126, CERN, Geneva, Nov 2010.

[36] Glen Cowan. Error analysis for efficiency. http://www.pp.rhul.ac.uk/ cowan/stat/notes/efferr.pdf.

[37] Schäfer, M and Ledroit, F and Trocmé, B. $Z' \rightarrow e^+e^-$ studies in full simulation (DC1). Technical Report ATL-PHYS-PUB-2005-010. ATL-COM-PHYS-2005-026, CERN, Geneva, 2005.

[38] S. I. Bityukov and N. V. Krasnikov. Signal significance in the presence of systematic and statistical uncertainties. *"Nuclear Instruments and Methods in Physics Research Section A: Accelerators, Spectrometers, Detectors and Associated Equipment"*, 502(2-3):795 – 798, 2003. "Proceedings of the VIII International Workshop on Advanced Computing and Analysis Techniques in Physics Research".

[39] The ATLAS Collaboration. Measurement of the $W \rightarrow l\nu$ and $Z/\gamma^* \rightarrow ll$ production cross sections in proton-proton collisions at $\sqrt{s} = 7$ TeV with the ATLAS detector. *ArXiv e-prints*, October 2010.

[40] The ATLAS Collaboration. Data-Quality Requirements and Event Cleaning for Jets and Missing Transverse Energy Reconstruction with the ATLAS Detector in Proton-Proton Collisions at a Center-of-Mass Energy of $\sqrt{s} = 7$ TeV. Technical Report ATLAS-CONF-2010-038, CERN, Geneva, Jul 2010.

[41] ATLAS. Updated distributions for $W \to l\nu$ and $Z \to ll$ production in proton-proton collisions at $\sqrt{s} = 7$ TeV with the ATLAS detector. Technical Report ATL-COM-PHYS-2010-898, CERN, Geneva, Nov 2010.

[42] Read, A L. Modified frequentist analysis of search results (the CL_s method). (CERN-OPEN-2000-205), 2000.

[43] Makovec, N and Donega, M and Hubaut, F and Ahmad, A. Calibrated $Z \to e^+e^-$ invariant mass with 36 pb^{-1}. Technical Report ATL-COM-PHYS-2010-895, CERN, Geneva, Nov 2010.